

An Optical Reference and Frequency Comb for Improved Spectroscopy of Helium

A thesis presented

by

Daniel Farkas

to

The Department of Physics

in partial fulfillment of the requirements

for the degree of

Doctor of Philosophy

in the subject of

Physics

Harvard University

Cambridge, Massachusetts

November 2006

©2006 - Daniel Farkas

All rights reserved.

Thesis advisor

Author

Gerald Gabrielse

Daniel Farkas

An Optical Reference and Frequency Comb for Improved Spectroscopy of Helium

Abstract

An optical frequency comb was used to transfer the high stability and narrow linewidth of an iodine optical frequency reference to a diode laser at 1083 nm. This new optical source was developed as an important step toward an improved measurement of the helium $2^3S - 2^3P_J$ optical transition frequencies and fine structure intervals, as needed to determine the fine structure constant α and test QED. The 1083 nm diode laser was used to perform saturated absorption spectroscopy on helium atoms in a variable-pressure discharge cell. Using the new source, what had been the largest source of drift was removed and an improved resolution of 100 Hz was achieved. This improved resolution was used to search for systematics that would affect helium spectroscopy at a higher level of precision. Although several improved studies of already-known systematics are presented, three new sources of systematic frequency shifts were discovered: laser beam misalignment, a residual linescan asymmetry, and an imbalance in signal sizes for transitions between resolved magnetic sublevels. As a contribution to future measurements at a higher accuracy, we measure and model these three dominant error sources, and explore their underlying physical mechanisms.

Contents

Title Page	i
Abstract	iii
Table of Contents	iv
List of Figures	viii
List of Tables	xix
Acknowledgments	xx
1 Introduction	1
2 Background and Motivation	5
2.1 Measurements of the Fine Structure Constant	5
2.1.1 Electron Anomalous Magnetic Moment	6
2.1.2 Muonium Hyperfine Structure	6
2.1.3 Fine Structure	8
2.1.4 Mass Ratios and h/M	10
2.1.5 Quantum Hall Effect	11
2.1.6 Proton Gyromagnetic Ratio	12
2.2 The Structure of Helium	14
2.2.1 The Non-Relativistic Hamiltonian	14
2.2.2 Finite Mass Corrections	19
2.2.3 Finite Nuclear Size	19
2.2.4 Relativistic Corrections	19
2.2.5 Complete Non-QED Energy	20
2.2.6 The 2^3P Fine Structure Intervals	21
2.2.7 The $2^3S - 2^3P$ Optical Transition Frequency	22
2.3 Experimental Measurements	22
2.3.1 Helium Fine Structure Measurements	22
2.3.2 The $2^3S - 2^3P$ Transition Frequency	27
3 The Molecular Iodine Optical Frequency Reference	32
3.1 Introduction	32

3.2	Improving Frequency Reference Stability	33
3.3	Modulation Transfer Spectroscopy	37
3.4	Experimental Setup	41
3.4.1	Nd:YAG Non-planar Ring Oscillator	41
3.4.2	Second Harmonic Generation in PPLN	45
3.4.3	Pump and Probe Beams	47
3.4.4	The Iodine Cell	50
3.4.5	Signal Detection and Electronics	51
3.5	Iodine Reference Stability	54
3.6	Conclusion	57
4	The Optical Frequency Comb	58
4.1	Principles of Mode-Locked Lasers	62
4.1.1	Time Domain Description	62
4.1.2	Frequency Domain Description	65
4.1.3	Operation of Mode-locked Lasers	66
4.1.4	Frequency Control of Mode-Locked Lasers	71
4.2	Experimental Apparatus	73
4.2.1	Kerr-Lens Mode-locked Titanium:Sapphire Laser	73
4.2.2	Nd:YVO ₄ Pump Laser	78
4.2.3	Spectral Broadening in a Microstructure Fiber	80
4.2.4	The Comb Offset δ	83
4.2.5	Stabilizing the Optical Comb to the Iodine Reference	98
4.2.6	Counting the Repetition Rate	101
4.3	The Comb-Stabilized Diode Laser	102
4.3.1	Phase-locking the Diode Laser to the Frequency Comb	102
4.3.2	Narrowing Laser Linewidth with a Stabilized Frequency Comb	104
4.3.3	Measuring the Optical Frequency of the Comb-Stabilized Diode Laser	107
4.3.4	The Accuracy of Optical Frequency Measurements	109
5	Experimental Setup for Helium Spectroscopy	112
5.1	Vacuum System	115
5.2	RF Discharge	117
5.3	Magnet	120
5.3.1	Magnet Power Supply	121
5.3.2	Magnetic Field Stability	123
5.3.3	Magnetic Field Homogeneity	123
5.4	External-Cavity Diode Lasers	125
5.4.1	Cavity Layout	126
5.4.2	Current Controller	126
5.4.3	Frequency Control	130

5.4.4	Measuring Diode Laser Linewidth	131
5.5	Optics Components and Signal Detection	132
5.5.1	The Scan and Comb-Stabilized Diode Lasers	132
5.5.2	Pump and Probe Optics	134
5.5.3	Signal Photodetection	139
5.5.4	Lock-in Detection	140
5.6	Scan Laser Offset-Lock	141
5.6.1	Beat Detection and Signal Processing	141
5.6.2	Digital Phase/Frequency Detector and PLL Filter	142
5.6.3	Offset-Locking Procedure	145
5.7	Measuring Background Channels	147
5.8	Computer Interface	148
6	Expected and Observed Lineshapes	150
6.1	Amplitude Modulation Transfer Spectroscopy	151
6.2	Light-Pressure	154
6.2.1	Atomic Recoil	155
6.2.2	Light-Pressure Shifts in a Closed Two-Level System	156
6.2.3	Correcting for Light-Pressure Shifts	159
6.3	The Zeeman Effect in Helium	160
6.3.1	Calculation of Zeeman Shifts	161
6.3.2	Helium Lineshapes in an External Magnetic Field	164
6.3.3	The P_1 Magnetometer	165
6.4	Velocity-Changing Collisions	166
6.5	Scan Patterns and Data Fitting	169
6.5.1	Scan Patterns	169
6.5.2	Frequency Patterns	169
6.5.3	Nonlinear Regression and Sample Linescans	171
6.5.4	Statistical Analysis	176
7	Well-Understood Systematic Effects	179
7.1	Light-Pressure Shifts	180
7.2	Linear Pressure Shifts	183
7.2.1	Correcting for Light-Pressure and Zeeman Shifts	183
7.2.2	Assigning Error Bars	184
7.2.3	Measurements of Linear Pressure Shifts	186
7.3	RF Discharge Power Shifts	193
7.4	Polarization Shifts	202
7.5	Conclusions	204

8	Systematics That Require Further Study	207
8.1	Laser Beam Misalignment Shifts	209
8.1.1	Beam Misalignment for Thermally-Distributed Gases	209
8.1.2	Dynamics of an RF Discharge	211
8.1.3	Residual Doppler Shifts in an RF Discharge	212
8.1.4	Measurements of Beam Misalignment Shifts	216
8.1.5	Misalignment Shifts for the Optical Transition Frequencies	225
8.1.6	Misalignment Shifts for the Fine Structure Intervals	226
8.2	Asymmetries in the Linescans	226
8.2.1	Asymmetry Due to Laser Light Pressure	230
8.2.2	Self-focusing	232
8.2.3	Analyzing the Linescan Asymmetry	241
8.2.4	Conclusions	249
8.3	Peak Imbalances	249
8.3.1	Measurements of Peak Imbalance	250
8.3.2	Searching for an Explanation for the Peak Imbalance	253
8.3.3	Frequency Shifts Due to Peak Imbalance	255
8.4	Optical Power Shifts	260
8.4.1	AC Stark Shifts Calculations	260
8.4.2	Measurements of Optical Power Shifts	263
8.4.3	AC Stark Shift Corrections	268
8.5	Conclusions	269
9	Conclusions	270
9.1	Experimental Resolution Has Been Significantly Improved	271
9.2	Preparing the Way for Improved Spectroscopy of the $2^3S - 2^3P_J$ Tran- sitions	273
9.2.1	Comparison of Known Systematic Effects	275
9.2.2	Understanding and Eliminating the Dominant Systematic Effects	277
9.2.3	Improving Experimental Resolution	280
9.3	Measurements of the $2^3S - 3^3P_J$ Fine Structure Intervals and Optical Transition Frequencies	282
9.4	Conclusions	283
	Bibliography	285

List of Figures

2.1	Comparison of the most accurate measurements of the fine structure constant α . Due to theoretical discrepancies, the value of α obtained from helium fine structure disagrees with the CODATA value by several standard deviations. As a result, this value is not included in the CODATA adjustment.	7
2.2	Energy diagram of the low-lying spin-triplet states of ^4He . The 2^3P splittings are not drawn to scale.	15
2.3	Comparison of experimental measurements and theoretical predictions for the (a) $2^3P_1 - 2^3P_2$, (b) $2^3P_0 - 2^3P_1$, and (c) $2^3P_0 - 2^3P_2$ fine structure intervals. Open symbols are indirect values calculated from direct values of the other two intervals.	24
2.4	(a) Measurements and most recent theoretical prediction for the $(2J + 1)$ -weighted mean value of the $2^3S - 2^3P$ transition frequency. (b) Over the past 20 years, the experimental accuracy of the $2^3S - 2^3P$ frequency has improved by almost four orders of magnitude.	28
3.1	(a) Measured frequencies between the ^3He reference and the $2^3S - 2^3P_0$ transition of ^4He drift approximately 15 kHz over four hours. (b) Measured with the new frequency reference system, the corresponding frequencies of the ^3He reference drift a similar amount. (c) Correlation plot of the helium frequencies in (a) and the optical frequencies in (b).	34
3.2	(a) Frequency measurements of the ^3He reference, measured by counting the repetition rate of the helium-stabilized optical frequency with respect to a Rb standard. (b) Allan deviation of the ^3He reference and Rb standard.	35
3.3	Nearly degenerate four-wave mixing in a two-level system emits a phase-conjugate photon: (a) absorption of pump carrier photon and emission of pump sideband photon; (b) absorption of pump sideband photon and emission of pump carrier photon [66].	40
3.4	Theoretical MTS lineshapes for different values of the modulation frequency δ : (a) $\delta = 10\gamma$; (b) $\delta = \gamma/2$; $\delta = \gamma/10$	41

3.5	Diagram of the molecular iodine optical frequency reference.	42
3.6	Layout of the Nd:YAG non-planar ring oscillator [68]. The crystal is pumped through the front face (A) that also serves as an output coupler. Non-planar reflections (B-C-D) introduce a polarization rotation. A positive Verdet constant turns the crystal into a Faraday rotator when an external magnetic field is applied.	43
3.7	Residual intensity noise of the NPRO: (a) low-frequency, resolution bandwidth of 10 kHz; (b) high-frequency, resolution bandwidth of 100 kHz. Both plots are averaged 100 times.	44
3.8	The resonant LC step-up circuit used to generate driving signals of several hundred volts across the EOM.	49
3.9	Voltage enhancement of the EOM driving signal in a resonant LC step-up circuit.	49
3.10	The servo circuit used for the iodine reference.	52
3.11	Experimental MTS lineshape of the R(56)32-0:a ₁₀ transition in ¹²⁷ I ₂ . The trace was averaged 16 times.	53
3.12	Measured closed-loop gain and phase of the iodine feedback loop. . .	54
3.13	Frequency measurements of the iodine-stabilized comb repetition rate. . .	55
3.14	Fractional frequency stabilities.	56
3.15	Fitted center frequencies of the 2 ³ S – 2 ³ P ₀ transition of ⁴ He show significantly less drift when stability is derived from the iodine reference instead of the helium reference. The y-axis scale is the same for both plots.	57
4.1	Diagram of the frequency chain used to perform the first measurement of an optical frequency with respect to a cesium standard [83, 84]. The equations on the left indicate the relationship between pairs of oscillator frequencies, with ν_{iB} (i=1,2,3,...) representing the beat note frequencies monitored with a spectrum analyzer or counter [85]. . . .	59
4.2	Schematic of the optical frequency comb. The comb offset δ is detected and phase-locked while a beat at 1064 nm between the comb and iodine reference is used to stabilize the repetition rate f_{rep} . A 1083 nm diode laser is stabilized using its beat with the comb. At the same time, f_{rep} is detected and counted.	63
4.3	A pulse-train in the (a) time domain corresponds to a comb in the (b) frequency domain. A pulse-to-pulse phase shift $\Delta\phi$ between the carrier and envelope causes the frequencies f_n to be offset from integer multiples of the repetition rate f_{rep} by δ [4].	64
4.4	Constructive interference between (a) 5 modes, and (b) 20 modes gives rise to a pulse-train. The more modes that contribute, the shorter the pulses [77].	67

4.5	A high-intensity Gaussian laser beam is focused in a Kerr medium due to an intensity-dependent index of refraction [98].	68
4.6	Self-phase modulation in a Kerr medium: (a) phase modulation is proportional to the intensity $I(t)$ of the pulse; (b) the instantaneous frequency modulation $\delta\omega(t)$ is proportional to $d(I)/dt$; (c) the frequency modulation generates upchirped pulses, where the front of the pulse is red-shifted with respect to the carrier, while the tail of the pulse is blue-shifted [71].	69
4.7	Negative dispersion mirrors: longer wavelengths penetrate farther into the stack, corresponding to a longer cavity round-trip travel time [100].	70
4.8	Power spectrum of the modelocked Ti:Saph pulses and microstructure fiber output, as measured with a monochromator.	74
4.9	Layout of the optical components in the Ti:Saph laser cavity [105]. . .	75
4.10	The Ti:Saph piezo driver.	77
4.11	Layout of the optical components in the Verdi laser cavity [106]. . . .	79
4.12	Switching power supply noise on the optical output of the Verdi. . . .	81
4.13	(a) In an air-silica microstructure fiber, a silica core is surrounded by a hexagonal array of air holes [87]; (b) Cross-sectional view of the air-silica microstructure fiber used in this work [107].	82
4.14	Optical layout of the frequency comb: CM = cold mirror; $\lambda/2$ = half-waveplate; Pol = polarizer; SHG = second harmonic generation; BS = beamsplitter; BPF = interference bandpass filter.	85
4.15	Photodetector and front-end amplifiers for detecting the comb offset δ .	86
4.16	Spectrum analyzer trace showing the two lowest comb offset beats at frequencies δ and $f_{rep} - \delta$	87
4.17	Layout of the comb offset tracking oscillator.	88
4.18	Loop filters and amplifiers for the comb offset tracking oscillator. . . .	90
4.19	Calculated Bode and phase plots for the tracking oscillator PLL. . . .	91
4.20	Spectrum analyzer trace of the tracking oscillator output when phase-locked to a 425 MHz synthesizer signal.	92
4.21	The EOM offset driver.	93
4.22	Layout of the ADF4110/4111 digital frequency synthesizer IC [111]. . .	95
4.23	The digital PFD charge pump filter and output buffers.	96
4.24	Calculated Bode and phase plots for the comb offset PLL.	98
4.25	Spectrum analyzer traces of the phase-locked comb offset δ . (a) The spikes at 105 kHz and harmonics is due to switching power supply noise in the Verdi pump laser. (b) The spikes are significantly reduced by floating the anodes of the diode arrays that power the Verdi.	99
4.26	The phase-advance filter used in the f_I PLL.	100
4.27	Calculated Bode and phase plots for the iodine-comb PLL.	101
4.28	Spectrum analyzer traces of the phase-locked beat f_I	102
4.29	Calculated Bode and phase plots for the CSDL PLL.	104

4.30	Spectrum analyzer trace of the phase-locked beat f_{1083}	105
4.31	The delayed self-heterodyne interferometer for measuring laser linewidth.	106
4.32	Spectrum analyzer trace of the 80 MHz NPRO beat from the delayed self-heterodyne interferometer.	107
4.33	Spectrum analyzer traces of the 80 MHz beat of the diode laser when free-running and phase-locked to the iodine-stabilized frequency comb.	108
4.34	Stability plot of the free-running Rb standard (red) and GPS 1 PPS signal (blue) used to infer the inaccuracy of the Rb standard for times shorter than the time constant of the GPS tracking ($\tau_0=18$ hours). The dashed line between 10^4 and 10^5 seconds shows the expected degradation of the stability of the Rb standard when tracking GPS.	110
5.1	Energy diagram of the low-lying states of ^4He . With a transition wavelength of 59 nm, direction excitation of the 2^3P_J states from the ground state is inaccessible with table-top laser systems.	113
5.2	Vacuum system used to stabilize the pressure of helium gas in the glass cell.	116
5.3	A discharge coil wrapped around the cell excites helium atoms to the metastable 2^3S_1 state.	118
5.4	RF electronics used to drive the discharge and monitor voltage standing-wave ratio. An antenna tuner matches the load impedance to the 50Ω output impedance of the amplifier.	119
5.5	The RF power absorbed by the helium atoms is stable to $\pm 0.1\%$ over several hours.	119
5.6	Cross-sectional view of the Helmholtz coils used to create a vertical magnetic field of up to 200 Gauss. Each coil consists of 238 turns of 16 AWG magnet wire that is wrapped onto a water-cooled aluminum frame.	120
5.7	The magnet is driven by a high-stability current supply that provides up to 7A of current with a stability of $<3\text{ppm}$	121
5.8	By measuring the frequency splitting of the $m = \pm 1$ sublevels of the $2^3S_1 \rightarrow 2^3P_1$ transition, the stability of the magnetic field is determined to be $<3\text{ppm}$ over several hours.	122
5.9	Histogram of numerically-simulated magnetic field values at (a) 108 Gauss and (b) 55 Gauss.	124
5.10	Layout of a 1083 nm external-cavity diode laser. Linearly-polarized light from an anode-grounded laser diode, after collimated by a lens, has its ellipticity removed by an anamorphic prism pair. Output coupling is controlled by a polarized beamsplitter and $\lambda/2$ -plate. Frequency tuning is achieved by modulating the cavity length with a piezoelectric transducer.	127

5.11	Schematic of the diode laser current controller. Using feedback, an op-amp (LT1128) controls a FET (2N7000) to stabilize the voltage across a pair of high-stability resistors (VPR221). The setpoint voltage is derived from either an internal voltage reference (MAX6250) or external DAC.	128
5.12	Diode laser output power scales linearly with drive current. The laser's output coupling is set to 50%. The jump at 200 mA is attributed to a mode-hop.	129
5.13	Diode laser linewidth versus output coupling.	132
5.14	Layout of the scan laser and CSDL. After amplification in a pair of Yb-doped fiber amplifiers, approximately 1 mW of each laser's output is used to form a heterodyne beat for offset-locking. A polarized beam-splitter cube and $\lambda/2$ -plate split the scan laser output into pump and probe beams.	133
5.15	Optical components for pump and probe beams. Each beam is spatially filtered in a PM fiber, power-stabilized, and expanded in a telescope. The polarization of each beam is purified with a Glan-Thompson polarizer. An autobalanced photodetector reduces the effects of amplitude noise.	135
5.16	Electronic setup for amplitude modulation of the pump beam.	136
5.17	Reduction of laser intensity noise using two power levellers.	136
5.18	(a) Presence of a background offset due to a weak reflection of the pump beam off a beamsplitter cube; (b) a four-fold reduction of this offset is achieved with a beamsplitter plate.	139
5.19	Reduction of laser intensity noise at 76 kHz with the autobalanced photodetector. The resolution bandwidth is 9.55 Hz.	140
5.20	Microwave electronics for detection and processing of the beat frequency between the scan laser and CSDL.	143
5.21	Loop filter for the diode laser offset PLL.	143
5.22	Spectrum analyzer traces of the phase-locked beat between the scan laser and CSDL show a 10-fold increase in locking bandwidth when the laser's piezo transducer is switched from (a) a low-bandwidth piezo tube to (b) a high-bandwidth monolithic piezo stack.	144
5.23	Spectrum analyzer traces of the phase-locked beat between the scan laser and CSDL show an increase in locking bandwidth to 500 kHz when current feedback is applied. (a) Several noise spikes are visible when the diode lasers are powered by commercial current supplies; (b) A cleaner spectrum is obtained when the lasers are powered by the circuit in Fig.5.11.	145

6.1	The in-phase component of the theoretical MTS lineshape for an amplitude-modulated pump. (a) For small modulation frequencies $\delta \ll \gamma$, the signal approximates a single Lorentzian centered at ω_0 . (b) For $\delta \sim \gamma$, two Lorentzian components are resolved. (c) For $\delta \gg \gamma$, the signal size decreases due to the inability of the atoms to respond to faster fields.	153
6.2	The quadrature component of the theoretical MTS lineshape for an amplitude-modulated pump. (a) For small modulation frequencies $\delta \ll \gamma$, the two dispersive components mostly cancel. (b) For $\delta \sim \gamma$, the two components are resolved and reach their maximum height. (c) For $\delta \gg \gamma$, the amplitude decreases due to the inability of the atoms to respond to faster fields.	153
6.3	Measured values of the (a) linewidth and (b) signal amplitude depend quadratically on modulation frequency for small modulation frequencies $\delta \ll \gamma$. The data is taken from measurements of the $2^3S - 2^3P_1$ transition at a cell pressure of 40 mtorr and laser power of 100 μW per beam.	154
6.4	Recoil of atoms upon absorption of pump photons leads to a small dispersive modification of the atomic velocity profile that in turn introduces systematic frequency shifts.	155
6.5	Allowed transitions when magnetic sublevels are resolved and both pump and probe beams have polarizations parallel to the magnetic field. Shown for each allowed transition is the mean number of photons $\langle n \rangle$ scattered before decaying to a ground state not resonant with the laser fields.	159
6.6	Clebsch-Gordan coefficients for the $2^3S - 2^3P_J$ transitions.	160
6.7	Position of signal peaks and dips for the $2^3S - 2^3P_J$ transitions in an external magnetic field when both pump and probe polarizations are parallel to the field [113]. The linear Zeeman splitting is $\Delta = \mu B$. The two dips in the P_2 lineshape are due to crossover resonances.	164
6.8	Depletion of a ground-state velocity class resonant with a laser leads to the formation of a Bennett hole [115]. Rethermalizing velocity-changing collisions (VCC) knock atoms into the hole, leading to an enhancement of the detected signal.	167
6.9	(a) Sample linescan of the $2^3S - 2^3P_0$ transition and best fit. (b) Residuals when a VCC Gaussian term is included in the fitting function. (c) A large Gaussian background appears in the residuals when the VCC Gaussian term is not included.	173
6.10	(a) Sample linescan of the $2^3S - 2^3P_1$ transition and best fit. (b) Residuals when VCC Gaussian terms are included in the fitting function. (c) Large Gaussian backgrounds appear in the residuals when VCC Gaussian terms are not included.	174

6.11	(a) Sample linescan of the $2^3S - 2^3P_2$ transition and best fit. (b) Residuals when VCC Gaussian terms are included in the fitting function. (c) Large Gaussian backgrounds appears in the residuals when VCC Gaussian terms are not included.	175
6.12	Measurements of the f_{12} fine structure interval. The cell pressure was 30 mtorr and the optical power of each laser beam was $100 \mu\text{W}$	177
6.13	Measurements of the $2^3S - 2^3P_1$ transition. The cell pressure was 30 mtorr and the optical power of each laser beam was $100 \mu\text{W}$	178
7.1	Histogram of measured values of δ_{LP} at (a) 30 mtorr, and (b) 15 mtorr. Each histogram fits well to a Gaussian function (solid line). Here, the optical power of each laser beam was $100 \mu\text{W}$, the discharge drive power was 4.5 Watts, and the external magnetic field was 108 Gauss.	181
7.2	Measured values of the light-pressure shift $\delta_{LP}(p)$, obtained by measuring the difference $\Delta(p)$ between the $m = 0$ peak frequency and the average of the $m = \pm 1$ peak frequencies of P_2 linescans. The data has been corrected for nonlinear Zeeman shifts.	181
7.3	Standard deviation versus pressure at 108 Gauss. The solid lines are best-fits.	187
7.4	Standard deviation versus pressure at 55 Gauss. The solid lines are best-fits.	188
7.5	Linear extrapolations to zero pressure at 55 Gauss. The power of the pump and probe beams was $100 \mu\text{W}$ each, and the power of the RF discharge was 1 Watt.	190
7.6	Linear extrapolations to zero pressure at 108 Gauss. The power of the pump and probe beams was $100 \mu\text{W}$ each, and the power of the RF discharge was 4.5 Watts.	191
7.7	Lorentzian amplitudes of the $2^3S - 2^3P_0$ transition as a function of discharge power.	194
7.8	Linear extrapolations to zero discharge power for a magnetic field of 55 Gauss and cell pressure of 20 mtorr.	196
7.9	Linear extrapolations to zero discharge power for a magnetic field of 55 Gauss and cell pressure of 40 mtorr.	197
7.10	Linear extrapolations to zero discharge power for a magnetic field of 108 Gauss and cell pressure of 30 mtorr.	198
7.11	Frequency shifts as a function of pump and probe polarization angle for the fine structure intervals and light-pressure shift δ_{LP} . The cell pressure was 30 mtorr, the optical power of each laser beam was $100 \mu\text{W}$, the discharge drive power was 1 Watt, and the external magnetic field was 55 Gauss.	204
7.12	Frequency shifts as a function of pump and probe polarization angle for the $2^3S - 2^3P_J$ optical transitions.	205

8.1	Imperfect alignment of pump k-vector \vec{k}_{pump} , probe k-vector \vec{k}_{probe} , and atomic velocity vector \vec{v}_{atom}	210
8.2	Ionization and recombination in a weakly-ionized gas. (a) Ionization: free electrons quickly travel throughout the cell, resulting in a population of helium ions at the center of the cell; (b) helium ions diffuse to the cell wall, where they recombine with electrons to form neutral helium atoms. These neutral atoms drift radially inward to replenish those atoms that are ionized at the center of the cell.	213
8.3	Side view of saturated absorption spectroscopy in an RF discharge cell. Due to the radial drift of the helium atoms, misaligned pump (blue) and probe (red) beams detect unequal numbers of oppositely-moving atoms (purple). (a) For a misalignment angle θ , more downward moving atoms are detected. (b) For a misalignment angle $-\theta$, more upward moving atoms are detected. The axis of the discharge is represented by the dashed line. Vertical arrows indicate the direction in which helium atoms diffuse.	214
8.4	Side view of saturated absorption spectroscopy in an RF discharge cell. Pump (blue) and probe (red) beams detect atoms to the side of the discharge axis (dashed line). For both misalignment angles (a) θ and (b) $-\theta$, more downward moving atoms are detected (purple). Vertical arrows indicate the direction in which helium atoms diffuse.	215
8.5	Experimental setup used to detect beam misalignment shifts. The horizontal and vertical angles at which the pump beam enters the cell are adjusted using a pair of micrometers mounted into a mirror mount.	216
8.6	Frequency shifts as a function of beam alignment angle θ in the (a) vertical and (b) horizontal directions. Residual Doppler broadening gives rise to (c,d) a broadening of the Lorentzian linewidth, and (e,f) a decrease in the Lorentzian amplitude. The angle 0 corresponds to the best alignment that could be achieved by maximizing transmission through irises located on each end of the cell. The cell pressure was 40 mtorr, the optical power of both laser beams was 100 μ W, the discharge drive power was 4.5 Watts, and the external magnetic field was 108 Gauss.	218
8.7	(a) The overlap (purple) between pump (blue) and probe (red) beams is small when the beams are parallel, but laterally displaced from each other by a distance D . (b) The overlap is improved when one of the beams is misaligned.	220

-
- 8.8 Frequency shifts as a function of beam alignment angle θ in the (a) vertical and (b) horizontal directions. Residual Doppler broadening gives rise to (c,d) a broadening of the Lorentzian linewidth, and (e,f) a decrease in the Lorentzian amplitude. The angle 0 corresponds to the best alignment that could be achieved using the technique of cross-coupling into single-mode fibers. The cell pressure was 40 mtorr, the optical power of both laser beams was 100 μW , the discharge drive power was 1 Watt, and the external magnetic field was 55 Gauss. 222
- 8.9 Beam misalignment shifts in the vertical direction have an angular sensitivity that decreases with pressure. The optical power of each laser beam was 100 μW , the discharge power was 4.5 Watts, and the external magnetic field was 108 Gauss. 223
- 8.10 Beam misalignment shifts in the vertical direction have an angular sensitivity that depends weakly on discharge drive power. The cell pressure is 40 mtorr, the optical power of each laser beam is 100 μW , and the external magnetic field is 108 Gauss. 224
- 8.11 The angular sensitivity of the beam misalignment shifts in the (a) vertical, and (b) horizontal directions show little dependence on the magnitude of the external magnetic field. The cell pressure is 40 mtorr, the optical power of each laser beam is 100 μW , and the discharge power is 3.2 Watts. 225
- 8.12 Measurements of the fine structure intervals as a function of beam alignment angle θ in the vertical and horizontal directions. The cell pressure was 40 mtorr, the optical power in each laser beam was 100 μW , the discharge drive power was 1 Watt, and the external magnetic field was 55 Gauss. 227
- 8.13 (a) A sample linescan of the $2^3S - 2^3P_0$ transition. (b) Residuals from a fit to a Lorentzian function and Gaussian background reveal an asymmetric component to the signal. (c) When a dispersive term $D(\Omega)$ is added to the fitting function, the asymmetry is largely removed. The cell pressure was 40 mtorr, the optical power of each laser beam was 100 μW , the external magnetic field was 108 Gauss, and the discharge power was 4.5 Watts. 228
- 8.14 To test for lineshape distortions due to laser light pressure, a linescan was simulated by summing a Lorentzian and a much smaller Lorentzian derivative. After fitting to a Lorentzian, the residuals are 100 times smaller than those observed in Fig. 8.13b. 231
- 8.15 An intensity-dependent index of refraction gives rise to self-focusing. (a) For positive, or blue, detuning, the laser beams are focused; (b) for negative, or red, detuning, the laser beams are defocused. 232

8.16	Experimental setup for observing self-focusing. A 2 mm aperture mounted on a translation stage clips the probe beam before being detected.	233
8.17	Sample linescans of the $2^3S - 2^3P_0$ transition when the 2 mm aperture is positioned (a) on the axis of the probe beam, and (b) 2 mm off the axis of the probe beam. The linescans are fit to the sum of a Lorentzian peak and Gaussian background. The residuals show a large dispersive component whose sign depends on the position of the aperture. The cell pressure was 40 mtorr, the optical power of each beam was $40 \mu\text{W}$, the discharge drive power was 1.9 Watts, and the external magnetic field was 108 Gauss.	234
8.18	The large dispersive component of the signal shifts the fitted center frequency of the $2^3S - 2^3P_0$ transition by as much as 300 kHz, or 20% of the linewidth. The size of the shifts increases slightly with pressure. The optical power of each laser beam was $40 \mu\text{W}$, the discharge drive power was 1.9 Watts, and the external magnetic field was 108 Gauss.	235
8.19	Lorentzian signals and fit residuals generated by the mathematical model for self-focusing. A 1 mm wide aperture is modeled (a) on the beam axis, and (b) 5 mm off the beam axis. The initial beam waist is 5 mm.	240
8.20	Histogram of dispersive shifts for the $2^3S - 2^3P_0$ transition. The values are obtained by subtracting the center frequencies of each linescan when fit with and without a dispersive term. The cell pressure was 30 mtorr, the discharge drive power was 4.5 Watts, and the external magnetic field was 108 Gauss.	243
8.21	Dispersive shifts vary linearly as a function of pressure for the three fine structure intervals and light-pressure shift δ_{LP} . The optical power of each laser beam was $100 \mu\text{W}$ and the discharge drive power was 1 Watt and 4.5 Watts for the data at 55 Gauss and 108 Gauss, respectively.	244
8.22	Dispersive shifts vary linearly as a function of pressure for the optical transition frequencies.	245
8.23	Dispersive shifts vary linearly as a function of optical power for the three fine structure intervals and light-pressure shift δ_{LP} . The cell pressure was 30 mtorr and the discharge drive power was 1 Watt and 4.5 Watts for the data at 55 Gauss and 108 Gauss, respectively.	247
8.24	Dispersive shifts vary linearly as a function of optical power for the optical transition frequencies.	248
8.25	Sample scans of the $2^3S - 2^3P_1$ transition for external magnetic fields of (a) 55 Gauss, and (b) 108 Gauss, show an imbalance in the amplitudes of the two peaks. The right peak, corresponding to the $m = +1$ transition, is larger. For both scans, the cell pressure was 40 mtorr and the optical power of each laser beam was $100 \mu\text{W}$	250

- 8.26 Sample scans of the $2^3S-2^3P_2$ transition for external magnetic fields of (a) 55 Gauss, and (b) 108 Gauss, show an imbalance in the amplitudes of the outer peaks. The left peak, corresponding to the $m = +1$ transition, is larger. For both scans, the cell pressure was 40 mtorr and the optical power of each laser beam was $100 \mu\text{W}$ 251
- 8.27 Ratios of the left and right peak amplitudes of P_1 and P_2 linescans scale linearly with the magnitude of the external magnetic field. The cell pressure was 30 mtorr, the optical power of each laser beam was $100 \mu\text{W}$, and the discharge drive power was 1 Watt. 252
- 8.28 The ratio of the amplitudes of the two peaks of P_1 (a) scales linearly with pressure, and (b) decreases nonlinearly with optical power. Weak dependencies on discharge drive power were observed at (c) 55 Gauss and (d) 108 Gauss. (e) No dependency on laser polarization was observed. 254
- 8.29 (a) P_1 and (b) P_2 linescans taken in an inhomogeneous magnetic field produced by running current through one of the Helmholtz coils. The cell pressure was 40 mtorr, the optical power of each laser beam was $100 \mu\text{W}$, the discharge drive power was 1 Watt, and the magnetic field in the cell was approximately 55 Gauss. 255
- 8.30 Dispersive shifts obtained by subtracting the center frequencies of P_1 linescans from fits with and without dispersive terms included in the fitting functions: (a) the $m = -1$ peak, and (b) the $m = +1$ peak as a function of optical power. Here, the cell pressure is 30 mtorr. (c) The $m = -1$ peak, and (d) the $m = +1$ peak as a function of cell pressure. Here, the optical power of each laser beam is $100 \mu\text{W}$. The discharge drive power is 1 Watt and 4.5 Watts for the data at 55 Gauss and 108 Gauss, respectively. 257
- 8.31 Dispersive shifts obtained from P_2 linescans: (a) the $m = -1$ peak, and (b) the $m = +1$ peak as a function of optical power. Here, the cell pressure is 30 mtorr. (c) The $m = -1$ peak, and (d) the $m = +1$ peak as a function of cell pressure. 258
- 8.32 Calculated AC Stark shifts (black) and measured optical power shifts at 55 Gauss (red) and 108 Gauss (blue) for the optical transitions. The colored lines are the best-fit results when the data is extrapolated to zero optical power. The cell pressure was 30 mtorr. 264
- 8.33 Calculated AC Stark shifts (black) and measured optical power shifts at 55 Gauss (red) and 108 Gauss (blue) for the fine structure intervals and light-pressure shift δ_{LP} . The colored lines are the best-fit results when the data is extrapolated to zero optical power. The cell pressure was 30 mtorr. 265

List of Tables

2.1	Contributions to the non-QED energies of the 2^3S_1 and 2^3P_J states. Values are given in MHz and are recomputed from the literature using 2002 CODATA recommended values for the fundamental constants. .	18
2.2	Contributions to the 2^3S and 2^3P ionization energies, used to determine the $2^3S - 2^3P$ optical transition frequency. E_{NR} is the non-relativistic energy from Table 2.1 [32, 33, 34].	23
5.1	Measured background signals with typical values and the instruments on which they are measured.	149
6.1	Frequency pattern parameters for the three transitions. A total span of 150-300 MHz accurately measures the VCC Gaussian backgrounds while a frequency spacing of 150-200 kHz on the peaks is used to accurately measure the Lorentzian components.	170
7.1	Results of linear extrapolations of fine structure intervals to zero pressure.	189
7.2	Results of linear extrapolations of optical transition frequencies to zero pressure.	192
7.3	Results of linear extrapolations of interval and optical transition frequencies to zero discharge power.	201
8.1	Results of linear extrapolations of the fine structure intervals, light-pressure shift, and optical transition frequencies to zero optical power.	267
9.1	Table of uncertainties and systematic frequency corrections for measurements of the three 2^3P fine structure intervals. All values are in kHz.	274
9.2	Table of uncertainties and systematic frequency corrections for measurements of the three $2^3S - 2^3P_J$ optical transition frequencies. All values are in kHz.	276

Acknowledgments

This work would not have been possible without the never-ending enthusiasm, support, and direction of Professor Gerald Gabrielse. I would like to thank him for teaching me so many skills that are necessary for being a good scientist. I would also like to thank Dr. Ron Walsworth and Professor Eric Mazur for their support, helpful suggestions, and energy. I am grateful to Tanya Zelevinsky, without whose contributions this experiment would never have succeeded. Jan Ragusa deserves a special thanks for her help with administrative tasks. I would like to acknowledge the advice, contributions, and technical support of Susannah Dickerson, Stan Coutreau, Vickie Greene, Sheila Ferguson, Jim MacArthur, Stuart McNeil, Billy Moura, Jun Ye, Scott Diddams, James Lawler, Ove Poulsen, Jacob Taylor, David Phillips, and David DeMille.

To say that this thesis would not have happened without the support of my wife, Sarah Bickman, is an enormous understatement. Only her love and encouragement could keep me going strong all these years. My family deserves a special thanks for their love and patience. I would also like to thank my in-laws for their support and constant thinking of me. Stephen Maxwell's friendship has helped me keep focus on what's truly important in life. Last, I would like to acknowledge Professors Diana Eck and Dorothy Austin for welcoming me to Lowell House. My five years spent in their community was a truly rewarding experience for which I am most grateful.

Chapter 1

Introduction

In this thesis, an optical frequency comb was used to phase-coherently transfer the high stability and narrow linewidth of an iodine optical frequency reference to a diode laser at 1083 nm. This laser source was used to improve both the precision and accuracy of spectroscopy of the $2^3S_1 - 2^3P_J$ ($J = 0, 1, 2$) transitions in helium. With an experimental resolution better than 1 part in 10^{-12} , the optical transition frequencies presented here are among the most precise ever measured in helium. Furthermore, by taking differences between pairs of optical frequencies, values for the 2^3P fine structure intervals are obtained with a resolution as low as 100 Hz. This significant improvement in resolution is a major step toward a more stringent test of two-electron Quantum Electrodynamics (QED) and an improved determination of the fine structure constant.

The recent development of the optical frequency comb [1, 2, 3, 4]. is one of the most exciting advances in laser spectroscopy because it has been used to achieve improvements in the accuracy and precision of several experiments by orders of mag-

nitude [2, 4, 5, 6, 7, 8, 9, 10]. With the comb, microwave and optical regimes are phase-coherently bridged in one step using a single femtosecond laser. As demonstrated by this thesis, the resulting system occupies only a few square feet of space and can be designed, built, and operated by a single person. In addition, the frequency comb operates at all optical and infrared wavelengths simultaneously. This ability to work at several wavelengths is demonstrated here, where the frequency comb transfers the high stability and narrow linewidth of an iodine frequency reference from 1064 nm to the helium wavelength of 1083 nm. This approach allowed us to use a frequency reference that is more stable than any that can be constructed at 1083 nm.

Although several helium fine structure experiments have been conducted in recent years, this work is unique for several reasons. First, it is one of the only experiments that completely integrates a frequency comb into an optical frequency reference [5, 11]. This contrasts with other experiments that use the comb to simply monitor or calibrate the frequency of an optical reference [12]. In this latter case, the experiment can still run without the frequency comb. Second, the experiment is performed in a discharge cell. While other experiments use a beam of metastable helium atoms, the cell gives high signal-to-noise ratios and the ability to study several systematic effects by varying cell pressure. Third, this is the only experiment that measures all three 2^3P fine structure intervals simultaneously. The different techniques used and the various systematic effects encountered in this experiment ensure consistency among all the helium fine structure measurements. As discussed in the next chapter, the good agreement among these measurements is especially important due to a large

disagreement between theory and experiment.

One of the most significant accomplishments of this work was a large improvement in experimental resolution. Previously, two months of data was needed to achieve statistical uncertainties of 500 Hz for measurements of the fine structure intervals [13]. Now, all three intervals can be measured to better than 200 Hz in only two weeks. Some of the changes that contributed to this improved resolution are: a new iodine optical frequency reference that, when compared to a previous ^3He reference, increased frequency stability by a factor of 40 and reduced laser linewidth by a factor of 10; a shift to a higher modulation frequency where the laser has less residual amplitude noise; the use of an autobalanced photodetector to cancel laser amplitude noise above the shot-noise limit; a new optics layout to reduce the influence of acoustic noise and drift; a change to equal-weighted fits of helium linescans that reduced scatter in the fitted center frequencies; and several improvements to the data-taking procedure that significantly increased the rate at which data was obtained.

Increased precision was an important tool for searching for new systematic shifts. In addition to several improved studies of systematics that are already well-understood, three new effects were discovered. The first is a residual Doppler shift that results from an improper alignment of pump and probe laser beams and the non-thermal distribution of atomic velocities in a discharge cell. Although this effect introduces shifts the measured optical frequencies by as much as 10 kHz, it was found to affect measurements of the fine structure intervals by a much smaller amount. The second systematic effect is an observed asymmetry in the linescans that shifts the fitted center frequencies by as much as 30 kHz. Affecting both optical and interval

measurements, an attempt was made to explain these shifts via self-focusing of the laser beams by the helium gas. The last systematic effect, an observed imbalance in the amplitudes of $m = +1$ and $m = -1$ peaks in linescans of the $2^3S - 2^3P_1$ and $2^3S - 2^3P_2$ transitions, currently has no known explanation.

In addition to a brief theoretical overview, Chapter 2 summarizes different measurements of the fine structure constant α , the 2^3P fine structure splittings, and the $2^3S - 2^3P_J$ optical transition frequencies. The experimental setups for the optical comb, iodine frequency reference, and helium apparatus are described in Chapters 3 through 5, respectively. Chapter 6 describes the observed lineshapes and how center frequencies are extracted from fits to experimental linescans. Improved studies of light-pressure shifts, linear pressure shifts, discharge power shifts, and laser polarization shifts are discussed in Chapter 7. New systematics due to laser beam misalignment, the linescan asymmetry, and the $m = \pm 1$ signal imbalance are discussed in Chapter 8. In addition, the linescan asymmetry has changed our understanding of optical power shifts, measurements of which are also presented in this chapter. After summarizing the results, this thesis concludes with discussions of future improvements to the experiment, including some suggestions for eliminating beam misalignment shifts.

Chapter 2

Background and Motivation

2.1 Measurements of the Fine Structure Constant

Introduced in 1916 by Arthur Sommerfeld to characterize relativistic effects in atomic spectral lines, the fine structure constant α is now realized to be the coupling constant in Quantum Electrodynamics (QED) that characterizes the strength of the electromagnetic interaction between photons and matter. In SI units, α is defined as

$$\alpha = \frac{1}{4\pi\epsilon_0} \frac{e^2}{\hbar c} \quad (2.1)$$

and has a value of approximately $1/137$ in the low-energy limit.

Due to its role as a fundamental constant, it is important to measure α many different ways in order to test the consistency of QED in a variety of physical systems. The Committee on Data for Science and Technology (CODATA) uses the most accurate measurements of α , shown in Fig. 2.1, to determine the recommended value

for international use. The 2002 CODATA adjustment is [14]

$$\alpha^{-1}(2002) = 137.035\,999\,11(46) \quad [3.4 \times 10^{-9}] \quad (2.2)$$

where the relative error is in square brackets. Details of the different experimental measurements are discussed below.

2.1.1 Electron Anomalous Magnetic Moment

The most accurate determination of α comes from a measurement of the electron anomalous magnetic moment performed by the Gabrielse group at Harvard [15, 16]. Theoretically, the anomaly a_e can be expressed in powers of α/π

$$a_e = \frac{g_e - 2}{2} = 0.5 \left(\frac{\alpha}{\pi}\right) - 0.328\dots \left(\frac{\alpha}{\pi}\right)^2 + 1.181\dots \left(\frac{\alpha}{\pi}\right)^3 - \dots \quad (2.3)$$

where g_e is the electron g-factor. Comparing to the experimental results determines α [16]

$$\alpha^{-1}(a_e) = 137.035\,999\,710(96) \quad [0.7 \times 10^{-9}] \quad (2.4)$$

This result, to be incorporated into the next CODATA adjustment, improves upon the value of a_e measured at the University of Washington in 1987 [17].

2.1.2 Muonium Hyperfine Structure

A value of α can be determined from measurements of ground-state hyperfine splittings. Although this has been measured in hydrogen to a very high accuracy of 7×10^{-13} , the theoretical complexity of the proton's structure prevents a determination of α that is better than 1 ppm [14]. The problem does not arise for muonium, where

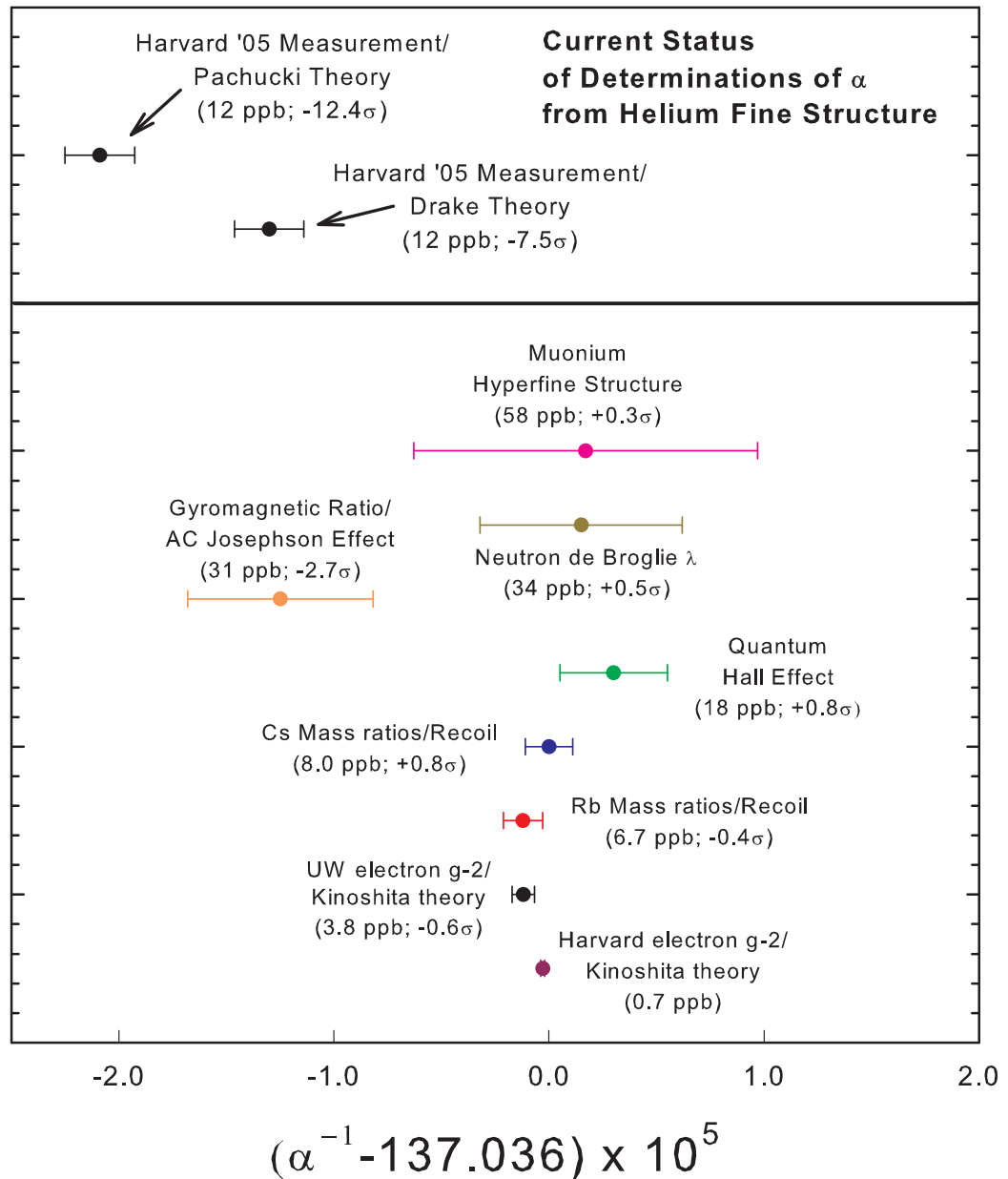


Figure 2.1: Comparison of the most accurate measurements of the fine structure constant α . Due to theoretical discrepancies, the value of α obtained from helium fine structure disagrees with the CODATA value by several standard deviations. As a result, this value is not included in the CODATA adjustment.

the proton has been replaced by a positively-charged muon, although the experimental uncertainty is much larger. Here, the ground-state hyperfine splitting depends on α by the relation [14]

$$\Delta\nu_{\text{Mu}} = \frac{16}{3}cR_\infty\alpha^2\left(1 + \frac{m_e}{m_\mu}\right)^{-3}\mathcal{F}(\alpha, m_e/m_\mu) \quad (2.5)$$

where \mathcal{F} depends weakly on α . Using microwave magnetic resonance spectroscopy, measurements of the splitting $\Delta\nu_{\text{Mu}}$ and mass ratio m_μ/m_e yield [18]

$$\alpha^{-1}(\Delta\nu_{\text{Mu}}) = 137.036\,0017(80) \quad [5.8 \times 10^{-8}] \quad (2.6)$$

where the uncertainty is due to the experimental error of measurements of m_μ/m_e .

2.1.3 Fine Structure

Similar to hyperfine splittings, fine structure splittings also scale as α^2 to lowest order and therefore can be used to determine the fine structure constant. The experimental figure of merit scales as $\gamma/\omega_{\text{fs}}$, where γ is the transition linewidth and ω_{fs} is the size of the splitting. With linewidths that are 60 times narrower and a splitting that is 3 times larger than the $2P$ splitting of hydrogen, the 2^3P state of helium is the most promising system for this measurement. For simplicity, the helium $2^3P_i - 2^3P_j$ fine structure interval is denoted as f_{ij} .

The helium fine structure interval f_{01} is better suited for determining α than the f_{12} interval because it is larger by a factor of 10. In addition, it is larger than any other fine structure splitting in helium since the size of the splittings decreases with increasing principal quantum number n .

The fine structure constant is obtained from f_{01} using the expression [19]

$$f_{01} = \alpha^2 \cdot 556\,200\,289.5(1) \text{ MHz} + \delta f_{01} \quad (2.7)$$

The coefficient of α^2 contains the leading order fine structure terms, including effects of the finite nuclear mass and anomalous magnetic moment of the electron. For δf_{01} , which contains QED terms of order $O(\alpha^4)$ and higher, the dependence on α is weak enough that only the first few digits of α are used without introducing any significant error. Two different values of δf_{01} , calculated by Drake [20] and Pachucki [21], are

$$\delta f_{01}^D = -1.472\,37(18) \text{ MHz} \quad (2.8)$$

$$\delta f_{01}^P = -1.475\,78(17) \text{ MHz} \quad (2.9)$$

where the uncertainties are obtained by estimating the size of the largest contributions of terms of order $O(\alpha^6)$. Due to the large disagreement between these values, the two theoretical calculations give values of α (Fig. 2.1) and predicted values of the f_{01} interval (Fig. 2.3) that disagree with each other. One explanation for the discrepancy is that errors were made in the derivation of operators of order $O(\alpha^5)$ [21]. Given that these two values should agree exactly, it seems likely that there are still theoretical problems that need to be resolved.

The most accurate experimental value of f_{01} (see Eqn. 2.51) [13] gives values for α of

$$\alpha^{-1}(\text{He,D}) = 137.035\,986\,99(162)(42) \quad [1.1 \times 10^{-8}] \quad (2.10)$$

$$\alpha^{-1}(\text{He,D}) = 137.035\,979\,10(162)(42) \quad [1.1 \times 10^{-8}] \quad (2.11)$$

where the first error is experimental and the second error is theoretical. As shown in Fig. 2.1, both of these values significantly disagree with other values of α . It is very

likely that these discrepancies are due to theory, given that the disagreement between calculated values of δf_{01} is unresolved. Although the disagreement between $\alpha^{-1}(\text{He})$ and other values of the fine structure constant could be due to the experimental value of f_{01} , four different experiments have demonstrated agreement to better than 1 kHz (see Fig. 2.3). By comparison, measured values of f_{01} would need to be shifted by 5 kHz and 8 kHz in order to bring $\alpha^{-1}(\text{He,D})$ and $\alpha^{-1}(\text{He,P})$, respectively, into agreement with the CODATA value.

2.1.4 Mass Ratios and h/M

Several promising fine structure constant measurements come from expressing α as

$$\alpha^{-1} = \frac{2R_{\infty}}{c} \cdot \frac{A_r(X)}{A_r(e)} \cdot \frac{h}{M_X} \quad (2.12)$$

where the Rydberg R_{∞} and the relative atomic mass of the electron $A_r(e)$ have relative uncertainties of 8×10^{-12} and 4.4×10^{-10} , respectively. For cesium and rubidium, the relative atomic masses $A_r(\text{Cs})$ and $A_r(\text{Rb})$ are known with relative uncertainties less than 2.0×10^{-10} [22]. For cesium, h/M_{Cs} is obtained by combining an interferometric measurement of the recoil shift [23] with a measurement of the D_1 optical transition frequency [5]. The resulting value for α is

$$\alpha^{-1}(\text{Cs}) = 137.036\ 0000(11) \quad [8.0 \times 10^{-9}] \quad (2.13)$$

For rubidium, the value [24]

$$\alpha^{-1}(\text{Rb}) = 137.035\ 998\ 78(91) \quad [6.7 \times 10^9] \quad (2.14)$$

is obtained from a non-interferometric measurement of h/M_{Rb} based on Bloch oscillations in an optical lattice.

A related method for measuring α has also been applied to neutrons, where h/λ_n is obtained by combining measurements of the velocity and de Broglie wavelength of slow neutrons reflecting off a silicon crystal [25]. The resulting value of α is

$$\alpha^{-1}(n) = 137.036\,0015(47) \quad [3.4 \times 10^{-8}] \quad (2.15)$$

where the relative atomic mass of the neutron $A_r(n)$ is known with a relative uncertainty of 5.8×10^{-10} [14].

2.1.5 Quantum Hall Effect

The von Klitzing constant $R_K = h/e^2$ is measured in quantum Hall experiments by comparing the quantized Hall resistance $R(n) = R_K/n$, where n is an integer, to a resistor whose value R is known with respect to the SI unit of resistance Ω [14, 26]. The fine structure constant is then determined using the relation

$$\alpha = \frac{\mu_0 c}{2R_K} \quad (2.16)$$

where μ_0 is the permeability of free space. The combined results of several experiments give [14]

$$\alpha^{-1}(\text{QH}) = 137.036\,0030(25) \quad [1.8 \times 10^{-8}] \quad (2.17)$$

where the error is due to the calculable capacitors and impedance chains used for the resistance comparison.

2.1.6 Proton Gyromagnetic Ratio

The fine structure constant can be obtained by combining measurements of the gyromagnetic ratio γ'_p of the shielded proton, the infinite-mass Rydberg R_∞ , the electron g-factor g_e , and the electron-to-shielded-proton magnetic moment ratio μ_{e-}/μ'_p , the von Klitzing constant R_J , and the AC Josephson constant K_J [14, 27]. The largest uncertainty is due to γ'_p

$$\gamma'_p = \frac{2\mu'_p}{\hbar} = \frac{\omega}{B} \quad (2.18)$$

where μ'_p is the magnetic moment of the shielded proton and ω is the angular precession frequency of the particle in an external magnetic flux density B . The protons are those in a spherical sample of pure H₂O at room temperature surrounded by vacuum. Generated by a solenoid driven with a current I , the magnetic flux density B is computed from the solenoid geometry and the measured value of I . A typical value of B is 1 mT.

The technique relies on measurements of the AC Josephson effect. An AC Josephson junction consists of a pair of superconductors separated by a thin non-conductive oxide barrier. When irradiated by microwaves of frequency f , the DC voltage U_J across the junction is quantized [28]:

$$U_J(n) = \frac{nf}{K_J} \quad (2.19)$$

where n is an integer and $K_J = 2e/h$ is the Josephson constant that characterizes the step size.

The solenoid current I is measured in terms of laboratory units

$$A_{90} = \frac{V_{90}}{\Omega_{90}} \quad (2.20)$$

where A_{90} is a laboratory unit of current based on V_{90} , a laboratory unit of voltage derived from the AC Josephson effect, and Ω_{90} , a laboratory unit of resistance derived from the quantum Hall effect. These laboratory units are converted to SI units V and Ω using the relations

$$\begin{aligned} V_{90} &= \frac{K_{J-90}}{K_J} V \\ \Omega_{90} &= \frac{R_K}{R_{K-90}} \Omega \end{aligned} \quad (2.21)$$

where

$$\begin{aligned} K_{J-90} &= 483\,597.9 \text{ GHz/Volt} \\ R_{K-90} &= 25\,812.807 \, \Omega \end{aligned} \quad (2.22)$$

are the assigned exact values of the Josephson constant and von Klitzing constant [14].

Eqns. 2.21 and 2.22 are used to convert the gyromagnetic ratio from its value measured in laboratory units (i.e. $\Gamma'_{90}(\text{lo})$) to SI units (i.e. γ'_p):

$$\gamma'_p = \Gamma'_{90}(\text{lo}) \frac{K_J R_K}{K_{J-90} R_{K-90}}. \quad (2.23)$$

Here, K_J and R_K are the values of the Josephson constant and von Klitzing constants measured from the laboratory voltage and resistance standards. They are included in Eqn. 2.23 to account for the real-world likelihood that $K_J \neq K_{J-90}$ and $R_K \neq R_{K-90}$.

The fine structure constant α is obtained from the relation

$$\alpha = \left(4\mu_0 \frac{\mu_{e-}}{\mu'_p} \frac{R_\infty}{g_e} \frac{\Gamma'_{90}(\text{lo})}{K_{J-90} R_{K-90}} \right)^{\frac{1}{3}} \quad (2.24)$$

where the measured values of the infinite-mass Rydberg R_∞ , the electron g-factor g_e , and the electron-to-shielded-proton magnetic moment ratio μ_{e-}/μ'_p contribute negligible errors to the uncertainty of α .

$\Gamma'_{90}(\text{lo})$ is measured with relative uncertainties as low as 110 ppb. The combined results of several experiments, including measurements of the gyromagnetic ratio γ'_h of the shielded helion, give a value for α of [14]

$$\alpha^{-1}(\gamma) = 137.035\,9875(43) \quad [3.1 \times 10^{-8}] \quad (2.25)$$

Compared to $\Gamma'_{90}(\text{lo})$, the uncertainty in α is smaller by factor of 3 due to the cube-root relationship.

2.2 The Structure of Helium

Figure 5.1 shows the lowest energy levels of spin-triplet states of ${}^4\text{He}$. Spin-singlet states are not considered since they do not exhibit fine structure. A large energy spacing of 19.8 eV exists between the ground 1^1S_0 state and the 2^3S_1 states. This transition is forbidden due to selection rules, and therefore the 2^3S_1 state is metastable with a lifetime of $\tau=8000$ seconds. Experimentally, an RF discharge is used to excite atoms from the ground state to the 2^3S_1 state. With a energy spacing corresponding to 1083 nm, the $2^3S_1 - 2^3P_J$ transitions are probed experimentally by an infrared diode laser.

2.2.1 The Non-Relativistic Hamiltonian

The non-relativistic Hamiltonian for the helium atom is [29]

$$H = -\frac{\hbar^2}{2M}\nabla_{\vec{R}_n}^2 - \frac{\hbar^2}{2m_e}\nabla_{\vec{R}_1}^2 - \frac{\hbar^2}{2m_e}\nabla_{\vec{R}_2}^2 - \frac{Ze^2}{|\vec{R}_n - \vec{R}_1|} - \frac{Ze^2}{|\vec{R}_n - \vec{R}_2|} + \frac{e^2}{|\vec{R}_1 - \vec{R}_2|} \quad (2.26)$$

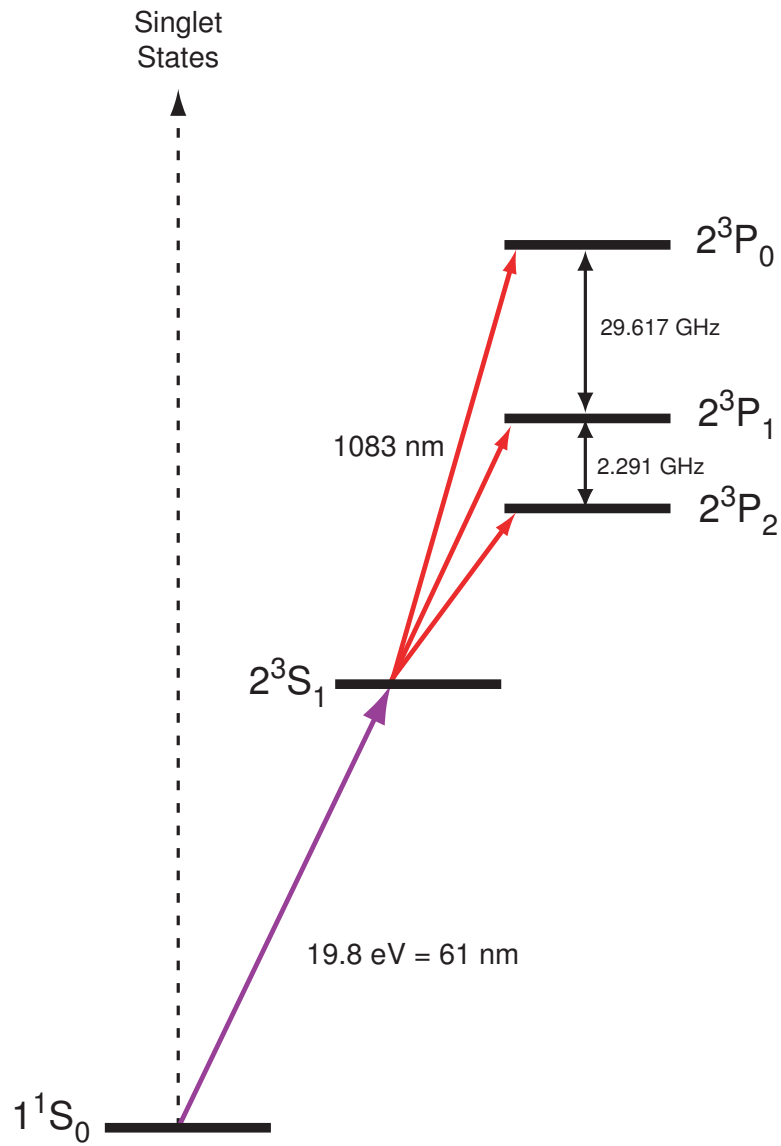


Figure 2.2: Energy diagram of the low-lying spin-triplet states of ${}^4\text{He}$. The 2^3P splittings are not drawn to scale.

where two electrons of mass m_e at positions \vec{R}_1 and \vec{R}_2 are bound to a nucleus of charge $Z = +2$, mass M , and position \vec{R}_n . Transforming to the dimensionless center-of-mass coordinate gives

$$H = -\frac{1}{2}\nabla_1^2 - \frac{1}{2}\nabla_2^2 - \frac{\mu}{M}\nabla_1 \cdot \nabla_2 - \frac{Z}{r_1} - \frac{Z}{r_2} + \frac{1}{r_{12}} \quad (2.27)$$

where $\mu = m_e M / (m_e + M)$ is the reduced mass. The relative position vectors are given by

$$\vec{r}_1 = (\vec{R}_1 - \vec{R}_n) / a_\mu \quad (2.28)$$

$$\vec{r}_2 = (\vec{R}_2 - \vec{R}_n) / a_\mu \quad (2.29)$$

where $a_\mu = (m_e / \mu) a_o$ is the reduced Bohr radius, $r_1 = |\vec{r}_1|$, $r_2 = |\vec{r}_2|$, and $r_{12} = |\vec{r}_1 - \vec{r}_2|$.

Since $\mu / M \ll 1$, the mass polarization term $(\mu / M) \nabla_1 \cdot \nabla_2$ is treated as a perturbation. The resulting two-electron Hamiltonian for an infinite nuclear mass is

$$H = -\frac{1}{2}\nabla_1^2 - \frac{1}{2}\nabla_2^2 - \frac{Z}{r_1} - \frac{Z}{r_2} + \frac{1}{r_{12}} \quad (2.30)$$

The electron-electron Coulomb interaction term $1/r_{12}$ prevents the Hamiltonian from being separable and therefore from having analytic solutions. However, since one of the two electrons is in the ground $1S$ state, it shields the nucleus from the other electron. Therefore, the system can be treated as a hydrogenic atom with the electron-electron interaction term acting as a perturbation. This gives the Hamiltonian

$$H_0 = -\frac{1}{2}\nabla_1^2 - \frac{1}{2}\nabla_2^2 - \frac{Z}{|\vec{r}_1|} - \frac{Z-1}{|\vec{r}_2|} \quad (2.31)$$

The solution to Eqn. 2.31 is a product of two hydrogenic wavefunctions

$$\Psi(1snl) = \phi(1s, Z)\phi(nl, Z-1) \quad (2.32)$$

where $\phi(nl, Z)$ is a hydrogen wavefunction of principal quantum number n , orbital angular momentum l and nuclear charge Z . The energy eigenvalues of

$$E(n) = -\frac{Z^2}{2} - \frac{(Z-1)^2}{2n^2} \quad (2.33)$$

are correct to several significant figures for states of large n , where the assumption of a screened nucleus is valid. For $n = 2$, this formula is accurate to a few percent.

The correction to Eqn. 2.33 can be computed by applying variational techniques to the perturbation $H' = 1/|\vec{r}_1 - \vec{r}_2|$. The goal of the variational method is to minimize the function

$$E(\Psi) = \frac{\langle \Psi | H - E_n | \Psi \rangle}{\langle \Psi | \Psi \rangle} = \frac{\langle \Psi | H' | \Psi \rangle}{\langle \Psi | \Psi \rangle} \quad (2.34)$$

where H' is the perturbation and $|\Psi\rangle$ is a trial wavefunction. Although any mathematical function can be used for $|\Psi\rangle$, $E(\Psi)$ is minimized for the function that most closely resembles the true wavefunction. Using a doubled Hylleraas basis set to represent $|\Psi\rangle$, Drake has computed the non-relativistic energy corrections to more than 15 significant digits. For the $2S$ and $2P$ states, the results in atomic units are [29]

$$\Delta E(2S) = -2.175\,229\,378\,236\,791\,23(10) \quad (2.35)$$

$$\Delta E(2P) = -2.133\,164\,190\,779\,283\,202(5). \quad (2.36)$$

The non-relativistic energies in MHz are listed below in Table 2.1. To convert from atomic units to energy units, the 2002 CODATA recommended values of the constants was used. The 6 kHz and 8 kHz errors are due to the uncertainty of the Rydberg constant [14].

Contribution	2^3S_1	2^3P_0	2^3P_1	2^3P_2
E_{NR}	-1152795881.767(8)	...	-876058183.130(6)	...
μ/M	6711.190	...	-58230.358	...
$(\mu/M)^2$	-7.110	...	-25.335	...
α^2	-57621.412	38998.523	9437.980	7121.065
$\alpha^2 \mu/M$	-3.62	17.331	14.107	10.779
Nuclear Size	2.60	...	-0.792	...
Non-QED Total	-1152846800.119(8)	-876077423.768(6)	-876106987.5291(6)	-876109307.772(6)

Table 2.1: Contributions to the non-QED energies of the 2^3S_1 and 2^3P_J states. Values are given in MHz and are recomputed from the literature using 2002 CODATA recommended values for the fundamental constants.

2.2.2 Finite Mass Corrections

The mass polarization term in Eqn. 2.27 is treated as a perturbation

$$E_M = E_\infty + \left(\frac{\mu}{M}\right) \epsilon_M^{(1)} + \left(\frac{\mu}{M}\right)^2 \epsilon_M^{(2)} \quad (2.37)$$

where E_∞ is the infinite mass energy, and $\epsilon_M^{(1)}$ and $\epsilon_M^{(2)}$ are the first and second-order finite mass corrections, respectively. The third order correction provides a negligible contribution. The values $\epsilon_M^{(1)}$ and $\epsilon_M^{(2)}$ have been calculated by Drake to a precision of less than 1 kHz. The values in MHz appear in Table 1.

2.2.3 Finite Nuclear Size

In the above discussion, it is assumed that the nucleus is infinitely small. However, the finite size of the nucleus has a small affect on the energy levels of the atoms by changing in the boundary condition for the electronic wavefunction at $r = 0$. The correction is given by

$$E_{nuc} = \frac{2\pi Z(R/a_0)^2}{3} \langle \delta(\vec{r}_1) + \delta(\vec{r}_2) \rangle \quad (2.38)$$

where R is the root-mean-square radius of the nuclear charge distribution. The value $R = 1.673(1)$ fm comes from studies of muonic helium [30].

2.2.4 Relativistic Corrections

Relativistic corrections of order α^2 are derived from the Breit interaction

$$H_{rel} = B_1 + B_2 + B_{3Z} + B_{e3} + B_5 + \frac{Z\pi\alpha^2}{2} \sum_{i=1}^2 \delta(\vec{r}_i) - \pi\alpha^2 \left(1 + \frac{8}{3} \vec{s}_1 \cdot \vec{s}_2\right) \delta(\vec{r}_{12}) \quad (2.39)$$

where the notation follows that of Bethe and Salpeter and an infinite nuclear mass is assumed [31]. $B_1 = (\alpha^2/8)(\nabla_1^4 + \nabla_2^4)$ is the first order relativistic correction to linear momentum, B_2 is the orbit-orbit interaction, B_{3Z} is the spin-orbit interaction, B_{3e} is the spin-other-orbit interaction, and B_5 is the spin-spin interaction. The finite mass of the nucleus adds additional corrections of $O(\alpha^2\mu/M)$ and $O(\alpha^2(\mu/M)^2)$.

The spin-orbit, spin-other-orbit, and spin-spin terms in Eqn. 2.39 give rise to fine structure. Due to the explicit dependence on electron spin, these terms have additional corrections of order $O(\alpha^3)$ that arise from the anomalous magnetic moment of the electron:

$$E_{a_e} = 2a_e \left\langle nLS' \left| B_{3Z} + \frac{2}{3}\delta_{S,S'}B_{3e} + B_5 \right| nLS \right\rangle. \quad (2.40)$$

Here a_e is the anomalous magnetic moment correction given by Eqn. 2.3.

2.2.5 Complete Non-QED Energy

Table 2.1 summarizes the contributions to the non-QED energies of the 2^3S and 2^3P states. Using the 2002 CODATA values of the fundamental constants to convert to frequency units, the $(2J + 1)$ -weighted averaged non-QED energy is

$$276\,741\,808.428(10) \text{ MHz} \quad (2.41)$$

where the error is due to the Rydberg constant.

2.2.6 The 2^3P Fine Structure Intervals

Energy corrections of order $O(\alpha^3)$ and higher that contribute to the fine structure splittings can be written as

$$\delta E_J = C^{(3)}\alpha^3 + C^{(4)}\alpha^4 + C^{(5L)}\alpha^5 \ln \alpha + C^{(5)}\alpha^5 + O(\alpha^6) \quad (2.42)$$

where each coefficient $C^{(i)}$ is expanded in powers of μ/M in order to account for the finite nuclear mass.

Two groups have calculated the fine structure QED terms up to order $O(\alpha^5)$. Drake's results are [20]

$$\begin{aligned} f_{12}^{(D)} &= 2\,291\,154.62(31) \text{ kHz} \\ f_{01}^{(D)} &= 29\,616\,946.42(18) \text{ kHz.} \end{aligned} \quad (2.43)$$

Pachucki's results are [21]

$$\begin{aligned} f_{12}^{(P)} &= 2\,291\,161.13(30) \text{ kHz} \\ f_{01}^{(P)} &= 29\,616\,943.01(17) \text{ kHz.} \end{aligned} \quad (2.44)$$

For both results, the uncertainties are estimated from the sizes of the largest contributions to terms of order $O(\alpha^6)$. As seen in Fig. 2.3, these theoretical calculations disagree with the experimental measurements by several kHz. In addition, the two calculations disagree significantly with each other. One explanation for the disagreement between the two sets of theoretical values is an error in the derivation of operators of order $O(\alpha^5)$ [21].

Given the large discrepancy between the two sets of theoretical values, it seems highly likely that there are still errors in the calculations that need to be resolved before a meaningful comparison between theory and experiment can be made. Until

these discrepancies can be resolved, the values of α obtained from helium fine structure should be viewed skeptically.

2.2.7 The $2^3S - 2^3P$ Optical Transition Frequency

A theoretical prediction for the optical frequency of the $2^3S - 2^3P$ transition must include all QED terms and not just those that contribute to fine structure splitting. The predicted value is obtained by taking the difference between the theoretical 2^3S and 2^3P ionization energies [32, 33, 34]. Summarized in table 2.2, the theoretical $(2J + 1)$ -weighted mean frequency is

$$E(2^3S) - E(2^3P) = 276\,736\,496.1(11) \text{ MHz} \quad (2.45)$$

The 1.1 MHz error of the theoretical prediction is almost three orders of magnitude worse than the uncertainty of the most accurate experimental results [12]. The error is due almost entirely to the 2^3S energy, whose 1 MHz error was chosen to be large enough to account for remaining terms of order $O(\alpha^5)$ that have yet to be calculated [33]. In addition, numerical uncertainties on the order of 10 kHz are also larger than the experimental error, signaling the need for improvements in computational methods.

2.3 Experimental Measurements

2.3.1 Helium Fine Structure Measurements

Several research groups have pursued high precision measurements of the 2^3P fine structure splittings in helium. As shown in Fig. 2.3, the excellent agreement obtained

Contribution	2^3S_1	$2^3P(\text{Centroid})$
E_{NR}	-1 152 846 800.119(8)	876 104 991.690(6)
α^3	3 998.65	-1 235.33(2)
α^4	65.24(1)	-20.42
α^5	-5.31(100)	2.00(40)
Total	-1 152 842 741.54(100)	-876 106 245.44(40)

Table 2.2: Contributions to the 2^3S and 2^3P ionization energies, used to determine the 2^3S-2^3P optical transition frequency. E_{NR} is the non-relativistic energy from Table 2.1 [32, 33, 34].

from a variety of experimental approaches helps confirm sub-kHz accuracy. Presented here is a brief overview of these measurements.

Yale University

The first precision measurements of the 2^3P fine structure intervals were carried out at Yale University between the late 1960s and early 1980s [35, 36, 37, 38]. An optical-microwave magnetic resonance technique was used with an atomic beam in an external magnetic field. After light from a discharge lamp excited metastable atoms to one of the 2^3P_J levels, microwaves probed transitions between pairs of the 2^3P_J levels. Uncertainties less than 40 kHz are impressive considering that no lasers were used.

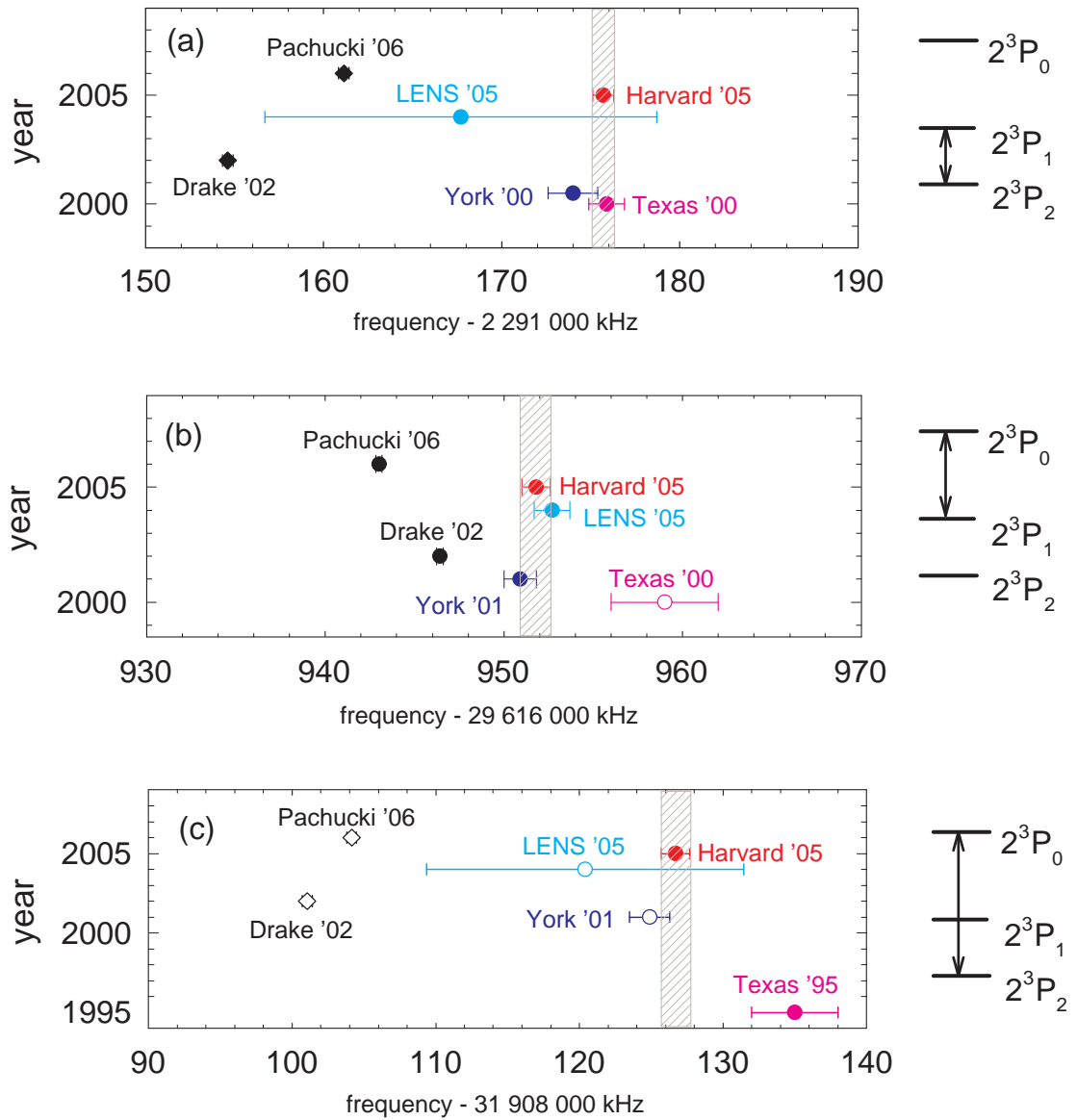


Figure 2.3: Comparison of experimental measurements and theoretical predictions for the (a) $2^3P_1 - 2^3P_2$, (b) $2^3P_0 - 2^3P_1$, and (c) $2^3P_0 - 2^3P_2$ fine structure intervals. Open symbols are indirect values calculated from direct values of the other two intervals.

University of North Texas

Experiments by Shiner at the University of North Texas use laser excitation of a polarized beam of metastable atoms. For f_{01} and f_{02} , an LNA laser was used to excite atoms in the $m = 0$ sublevel of the 2^3S state to one of the 2^3P_J levels [39, 40]. Atoms that decay to the $m = \pm 1$ sublevel of the 2^3S state are counted as a function of laser frequency to obtain a Lorentzian profile. The results are

$$f_{01}^{(\text{UNT})} = 29\,616\,961(9) \text{ kHz} \quad [3.0 \times 10^{-7}] \quad (2.46)$$

$$f_{02}^{(\text{UNT})} = 31\,908\,135(3) \text{ kHz} \quad [9.4 \times 10^{-8}] \quad (2.47)$$

where the error is due to the interferometer used to transfer the stability of an iodine-stabilized He-Ne reference laser at 633 nm to the helium wavelength of 1083 nm.

In the more recent measurement of the f_{12} interval, the 2^3P_J levels are probed by applying frequency sidebands to a diode laser with an electro-optic modulator [41]. Here, the modulation frequency is chosen such that the upper and lower sidebands are resonant with two different states. The result is

$$f_{12}^{(\text{UNT})} = 2\,291\,175.9(1.0) \text{ kHz} \quad [4.3 \times 10^{-7}]. \quad (2.48)$$

The smaller error is due the cancelation of drift from the frequency reference upon subtraction of the $2^3S - 2^3P_1$ and $2^3S - 2^3P_2$ frequencies.

York University

At York University, metastable atoms in a beam are excited to the $2^3S_1(m = +1)$ state using a circularly-polarized diode laser at 1083 nm [42, 43]. Another diode laser excites these atoms to the $2^3P_1(m = 0)$ level where, due to selection rules, they are

forbidden from decaying to the $2^3S_1(m=0)$ state. After excitation by microwaves to the $m=0$ sublevel of either the 2^3P_0 or 2^3P_2 state, depending on the transition being measured, some of these atoms will then decay to the $2^3S_1(m=0)$ state. The population of atoms in the $2^3S_1(m=0)$, measured as a function of microwave frequency, is detected by observing fluorescence after excitation to the 2^3P_0 state. The results are

$$\begin{aligned} f_{12}^{(\text{York})} &= 2\,291\,174.0(14) \text{ kHz} & [6.1 \times 10^{-7}] \\ f_{01}^{(\text{York})} &= 29\,616\,950.9(9) \text{ kHz} & [3.0 \times 10^{-8}] \end{aligned} \quad (2.49)$$

where the errors are dominated by microwave power that leaks out of the grid through which the atoms pass when entering the microwave excitation region.

The European Laboratory for Nonlinear Spectroscopy (LENS)

At LENS in Florence, Italy, atoms from a metastable beam are probed using saturated absorption spectroscopy with a diode laser at 1083 nm [44]. Magnetic sublevels are not resolved and the signal is detected by measuring the fluorescence with a photo-multiplier tube. The laser is stabilized by offset-locking to a second diode laser whose output is frequency doubled and locked to a hyperfine transition in molecular iodine at 541.5 nm. The experiment is similar to the Harvard experiment in that frequencies obtained from pairs of transitions are subtracted in order to cancel reference drift. The most recent results are

$$\begin{aligned} f_{12}^{(\text{LENS})} &= 2\,291\,167.7(110) \text{ kHz} & [4.8 \times 10^{-6}] \\ f_{01}^{(\text{LENS})} &= 29\,616\,952.7(10) \text{ kHz} & [3.4 \times 10^{-8}] \end{aligned} \quad (2.50)$$

where the large 11 kHz error for the f_{12} interval is due to the effects of laser light pressure [45].

Harvard University

In this work, saturated absorption spectroscopy with a diode laser at 1083 nm is used to probe metastable helium atoms in an RF discharge cell. Although collisional effects are observed, very high signal-to-noise ratios are obtained due to the large number of atoms that interact with the laser beams. A homogeneous magnetic field resolves the Zeeman sublevels, allowing for implementation of a method to correct for light-induced pressure shifts [13]. The most recent results from this experiment are [13]

$$\begin{aligned}
 f_{12}^{(\text{H}^{05})} &= 2\,291\,174.97(30) \text{ kHz} & [1.3 \times 10^{-7}] \\
 f_{01}^{(\text{H}^{05})} &= 29\,616\,951.78(60) \text{ kHz} & [2.0 \times 10^{-8}] \\
 f_{02}^{(\text{H}^{05})} &= 31\,908\,126.73(50) \text{ kHz} & [1.6 \times 10^{-8}].
 \end{aligned}
 \tag{2.51}$$

As discussed in Chapter 8, our inability to determine the size of frequency shifts due to small asymmetries in the experimental linescans prevent us from publishing improved values of these intervals at this time.

2.3.2 The $2^3S - 2^3P$ Transition Frequency

As shown in Fig. 2.4, measurements of the $2^3S - 2^3P$ transition frequency have had significant improvements in experimental resolution over the past twenty years. Presented here is a brief description of these experiments.

Indirect Measurements at Paris and Orsay

The Paris/Orsay measurement was obtained by subtracting the measured value of the $2^3P - 3^3D$ transition at 588 nm [46] from the measured value of the two-

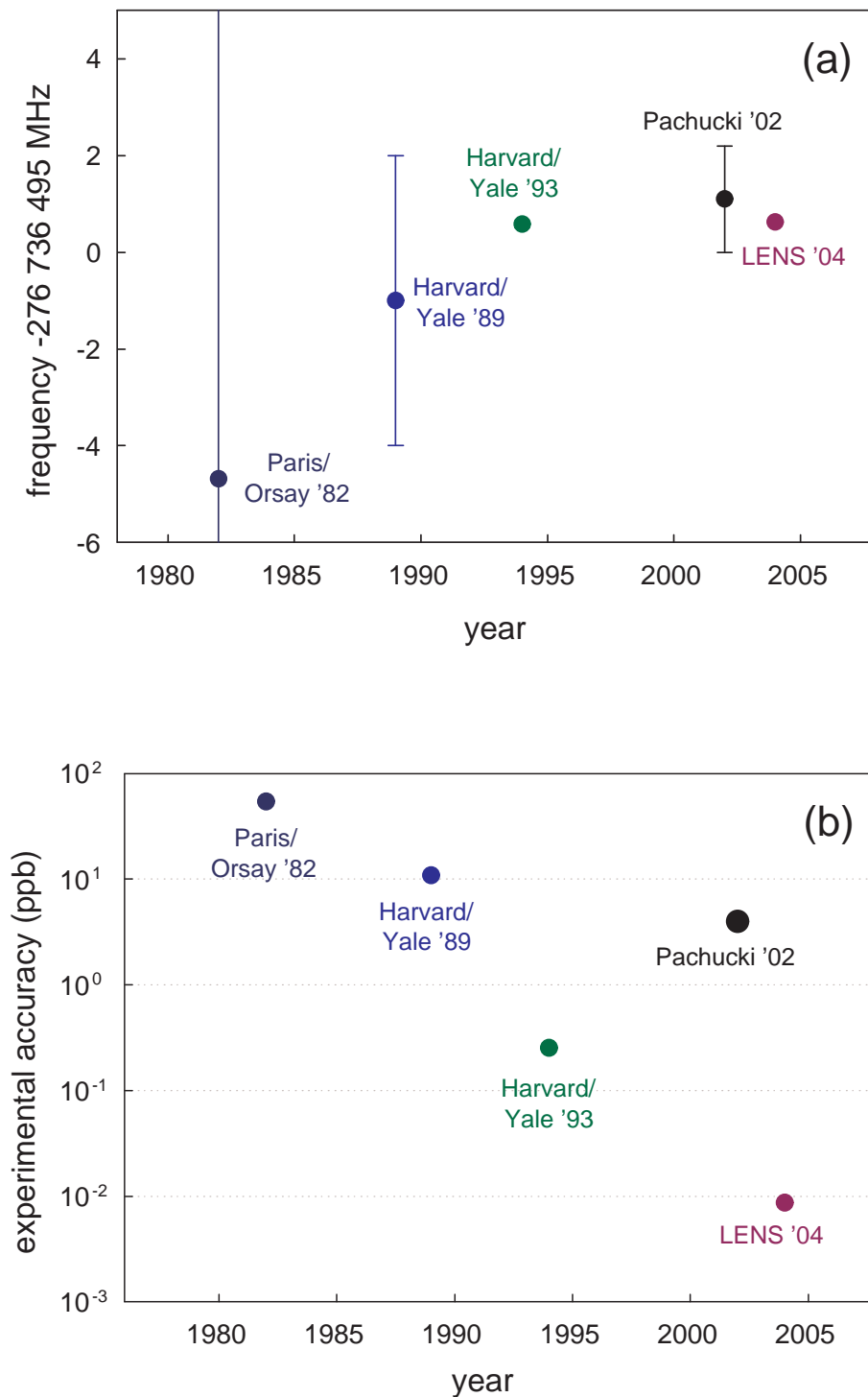


Figure 2.4: (a) Measurements and most recent theoretical prediction for the $(2J+1)$ -weighted mean value of the $2^3S - 2^3P$ transition frequency. (b) Over the past 20 years, the experimental accuracy of the $2^3S - 2^3P$ frequency has improved by almost four orders of magnitude.

photon $2^3S - 3^3D$ transition at 381 nm [47]. Both measurements used tunable dye lasers to perform Doppler-free spectroscopy in a discharge cell. The result for the $(2J + 1)$ -weighted mean frequency is

$$E^{(P/O)} = 276\,736\,490(15) \text{ MHz} \quad [5.4 \times 10^{-8}]. \quad (2.52)$$

The error was attributed to the interferometer used for absolute calibration of the laser frequency.

Direct Measurements at Harvard and Yale

The first direct laser measurement of the $2^3S - 2^3P$ transition was done by Pipken at Harvard and Lichten at Yale [48]. Here, an LNA laser was used to perform saturated-absorption spectroscopy in a magnetically-shielded RF discharge cell. Their result of

$$E^{(\text{HY}'89)} = 276\,736\,494.0(3.0) \text{ MHz} \quad [1.1 \times 10^{-8}] \quad (2.53)$$

was limited by imperfect alignment of a wavemeter used to compare the LNA laser wavelength to a calibrated Zeeman-stabilized He-Ne laser.

A later experiment by Shiner, Dixson, and Zhao [39] used the same approach described in Section 2.3.1. Their result was

$$E^{(\text{HY}'94)} = 276\,736\,495.58(7) \text{ MHz} \quad [2.5 \times 10^{-10}]. \quad (2.54)$$

Similar to previous measurements, the error was dominated by the interferometer used to calibrate the LNA laser against an iodine-stabilized He-Ne laser.

The European Laboratory for Nonlinear Spectroscopy (LENS)

The most accurate measurement of the $2^3S - 2^3P$ transition was done by Inguscio in 2004 [12]. Their approach is described in Section 2.3.1. The work used an optical frequency comb to measure the frequency of a stabilized 1083 nm diode laser with respect to a GPS receiver. Their result for the $(2J + 1)$ -weighted mean value,

$$E^{(\text{LENS})} = 276\,736\,495.6246(24) \text{ MHz} \quad [8.7 \times 10^{-12}], \quad (2.55)$$

was obtained by combining their result for the $2^3S - 2^3P_0$ transition with direct measurements of the fine structure intervals. For the $2^3S - 2^3P_0$ and $2^3S - 2^3P_1$ transitions, uncertainties of 2.0 and 2.1 kHz are attributed to laser beam alignment. A 15 kHz error for the $2^3S - 2^3P_2$ transition is attributed to a recoil-induced frequency shift [45].

Harvard University

Although the work presented here also uses an optical frequency comb, there is an important difference that differentiates this work from the recent LENS results: the optical comb is integrated into the frequency reference by transferring the high stability of an iodine reference from 532 nm to the helium wavelength of 1083 nm. This arrangement allows use of an optical reference that is significantly more stable than any that can be constructed at 1083 nm.

Although an experimental resolution as low as 100 Hz is achieved with this system, three systematic effects shift the results by as much as 10 kHz. The first is a residual Doppler shift due to misalignment of the counterpropagating pump and probe laser beams. The second is an observed asymmetry in the linescans whose physical origins

remain uncertain. As discussed in Chapter 8, our inability to determine upper bounds on the sizes of these shifts prevent us from publishing results at this time.

Chapter 3

The Molecular Iodine Optical Frequency Reference

3.1 Introduction

A central objective of this work was to both improve the frequency stability and linewidth of the laser used for helium spectroscopy and to measure the optical frequency of this laser accurately with respect to the SI second. This chapter describes the molecular iodine optical frequency reference used to provide the high stability and narrow linewidth. The next chapter describes the optical frequency comb and how it is used to transfer this high stability and narrow linewidth to 1083 nm for helium spectroscopy.

Prior to this work, the frequency stability was derived from an optical frequency reference based on transitions in ^3He at 1083 nm. In a sealed 6" long cell containing 200 mT of ^3He , an RF discharge excited atoms to the metastable 2^3S_1 state. A diode

laser at 1083 nm was locked to a hyperfine state at this wavelength using a first-derivative lock. A second 1083 nm diode laser, phase-locked to the reference with offset frequencies between 6 and 40 GHz, was used to probe ^4He transitions.

Fig. 3.1 demonstrates the performance of the ^3He reference. In Fig. 3.1a, the beat frequency between the ^3He reference and the fitted center frequencies of the $2^3S - 2^3P_0$ transition of ^4He drifts approximately 15 kHz over four hours. To confirm that this drift is due to the ^3He reference and not the ^4He transitions, Fig. 3.1b shows the corresponding optical frequencies of the ^3He reference, as measured with respect to a GPS receiver using the optical frequency comb and the iodine clock described here. An upward drift of approximately 10-15 kHz in the frequency of the reference closely matches the drift in Fig. 3.1a. Fig. 3.1c is a correlation plot of the two sets of frequencies. A fit to a straight line gives a slope of 0.995(88), indicating a strong correlation.

While drift was removed from measurements of the fine structure intervals by measuring pairs of transitions in an ABBA sequence, a better solution was to remove the drift from the source. To achieve this, a new frequency reference was needed.

3.2 Improving Frequency Reference Stability

A more methodical approach to calculating reference drift and jitter is to use Allan deviation [49]. Allan deviation is the accepted measure of frequency instability because it converges for all of the common types of noise found in clocks and oscillators. Although standard deviation converges for some of these noise types, such as white FM noise and 1/f flicker PM noise, it does not converge for 1/f FM noise or

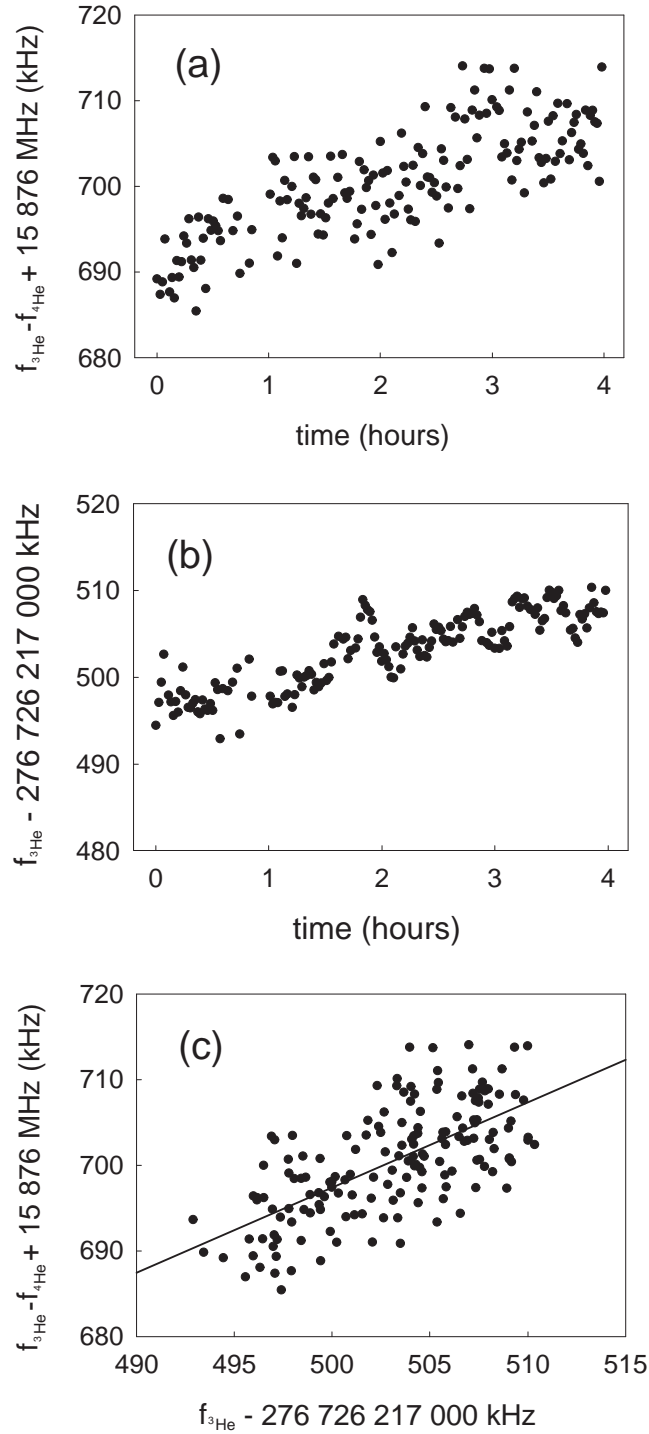


Figure 3.1: (a) Measured frequencies between the ^3He reference and the $2^3S - 2^3P_0$ transition of ^4He drift approximately 15 kHz over four hours. (b) Measured with the new frequency reference system, the corresponding frequencies of the ^3He reference drift a similar amount. (c) Correlation plot of the helium frequencies in (a) and the optical frequencies in (b).

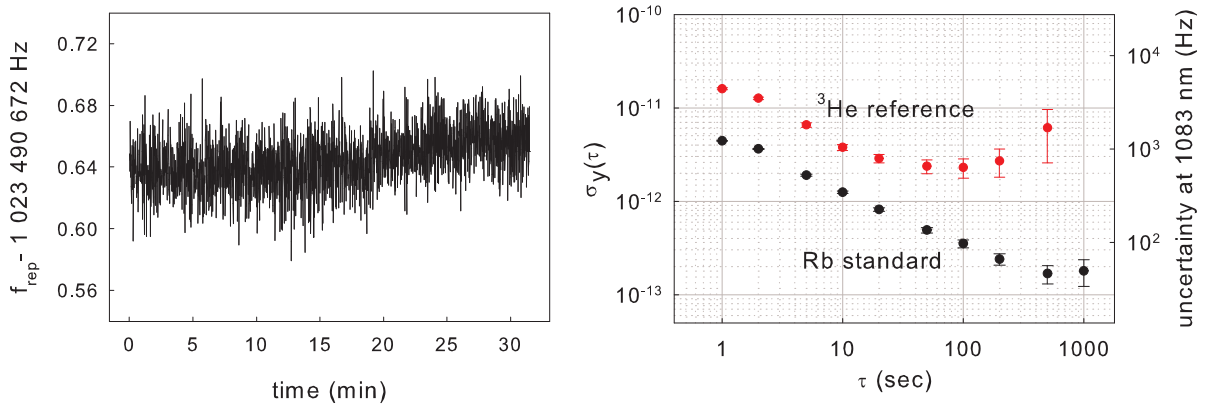


Figure 3.2: (a) Frequency measurements of the ^3He reference, measured by counting the repetition rate of the helium-stabilized optical frequency with respect to a Rb standard. (b) Allan deviation of the ^3He reference and Rb standard.

random-walk FM noise. The Allan deviation σ_y is defined by [49]

$$\sigma_y(\tau) = \frac{1}{\sqrt{2(N-2)}} \sqrt{\sum_{i=1}^N (x_{i+1} - x_i)^2}, \quad (3.1)$$

where $\{x_i\}$ is a set of N frequency measurements taken at equally-spaced intervals of time τ . The Allan deviation for longer times $n\tau$, where n is an integer, can be computed by first dividing the data set into blocks of n neighboring points, and then applying Eqn. 3.1 to the average values of the blocks.

Fig. 3.2a shows a series of 1-second frequency measurements of the ^3He reference, measured by counting the repetition rate of the optical frequency comb with respect to a Rb standard (Ball/Efratom MRT-H/LN). Here, the optical frequency comb is stabilized by phase-locking to the ^3He reference. The corresponding Allan deviation, calculated using Eqn. 3.1, is shown in Fig. 3.2b. For comparison, the Allan deviation of the Rb standard is also plotted. At $\tau = 100$ sec, the ^3He reference achieves its best

instability of $2 \cdot 10^{-12}$, corresponding to a frequency error of 700 Hz at 1083 nm.

Without an optical frequency comb, there were only three options for improving reference stability, all of which were undesirable. The first option, improving the existing ^3He reference, was unattractive because of the intrinsic limitation posed by the transition's broad linewidth of 1.6 MHz. A second approach, locking a frequency-doubled 1083 nm diode laser to iodine transitions at 541.5 nm, has only demonstrated an instability of $\sigma_y(\tau = 1000 \text{ sec}) = 5 \cdot 10^{-12}$ [44]. A third option of locking a 1083 nm diode laser to a high-finesse Fabry-Perot cavity has the benefit of significantly narrowing laser linewidth, but the cavity resonances will drift on longer time without excellent temperature stabilization [50, 51].

Incorporating an optical frequency comb into the experiment presented several additional alternatives to improve reference stability. One option was to generate stable optical signals at 1083 nm by phase-locking the comb to a microwave or RF standard [4]. However, the large multiplication factor between microwave and optical regimes causes the phase noise of these optical signals to be excessive. These signals will have absolute accuracy if the RF standard is a Cs clock or GPS receiver, but their broad linewidth is unattractive for directly probing helium atoms. Although the helium diode laser could be phase-locked to these broad comb components with a long time constant, the resulting feedback loop would not be robust.

The approach used in this work was to transfer the stability of a narrow-linewidth, high-stability optical frequency reference to 1083 nm using an optical frequency comb as a transfer oscillator [52]. Although a frequency reference at any wavelength in the optical or infrared regimes could have been used, stabilization of a monolithic non-

planar ring oscillator (NPRO) to transitions in molecular iodine $^{127}\text{I}_2$ at 532 nm was chosen for several reasons. First, iodine references have been demonstrated to have stabilities up to two orders of magnitude better than the ^3He reference [53, 54, 55, 56]. In fact, stabilities equal to that of a hydrogen maser are routinely achieved. Second, the reference has very few components, making it compact and relatively easy to construct. Third, the use of a monolithic laser reduces the effects of acoustical noise on the laser's performance, helping to improve the robustness of the setup [57]. Last, a large body of literature written over the past 25 years facilitates understanding of both experimental and theoretical issues involved in making high-stability iodine references [58, 59, 60, 61, 62]

3.3 Modulation Transfer Spectroscopy

Although there are several variations of saturation absorption spectroscopy that can be used to stabilize the frequency of a laser to an atomic or molecular transition (third-derivative locking, frequency modulation spectroscopy, etc.), modulation transfer spectroscopy (MTS) was chosen because it tends to give the best stabilities [53, 54, 63]. In MTS, nearly-degenerate four-wave mixing between a multiple-frequency pump beam and a monochromatic probe beam gives rise to sidebands on the probe [64, 65, 66]. The four-wave mixing process is facilitated by a third-order nonlinear susceptibility $\chi^{(3)}$ in the molecular vapor. When driven by two of the pump's frequencies and the probe's single frequency, the nonlinear susceptibility induces an electric dipole polarization in the vapor that radiates a fourth phase-conjugate (PC) electromagnetic wave in the same direction as the probe. The amplitude and phase

of this PC wave are detected by observing its beat with the probe on a photodiode.

Although multiple frequency components can be generated in the saturating pump beam by either phase modulation or amplitude modulation, only phase modulation gives rise to dispersive lineshapes. The saturating pump beam, phase-modulated at frequency δ , is expressed [66]

$$E_S(z, t) = \frac{\mathcal{E}_S}{2} \sum_{n=-\infty}^{\infty} e^{i[(\omega+\Delta)t+\beta\sin(\delta t)-kz+\phi]} + \text{c.c.} \quad (3.2)$$

$$= \frac{\mathcal{E}_S}{2} \sum_{n=-\infty}^{\infty} J_n(\beta) e^{i[(\omega+\Delta+n\delta)t-kz+\phi]} + \text{c.c.} \quad (3.3)$$

where J_n are Bessel functions of order n , β is the modulation index, Δ is a frequency offset between the pump and probe beams, k is the wavenumber, and ϕ is a phase offset. Only the carrier ($n=0$) and first order sidebands ($n=\pm 1$) are considered here.

The probe beam is expressed

$$E_P(z, t) = \frac{\mathcal{E}_P}{2} e^{i(\omega t+kz)} + \text{c.c.} \quad (3.4)$$

Energy conservation forces the frequency of the phase-conjugate beam to be $\omega \pm \delta$ while momentum conservation ensures that these photons are emitted collinearly with respect to the probe. The PC beam is expressed

$$E_{PC}^{(\pm)}(z, t) = \frac{\mathcal{E}_{PC}^{(\pm)}}{2} e^{i[(\omega \pm \delta)t+kz]} + \text{c.c.} \quad (3.5)$$

The intensity of the detected signal is obtained from the beat between the PC and probe beams at frequency δ :

$$I = \frac{1}{2} \epsilon_0 c \mathcal{E}_P \left[\mathcal{E}_{PC}^{(+)} + \mathcal{E}_{PC}^{(-)*} \right] e^{i\delta t} + \text{c.c.} \quad (3.6)$$

The amplitude of the PC beam $\mathcal{E}_{PC}^{(\pm)}$ can be calculated by computing the magnitude of the macroscopic polarization of a sample of two-level molecules. Details of the calculation are found in reference [66].

The frequencies at which PC emission is maximized occur when one-photon and three-photon absorptions are simultaneously resonant for the same velocity class [64, 66]. The two four-photon processes involving the pump carrier and higher-frequency sideband are shown in Fig. 3.3. For Fig. 3.3a, the condition for single-photon absorption of a pump carrier photon by a molecule with velocity v and transition frequency ω_0 is

$$\omega + \Delta - kv = \omega_0$$

For the three-photon absorption process,

$$(\omega + \Delta - kv) - (\omega + \Delta + \delta - kv) + (\omega + kv) = \omega_0$$

Combining these two constraints yields the resonant frequency

$$\omega = \omega_0 - \frac{\Delta}{2} + \frac{\delta}{2} \quad (3.7)$$

For the process in Fig. 3.3b, the resonant frequency is

$$\omega = \omega_0 - \frac{\Delta}{2} - \delta \quad (3.8)$$

Here, a pair of pump frequency components interacting with a single transition gives rise to a pair of resonances separated in frequency by $3\delta/2$. Furthermore, shifting the pump beam by a frequency Δ changes the frequency of the resonance by $-\Delta/2$.

The pump carrier and lower-frequency sideband also generate a pair of resonances. Together, the three pump frequencies generate four resonances. Mathematically, the

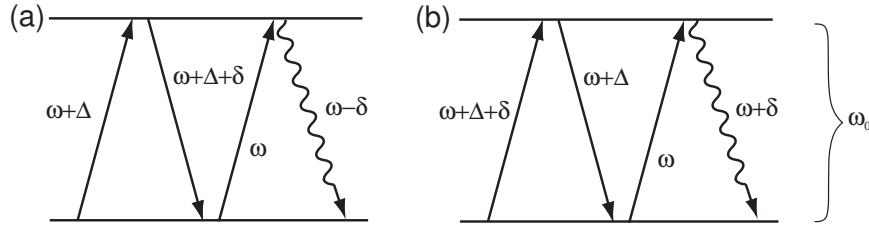


Figure 3.3: Nearly degenerate four-wave mixing in a two-level system emits a phase-conjugate photon: (a) absorption of pump carrier photon and emission of pump sideband photon; (b) absorption of pump sideband photon and emission of pump carrier photon [66].

detected signal is [61, 62]

$$S = C \frac{J_0(\beta) J_1(\beta)}{\sqrt{\gamma^2 + \delta^2}} \left[(L_{-1} - L_{-1/2} + L_{1/2} - L_1) \cos(\delta t + \phi) + (D_{-1} - D_{-1/2} - D_{1/2} + D_1) \sin(\delta t + \phi) \right] \quad (3.9)$$

where C contains constants that are properties of the medium, and L_n and D_n are given by

$$L_n = \frac{\gamma^2}{\gamma^2 + (\omega - \omega_0 - \Delta/2 - n\delta)^2} \quad (3.10)$$

$$D_n = \frac{\gamma(\omega - \omega_0 - \Delta/2 - n\delta)}{\gamma^2 + (\omega - \omega_0 - \Delta/2 - n\delta)^2} \quad (3.11)$$

The pump carrier and higher-frequency sideband generate the signal $-(L_{-1/2} + L_1)$ while the carrier and lower-frequency sideband generate $(L_{-1} + L_{1/2})$. For a modulation frequency equal to half the transition linewidth ($\delta = \gamma/2$), the in-phase component of the detected signal ($\phi = 0$ in Eqn. 3.9) is a dispersive lineshape that can be used as a frequency discriminator for laser stabilization (Fig. 3.4b). For larger modulation frequencies ($\delta > \gamma$), where all four Lorentzian components are resolved (Fig. 3.4a), the signal size decreases because of the molecule's inability to respond to such rapidly varying fields. For smaller modulation frequencies ($\delta < \gamma$), the over-

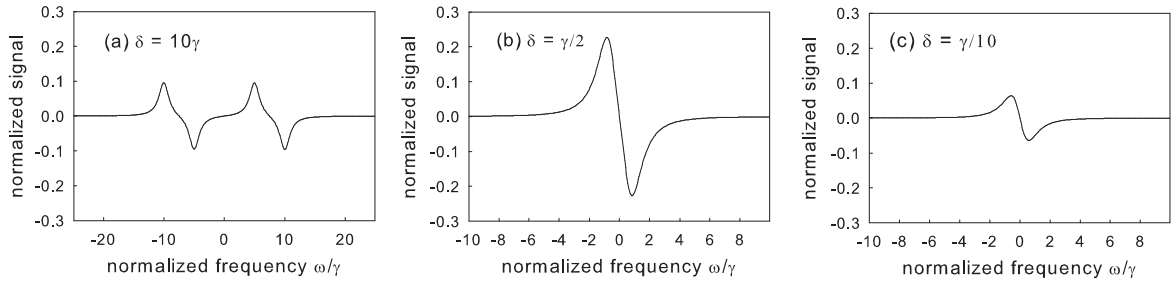


Figure 3.4: Theoretical MTS lineshapes for different values of the modulation frequency δ : (a) $\delta = 10\gamma$; (b) $\delta = \gamma/2$; (c) $\delta = \gamma/10$

lapping Lorentzian components partially cancel, giving rise to lineshapes that are dispersive, yet smaller in magnitude (Fig. 3.4c).

The dispersive signal is largest when the term $J_0(\beta)J_1(\beta)$ is maximized, which occurs for $\beta=1.08$. When higher order pump frequency components are considered, the signal size is maximized for larger values of β [67].

3.4 Experimental Setup

3.4.1 Nd:YAG Non-planar Ring Oscillator

The experimental setup of the iodine reference is shown in Fig. 3.5. The oscillator is a monolithic Nd:YAG non-planar ring oscillator (NPRO) that outputs 500 mW of power at 1064 nm [57, 68]. The laser (Lightwave Electronics 126), shown in Fig. 3.6, is constructed out of a single, monolithic Nd:YAG crystal with three faces cut at angles that give rise to total internal reflection. The front face A acts as an output coupler by providing only partial reflection.

To ensure that the NPRO always lases in the same longitudinal mode, an optical

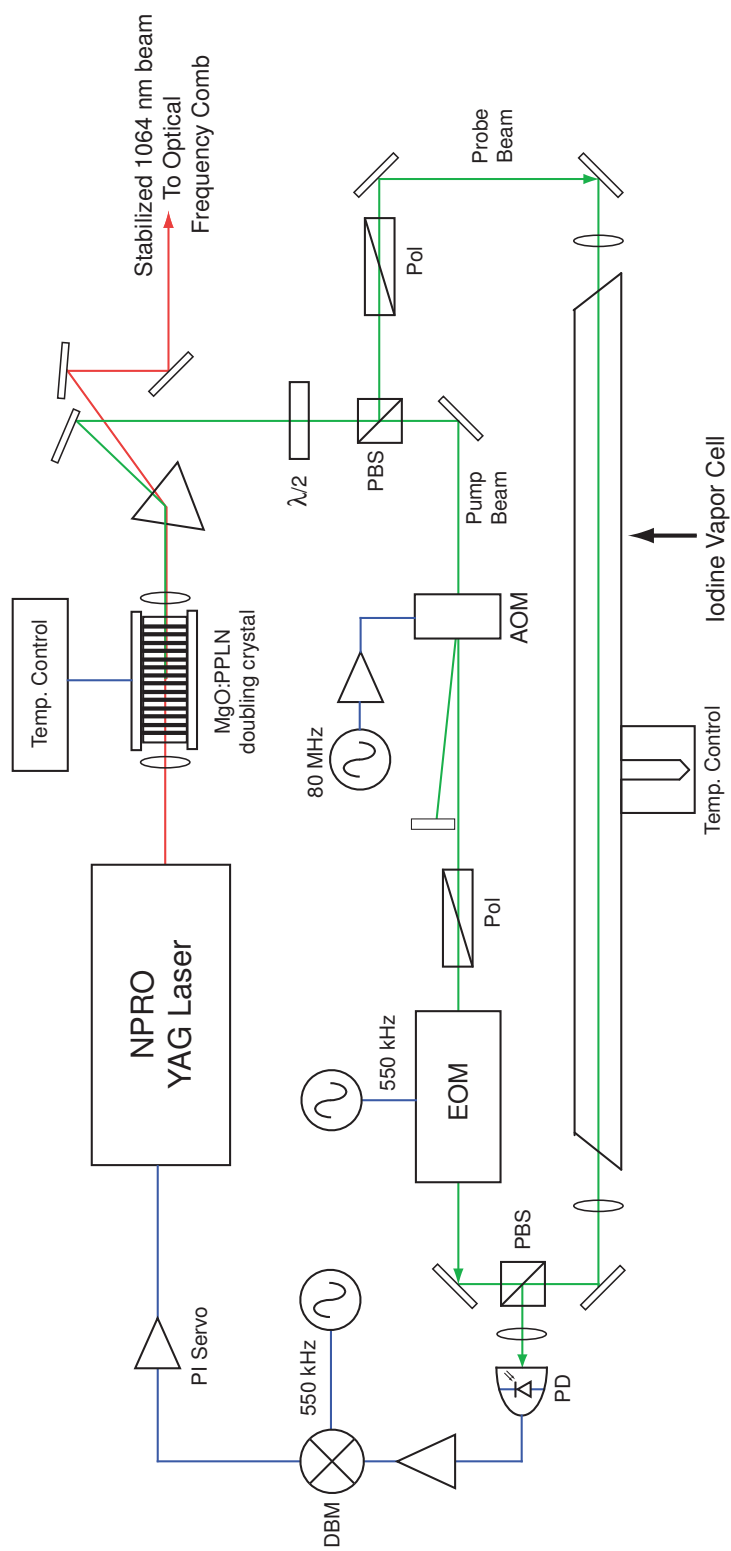


Figure 3.5: Diagram of the molecular iodine optical frequency reference.

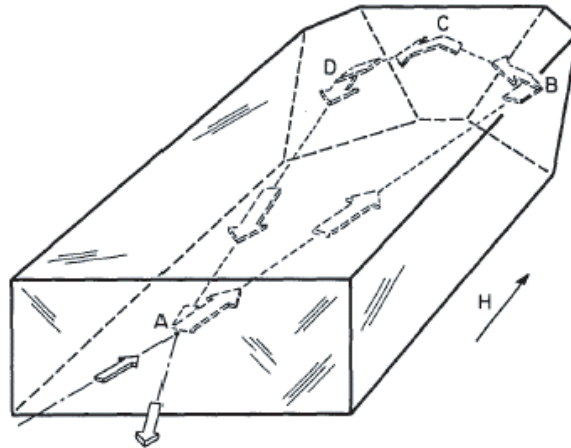


Figure 3.6: Layout of the Nd:YAG non-planar ring oscillator [68]. The crystal is pumped through the front face (A) that also serves as an output coupler. Non-planar reflections (B-C-D) introduce a polarization rotation. A positive Verdet constant turns the crystal into a Faraday rotator when an external magnetic field is applied.

diode in the form of a polarizer, half-waveplate and Faraday isolator is incorporated into the design. The output face acts as a polarizer due to a coating that transmits more P-polarized light than S-polarized light. A polarization rotation is achieved by the non-planar reflections off of faces B and D, which form an angle R with respect to the horizontal. The polarization of light reflecting off these faces is rotated by R . Applying a magnetic field turns the entire crystal into a Faraday rotator due to the positive Verdet constant of Nd:YAG.

The NPRO has fast and slow frequency tuning controls [69]. The slow tuning control is achieved by changing the temperature of the crystal, which changes the cavity length due to the thermal expansion of the Nd:YAG crystal. Although this control can change the NPRO frequency over tens of GHz mode-hop free, the time constant of 0.1 to 1 seconds is slow. The fast tuning control is achieved by changing

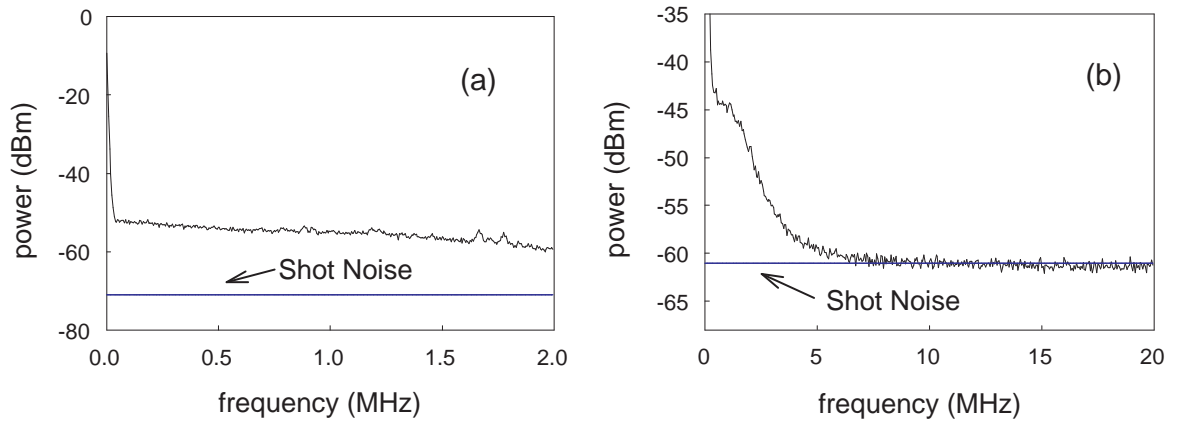


Figure 3.7: Residual intensity noise of the NPRO: (a) low-frequency, resolution bandwidth of 10 kHz; (b) high-frequency, resolution bandwidth of 100 kHz. Both plots are averaged 100 times.

the NPRO crystal length with a piezoelectric transducer that is bonded directly to one facet of the Nd:YAG crystal. The piezo can tune the NPRO frequency over a 100 MHz range with a bandwidth of 100 kHz.

The monolithic design of the NPRO ensures that the cavity length is insensitive to acoustic vibrations and noise, resulting in exceptionally low phase noise. The NPRO linewidth was measured using the same delayed self-heterodyne interferometer described in Section 4.3.2 (Fig. 4.31). A 22.4 km piece of optical fiber provided a delay time of $\tau = 110 \mu\text{sec}$. The FWHM of the the spectrum analyzer trace of the interferometer's output (Fig. 4.32) shows a FWHM linewidth of 1.8 kHz at 1064 nm.

Fig. 3.7 shows two spectrum analyzer traces of the NPRO's residual intensity noise, measured from the output of a 125 MHz amplified photodetector (New Focus 1801) illuminated by a few mW of the NPRO's output. At 500 kHz off the carrier, the measured noise of -54 dBm is 17 dB higher than the shot noise level. As seen in

Fig. 3.7b, the shot noise level is not reached until 7 MHz. This laser intensity noise above shot noise limits SNR, adversely affecting reference stability by almost an order of magnitude. A possible modification to the iodine reference is the use of a balanced photodetection system to remove the effects of this laser intensity noise [70].

3.4.2 Second Harmonic Generation in PPLN

To generate light at 532 nm, the NPRO output is frequency-doubled via second-harmonic generation (SHG) in a nonlinear crystal. Efficient doubling requires proper phase-matching between fundamental and second-harmonic components, which ensures that the radiation emitted by the electric dipoles in the crystal remain in phase. Dispersion causes the phases of the fundamental and second-harmonic beams to become misaligned as they propagate through the crystal. This phase mismatch leads to destructive interference between dipoles in different parts of the crystal, which reduces the intensity of the second-harmonic signal [71].

The phase mismatch Δk is given by

$$\Delta k = 2k_f - k_{sh} = 2\pi \left(2\frac{n_f}{\lambda_f} - \frac{n_{sh}}{\lambda_{sh}} \right) = \frac{4\pi}{\lambda_f} (n_f - n_{sh}), \quad (3.12)$$

where n_f and n_{sh} are the indices of refraction for the fundamental and second harmonic components, and λ_f and λ_{sh} are the wavelengths of the fundamental and second harmonic components. The power of the second-harmonic component P_{sh} depends on phase mismatch Δk by [71]

$$P_{sh} = \frac{(2\pi)^5 d^2 I_f^2}{n_f^2 n_{sh} \lambda_{sh}^2 c} L^2 \frac{\sin^2(\Delta k L/2)}{(\Delta k L/2)^2} \quad (3.13)$$

where $d = \chi^{(2)}/2$ is the nonlinear coefficient, I_f is the intensity of the fundamental

component, and L is the length of the crystal. The term $2/\Delta k$, defined as the coherence length L_C , is the distance over which doubling efficiency is high because of minimal phase mismatch. L_C is approximately $3.25 \mu\text{m}$ for second-harmonic generation of 1064 nm light in lithium niobate.

Although doubling efficiency can be improved by placing the nonlinear crystal in a resonant cavity, where higher circulating powers lead to more efficient SHG, these cavities are difficult to work with because they require very precise alignment and the need to lock the cavity's resonance to the fundamental wavelength [72].

A simpler approach to efficient SHG is single-pass doubling in a periodically-poled crystal [73]. Here, flipping the direction of the ferroelectric domains in the crystal every other coherence length provides quasi-phase matching. This reversal of the domains flips the sign of the crystal's nonlinear coefficient d , thereby introducing a 180° phase shift between fundamental and second-harmonic components. The phase mismatch Δk_{PP} in a periodically-poled crystal is given by

$$\Delta k_{PP} = 2\pi \left(\frac{n_{sh}}{\lambda_{sh}} - 2\frac{n_f}{\lambda_f} - \frac{1}{\Lambda} \right) \quad (3.14)$$

where Λ is the period of the domain-flipping in the crystal. When Λ equals twice the coherence length, the phase mismatch Δk_{PP} is 0, ensuring high doubling efficiency throughout the entire length of the crystal.

The doubling crystal used in the iodine reference is a 40mm long MgO-doped periodically-poled lithium niobate (MgO:PPLN) chip heated to $61.6 \pm 0.1 \text{ }^\circ\text{C}$ (HC Photonics). Heating the crystal serves two important functions. First, heating controls the period Λ via the thermal expansion of the crystal [74]. Second, heating prevents photorefractive damage [75]. In this phenomenon, electrons in the crystal

become free-charge carriers via optical excitation. These electrons diffuse through the crystal, giving rise to internal electric fields that modify the crystal's index of refraction via the nonlinear electro-optic effect. The distortion in refractive index in turn distorts the focusing of the laser beam, which adversely affects conversion efficiency. Heating the crystal gives these displaced electrons enough thermal energy to overcome the electrostatic potential barrier of the charge distribution, allowing them to diffuse through the crystal and recombine with holes in the lattice. While temperatures of at least 200°C are needed to prevent photorefractive damage in undoped PPLN, the addition of an MgO dopant increases the photoconductivity of the crystal (i.e. the amount of energy needed to excite a lattice electron into a free-charge carrier). As a result, MgO:PPLN can operate at temperatures almost an order of magnitude lower than undoped PPLN.

The doubling efficiency η is defined by the relation

$$P_{sh} = \eta L P_f^2 \quad (3.15)$$

where P_{sh} is the generated power at the second harmonic, and P_f is the power of the input fundamental beam. For 500 mW of light at 1064 nm, we obtain 5 mW of green light at 532 nm. The resulting efficiency of 2%/Watt-meter is comparable to results obtained by other groups [63, 76].

3.4.3 Pump and Probe Beams

The fundamental and second harmonic components from the PPLN crystal are separated by a prism. The fundamental forms a beat with the frequency comb while the second harmonic is split into pump and probe beams with a half-waveplate and

polarized beamsplitter. To improve optical isolation between pump and probe beams, the pump beam is frequency-shifted in a Pb:MbO₄ acousto-optic modulator (AOM) that is powered by 2 Watts of RF power at 80 MHz.

Frequency sidebands are added to the pump beam via phase-modulation in a 52 mm long KD*P EOM (Conoptics 350-52). In a tranverse EOM, the modulation index β is given by [77]

$$\beta = \frac{2\pi r_{63} n_0^3 L V}{2t\lambda} \quad (3.16)$$

where $r_{63} = 24 \cdot 10^{-12}$ m/V is the nonlinear optical coefficient, $n_0 = 1.508$ is the ordinary index of refraction, L is the crystal length, $t = 3.3$ mm is the crystal thickness, and $\lambda = 532$ nm is the wavelength. These numbers yield a phase-modulation index of $\beta = 8 \cdot 10^{-3}$ /volt.

To obtain modulation indices large enough for there to be significant power in the sidebands ($\beta \approx 1-2$), the EOM driving signal must have an amplitude of several hundred volts. To obtain such large amplitudes from a standard laboratory function generator, three tunable inductors interact with the EOM's capacitance to form a resonant LC step-up circuit (Fig. 3.8). The amplitude of the driving signal across the EOM, as measured with a high-voltage 10X probe, is shown in Fig. 3.9. A phase modulation $\beta=2$ is used in the final setup, since this gives the largest signal sizes.

To reduce the effects of residual amplitude-modulation (RAM) in the EOM, the crystal is submerged in a bath of index-matching fluid that matches the ordinary refractive index of the KD*P with the glass windows of the unit [78, 79]. The outer faces of the windows are AR coated. In addition, a Glan-Thompson polarizer purifies the polarization of the pump beam before passing through the EOM.

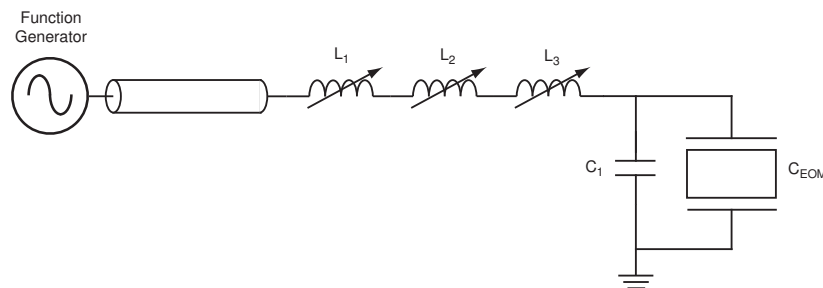


Figure 3.8: The resonant LC step-up circuit used to generate driving signals of several hundred volts across the EOM.

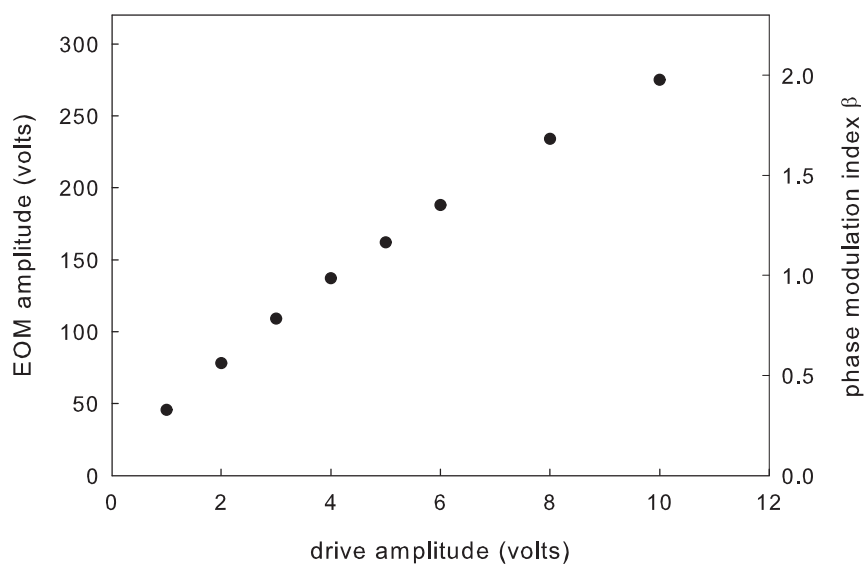


Figure 3.9: Voltage enhancement of the EOM driving signal in a resonant LC step-up circuit.

3.4.4 The Iodine Cell

Purified molecular iodine $^{127}\text{I}_2$ is contained in a 1-meter long borofloat glass cell with Brewster-angled windows (Newport Corporation). Because the pump and probe beams have crossed polarizations, the cell is oriented so that the vertically-polarized probe beam is transmitted through the windows at Brewster's angle; the pump beam experiences small reflective losses at the windows. A pair of lenses, one near each end of the cell, improve collimation of pump and probe beams as they propagate through the cell. The entire cell is wrapped in insulating pipe foam to physically protect it and to isolate it from vibrations.

A small cold finger located a few inches from one of the windows is used to control the vapor pressure of the iodine. Cooling this small glass extrusion allows iodine vapor to condense into solid form on the glass surface. The normal vapor pressure of the iodine P_I depends on the temperature T of the solid iodine as [80]

$$\text{Log}_{10} P_I = \frac{-3512.830}{T} - 2.013 \text{Log}_{10} T + 13.37400$$

The temperature of the cold finger is stabilized to approximately $-15 \pm 0.01^\circ\text{C}$, corresponding to a pressure of 6.2 mTorr. While low operating pressures are usually chosen to improve the reference accuracy by minimizing pressure shifts, low pressures are used here because the reduced linear absorption of the pump and probe beams allows for the reference to be operated at lower laser powers. Note that clock stability is expected to be the same over a broad range of pressures since SNR, which increases as $\sqrt{P_I}$, is balanced by pressure-broadening of the linewidth, which also increases as $\sqrt{P_I}$.

The cold finger's temperature is controlled using a thermo-electric cooler (TEC)

(HiTECH QTEC 2-035.08) driven by an analog PID controller (Wavelength Electronics HTC-3000). To improve efficiency, the hot side of the TEC is cooled using a water-cooled copper plate. The cold finger sits in a 1" deep bath of thermal compound contained in a copper block that is mounted directly onto the cold side of the TEC. This copper block is surrounded on its five other sides by thick pieces of PVC plastic that help insulate the bath from room temperature. Because the cold finger's temperature is reduced below the dew point, air gaps between the bath and outside air are blocked with tape and styrofoam. The temperature sensor, a 1 k Ω platinum RTD, is mounted directly on the glass of the cold finger.

3.4.5 Signal Detection and Electronics

The signal from the iodine reference is detected with an amplified photodetector (New Focus 2017) and demodulated in a double-balanced mixer (Mini-Circuits ZAD-1-1). The local oscillator signal is obtained from a digitally-synthesized function generator that is phase-locked to the function generator that drives the EOM. Changing the phase of the function generator output selects between the in-phase and quadrature components of the detected signal.

Fig. 3.10 is a circuit schematic of the servo lock used for controlling the NPRO. The 50 Ω and 500 Ω resistors on the output of the mixer divide any offsets on the input of the op-amp by 10, helping to reducing DC voltages on the IF port that can affect the balance of the mixer. The 500 Ω resistor and 0.1 μ F capacitor form a low-pass filter that removes components in the mixer output at the modulation frequency. The first op-amp is an amplified lead-lag filter with a DC gain of 100 and high-frequency gain of

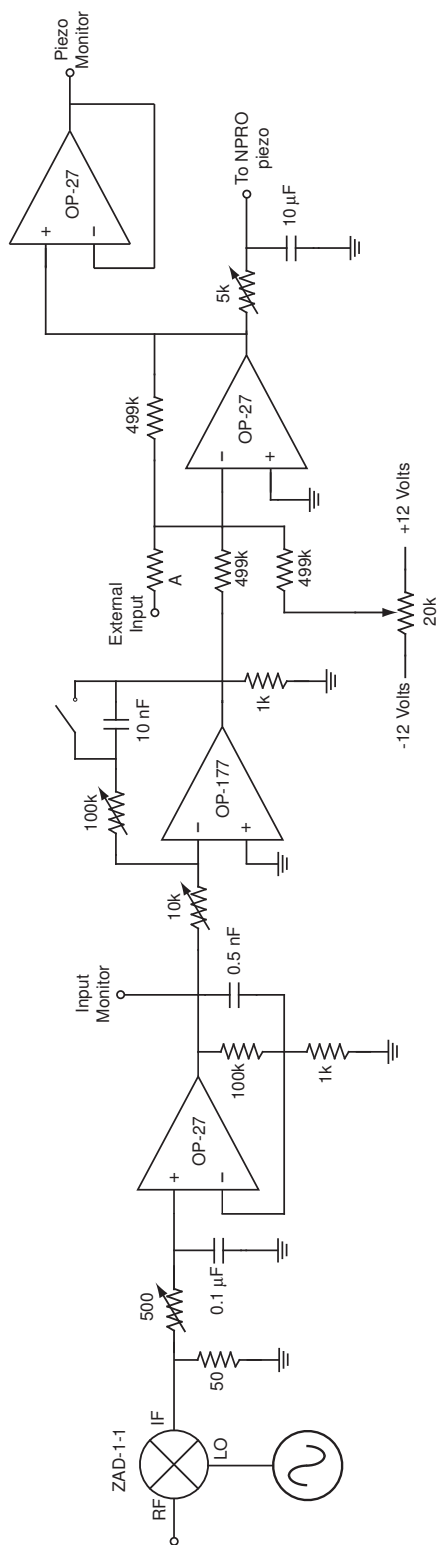


Figure 3.10: The servo circuit used for the iodine reference.

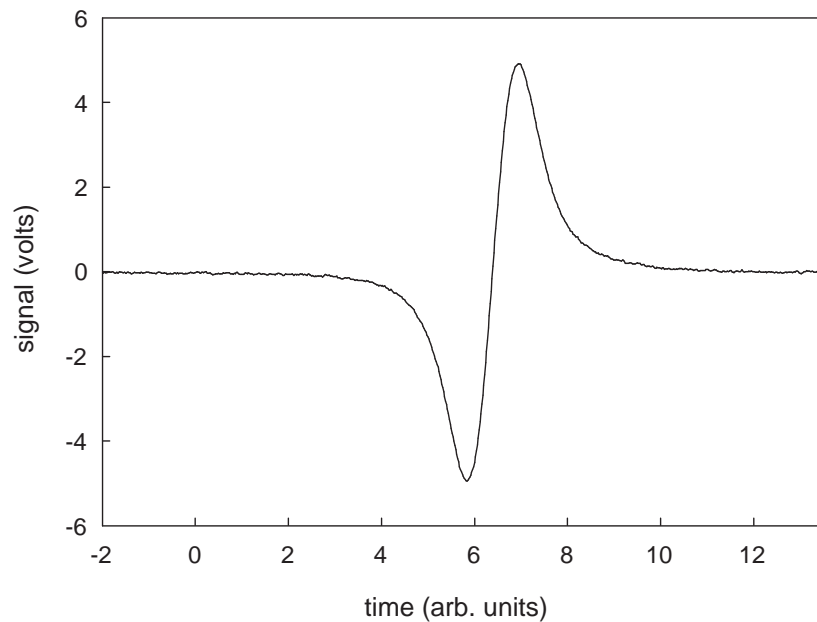


Figure 3.11: Experimental MTS lineshape of the R(56)32-0:a₁₀ transition in ¹²⁷I₂. The trace was averaged 16 times.

unity. The second op-amp (OP-177) is a proportional-integrator (PI) amplifier used to significantly increase low-frequency gain. A resistor and capacitor on the output of the circuit provides further filtering.

Fig. 3.11 shows an oscilloscope trace of the a₁₀ hyperfine component of the R(56)32-0 transition, as measured at the input monitor of the locking circuit [81]. The trace was averaged 16 times to reduce noise in the detection bandwidth. Signal-to-noise is approximately 25 in a 3 kHz bandwidth. This value, which is lower than that obtained by other groups, adversely affects reference stability.

With the feedback loop closed, the closed-loop gain is measured by injecting an AC signal into the external input of the servo circuit and measuring the response at the input monitor with a lock-in amplifier. The gain and phase are plotted in

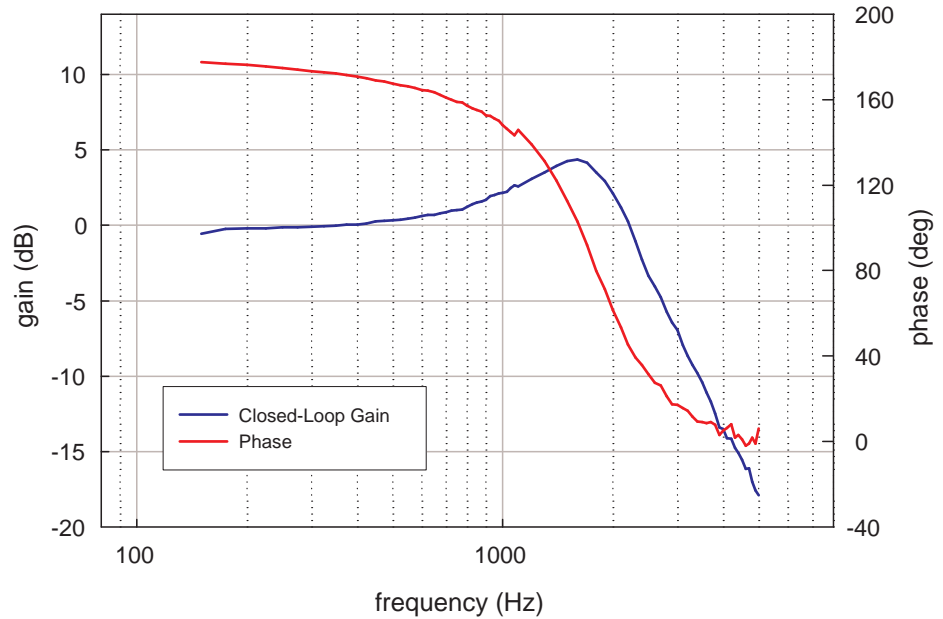


Figure 3.12: Measured closed-loop gain and phase of the iodine feedback loop.

Fig. 3.12. The 2kHz bandwidth of the feedback loop is large enough to remove the frequency fluctuations due to the laser's phase noise and external acoustical noise.

3.5 Iodine Reference Stability

Typically, the stability of an optical frequency reference is measured by observing the beat between two identical references. However, the optical frequency comb allows comparisons between optical and microwave references by phase-coherently dividing the iodine frequency down to the ~ 1 GHz comb repetition rate f_{rep} . Comparing f_{rep} to an RF clock or microwave standard determines the stability of the iodine reference. Because the iodine stability is better than that of GPS receivers and Rb standards, a hydrogen maser was used for the comparison [82].

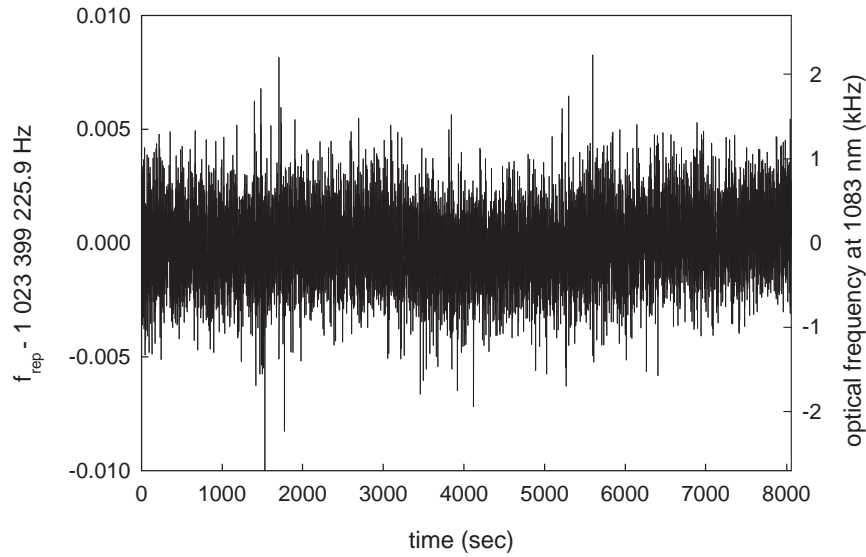


Figure 3.13: Frequency measurements of the iodine-stabilized comb repetition rate.

To increase the resolution of the frequency measurements, the 1 GHz repetition rate is mixed down to a low-frequency signal (~ 100 kHz) in a double-balanced mixer (Mini-Circuits ZP-5MH). The local oscillator signal comes from a frequency synthesizer (HP8662A) referenced to the maser. The low-frequency signal is low-pass filtered and its frequency is measured using a high-resolution counter (Stanford Research Systems SR620). A time sequence of the mixed-down repetition rate is shown in Fig. 3.13.

Fig. 3.14 compares the fractional frequency instability of the iodine reference, as measured by applying Eqn. 3.1 to the frequency measurements in Fig. 3.13, to the instabilities of the helium reference, a GPS receiver (HP58503A), and a hydrogen maser. The iodine reference, significantly more stable than the helium reference and GPS, performs almost as well as a hydrogen maser. Its stability reaches its lowest

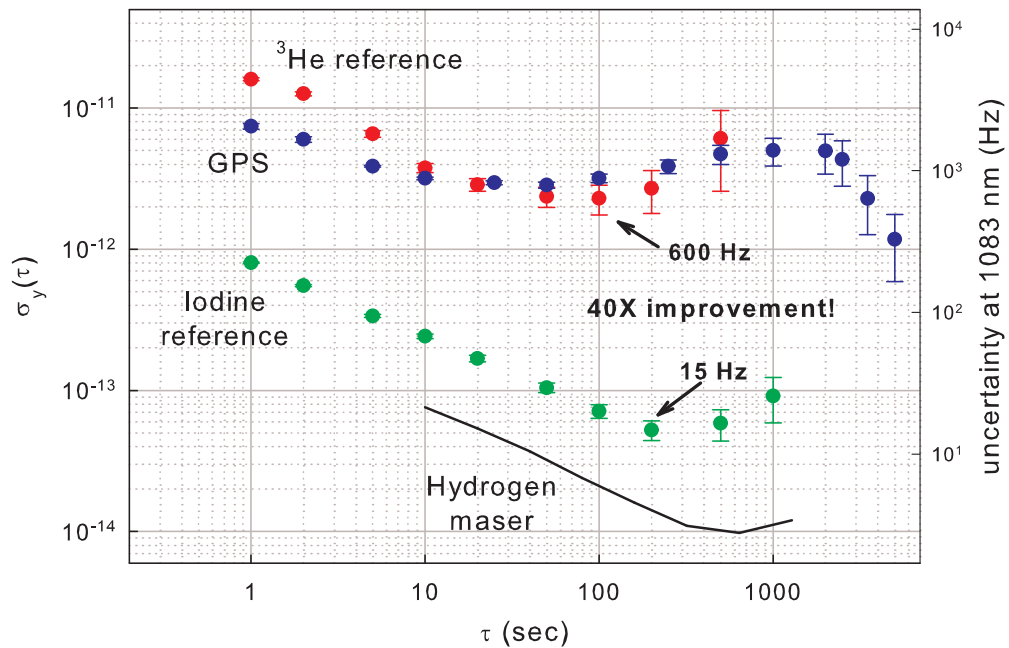


Figure 3.14: Fractional frequency stabilities.

value of $5 \cdot 10^{-14}$ between 200 and 500 seconds. At 1083 nm, this frequency instability corresponds to only 15 Hz, much less than what is needed for the helium setup in this work.

The 40-fold improvement in reference stability removes frequency drift as a significant source of experimental error. As a demonstration, Fig. 3.15 shows fitted center frequencies of the $2^3S - 2^3P_0$ transition of ^4He when the experiment derives its stability from the iodine reference via the optical frequency comb. The frequencies exhibit no detectable drift at the 1 kHz level.

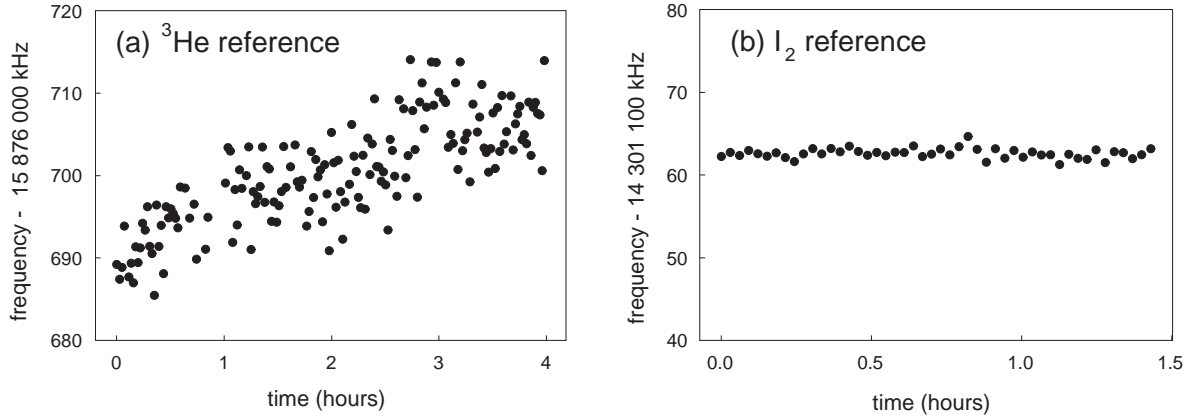


Figure 3.15: Fitted center frequencies of the $2^3S - 2^3P_0$ transition of ^4He show significantly less drift when stability is derived from the iodine reference instead of the helium reference. The y-axis scale is the same for both plots.

3.6 Conclusion

In conclusion, a new optical frequency reference based on transitions in molecular iodine at 532 nm was constructed to both improve the frequency stability and linewidth of a diode laser used to probe the $2^3S - 2^3P_J$ transitions in ^4He at 1083 nm. The high stability and narrow linewidth of the reference, transferred to 1083 nm using the optical frequency comb, has significantly reduced drift and scatter in frequency measurements of helium transitions. In conjunction with the optical frequency comb, the iodine reference allows for measurements of optical transition frequencies that are accurate with respect to the SI second to less than 1 kHz.

Chapter 4

The Optical Frequency Comb

The optical frequency comb represents a major advance in the long-standing problem of accurately measuring optical frequencies. Previously, accuracy was achieved by using complicated frequency chains that multiplied the 9.2 GHz frequency of a cesium clock up to the optical regime [83, 84]. As shown in Fig. 4.1, a chain consisted of multiple oscillators in all regions of the electromagnetic spectrum that were phase-locked together [85]. The apparatus was large enough to fill an entire laboratory and required several people to develop and operate. Furthermore, it was designed to provide accuracy at only one wavelength.

With an optical frequency comb, microwave and optical regimes are phase-coherently bridged in one step using a mode-locked femtosecond laser. Although the idea of using mode-locked lasers for spectroscopy dates back to the 1970s [86], it was not until 1999 that these lasers could be used to easily measure optical frequencies with respect to the Cs second. In that year, the first demonstration of super-continuum generation in an air-silica microstructure fiber [87, 88] quickly led to the construction of

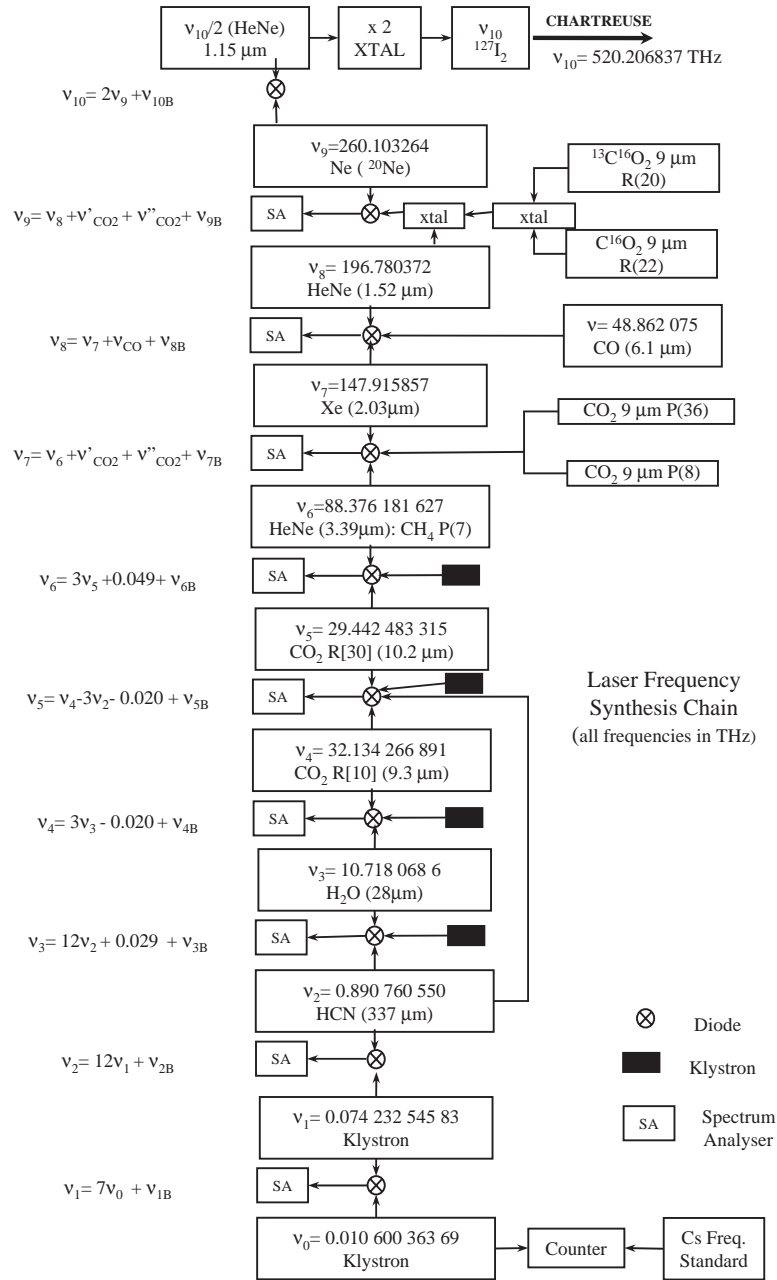


Figure 4.1: Diagram of the frequency chain used to perform the first measurement of an optical frequency with respect to a cesium standard [83, 84]. The equations on the left indicate the relationship between pairs of oscillator frequencies, with ν_{iB} ($i=1,2,3,\dots$) representing the beat note frequencies monitored with a spectrum analyzer or counter [85].

the first optical frequency combs that directly linked optical and microwave regimes [1, 2, 3]. As described below, spectral broadening in the microstructure fiber allows for detection of a frequency offset δ that can be measured when the spectral components extend over an octave, or factor of 2 in frequency. Since then, measurements of several optical transitions have relied on progress in mode-locked lasers and optical combs to achieve improvements by orders of magnitude [1, 2, 4, 11, 12, 52, 89, 90, 91].

An optical frequency comb is a coherent beam of light whose frequency components obey the relationship [3]

$$f_n = n f_{rep} + \delta \quad (4.1)$$

Hundreds of thousands of optical frequencies f_n are determined by two RF frequencies: the repetition rate f_{rep} , which is a common frequency spacing on the order of 1 GHz, and an offset δ (Fig.4.2). The integer n is typically between 10^5 and 10^6 . Experimentally, the validity of Eqn. 4.1 has been demonstrated to better than 1 part in 10^{-19} [3, 92, 93, 94].

The regular spacing of the frequency components acts as a reference grid for measuring optical frequencies in the same way that the equally-spaced tick marks on a ruler are used to measure length. The simplest approach to using the comb for laser spectroscopy is to generate stable optical components f_n by phase-locking f_{rep} and δ to a microwave standard or RF clock. Although the stability and accuracy of these optical signals will be equal to that of the standard, their phase noise will be excessive due to the large integer n that multiplies f_{rep} . The broad linewidth makes these components useful only for measuring optical frequencies and not for controlling lasers.

A more sophisticated approach stabilizes every component of the comb by phase-locking a single component f_n to an optical reference with frequency f_{opt} [95, 96]. With δ stabilized to a microwave reference, f_n is tuned by controlling the repetition rate f_{rep} . The resulting value of f_{rep} is

$$f_{rep} = \frac{f_{opt}}{n} - \frac{\delta}{n} - \frac{f_{beat}}{n} \quad (4.2)$$

where $f_{beat} = f_{opt} - f_n$ is the phase-locked RF beat between the optical reference and comb. The term f_{opt}/n dominates because f_{opt} is orders of magnitude larger than δ and f_{beat} . Consequently, the stability and phase noise of f_{rep} are determined by the optical reference. With f_{rep} and δ stabilized, every optical component f_n inherits the stability and phase noise of the reference, even those with wavelengths far from that of the standard. With their high stability and narrow linewidth, these components are excellent light sources for controlling spectroscopy lasers.

In this work, the frequency comb transfers the high stability and narrow linewidth of an optical frequency reference based on transitions in molecular iodine from 532 nm to 1083 nm, where it serves as the light source for spectroscopy of the $2^3S_1 - 2^3P_J$ transitions in helium (Fig. 4.2). In addition, by counting the comb repetition rate f_{rep} with respect to a GPS-steered Rb standard, the optical frequencies of both the iodine reference and helium transitions can be accurately determined with respect to the Cs second.

After an introduction to the frequency comb and the operation of mode-locked lasers, this chapter describes the experimental setup for the frequency comb, including its interface with the iodine frequency reference and helium spectroscopy experiment. Much attention is given to three important phase-lock loops (PLL): the comb offset

δ , the iodine-comb beat f_I at 1064 nm, and the helium-comb beat f_{1083} at 1083 nm. Presented is a demonstration of the comb's ability to phase-coherently transfer the narrow linewidth of the NPRO laser in the iodine reference to a diode laser at 1083 nm, showing how phase-locking to a stabilized frequency comb can significantly narrow laser linewidth [97]. The chapter concludes by showing how optical frequencies are obtained from the comb parameters and how the accuracy of these optical frequency measurements is determined.

4.1 Principles of Mode-Locked Lasers

4.1.1 Time Domain Description

Experimentally, an optical frequency comb starts with the short, regularly-spaced pulses emitted by a mode-locked laser. In the time domain, the pulse-train consists of a carrier wave modulated by a periodic envelope [98]. The carrier signal is expressed

$$E_c(x, t) = E_0 e^{i\phi(x,t)} = E_0 e^{i(k_c x - \omega_c t + \phi_0)} \quad (4.3)$$

where k_c is the carrier wave number, ω_c is the carrier frequency, and ϕ_0 is an arbitrary phase offset. The repetition rate f_{rep} , defined as the frequency at which the pulses are emitted from the cavity, is given by the inverse of the pulse travel time through the cavity:

$$f_{rep} = \frac{v_g}{L} = \frac{1}{\tau} \quad (4.4)$$

where v_g is the group velocity of the pulse, L is the length of the laser cavity, and $\tau = L/v_g$ is the pulse travel time of one round-trip through the cavity.

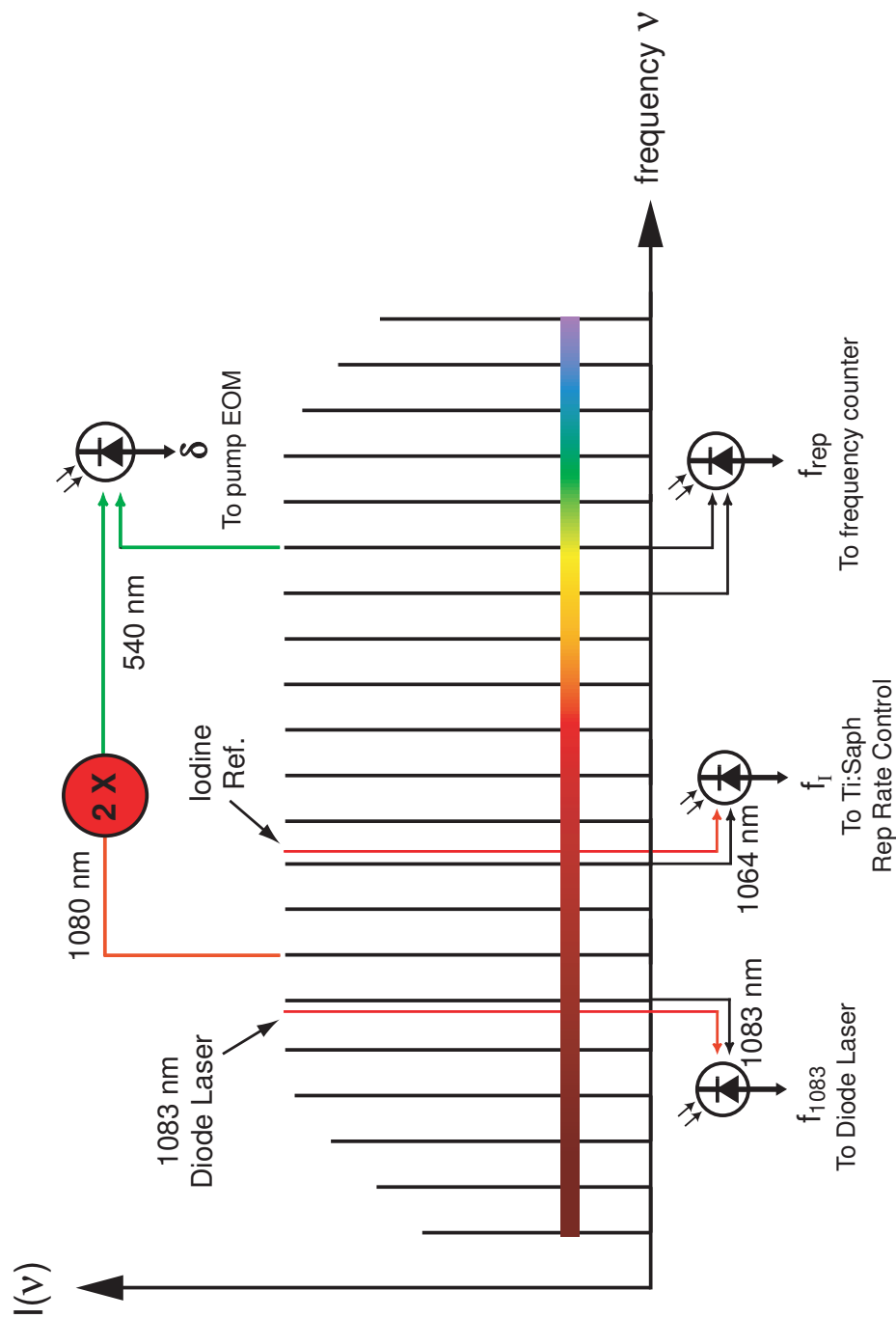


Figure 4.2: Schematic of the optical frequency comb. The comb offset δ is detected and phase-locked while a beat at 1064 nm between the comb and iodine reference is used to stabilize the repetition rate f_{rep} . A 1083 nm diode laser is stabilized using its beat with the comb. At the same time, f_{rep} is detected and counted.

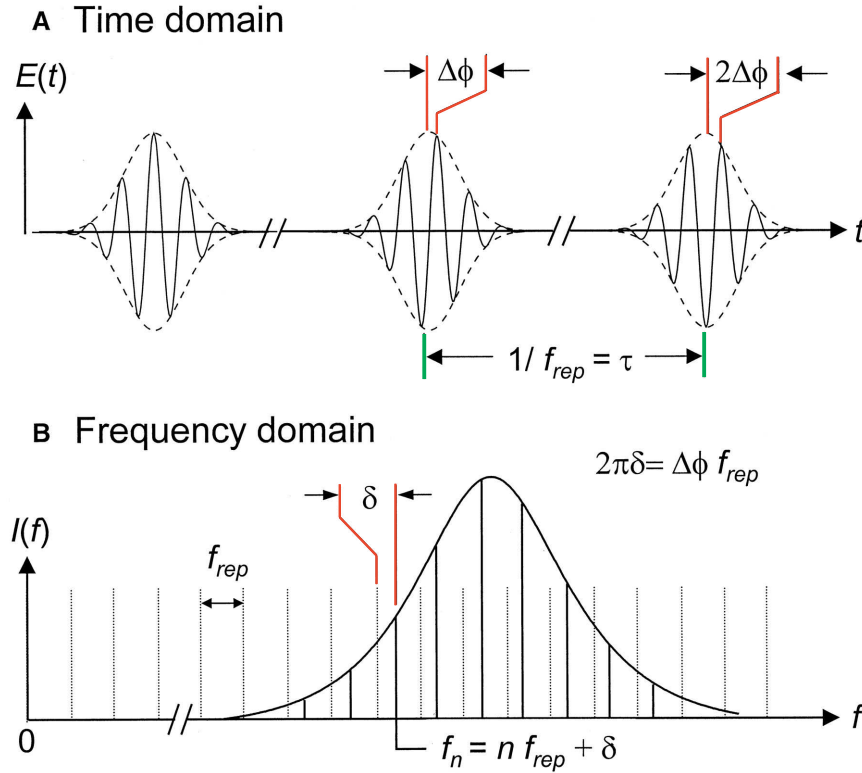


Figure 4.3: A pulse-train in the (a) time domain corresponds to a comb in the (b) frequency domain. A pulse-to-pulse phase shift $\Delta\phi$ between the carrier and envelope causes the frequencies f_n to be offset from integer multiples of the repetition rate f_{rep} by δ [4].

A difference between group velocity v_g and phase velocity v_p , which arises from dispersion, introduces a phase shift $\Delta\phi$ between the carrier and the peak of the pulse envelope during one round trip in the cavity [98, 99]. The effects of $\Delta\phi$ in the time domain are shown in Fig.4.3a [4]. Consider a pulse where the carrier maximum occurs at the envelope peak. For the next pulse, the carrier maximum will be offset from the envelope peak by an amount $\Delta\phi$. In the absence of cavity jitter, the phase shift is cumulative: the carrier will be offset from the envelope by $2\Delta\phi$ for the second pulse, $3\Delta\phi$ for the third pulse, etc.

We can calculate $\Delta\phi$ by considering a pulse that travels from $x = 0$ at time $t = 0$ to $x = L$ at time $t = \tau$ [98]. During this time, the carrier phase $\phi(x, t)$ changes by the amount $\phi(x = L, t = \tau) - \phi(x = 0, t = 0)$. The pulse-to-pulse phase shift $\Delta\phi$ is given by

$$\Delta\phi = [\phi(x = L, t = \tau) - \phi(x = 0, t = 0)] \bmod 2\pi \quad (4.5)$$

$$= [k_c L - \omega_c \tau] \bmod 2\pi \quad (4.6)$$

$$= \left[\omega_c L \left(\frac{1}{v_g} - \frac{1}{v_p} \right) \right] \bmod 2\pi \quad (4.7)$$

where $\bmod 2\pi$ is added so that $\Delta\phi$ has a value between 0 and 2π .

4.1.2 Frequency Domain Description

The pulse-to-pulse phase shift $\Delta\phi$ between carrier and envelope is important because it shifts the frequency of all of the pulses' Fourier components by the comb offset δ (Fig. 4.3b). To better understand this effect, we compute the Fourier transform of the pulse train [98]. At a fixed position, the pulse-train is represented mathematically as

$$E(t) = \sum_n \hat{E}(t - n\tau) e^{i(\omega_c t - n\omega_c \tau + n\Delta\phi + \phi_0)} \quad (4.8)$$

where $\hat{E}(t)$ is the envelope. The Fourier transform of the pulse-train is

$$E(\omega) = \int \hat{E}(t) e^{-i\omega t} dt \quad (4.9)$$

$$= \int \sum_n \hat{E}(t - n\tau) e^{i(\omega_c t - n\omega_c \tau + n\Delta\phi + \phi_0)} e^{-i\omega t} dt \quad (4.10)$$

$$= \sum_n e^{i[n(\Delta\phi - \omega_c \tau) + \phi_0]} \int \hat{E}(t - n\tau) e^{-i[(\omega - \omega_c)t]} dt \quad (4.11)$$

We use the identity

$$\int f(x - a)e^{-i\alpha x} dx = e^{-i\alpha a} \int f(x)e^{-i\alpha x} dx \quad (4.12)$$

This gives

$$E(\omega) = \sum_n e^{i[n(\Delta\phi - \omega_c\tau) + \phi_0]} e^{-in(\omega - \omega_c)\tau} E(\omega - \omega_c) \quad (4.13)$$

$$= e^{i\phi_0} \sum_n e^{i(n\Delta\phi - n\omega\tau)} E(\omega - \omega_c) \quad (4.14)$$

The frequency components that dominate have phases that give rise to constructive interference. This occurs when the phase shift between neighboring components is a multiple of 2π , or $\Delta\phi - \omega\tau = 2n\pi$. The resulting Fourier components are

$$\omega_n = \frac{\Delta\phi}{\tau} - \frac{2n\pi}{\tau} \quad (4.15)$$

The common offset δ is given by

$$\delta = \frac{\Delta\phi f_{rep}}{2\pi} \quad (4.16)$$

When expressed in Hz, the components $f_n = nf_{rep} + \delta$ consist of a comb-like structure of frequencies equally-spaced by f_{rep} and offset from 0 by δ .

4.1.3 Operation of Mode-locked Lasers

In a mode-locked laser, several frequency components add constructively at one point in the cavity (the pulse) and destructively everywhere else. A method of generating these multiple frequencies is needed, as well as a way of keeping their phases aligned as the pulse propagates through dispersive elements in the laser cavity. The more frequency components that contribute to the process, the shorter the pulses (Fig. 4.4) [77].

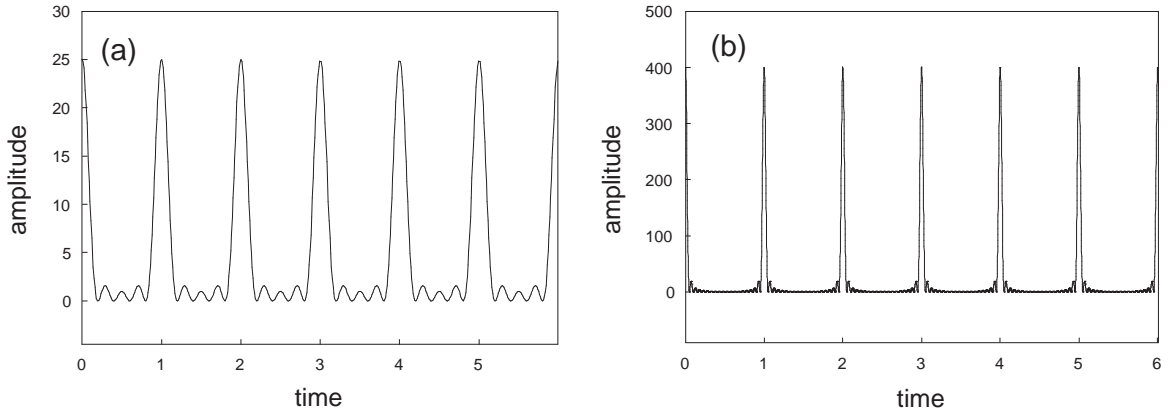


Figure 4.4: Constructive interference between (a) 5 modes, and (b) 20 modes gives rise to a pulse-train. The more modes that contribute, the shorter the pulses [77].

Although there are many ways to achieve mode-locking of a laser, the optical Kerr effect is the most common. The optical Kerr effect is characterized by a medium having an intensity-dependent index of refraction

$$n = n_0 + n_2 I \quad (4.17)$$

where n_0 is the “conventional” refractive index, and n_2 arises from a nonlinear, third-order susceptibility in the laser gain medium, and I is the laser intensity. When $n_2 > 0$, the Kerr effect causes an intense laser beam with a Gaussian profile to be focused (Fig. 4.5) [98]. This focusing leads to better spatial overlap between the pulse and the pumped part of the crystal, allowing for more efficient extraction of energy from the pump. At the edge of the beam in both the transverse and longitudinal directions, weaker light is focused less and extracts less energy from the pump. In other words, the Kerr effect favors short, intense pulses over cw operation.

Self-phase modulation in the crystal generates new frequency components. A

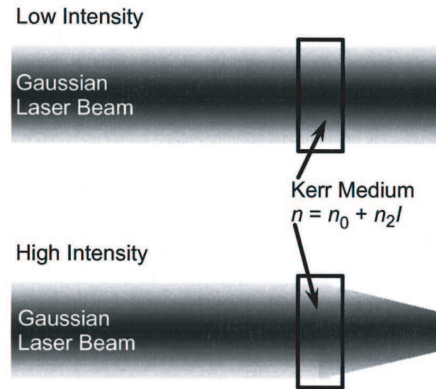


Figure 4.5: A high-intensity Gaussian laser beam is focused in a Kerr medium due to an intensity-dependent index of refraction [98].

pulse propagating through a Kerr medium will have its carrier phase modulated with the time-dependent phase

$$\phi_{SPM}(t) = -\frac{n_2\omega_0 L}{c}I(t) \quad (4.18)$$

where ω_0 is the carrier frequency, L is the length of the nonlinear medium, and $I(t)$ is the intensity envelope of the pulse (Fig. 4.6a) [71]. The new frequency components $\delta\omega$ are given by the time-derivative of ϕ_{SPM} (Fig. 4.6b)

$$\delta\omega(t) = \frac{d\phi_{SPM}(t)}{dt} = -\frac{n_2\omega_0 L}{c} \frac{dI(t)}{dt} \quad (4.19)$$

Only those frequencies that are resonant with the cavity ($f_n = nf_{rep} + \delta$) can have their phases aligned with the pulse. All other frequencies are attenuated.

As shown in Figs. 4.6b and 4.6c, a self-phase-modulated pulse is upchirped: the front of the pulse is red-shifted with respect to the carrier, while the tail of the pulse is blue-shifted. The pulse must be recompressed in order to reach its transform-limited width. In addition, dispersion leads to chirped pulses by introducing different

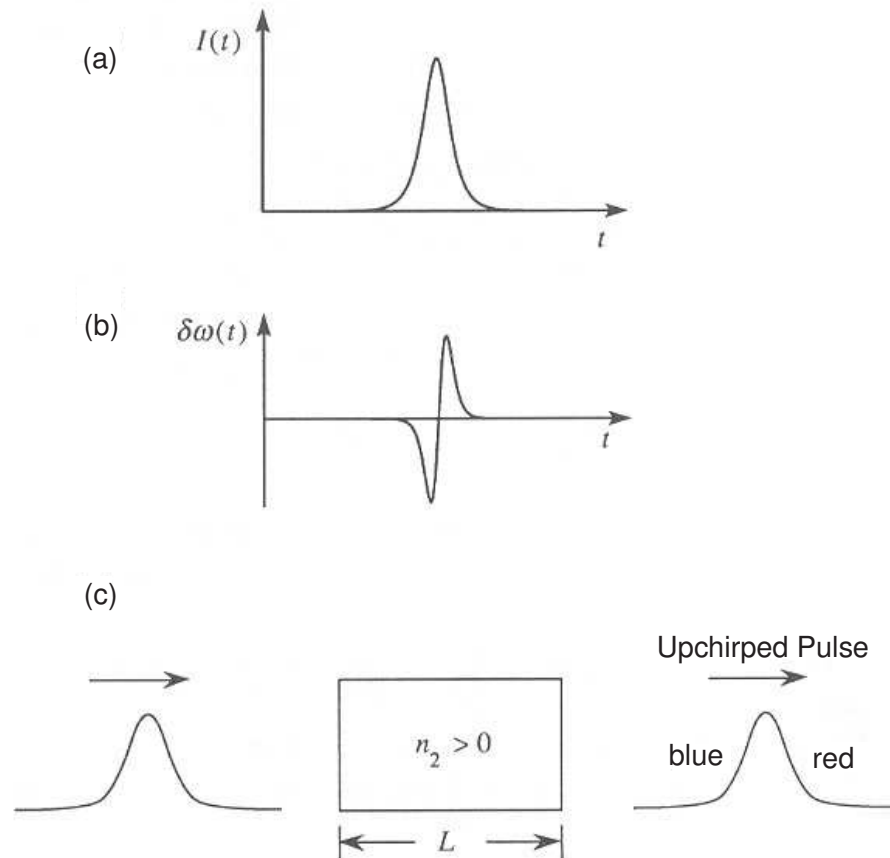


Figure 4.6: Self-phase modulation in a Kerr medium: (a) phase modulation is proportional to the intensity $I(t)$ of the pulse; (b) the instantaneous frequency modulation $\delta\omega(t)$ is proportional to dI/dt ; (c) the frequency modulation generates upchirped pulses, where the front of the pulse is red-shifted with respect to the carrier, while the tail of the pulse is blue-shifted [71].

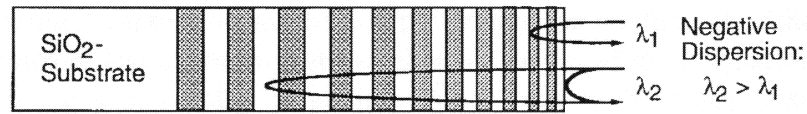


Figure 4.7: Negative dispersion mirrors: longer wavelengths penetrate farther into the stack, corresponding to a longer cavity round-trip travel time [100].

velocities for different frequency components. After several round-trips through the cavity, the phases of the frequency components become unaligned, reducing the peak intensity of the pulse and therefore limiting further amplification.

The main source of dispersion is the Ti:Saph crystal, although other optics (mirror coatings, prisms, etc.) can contribute. To counter it, negative or anomalous dispersion is introduced using “chirped” mirrors (Fig. 4.7) [100]. These dielectric mirrors consist of alternating layers of TiO_2 ($n=2.4$) and SiO_2 ($n=1.45$). The width of these layers depends on their position in the stack: thinner layers are on the surface, while thicker layers are closer to the substrate. The alternating layers form a Bragg reflector that reflects light when the half-wavelength equals the width of a layer. Longer wavelengths penetrate the stack more than shorter wavelengths, and therefore travel a longer distance through the cavity.

Negative dispersion is typically introduced with an intracavity prism pair, which significantly increases the cavity length. By contrast, modelocked Ti:Saph lasers with negatively chirped mirrors have attained repetition rates as high as 3 GHz, corresponding to a cavity length of only 5 cm [101]. Furthermore, prism pairs can only compensate for group-velocity dispersion, limiting the shortest attainable (Fourier-

transform limited) pulses to approximately 75 fsec. On the other hand, by slightly modifying the width of the dielectric layers in the mirrors, third and fourth-order dispersion can be compensated, giving rise to pulses as short as 5 fsec and spectra covering almost 800 nm of optical bandwidth [102].

4.1.4 Frequency Control of Mode-Locked Lasers

In order to stabilize the frequency comb, a pair of control mechanisms are needed for tuning the spacing f_{rep} and the offset δ . The repetition rate is tuned by changing the round-trip pulse travel time, and therefore the rate at which pulses are emitted from the cavity. This is achieved by changing the cavity length L

$$\frac{df_{rep}}{dL} = \frac{f_{rep}}{L} = -\frac{v_g}{L^2} \quad (4.20)$$

Experimentally, the cavity length is controlled with a piezoelectric transducer mounted behind one of the laser cavity mirrors.

The second control mechanism, modulation of the pulse intensity in the laser cavity, is used to control the offset δ [103]. This mechanism is easily implemented by modulating the Ti:Saph pump power with either an electro-optic modulator (EOM) or an acousto-optic modulator (AOM). In this work, an EOM is used. The optical Kerr effect causes changes in the intensity to modify the refractive index of Ti:Saph, and consequently the group and phase velocities. The group velocity v_g of a pulse in a dispersive material is [104]

$$v_g = \frac{c}{\bar{n} + \omega_c \left. \frac{d\bar{n}}{d\omega} \right|_{\omega_c}} \quad (4.21)$$

where $\bar{n} = \bar{n}_0 + \bar{n}_2 I$ is the intensity-dependent index of refraction when averaged

around the entire laser cavity. The phase velocity is given by

$$v_p = \frac{c}{\bar{n}} \quad (4.22)$$

Plugging Eqns. 4.21 and 4.22 into Eqn. 4.7 yields the intensity-dependence for δ :

$$\frac{d\delta}{dI} = \frac{\omega_c^2 v_g^2}{2\pi c^2} \left[\bar{n}_0 \left(\frac{d\bar{n}_2}{d\omega} \right)_{\omega_c} - \bar{n}_2 \left(\frac{d\bar{n}_0}{d\omega} \right)_{\omega_c} \right] \quad (4.23)$$

$$+ \frac{1}{2\pi} \frac{\partial \omega_c}{\partial I} \left\{ \left(1 - \frac{v_g}{v_p} \right) + \frac{\omega_c v_g^2}{v_p} \frac{\partial}{\partial \omega_c} \left(\frac{1}{v_g} \right) - \frac{\omega_c v_g}{c} \frac{\partial \bar{n}}{\partial \omega_c} \right\} \quad (4.24)$$

The first term in square brackets, which reflects changes in group and phase velocities due explicitly to the intensity-dependent index of refraction, depends primarily on properties of the Ti:Saph crystal. The second term in brackets are changes in δ due to an intensity-dependent change in the carrier frequency (i.e. a shift in the laser's output spectrum). A change in the carrier frequency affects the offset δ in three ways, corresponding to the three terms in the bracket. The first term is the explicit dependence of the carrier-envelope phase shift $\Delta\phi$ on the carrier frequency, as shown in Eqn. 4.7. The second term arises because Ti:Saph is a group-velocity-dispersive material, i.e. group velocity depends on carrier frequency. Last, because Ti:Saph is a dispersive medium, a change in carrier frequency leads to a different value for the refractive index, and therefore phase velocity.

Although we treat the tuning mechanisms for δ and f_{rep} as being orthogonal, the two are not completely independent. For instance, a change in pulse intensity affects f_{rep} as well as δ . This shift can be computed by taking the derivative of Eqn. 4.4 with respect to intensity. The result is

$$\frac{df_{rep}}{dI} = -\frac{1}{L} \frac{v_g^2}{c} \left[\bar{n}_2 + \omega_c \left(\frac{d\bar{n}_2}{d\omega} \right)_{\omega_c} + c \frac{\partial \omega_c}{\partial I} \frac{\partial}{\partial \omega_c} \left(\frac{1}{v_g} \right) \right] \quad (4.25)$$

The concept behind Eqn. 4.25 is that self-focusing in the Ti:Saph medium changes the effective cavity length.

Non-orthogonality of the two control mechanisms necessitates careful implementation of the phase-locked loops (PLL) that control f_{rep} and δ . Intracavity power is modulated to control the offset δ while fluctuations in f_{rep} introduced by this power modulation are removed by the iodine-comb PLL. The 75 kHz bandwidth of the iodine-comb PLL is smaller than the 1 MHz bandwidth of the comb offset PLL. By using two different time constants for the feedback loops, the faster loop can correct for non-orthogonality introduced by the slower loop.

4.2 Experimental Apparatus

4.2.1 Kerr-Lens Mode-locked Titanium:Sapphire Laser

The optical comb starts with a commercial Kerr-lens mode-locked Ti:Saph laser (GigaOptics GigaJet 20) which we have significantly modified [105]. Pumped with 6 Watts of 532 nm light, the laser outputs approximately 550-650 mW average power centered at 800 nm. The pulses, which come at a repetition rate of 1 GHz, are 25 fsec in duration and have a pulse energy of 0.1 nJ. A spectral plot of the laser output, measured with a monochromator, is shown in Fig. 4.8.

Fig. 4.9 shows a layout of the components in the Ti:Saph cavity. The Ti:Saph crystal is 1.9 mm wide and cut at Brewster's angle for 800 nm. To remove excess heat caused by the large pump powers, the crystal is mounted with indium foil onto a small copper mount, which in turn is screwed into a larger water-cooled copper

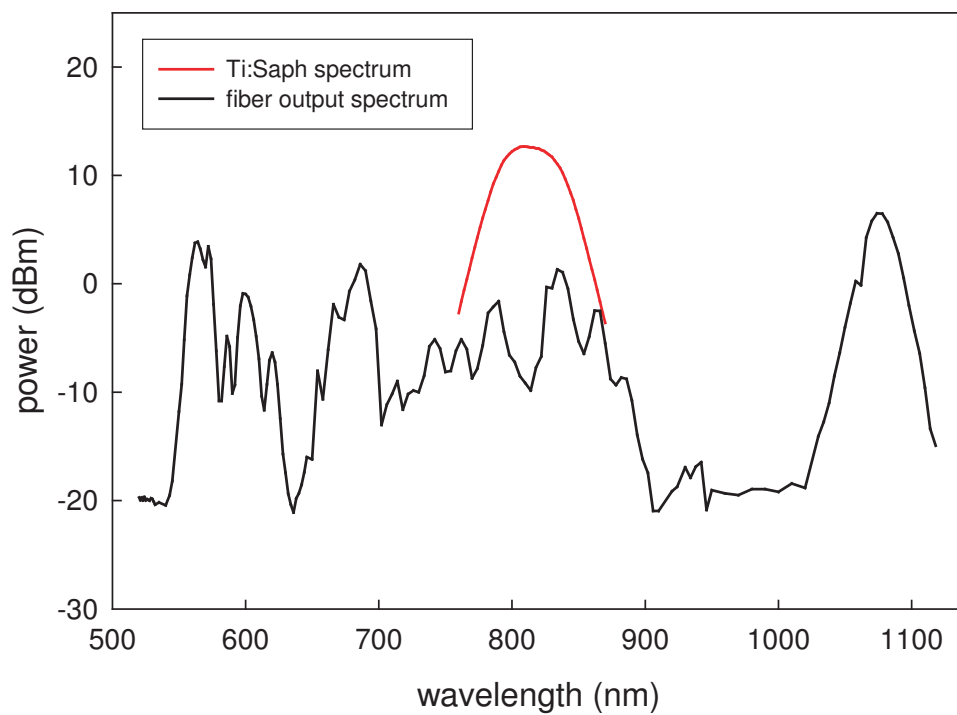


Figure 4.8: Power spectrum of the modelocked Ti:Saph pulses and microstructure fiber output, as measured with a monochromator.

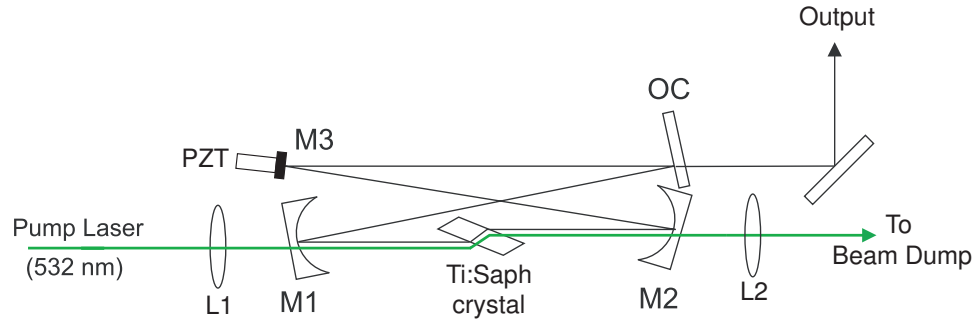


Figure 4.9: Layout of the optical components in the Ti:Saph laser cavity [105].

block. The cavity, formed by three mirrors and an output coupler, is in a bow-tie configuration to help prevent loss of mode-locked operation caused by reflections of the output back into the cavity. The backs of mirrors M1 and M2 are anti-reflection coated at 532 nm to allow for maximum transmission of the pump beam, which is focused onto the Ti:Saph crystal with lens L1. Unabsorbed pump power leaves the cavity through the back face of M2. To prevent heating of the enclosure due this unabsorbed pump light, a second lens L2 collimates this light and directs it into a beam dump.

The length of the cavity is approximately 30 cm, corresponding to a repetition rate of $f_{rep} = c/L = 1$ GHz. There are two benefits to using a high repetition rate. First, the comb's total power is distributed over hundreds of thousands of optical components, with typically less than $1 \mu\text{W}$ of power per component. With so little power, it can be difficult to observe a beat with a large enough signal-to-noise ratio (SNR) to properly phase-lock or count the beat. This power would be even lower if the repetition rate was decreased. Second, the method for determining the integer n for a single comb component, discussed at the end of this chapter, requires the use

of a wavemeter with resolution better than $f_{rep}/2$. This is easier to achieve with a higher repetition rate.

The comb spacing f_{rep} is tuned by changing the cavity length with a piezoelectric transducer (Physik Instrumente PL055) mounted behind mirror M3. To increase the bandwidth, several steps were taken to increase the mechanical resonance frequencies of the system. First, to reduce the mass of the load, a mirror only 1/4" in diameter was used (all other optics are 1/2" diameter). The mirror is epoxied onto the piezo, which in its turn is epoxied onto a 1/2" brass disc that is epoxied into a miniature mirror mount. Second, the PL055 was chosen because it is the smallest piezo found that still provides a large enough frequency tuning range. Smaller piezos are stiffer than their larger counterparts, and therefore have higher resonance frequencies. The PL055 measures 5x5x2 mm and has 2.3 μm of travel, which is enough to change the frequency of an optical component at 1064 nm by $\Delta\nu = (\nu/L)\Delta l = 2.2$ GHz. This large tuning range lets the beat with the iodine reference to be tuned to any frequency between 0 and f_{rep} , giving flexibility in the choice of a locking frequency.

The piezo is tuned by applying a voltage between 0 and 100 volts. The large capacitance of the piezo, $C_{PZT}=0.25$ μF , forms an RC low-pass filter with the output impedance R_{out} of the piezo driver. The Apex Microtech PA85 high-voltage op-amp was chosen because of its high bandwidth and low output impedance of 50 Ω (Fig. 4.10). The transfer function of the driver and piezo is

$$F_{PZT}(s) = -\frac{K_{PZT}}{1 + sR_{out}C_{PZT}} \quad (4.26)$$

where $K_{PZT} = 21$ MHz/Volt is the tuning sensitivity of an optical frequency component at 1064 nm. The measured value of the -3dB rolloff frequency is 20 kHz, slightly

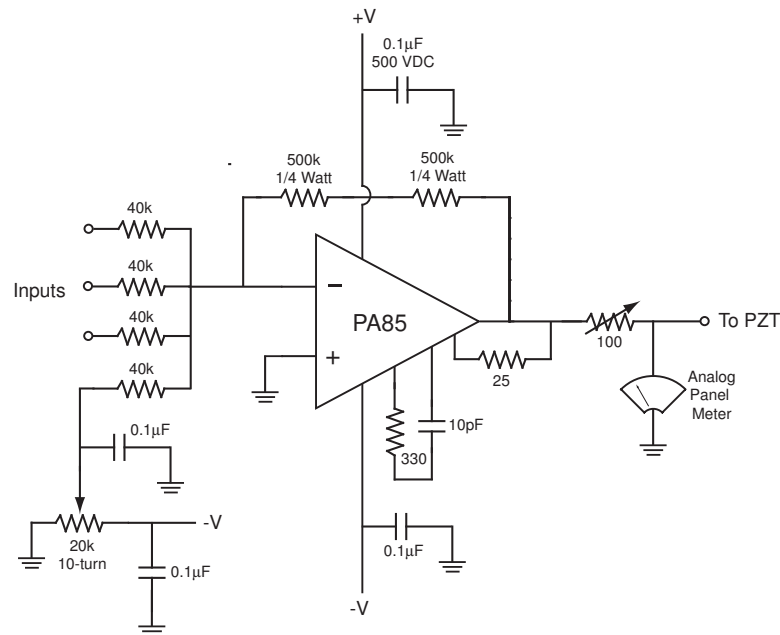


Figure 4.10: The Ti:Saph piezo driver.

higher than the computed value of $(2\pi)f = 1/(0.25\mu\text{F} \cdot 50\Omega) = 12 \text{ kHz}$.

Several steps were taken to improve the stability of the Ti:Saph laser. All elements are re-mounted in a 3/8" thick stainless steel enclosure. An o-ring seal is used with the aluminum lid of the enclosure to eliminate noise caused by air currents blowing through the laser cavity. All windows are attached to welded ports with o-ring seals. Electrical connections are passed into the enclosure through vacuum electrical feedthroughs. All optical components are mounted on a temperature-stabilized Invar baseplate. A resistive heater is used to keep this baseplate at 27 °C, slightly above room temperature. In order to improve thermal conductivity, the heater is first bolted onto a copper plate which in turn is bolted into the Invar in the center of the cavity. The temperature sensor is a thermistor that is epoxied into a brass screw and bolted into the Invar baseplate. The electronic servo is a commercial digital PID

temperature controller (Neocera LTC-11) with auto-tuning of the PID parameters. Typical stabilities of $\pm 3\text{mK}$ are achieved over 24 hours.

All mirrors are epoxied into their mounts to achieve maximum stability. To reduce the effects of vibrations, the enclosure rests on a 2" thick piece of PVC plastic plus two layers of 1/4" thick rubber. The Ti:Saph laser, pump laser, and EOM are enclosed in a larger plastic box that is lined on the inside and outside with acoustical damping foam.

Although the Ti:Saph laser can remain modelocked for several days, over time (16-24 hours) the output power degrades due to the accumulation of dirt on the face of the Ti:Saph crystal. The high intensity of the focused pump beam acts like a dipole trap, causing small particles caught in the pump beam to be pushed toward the beam waist. Although the waist occurs inside the Ti:Saph crystal, the trajectories of the dust particles stop when they hit the face of the Ti:Saph crystal. Their accumulation scatters pump light out of the cavity, reducing the laser's gain.

The accumulation of dirt on the face of the Ti:Saph crystal is remedied in three ways. First, to prevent dust from getting into the laser, the enclosure is opened only when necessary. Second, the air on the optics table is kept clean using a HEPA filter. Third, the Ti:Saph crystal is occasionally removed and ultrasonically cleaned in a bath of acetone (to remove the dirt) and isopropyl (to remove the acetone residue).

4.2.2 Nd:YVO₄ Pump Laser

The Ti:Saph laser is pumped by 6 Watts of 532 nm light from a Nd:YVO₄ laser (Coherent Verdi V-8). A diagram of this laser is shown in Fig. 4.11 [106]. A pair

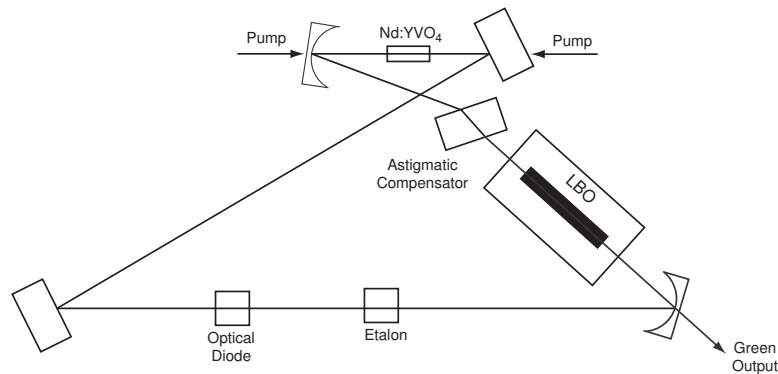


Figure 4.11: Layout of the optical components in the Verdi laser cavity [106].

of high power diode arrays at 980 nm pump a Nd:YVO₄ crystal that lases at 1064 nm. This output is doubled using intracavity second-harmonic generation with an LBO crystal that is temperature-stabilized to $\sim 150 \pm 0.1^{\circ}\text{C}$ using a digital servo. With powers as high as 100 watts circulating in the cavity, a conversion efficiency of $\sim 8\%$ generates up to 8 Watts of doubled light. The vertically polarized output is steered into the Ti:Saph laser with a pair of mirrors. To achieve maximum stability, these mirrors are epoxied into high-stability pressed and sintered powdered-metal stainless steel mirror mounts (Newport Suprema). To electronically modulate the pump power, the beam passes through an electro-optic modulator (EOM) configured as an amplitude modulator (Conoptics). The EOM is configured to pass horizontally polarized light, as needed for the input to the Ti:Saph laser. Operation therefore requires the EOM to be driven near its half-wave voltage of 300 volts DC.

The pump laser was modified to reduce the effects of switching power supply spikes on the laser output. Spectrum analyzer traces of the laser amplitude noise (Fig. 4.12), as detected with a photodiode and low-noise amplifier, show spikes at 105 kHz and several harmonics. We eventually traced these spikes to the switching power

supplies that power the two diode arrays (FAPS). They are coupled into the diode arrays through a pair of grounding wires that connect the anodes of the diode array modules to the power supply chassis. These grounding wires are a safety mechanism used to prevent the anode voltage from drifting far from the chassis ground.

The laser's amplitude noise was significantly reduced by removing the anode-chassis grounding wires. These grounding connections are redundant because the anodes were already grounded to the chassis elsewhere in the power supply circuit. However, this grounding connection occurs before an LC low-pass filter that significantly filters the currents that power the diode arrays. By removing these anode-chassis wires, a significant reduction in the magnitude of these spikes was observed (Fig. 4.12). The spikes at 105 kHz and 210 kHz were reduced by 10 dB and 20 dB, respectively, while the spikes at 315 and 420 kHz were reduced below the laser's noise floor. With these reduced spikes, we found that the comb offset has a cleaner spectrum (Fig. 4.25) and that the robustness of the comb offset PLL is significantly improved.

4.2.3 Spectral Broadening in a Microstructure Fiber

The 25 fsec pulses from the Ti:Saph laser have an optical bandwidth of 50 nm, from 775 - 825 nm. This spectrum needs to be broadened to other wavelengths for two reasons. First, in order to detect the offset δ , the comb needs to extend over an octave. Second, to use the comb with the helium experiment, its spectral components need to extend up to 1083 nm.

Spectral broadening is done with a 1 meter long piece of air-silica microstructure

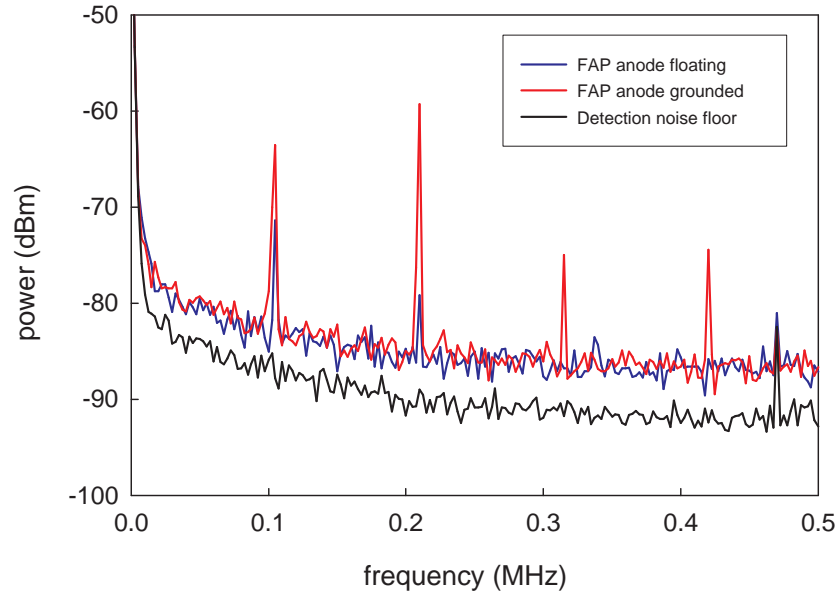


Figure 4.12: Switching power supply noise on the optical output of the Verdi.

fiber [87, 88]. As shown in the cross-sectional diagram and picture in Fig. 4.13, the center core is surrounded by air holes in a hexagonal pattern [87, 107]. Total internal reflection is achieved in the core due to the large difference in indices of refraction between the core and the air. Very high intensities are achieved in the core due its very small $2\ \mu\text{m}$ diameter, giving rise to many nonlinear optical effects. The most important of these effects is four-wave mixing, which spectrally broadens the Ti:Saph pulses to produce hundreds of thousands of optical components across hundreds of nanometers of bandwidth. The four-wave mixing process preserves the equally-spaced structure of the Fourier components.

Care is needed to effectively couple the Ti:Saph laser output into such a small core fiber. To improve long-term drift of the coupling, both ends of the fiber are spliced

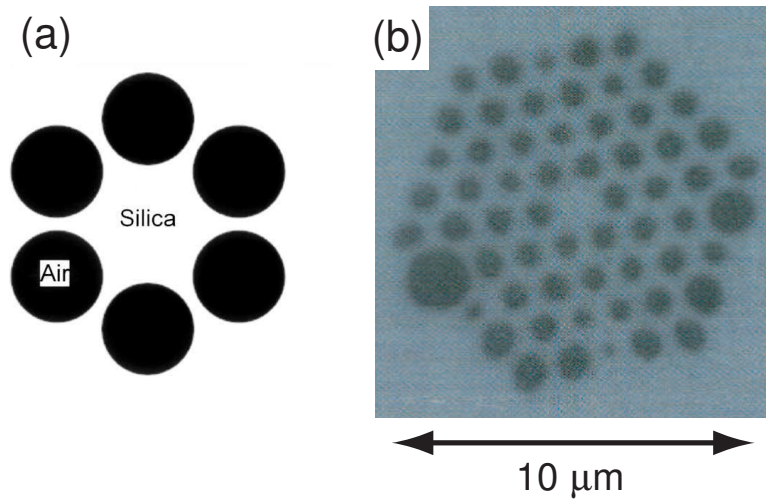


Figure 4.13: (a) In an air-silica microstructure fiber, a silica core is surrounded by a hexagonal array of air holes [87]; (b) Cross-sectional view of the air-silica microstructure fiber used in this work [107].

to a few mm of standard, 4 μm core single-mode fiber and connectorized [108]. The junction between the two fibers forms a taper that focuses light from the larger core single-mode fiber to the smaller core microstructure fiber.

The fiber is mounted and positioned using a high-stability 3-axis flexure mount. Although an achromatic microscope objective is usually used as the focusing lens, we found that a laser diode collimating lens works better. Although such a lens isn't achromatic, it's higher transmission (97% versus 89% for an objective) helps get more power into the fiber, and therefore improves spectral broadening. The output of the fiber, which is also mounted a 3-axis flexure stage, is collimated with a microscope objective.

Typical transmission through the fiber is 40-45%. The output spans more than an octave, from 530 nm to 1150 nm (Fig. 4.8). To improve broadening, an achromatic half-waveplate rotates the polarization of the Ti:Saph output so that the polarization of the pulses is aligned along one of the fiber's six axes. The polarization axis is chosen to maximize the spectrum between 1064 nm and 1083 nm.

4.2.4 The Comb Offset δ

Detecting the Comb Offset δ

Consider a comb component $f_n = nf_{rep} + \delta$ in the low-frequency, or infrared, part of a comb that extends over an octave in frequency. Doubling this component yields

$$2f_n = 2nf_{rep} + 2\delta$$

Consider a second component $f_{n'} = n'f_{rep} + \delta$ in the high-frequency, or blue-green, part of the comb. The beat between $2f_n$ and $f_{n'}$ is

$$2f_n - f_{n'} = (2n - n')f_{rep} + (2\delta - \delta)$$

The lowest frequency beat occurs when $2n = n'$, yielding

$$2f_n - f_{n'} = \delta$$

This simple procedure therefore gives a method to directly measure δ , as needed for stabilization [4].

Experimental Setup

The comb offset δ is detected with a nonlinear Mach-Zender interferometer (Fig. 4.14). The octave-spanning output of the microstructure fiber is split into two paths using a cold mirror that reflects higher frequency visible components and transmits lower-frequency infrared components. Frequencies around 1080 nm are frequency doubled using angle-tuning in a KNbO₃ crystal. Due to the high peak powers in a pulse, efficient single-pass doubling generate approximately 200 μ W of light at 540 nm. This light is reflected with a second cold mirror and recombined with the other beam of the interferometer using a polarized beamsplitter cube. A polarizer projects the polarizations of both beams onto a common axis, while a grating disperses the different colors, preventing light at wavelengths other than 540 nm from hitting the photodiode.

Beats will only be observed when the pulses from both arms of the interferometer hit the photodiode simultaneously. To achieve this, the visible arm must be slightly delayed to compensate for the delay of the infrared beam through the doubling crystal.

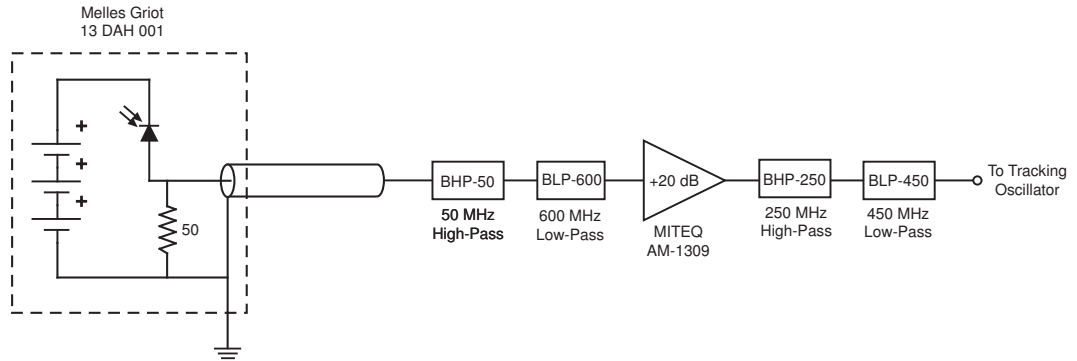


Figure 4.15: Photodetector and front-end amplifiers for detecting the comb offset δ .

This delay is introduced by misaligning the first cold mirror to reflect light at slightly less than 90 degrees; the two arms of the interferometer form a trapezoid rather than a rectangle.

The signal is detected with a high-speed silicon PIN photodiode (Melles Griot 13 DAH 001) powered by 3 lithium cells. A 50Ω resistor converts the signal photocurrent into a voltage (Fig. 4.15). The DC output is removed by a 50 MHz high-pass filter while a 450 MHz low-pass filter removes the large beat at the 1 GHz repetition rate. The filtered signal is amplified in a 20 dB low-noise RF amplifier with a bandwidth of 1-1000 MHz (MITEQ AM-1309). Fig. 4.16 shows a spectrum analyzer trace of the amplifier output. The two lowest comb offset beats, at frequencies δ and $f_{rep} - \delta$ are visible, as is the attenuated rep rate. Typically, the SNR of δ is 30 to 40 dB in a 1 MHz bandwidth.

Tracking Oscillator

Phase-locking and counting are the two most important RF signal processing tasks for all of the comb beat notes. Both the digital phase/frequency detectors (PFD) used

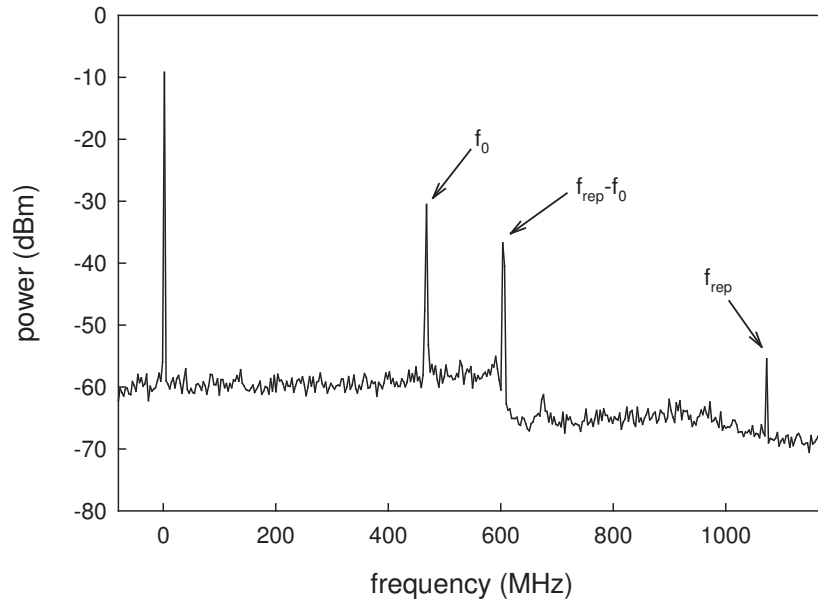


Figure 4.16: Spectrum analyzer trace showing the two lowest comb offset beats at frequencies δ and $f_{rep} - \delta$.

for phase-locking and the frequency counters used to measure beats have prescalers at their inputs with bandwidths greater than 1 GHz. For the digital PFD, the phase noise integrated over this bandwidth can be excessive, causing cycle-slips or loss of lock. For the frequency counter, excessive noise changes the number of zero-crossings read during the gate time, giving rise to inaccurate readings. For proper operation, these wide bandwidth circuits require good filtering of their inputs. However, the SNR of δ is sometimes not good enough to ensure robust phase-locking and accurate counting.

To improve SNR, δ is bandpass filtered with a tracking oscillator. The circuit consists of an RF voltage-controlled oscillator (VCO) that is phase-locked to the input using an analog PLL. The bandwidth of the loop sets the frequency passband

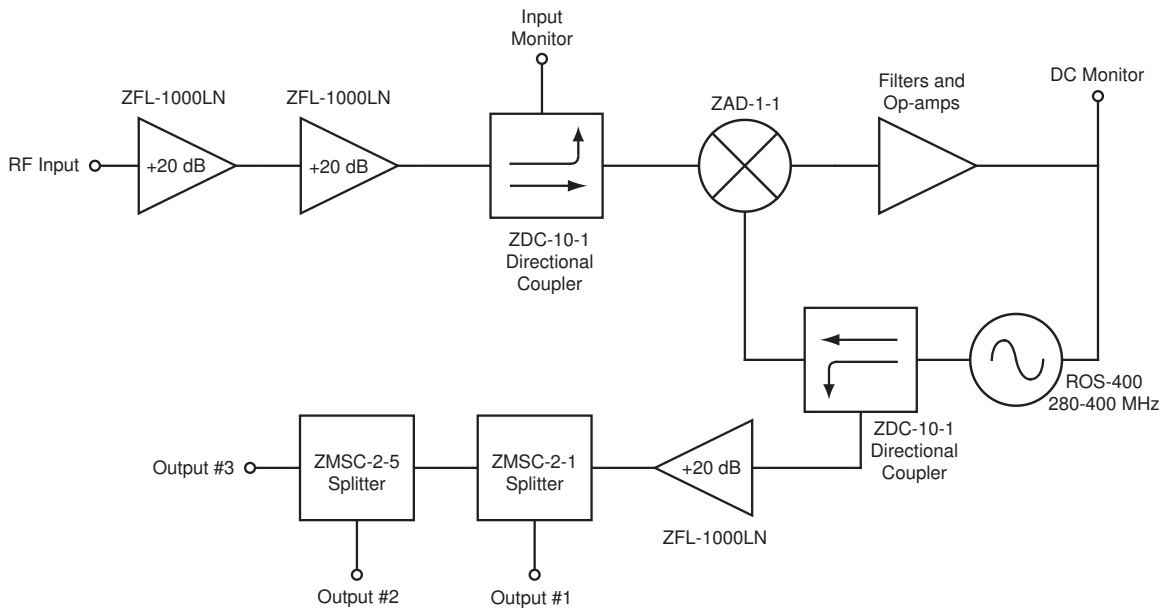


Figure 4.17: Layout of the comb offset tracking oscillator.

of the filter. All of the phase and frequency information on the input that is within this passband is transferred to the VCO, while the wide-bandwidth noise pedestal is rejected.

Fig. 4.17 is a schematic of the tracking oscillator. The VCO (Minicircuits JTOS-535) has a tuning coefficient of $K_{VCO} = 15 \text{ MHz/Volt}$ and outputs a $+9.5 \text{ dBm}$ signal between 250 and 550 MHz for a control voltage between 0 and 16 volts. A double-balanced mixer acts as a phase detector with sensitivity $K_{PD} = 0.20 \text{ volts/rad}$. To reduce the loop's dependency on amplitude fluctuations, the input is amplified to a level great enough to saturate the mixer's diodes.

Fig. 4.18 shows the loop filter and VCO control circuit. The VCO frequency is coarsely tuned with a DC voltage set by a $20 \text{ k}\Omega$ 10-turn potentiometer. Attenuation is controlled by a single-turn $10 \text{ k}\Omega$ potentiometer. A low-pass filter at 300 kHz

is formed by the 15Ω output impedance of the second op-amp and the 28 nF input capacitance of the VCO. To extend the loop bandwidth up to 1 MHz, a phase-advance filter (R1, R2, C1, and C2) was inserted directly after the phase detector. The transfer function $F_1(s)$ of the filter, assuming $C_1 \ll C_2$, consists of two poles and two zeros:

$$F_1(s) = \frac{(1 + sR_2C_2)(1 + sR_1C_1)}{(1 + s(R_1 + R_2)C_2)(1 + s\frac{R_1R_2}{R_1+R_2}C_1)} \quad (4.27)$$

Extra gain at low frequencies is introduced via the first op-amp, which is configured as a lead-lag filter. The transfer function $F_2(s)$ of this op-amp consists of one pole and zero:

$$F_2(s) = - \left(\frac{R_4 + R_5}{R_3} \right) \frac{(1 + s\frac{R_4R_5}{R_4+R_5}C_5)}{(1 + sR_5C_5)} \quad (4.28)$$

where the DC gain is $-(R_4 + R_5)/R_3$ and the high frequency gain is $-R_4/R_3$. The second op-amp, an inverting summing amplifier with a 2 pF feedback capacitor to roll off gain at frequencies above $1/R_6C_6) = (2\pi)900$ kHz, has a transfer function

$$F_3(s) = - \frac{1}{1 + sR_6C_6} \quad (4.29)$$

The transfer function F_{VCO} of the VCO is

$$F_{VCO}(s) = \frac{K_{VCO}}{s} \frac{1}{1 + sR_{OUT}C_{VCO}} \quad (4.30)$$

F_{VCO} has two poles, one at DC and one at $1/R_{OUT}C_{VCO} = (2\pi)300$ kHz.

The open-loop gain is obtained by multiplying together the transfer functions of the phase detector, loop filters, and VCO [109]. Mathematically, the open-loop gain $\Theta(s)$ and closed-loop gain $H(s)$ are

$$\Theta(s) = K_{PD}F_1(s)F_2(s)F_3(s)F_{VCO}(s) \quad (4.31)$$

$$H(s) = \frac{\Theta(s)}{1 + \Theta(s)} \quad (4.32)$$

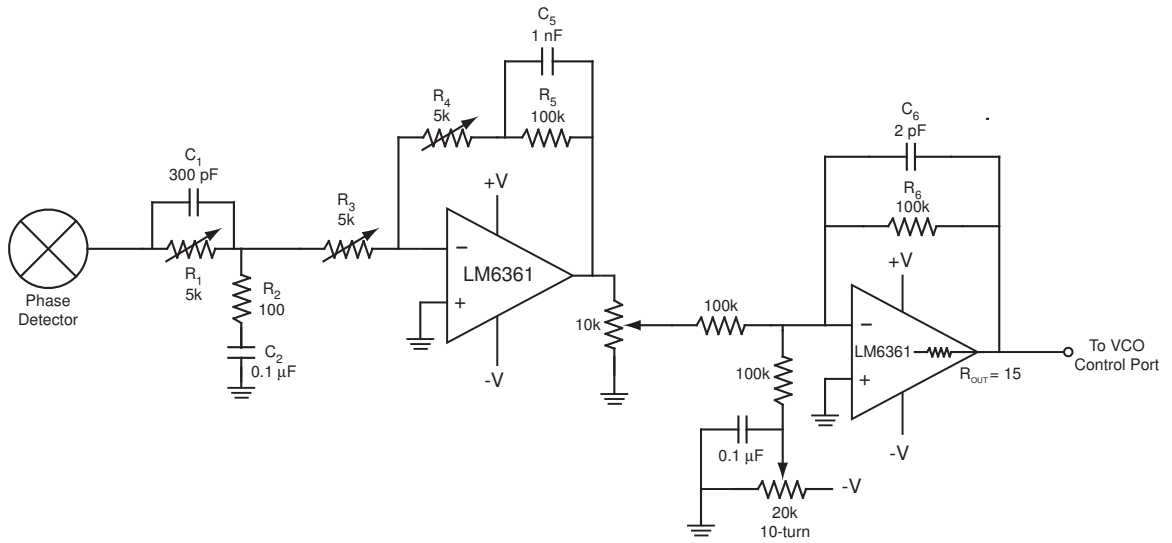


Figure 4.18: Loop filters and amplifiers for the comb offset tracking oscillator.

The magnitude and phase of $\Theta(s)$ and the magnitude of $H(s)$ are plotted in Fig. 4.19. Fig. 4.20 shows the tracking oscillator output with a 425 MHz synthesizer signal as the input. The small "bumps" indicate a bandwidth of 2.5 MHz. At 425 MHz, the Q of this filter is 170.

The VCO output is split into three using an RF splitter. These outputs contain the same phase and frequency information as the input, but have greater than 80 dB SNR in a 1 MHz bandwidth, enough to ensure correct phase-locking and counting.

Controlling the Comb Offset

Intracavity power is controlled by amplitude modulating the green pump power with an ADP electro-optic modulator (Conoptics 370-LA). One of the EOM electrodes is controlled by a high-bandwidth op-amp used for phase-locking δ . The other electrode is controlled by a low-bandwidth, high-voltage op-amp (Fig. 4.21) for course-

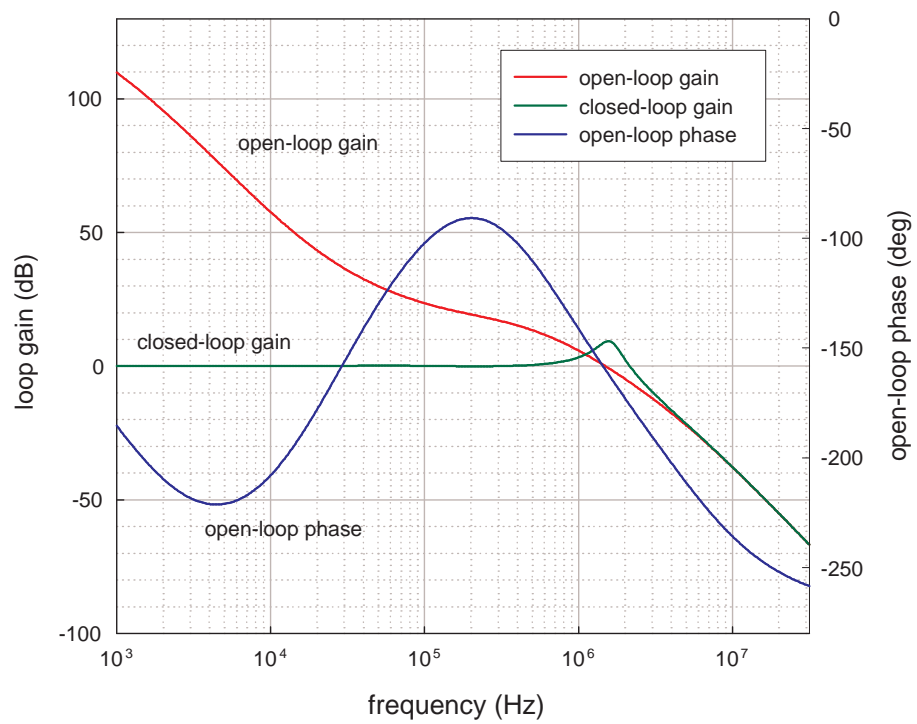


Figure 4.19: Calculated Bode and phase plots for the tracking oscillator PLL.

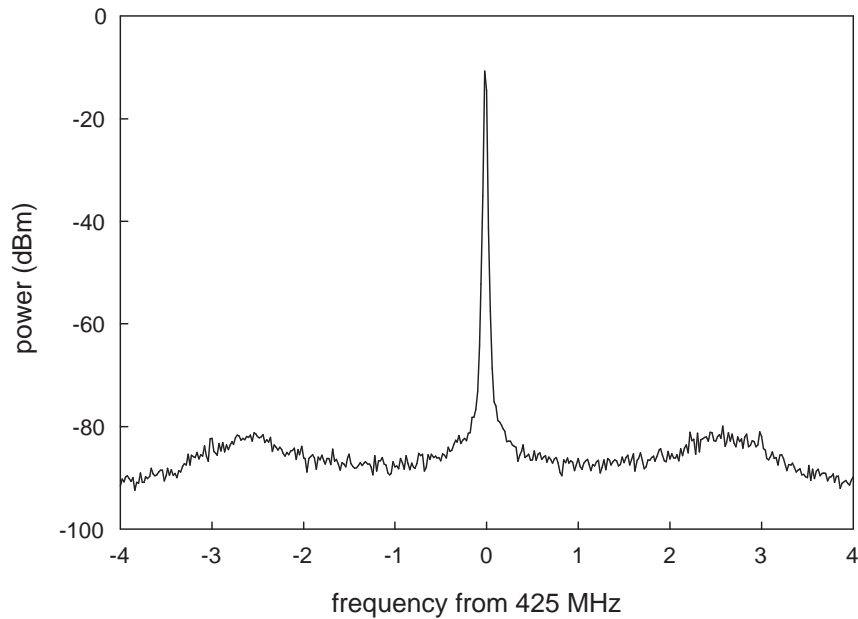


Figure 4.20: Spectrum analyzer trace of the tracking oscillator output when phase-locked to a 425 MHz synthesizer signal.

tuning of δ . A voltage less than the half-wave voltage of the modulator is applied, rotating the vertically polarized pump beam into a predominately horizontally-polarized beam; diverting some of the pump beam allows for a locking setpoint. The op-amp's output is controlled by a ten-turn potentiometer and an external DAC. The tuning sensitivity K_{EOM} is 1 MHz/Volt.

Phase-Locking the Comb Offset δ

A digital PLL circuit, based on a digital phase/frequency detector (PFD), was used to phase-lock the comb offset δ . Originally, we chose a digital PLL because it is easier to incorporate prescalers, which digitally divide frequencies by integer values, to improve lock robustness by preventing cycle slips when signal-to-noise ratio (SNR) is

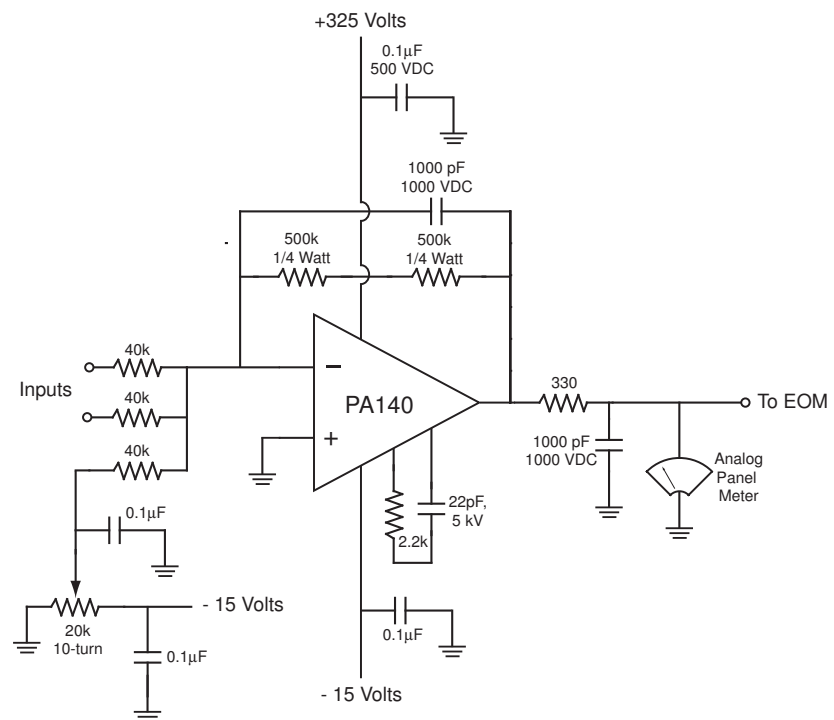


Figure 4.21: The EOM offset driver.

poor [110]. However, we found that with tracking oscillators, the SNR of our detected beats is large enough to prevent cycle slips from occurring. Instead, the digital PLLs are convenient because they are available as integrated circuits, making them easy to construct and integrate with a computer.

Fig. 4.22 is a block diagram of the RF digital PLL synthesizer IC, (Analog Devices ADF4110/4111) [111]. The REF input is connected to a GPS-referenced frequency synthesizer signal between 5 and 100 MHz. A 14-bit counter divides the synthesizer frequency f_{syn} by an integer R between 1 and 16384. The RF input, which accepts frequencies between 80 and 550/1200 MHz (ADF4110/ADF4111), is connected to one of the outputs of the comb offset tracking oscillator. A prescaler, 13-bit counter, and 6-bit counter divide the RF frequency by an integer N between 24 and 65536. The phases of the divided frequencies are compared using a digital PFD at a comparison frequency $f_{comp} = f_{syn}/R$. The two outputs of the PFD drive a charge pump whose maximum output current is set by R_{SET} . The PFD transfer function K_{PFD} is

$$K_{PFD} = \alpha \frac{I_{CP}}{2\pi} = \alpha \frac{V/R_{SET}}{2\pi} \quad (4.33)$$

where α is a programmable gain parameter between 1/20 and 1.

The PLL IC is programmed with Clock, Data, and LE signals from a microprocessor board that is controlled by a computer over a serial fiber ring. The PLL IC contains a digital lock detector that outputs a high TTL signal when the phase error is less than 15 nsec for five consecutive cycles of f_{comp} . In practice, the utility of this lock detector is limited when used with the tracking oscillator because the tracking oscillator outputs a frequency close to the locking frequency even when it is unlocked. This causes the lock detector to always read high. As a more accurate alternative,

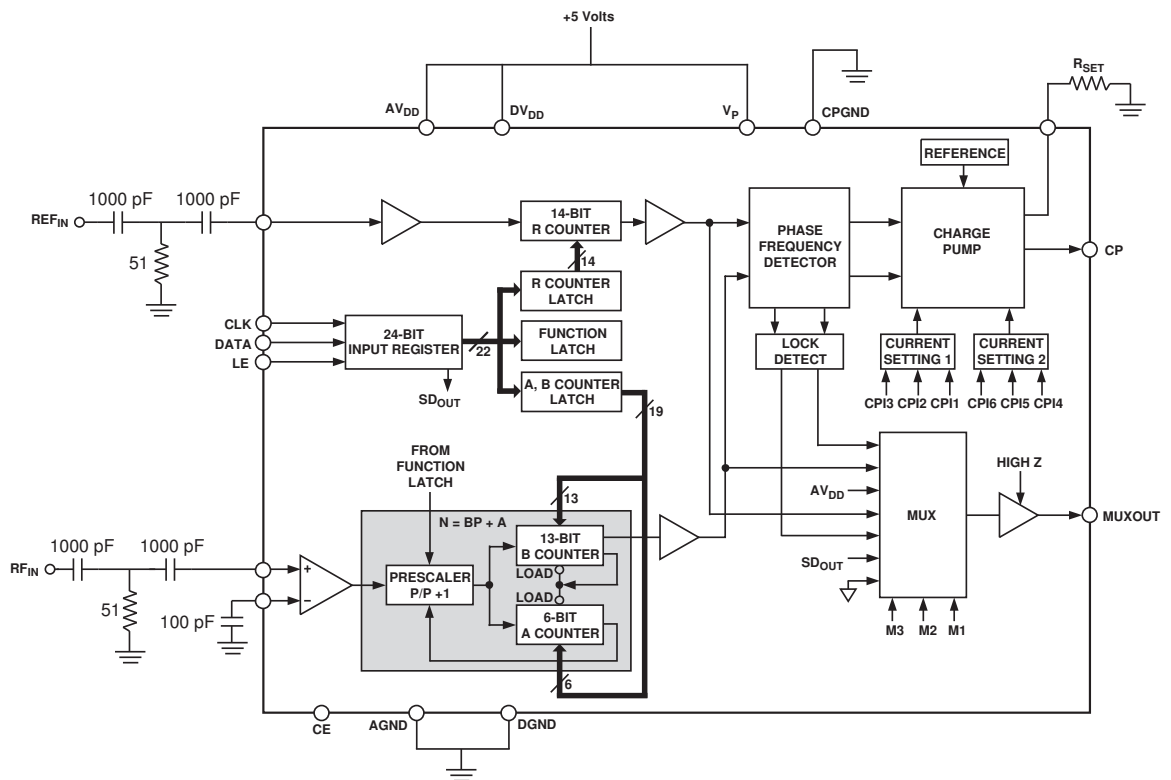


Figure 4.22: Layout of the ADF4110/4111 digital frequency synthesizer IC [111].

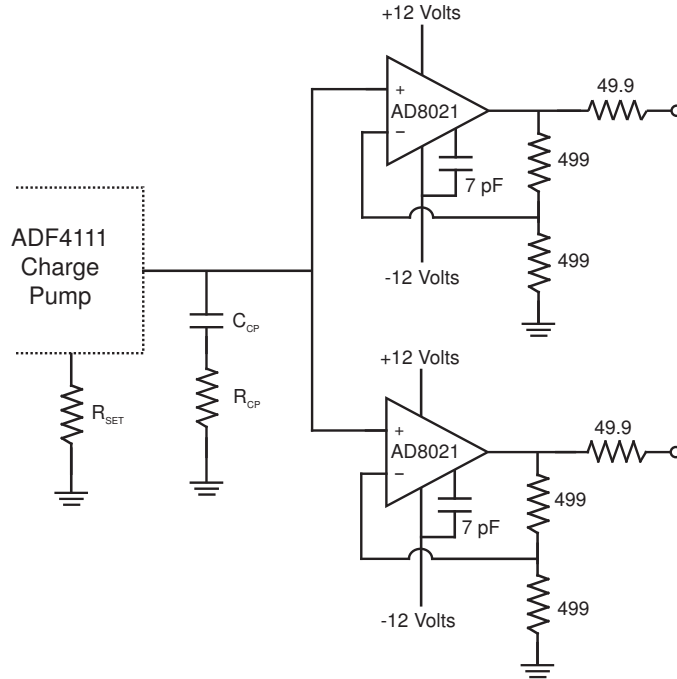


Figure 4.23: The digital PFD charge pump filter and output buffers.

we check the lock status of δ by counting one of the tracking oscillator outputs and ensuring that the read frequency agrees with the lock frequency to within a few Hz.

Fig. 4.23 is a schematic of the PLL filter and output drivers [112]. The current pulses emitted by the charge pump are integrated by the capacitor C_{CP} , giving rise to a DC correction voltage between 0 and 5 volts. The transfer function of the filter $F(s)$ is its impedance to ground

$$F_{CP}(s) = \frac{V_{out}}{I_{in}} = \frac{1 + sR_{CP}C_{CP}}{sC_{CP}} \quad (4.34)$$

The resistor R_{CP} forms a zero at frequency $(2\pi)f = 1/(R_{CP}C_{CP})$ that reduces phase shifts at higher frequencies.

A pair of non-inverting op-amps buffer the output by presenting a high-impedance load at the filter's output. The op-amps are configured to have a gain of 2 in order to

increase the DC locking range to 10 volts. The AD8021 was chosen for several reasons. First, the amplifier ideally should not introduce any phase shifts at frequencies below the loop bandwidth (≈ 1 MHz). This implies an op-amp gain-bandwidth product (GBP) of at least 20 MHz, easily achieved by the AD8021's GBP of 60 MHz. Second, the low input capacitance of 1 pF prevents additional low-pass filters from forming with R_{CP} . Third, the AD8021 outputs enough current to drive 10 volts across 100Ω , allowing it to be easily configured as a 50Ω cable driver. Although it is not necessary to have a 50Ω load because reflections caused by impedance mismatch are negligible at frequencies below 1 MHz, the option was made available for diagnostic testing or for future modifications to the experiment. One of the buffer outputs is connected directly to the EOM. A low-pass filter at 45 MHz, formed by the 50Ω output impedance of the PFD filter circuit and the 70 pF capacitance of the EOM's electrodes, contributes negligible phase shift within the loop bandwidth.

The open-loop gain $\Theta(s)$ of the loop is obtained by multiplying together the transfer functions of the prescaler ($=1/N$), PFD (Eqn. 4.33), charge-pump filter (Eqn. 4.34), and EOM ($=K_{EOM}/s$). Mathematically, the open-loop gain $\Theta(s)$ and closed-loop gain $H(s)$ are given by:

$$\Theta(s) = \frac{1}{N} \frac{K_{PFD} F_{CP}(s) K_{VCO}}{s} \quad (4.35)$$

$$= \frac{1}{N} \frac{\alpha I_{CP} K_{VCO}}{2\pi} \frac{(1 + sR_{CP}C_{CP})}{s C_{CP}} \quad (4.36)$$

$$H(s) = \frac{\Theta(s)}{1 + N\Theta(s)} \quad (4.37)$$

The magnitude and phase of $\Theta(s)$ and the magnitude of $H(s)$ are plotted in Fig4.24. Spectrum analyzer traces of the phase-locked offset are shown in Fig. 4.25. The bandwidth of the loop, as determined by the ‘‘bumps’’ off the carrier, is approximately

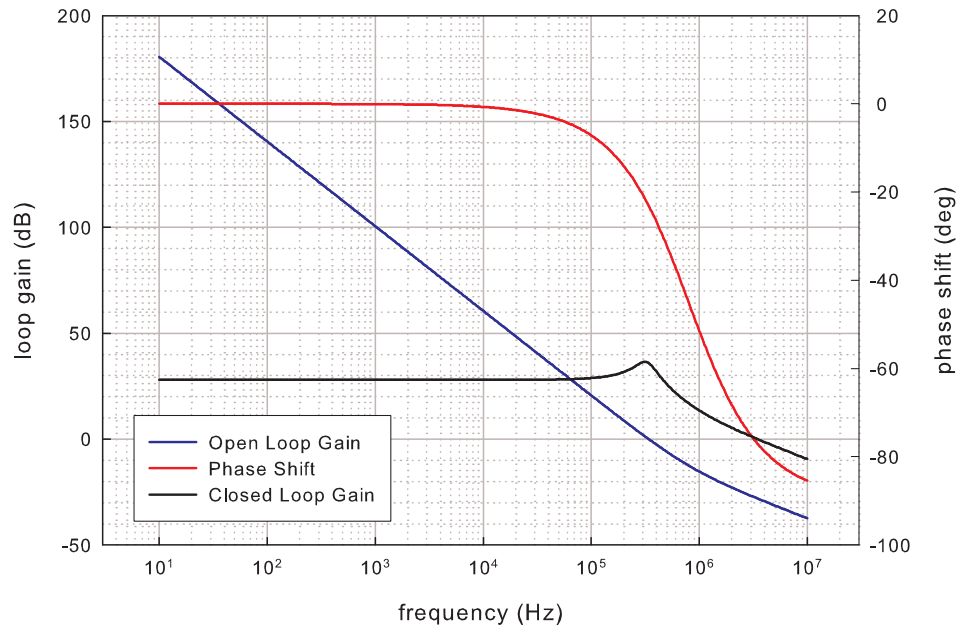


Figure 4.24: Calculated Bode and phase plots for the comb offset PLL.

500 kHz. The presence of a resolution bandwidth-limited carrier indicates that the loop is effective at stripping the phase noise off the carrier and replacing it with the phase noise of the reference signal.

4.2.5 Stabilizing the Optical Comb to the Iodine Reference

To stabilize the optical frequency comb to the iodine reference, a beat f_I is detected at 1064 nm (Fig. 4.14). Unwanted comb components are removed using a 1064 nm bandpass interference filter. The two beams are combined with a polarized beamsplitter cube and projected onto the same polarization axis using a polarizer. The signal is detected with an amplified InGaAs photodetector (New Focus 1801).

The beat f_I is detected at 1064 nm instead of 532 nm for two reasons. First,

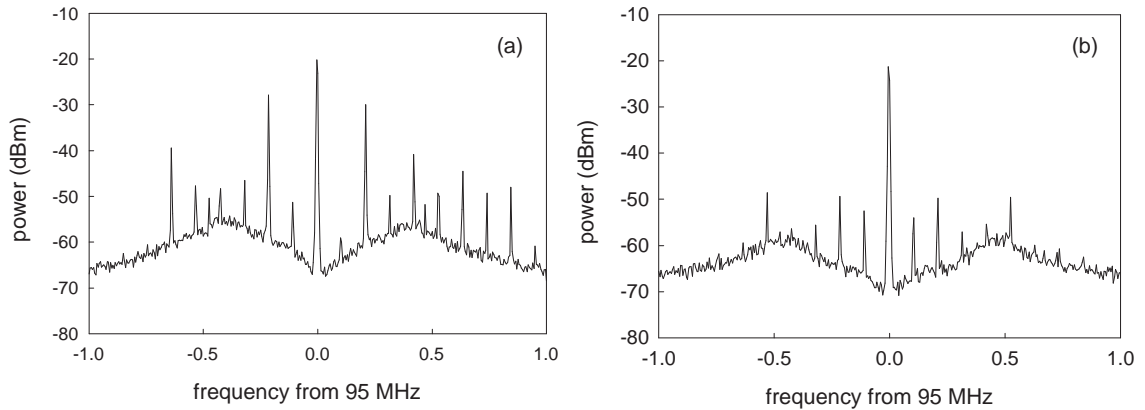
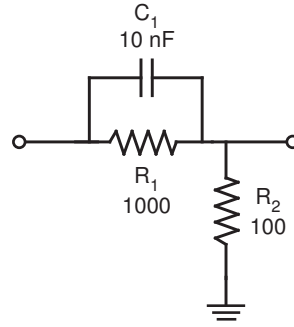


Figure 4.25: Spectrum analyzer traces of the phase-locked comb offset δ . (a) The spikes at 105 kHz and harmonics is due to switching power supply noise in the Verdi pump laser. (b) The spikes are significantly reduced by floating the anodes of the diode arrays that power the Verdi.

there is significantly more power available from the iodine reference at 1064 nm (100 mW) than 532 nm (<0.5 mW). Second, the large peak at 1083 nm in the infrared part of the spectrum (Fig. 4.8) also overlaps 1064 nm, therefore allowing good SNR to be achieved for both beats simultaneously. However, when the beat at 1083 nm is optimized, there is little power at 532 nm.

The PLL for f_I is similar to that of the comb offset δ . A tracking oscillator based on a 50-100 MHz VCO (Minicircuits ZOS-100) is used to phase-lock f_I to 60 MHz, a frequency chosen based on the bandwidth of the photodetector and the availability of commercial RF components in this frequency range. The digital PFD and filter is identical to that of the comb offset PLL (Fig. 4.23) with $R_{CP} = 500\Omega$ and $C_{CP} = 10$ nF. The output of the PFD goes to the piezo driver in Fig. 4.10. In order to extend the locking bandwidth, a phase-advance filter was inserted between the PFD and piezo driver (Fig. 4.26). The filter, which has a zero at the same frequency of the

Figure 4.26: The phase-advance filter used in the f_I PLL.

pole in equation 4.26, has a transfer function

$$F_{PA}(s) = \frac{R_2}{R_1 + R_2} \frac{(1 + sR_1C_1)}{(1 + s\frac{R_1R_2}{R_1+R_2}C_1)} \quad (4.38)$$

The open-loop gain is obtained by multiplying together the transfer functions of the prescaler ($=1/N$), PFD (Eqn. 4.33), charge-pump filter (Eqn. 4.34), phase-advance filter (Eqn. 4.38), and piezo driver (Eqn. 4.26). Mathematically the open-loop gain $\Theta(s)$ and closed-loop gain $H(s)$ are given by

$$\Theta(s) = \frac{K_{PFD}F_{CP}(s)F_{PA}(s)F_{PZT}}{s} \quad (4.39)$$

$$= \frac{\alpha I_{CP}}{N 2\pi} \left(\frac{1}{s}\right) \left(\frac{1 + sR_{CP}C_{CP}}{sC_{CP}}\right) \quad (4.40)$$

$$\left(\frac{R_2}{R_1 + R_2} \frac{(1 + sR_1C_1)}{(1 + s\frac{R_1R_2}{R_1+R_2}C_1)}\right) \left(\frac{K_{PZT}}{1 + sR_{out}C_{PZT}}\right) \quad (4.41)$$

$$H(s) = \frac{\Theta(s)}{1 + N\Theta(s)} \quad (4.42)$$

The magnitude of $\Theta(s)$, phase of $\Theta(s)$, and magnitude of $H(s)$ are plotted in Fig. 4.27.

Fig. 4.28a shows a spectrum analyzer trace of f_I when phase-locked. The loop bandwidth is approximately 75 kHz. Although this is a large bandwidth, there is not enough gain to remove all the phase noise at low frequencies off the carrier. As shown

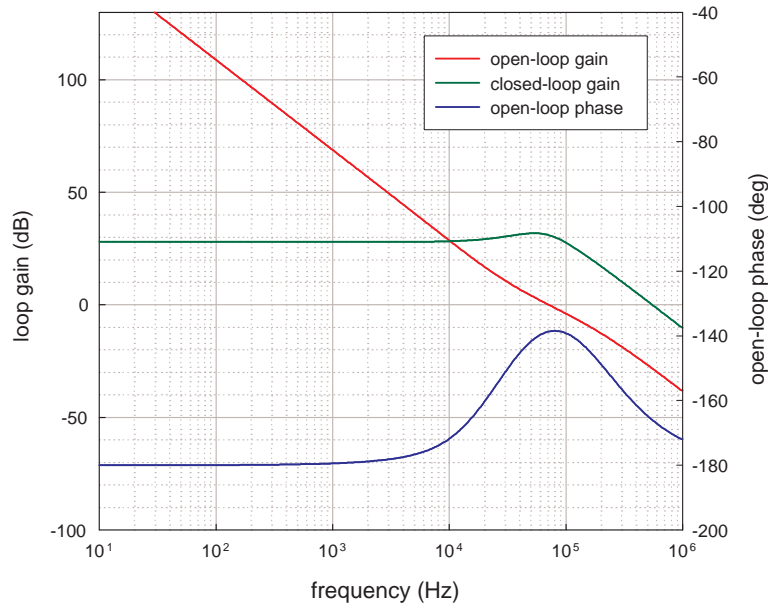


Figure 4.27: Calculated Bode and phase plots for the iodine-comb PLL.

in Fig. 4.28b, noise on the locked beat note increases for frequencies within a few kHz of the carrier. Nevertheless, the lock is robust and accurately transfers the stability and most of the phase noise of the iodine reference to the comb.

4.2.6 Counting the Repetition Rate

Counting the repetition rate f_{rep} is necessary for determining the absolute optical frequencies of the helium transitions. The signal is detected by reflecting light from an unused part of the spectrum ($<1 \mu\text{m}$) onto a high-speed photodiode (Fig. 4.14). After amplification, the SNR is greater than 100 dB in a 100 kHz bandwidth. To improve counter resolution, f_{rep} is mixed down to 10 kHz using a 1 GHz signal from a frequency synthesizer referenced to a GPS-steered Rb standard.

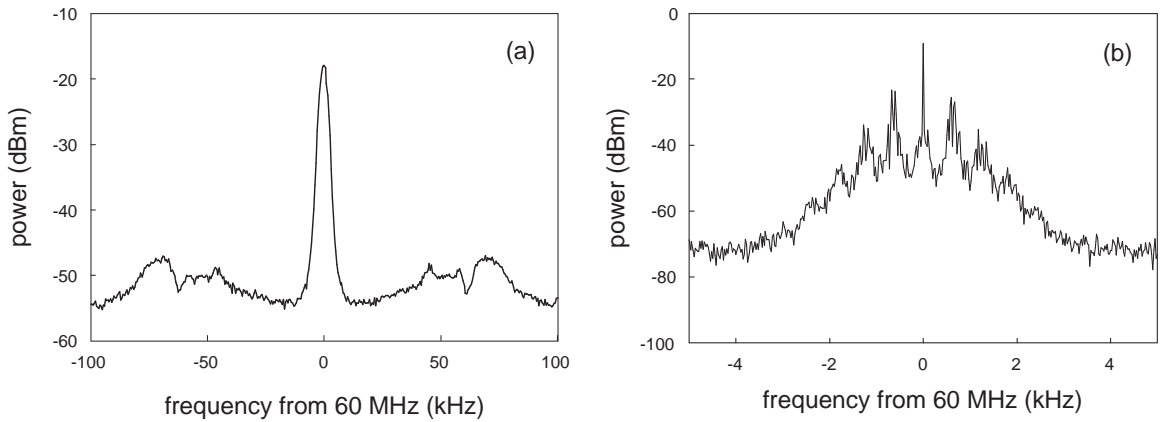


Figure 4.28: Spectrum analyzer traces of the phase-locked beat f_I .

4.3 The Comb-Stabilized Diode Laser

4.3.1 Phase-locking the Diode Laser to the Frequency Comb

Although it is possible to phase-lock the helium scan laser to the comb directly at 1083 nm, we instead phase-lock a second 1083 nm reference diode laser to the comb and offset lock the helium scan laser from the reference diode laser. This arrangement allows for the comb to be integrated into the experiment without having to make major modifications to the microwave offset-lock electronics or data-taking routines.

The comb-stabilized diode laser (CSDL) is based on a 1083 nm Distributed Bragg Reflector laser diode (Spectra Labs SDL-6702-H1) that emits 20 mW of light when powered by a 180 mA DC current. To narrow the laser linewidth, a 45 cm external cavity is constructed out of the laser diode's output facet and a mirror. Four cylindrical Invar rods reduce the impact of temperature fluctuations on the cavity length.

Approximately 50% of the diode's output is deflected from the external cavity using a $\lambda/2$ plate and polarized beamsplitter cube. Course frequency tuning is achieved by temperature-tuning the diode to $27.7 \pm 0.01^\circ\text{C}$. Tuning of the external cavity is achieved with a piezo transducer (Physik Instrumente PL055) mounted behind the mirror. The mechanical resonance frequencies of the piezo are increased by using a small, light mirror measuring 5 mm in diameter and 2 mm in thickness. The piezo driver is identical to the high-voltage op-amp circuit used for controlling the Ti:Saph repetition rate (Fig. 4.26). The tuning coefficient is 13 MHz/Volt.

After amplification in a Yb fiber amplifier (Keopsys KPS-BT2-YFA-1083-SLM-PM-05-FA), approximately 10 mW of light from the CSDL is transferred from the helium optical bench to the comb optical bench via a multimode fiber. The infrared part of the comb and the fiber output are combined with a polarized beamsplitter cube (Fig. 4.14). A grating prevents unwanted comb components from reaching the photodetector while a linear polarizer projects the polarization of both beams onto the same axis. A high-speed, amplified InGaAs photodetector (New Focus 1801) detects the beat f_{1083} .

Phase-locking of f_{1083} is similar to the comb offset and iodine-comb PLLs. A tracking oscillator is used to improve SNR. The digital PFD and charge-pump filter are identical to that for the iodine-comb PLL (Fig. 4.23). For the CP filter, $R_{CP}=500\Omega$ and $C_{CP}=10$ nF. To extend the locking bandwidth of the external cavity piezo, a phase-advance filter identical to that used in the tracking oscillator was inserted before the piezo driver (Fig. 4.18).

Calculations for the open-loop and closed-loop gains are similar to those for the

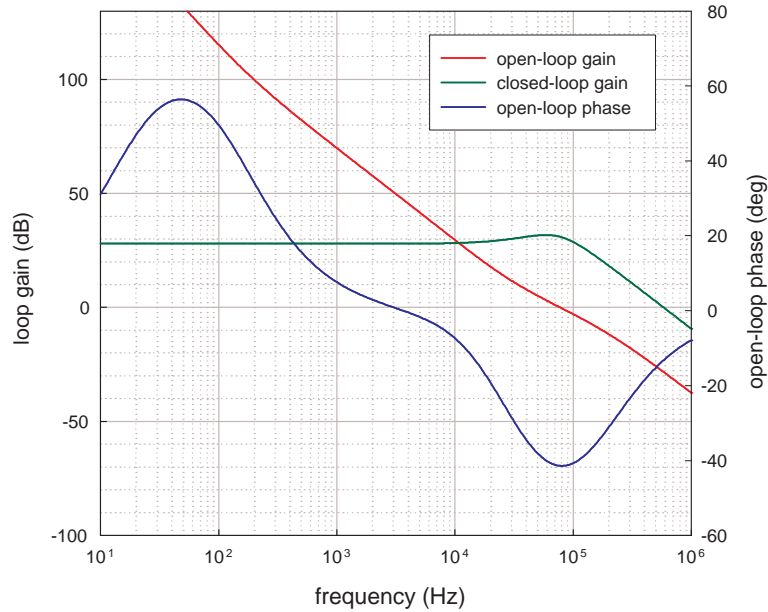


Figure 4.29: Calculated Bode and phase plots for the CSDL PLL.

comb offset and iodine-comb PLLs. Fig. 4.29 shows Bode and phase plots of the open-loop and closed-loop gains. Fig. 4.30 shows a spectrum analyzer trace of f_{1083} when phase-locked. The bandwidth of the PLL is 50 kHz.

4.3.2 Narrowing Laser Linewidth with a Stabilized Frequency Comb

When the optical comb is phase-locked to the iodine reference, every comb component inherits the narrow linewidth of the NPRO used as the reference oscillator [97]. In turn, the linewidth of the CSDL is narrowed by a factor of 10, from 50 kHz to 5 kHz, when it is phase-locked to the iodine-stabilized frequency comb.

The linewidths of the NPRO and diode laser are measured using a delayed self-

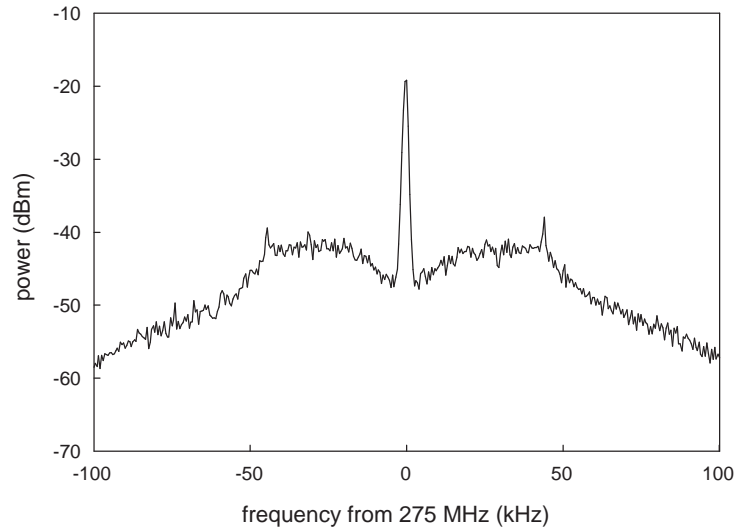


Figure 4.30: Spectrum analyzer trace of the phase-locked beat f_{1083} .

heterodyne interferometer (Fig. 4.31) [113]. Decoherence between the two paths of the interferometer is introduced by delaying one arm through 18-25 km of optical fiber. To detect the linewidth at a non-zero frequency, one path is frequency shifted in an AOM by 80 MHz. The two paths are recombined using a beamsplitter cube and the 80 MHz beat is detected with an amplified InGaAs photodetector (New Focus 1801).

The photodetector output is observed on a spectrum analyzer. The width Δf_{beat} of the 80 MHz beat is

$$\Delta f_{beat} = \sqrt{2} \Delta f_L \sqrt{1 - e^{-\pi \tau_D \Delta f_L}} \quad (4.43)$$

where τ_D is the optical delay time of the fiber and Δf_L is the FWHM laser linewidth. Since the laser beats against itself, the measured width is $\sqrt{2}$ larger than the laser linewidth. The factor of $\sqrt{1 - e^{-\pi \tau_D \Delta f_L}}$ on the right side of equation 4.43 accounts

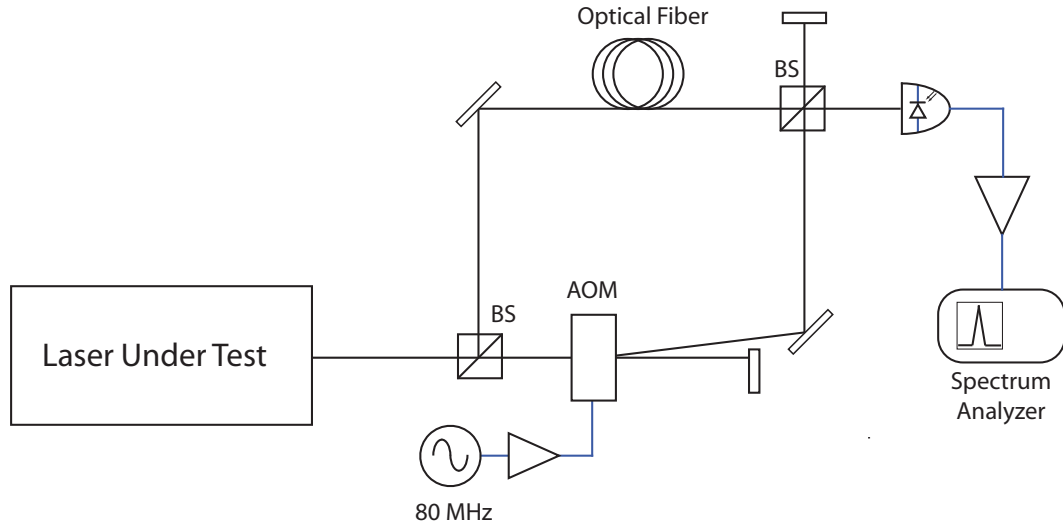


Figure 4.31: The delayed self-heterodyne interferometer for measuring laser linewidth.

for the lack of decoherence for frequencies less than $1/\tau_D$, which causes the measured width to be narrower than $\sqrt{2}\Delta f_L$.

The frequency spectrum is fitted to a three-parameter Lorentzian lineshape. The fitted width is used with the known optical delay time, $\tau_D=110 \mu\text{sec}$ for a 22.4 km length of fiber, to determine the laser linewidth Δf_L in equation 4.43. For the NPRO (Fig. 4.32), the fitted FWHM of 2.0 kHz yields a linewidth of $\Delta f_L=1.8 \text{ kHz}$.

Fig. 4.33 compares the linewidth of the diode laser when free-running and phase-locked to the iodine-stabilized frequency comb. An 18 km length of fiber was used, corresponding to $\tau_D=90 \mu\text{sec}$. For the free-running laser, the fitted FWHM of 76 kHz gives a laser linewidth of $\Delta f_L= 54 \text{ kHz}$. When phase-locked to the stabilized frequency comb, a FWHM of 7.7 kHz gives a laser linewidth of $\Delta f_L=5.5 \text{ kHz}$. This 10-fold reduction in diode laser linewidth gives a value close to the 1.8 kHz linewidth of the NPRO. We believe the 5.5 kHz diode laser linewidth could be reduced down to

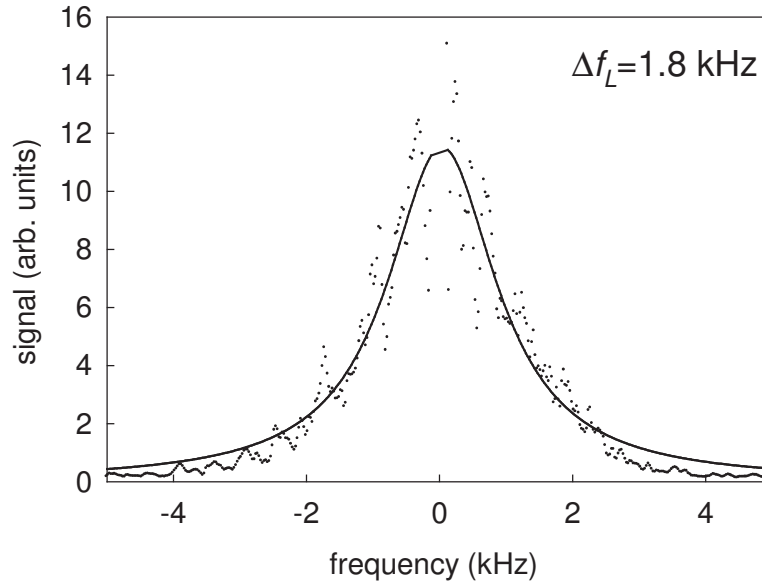


Figure 4.32: Spectrum analyzer trace of the 80 MHz NPRO beat from the delayed self-heterodyne interferometer.

the 1.8 kHz NPRO linewidth by increasing low-frequency gain in the iodine-comb lock loop. As seen in Fig. 4.28, the width of the locked carrier is not resolution-bandwidth limited, indicating the presence of low frequency (<5 kHz) noise off the carrier that is not effectively removed by the PLL.

4.3.3 Measuring the Optical Frequency of the Comb-Stabilized Diode Laser

The optical frequency of the CSDL is needed for two reasons. First, the microwave offset frequency between the reference and scan lasers is the difference between the optical frequencies of the helium transition and the CSDL. Second, the optical frequency of a helium transition is obtained by adding the frequency of the CSDL to the fitted center frequency of a helium scan.

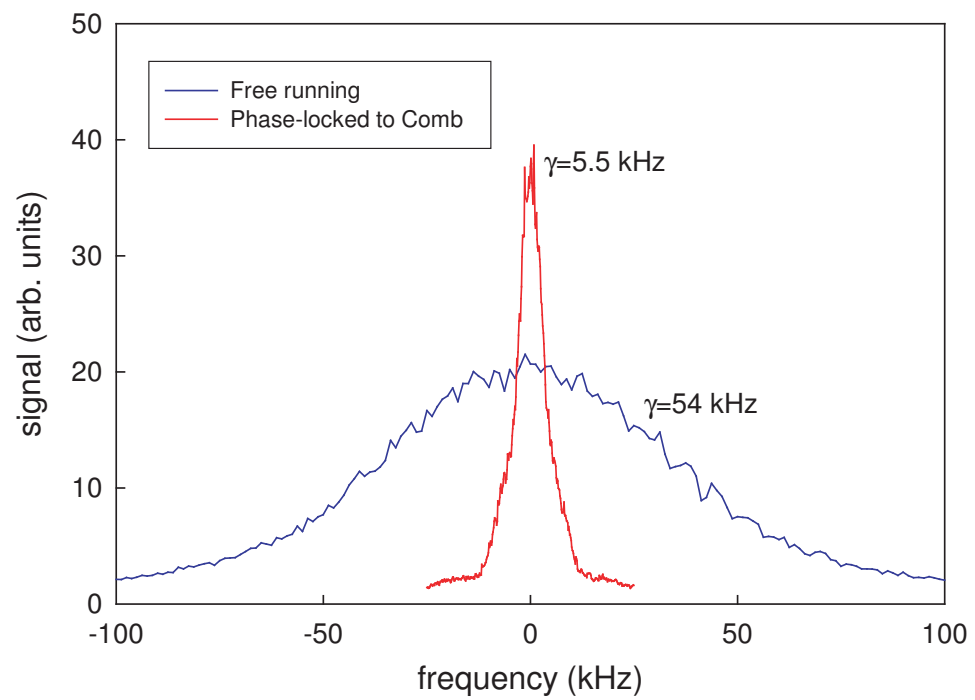


Figure 4.33: Spectrum analyzer traces of the 80 MHz beat of the diode laser when free-running and phase-locked to the iodine-stabilized frequency comb.

The optical frequency f_{CSDL} of the CSDL is

$$f_{CSDL} = nf_{rep} \pm \delta \pm f_{1083}. \quad (4.44)$$

The frequencies δ and f_{1083} are known with absolute accuracy because they are phase-locked with respect to GPS. The sign of f_{1083} is determined from the polarity of the CSDL PLL. The repetition rate f_{rep} is measured with respect to a GPS-steered Rb standard using a frequency counter; a 1 sec measurement determines f_{CSDL} to a few kHz. The two remaining unknowns, the integer n and the sign of δ , are determined by measuring the frequency of the CSDL with a high-resolution (~ 100 MHz) wavemeter and solving for the two values

$$n_{\pm} = \frac{f_{wavemeter} - f_{1083} \pm \delta}{f_{rep}} \quad (4.45)$$

The value of n_{\pm} closest to an integer is chosen, and then rounded to that integer.

4.3.4 The Accuracy of Optical Frequency Measurements

A single helium linescan is acquired in 150-450 seconds. During this time, the comb repetition rate f_{rep} is counted with respect to a Rb standard that slowly tracks GPS using a phase-locked loop (PLL). On these relatively short timescales, the resolution of an optical frequency measurement is determined by the stability of the Rb standard. However, the accuracy of these measurements are limited by the long-term drift of the Rb standard and the choice of PLL time constant.

Fig. 4.34 is an instability plot (see Section 3.2) that can be used to infer the accuracy limitation of the Rb standard. The red line is the typical instability of the free-running Rb standard while the blue line is the instability of the 1 pulse-per-second

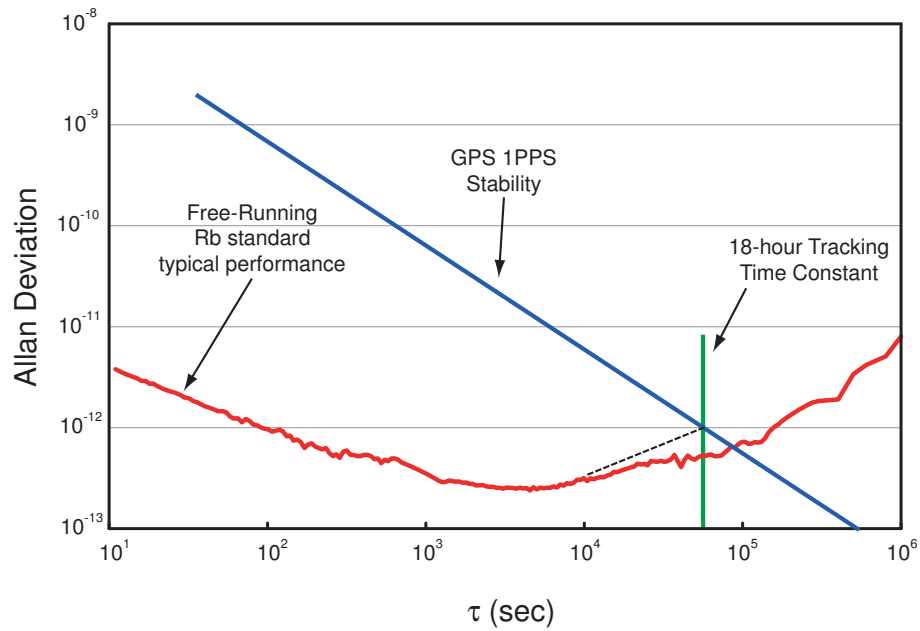


Figure 4.34: Stability plot of the free-running Rb standard (red) and GPS 1 PPS signal (blue) used to infer the inaccuracy of the Rb standard for times shorter than the time constant of the GPS tracking ($\tau_0=18$ hours). The dashed line between 10^4 and 10^5 seconds shows the expected degradation of the stability of the Rb standard when tracking GPS.

(PPS) GPS timing signal. The PLL time constant $\tau_0 = 18$ hours is represented by the vertical green line. For integration times $\tau > \tau_0$, the stability of the Rb standard will be the same as GPS. When tracking GPS, the performance of the Rb standard will be slightly degraded for τ between 10^4 and 10^5 seconds, as shown by the dashed line, because the free-running Rb standard is more stable than GPS for τ shorter than 18 hours.

Fig. 4.34 shows that for τ starting at 10^4 seconds, the stability of the GPS-steered degrades out to time $\tau \sim \tau_0$, at which point the stability improves again. The peak value of the Allan deviation of 10^{-12} at $\tau = \tau_0$ sets the accuracy for all frequency measurements with integration times $\tau < \tau_0$. Corresponding to approximately 300

Hz out of 276 THz (i.e. 1083 nm), this systematic error is added in quadrature to the statistical error of all measured optical frequencies. In addition, correlations between the three optical transition frequencies are visible in the data due to the fact that this calibration represents a well-defined frequency shift that is stable on data-taking timescales and larger than the experimental resolution. This correlations can be seen in data presented in Chapters 7 and 8

Chapter 5

Experimental Setup for Helium Spectroscopy

The technique of saturated-absorption spectroscopy is used to generate absorption lineshapes of the $2^3S_1 \rightarrow 2^3P_J$ transitions in ^4He . With this approach, the effects of first-order Doppler broadening are removed by using counter-propagating pump and probe beams to select a single velocity-class of atoms. The result is absorption profiles with linewidths determined primarily by the natural lifetime of the state.

What separates this work from other helium fine structure experiments is the use of a cell instead of an atomic beam. The advantage of a cell is a significantly higher signal-to-noise ratio due to the larger number of atoms that interact with the laser. On the other hand, collisions between the atoms introduce systematic effects such as pressure shifts and light-pressure shifts. Nevertheless, the ability to vary the pressure is an important experimental “knob” that is useful for studying collisional effects. To minimize these pressure-related frequency shifts, low pressures (<40 mTorr) are used.

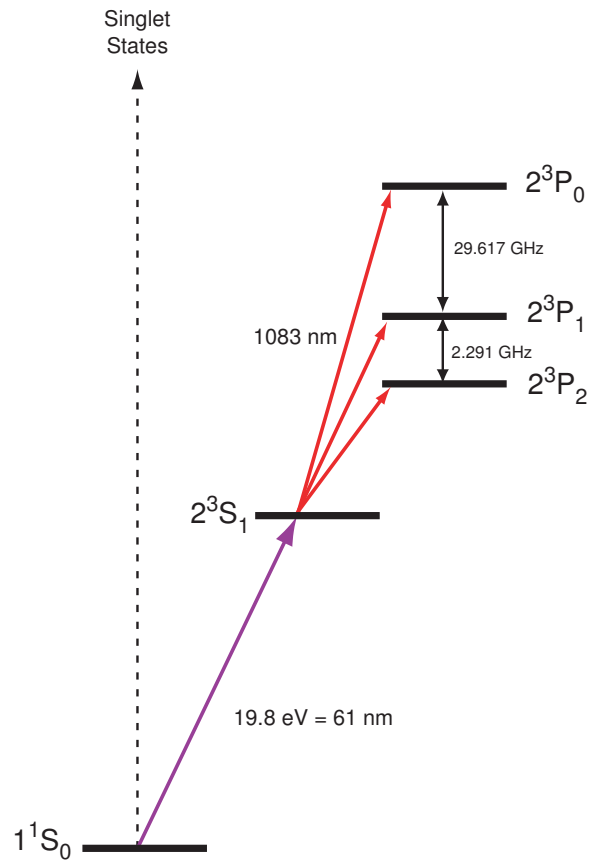


Figure 5.1: Energy diagram of the low-lying states of ^4He . With a transition wavelength of 59 nm, direction excitation of the 2^3P_J states from the ground state is inaccessible with table-top laser systems.

Although the 2^3P_J states can be excited directly from the helium ground state (Fig.5.1), the energy gap between these levels, corresponding to a wavelength of 59 nm, is inaccessible with table-top laser systems. An alternative scheme, accessing the 2^3P_J states via the metastable 2^3S_1 state, relies on inexpensive and readily available diode lasers at 1083 nm.

A population of metastable atoms is created using an RF discharge. There are two disadvantages to this approach. First, signal-to-noise is degraded because only 1 in 10^6 atoms reaches the metastable state. Second, the presence of a plasma in the cell introduces a DC electric field that can couple to the atoms via the Stark effect. Systematic shifts that arise from the discharge are studied in Chapter 5.

To correct for systematic frequency shifts introduced by the light-pressure effect, the sublevels of the helium states are resolved by several linewidths using a pair of Helmholtz coils that generate a homogeneous magnetic field. A measurement of the frequency splitting between the $m = \pm 1$ states of the $2^3S_1 \rightarrow 2^3P_1$ transition serves as a magnetometer. The measured value of the field is used to compute higher-order Zeeman corrections to the data.

One of the main contributions of this work has been the improvement of several components of the helium spectroscopy apparatus. Signal-to-noise was improved significantly by modulating the pump beam at a higher frequency, where laser intensity noise is lower. An additional three-fold improvement in signal-to-noise was achieved by both reducing laser pointing instability induced by optical-mount drift and by switching to an autobalanced photodetection system. Several modifications were made to the diode laser systems, including lower noise current controllers and high-

bandwidth current feedback to the laser diodes. The use of a digital phase/frequency detector for this lock and faster data transfer has increased the data collection rate by a factor of 30.

This chapter describes the experimental apparatus for performing saturated absorption spectroscopy of helium, including specific details about the gas-handling system, RF discharge, magnet, external-cavity diode lasers, pump and probe optics, and offset-lock.

5.1 Vacuum System

Helium gas is pumped into a glass cell using the apparatus shown in Fig.5.2. Measuring 6" in length and 1" in diameter, the glass cell has windows made of fused silica that are tilted at Brewster's angle for vertically polarized light at 1083 nm. A 1/4" diameter sidearm is used to pump helium into the main body of the cell. The sidearm, measuring 12" in length, is connected to a bellows and conflat flange using a glass-to-metal seal.

A rotary vane pump (Varian SD-91) continuously pumps gas out of the cell. A foreline trap (Varian 345) between the cell and the pump prevents backstreaming oil from contaminating the cell and absorbs water vapor in the system. To ensure proper functioning of the trap, the molecular sieve material was baked at 450°C for several hours. To minimize the effects of pump vibrations on the experiment, the pump rests on a set of four vibration-isolation springs. In addition, a large cement block acting as a vibration absorber rests on top of the bellows connecting the pump to the foreline trap.

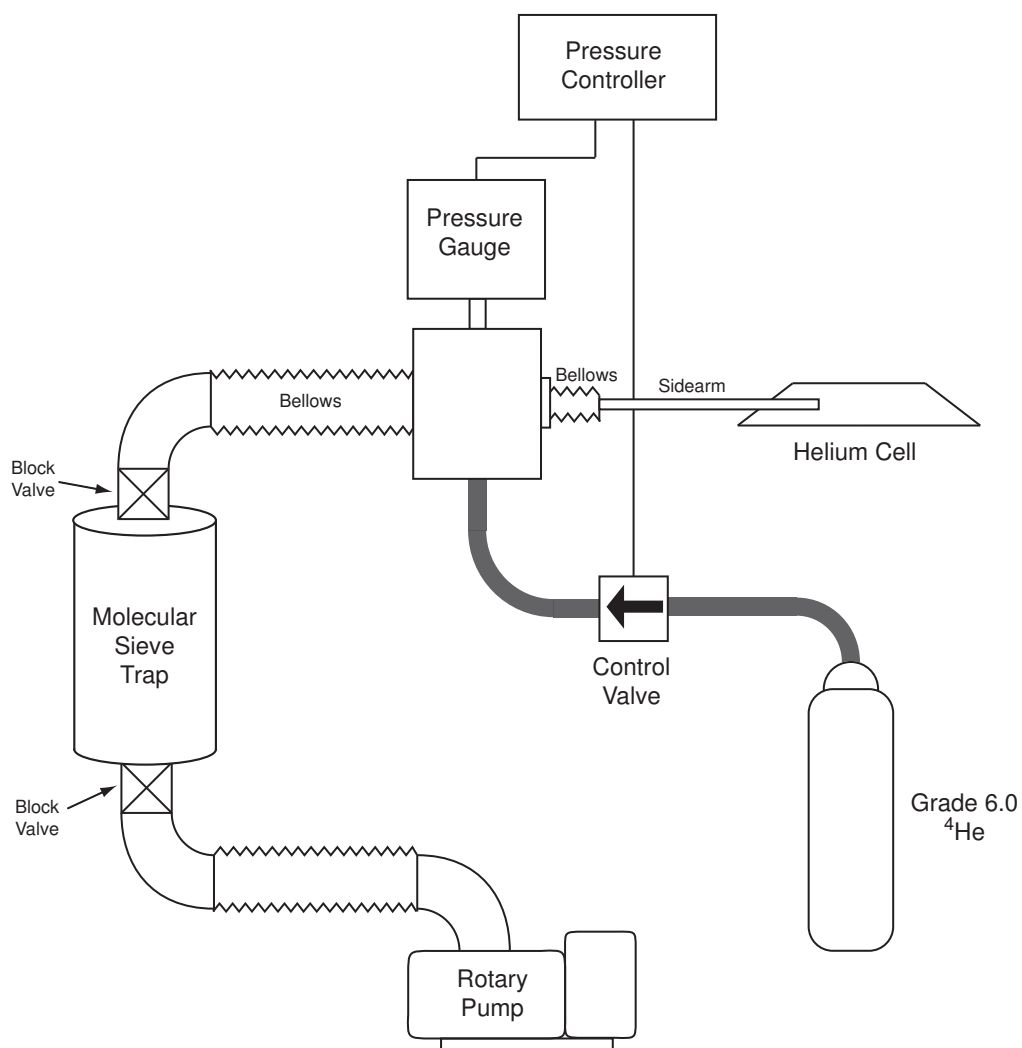


Figure 5.2: Vacuum system used to stabilize the pressure of helium gas in the glass cell.

The flow of grade 6.0 helium into the cell is varied using a control valve (MKS Type 248). An absolute pressure transducer (MKS Baratron 627A) measures the pressure of the helium gas outside the cell. The transducer outputs a DC voltage between 0 and 10 volts that varies linearly with pressure between 0 and 1 Torr. The DC voltage is monitored with a flow controller (MKS Type 250E) and stabilized using feedback to the control valve. Long-term stabilities of 0.01 mTorr are typically achieved. Pressures between 12 and 40 mTorr are used for data collection.

To ensure accuracy of extrapolations to zero pressure, the DC output voltage of the of the transducer was nulled while the vacuum system was pumped to less than 10^{-5} Torr with a turbo pump. A residual DC voltage of ± 0.3 mV at zero pressure corresponds to 0.03 mTorr. This calibration error has a negligible effect on the fine structure intervals because of their weak dependency on pressure. For the optical transition frequencies, however, this error source is not negligible.

5.2 RF Discharge

A large population of metastable helium atoms is produced in the cell using an RF discharge (Fig.8.2). Energetic RF photons ionize the helium gas, creating a plasma of helium ions. Highly-excited atoms, formed when an ion and electron recombine, decay through all possible channels, emitting light at every wavelength in the helium spectrum. A significant proportion of these atoms decay to the metastable 2^3S_1 state, where light at 1083 nm excites them to the 2^3P_J states. Although the metastable atoms have a natural lifetime of 8000 seconds, most fall to the ground state via collisions with the cell walls or with other atoms.

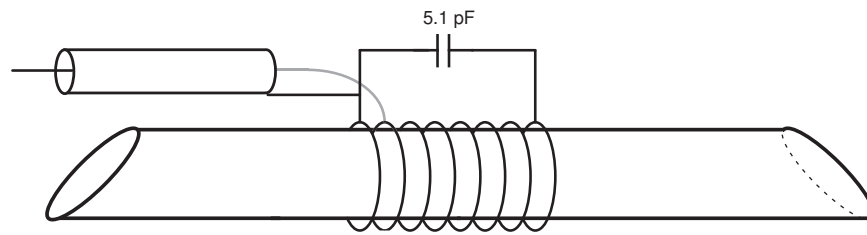


Figure 5.3: A discharge coil wrapped around the cell excites helium atoms to the metastable 2^3S_1 state.

The discharge consists of 8 turns of 12 gauge silver-coated copper wire that is tapped at the second winding in order to improve impedance matching. A 5.1 pF capacitor creates a resonance at 60 MHz. To shield electronics in the laboratory from the high-power RF signals used in the discharge, the coil is centered in a 6" long gold-plated copper can. The RF signal is sent to the coil via a rigid copper coaxial cable whose outer conductor is soldered directly to the can.

Fig.5.4 shows the RF electronics used to drive the discharge. A 60 MHz signal from a frequency synthesizer is amplified up to 50 watts in a high-power amplifier (Mini-Circuits LZY-1). An antenna tuner, in the form of two variable capacitors and a variable inductor, matches the impedance of the load to the 50Ω output impedance of the amplifier. For monitoring voltage standing-wave ratio, a dual directional coupler (Werlatone C5967-200) samples forward and reflected signals. A pair of mixers (Mini-Circuits ZAD-1-1) convert these sampled signals into DC voltages proportional to RF power. The DC signals are low-pass filtered with a $5\text{ k}\Omega$ resistor and $0.1\ \mu\text{F}$ capacitor.

The performance of the RF discharge is shown in Fig.5.5, where the fractional absorbed power is stable to $\pm 0.1\%$ over several hours. Because the helium atoms

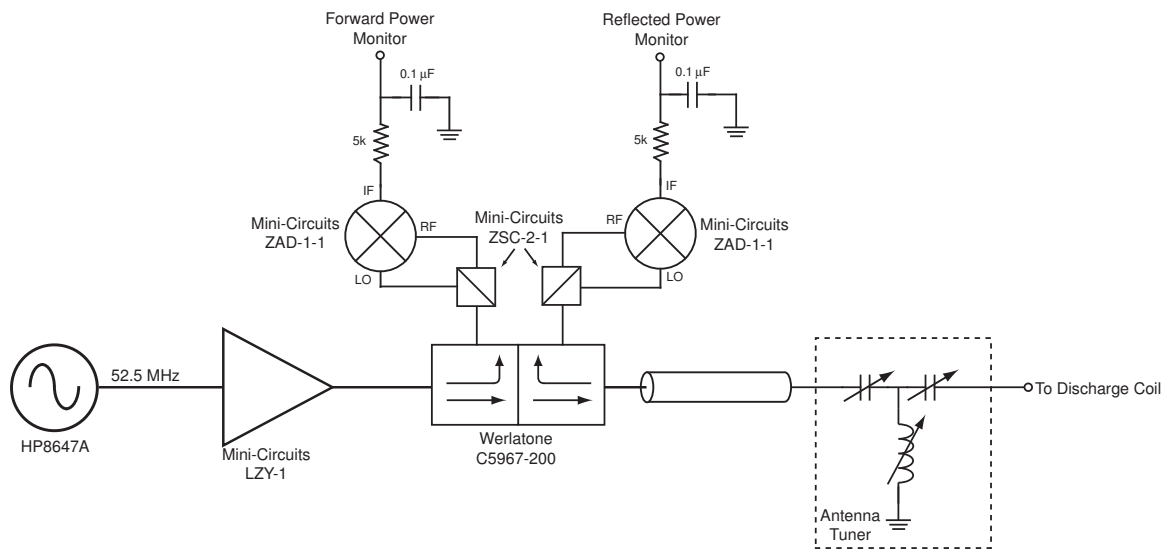


Figure 5.4: RF electronics used to drive the discharge and monitor voltage standing-wave ratio. An antenna tuner matches the load impedance to the 50Ω output impedance of the amplifier.

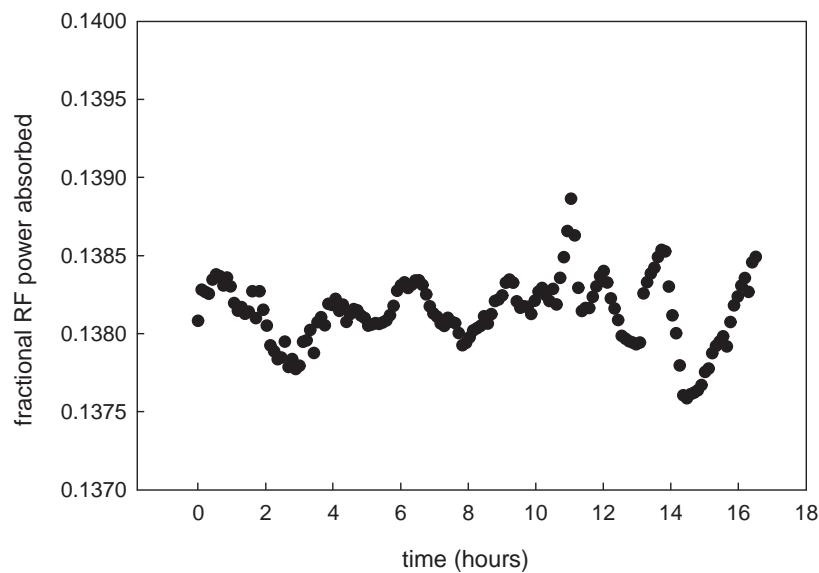


Figure 5.5: The RF power absorbed by the helium atoms is stable to $\pm 0.1\%$ over several hours.

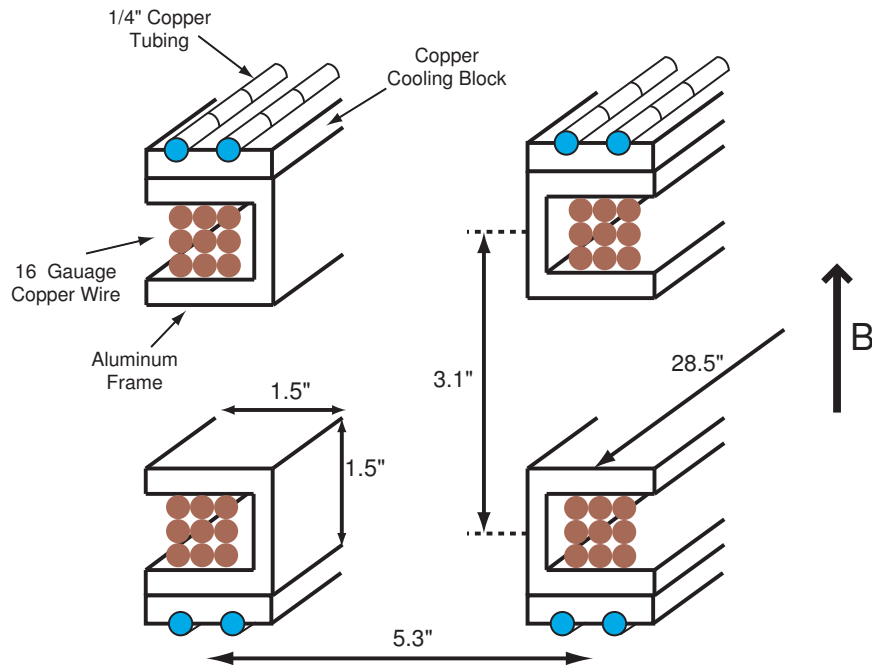


Figure 5.6: Cross-sectional view of the Helmholtz coils used to create a vertical magnetic field of up to 200 Gauss. Each coil consists of 238 turns of 16 AWG magnet wire that is wrapped onto a water-cooled aluminum frame.

act as a dissipative load, the load impedance depends on pressure. To account for this pressure-dependency, the tuner is adjusted to minimize the reflected power every time the cell pressure is changed.

5.3 Magnet

In order to resolve the Zeeman sublevels of the helium transitions, a uniform magnetic field of up to 200 Gauss is applied using a pair of coils arranged in a Helmholtz configuration. A cross-sectional view of the windings is shown in Fig.5.6. Wound on a 1/4"-thick rectangular aluminum frame that is 28.5" long and 5.3" wide, each coil consists of 238 turns of 16 AWG magnet wire that are packed in 14 layers

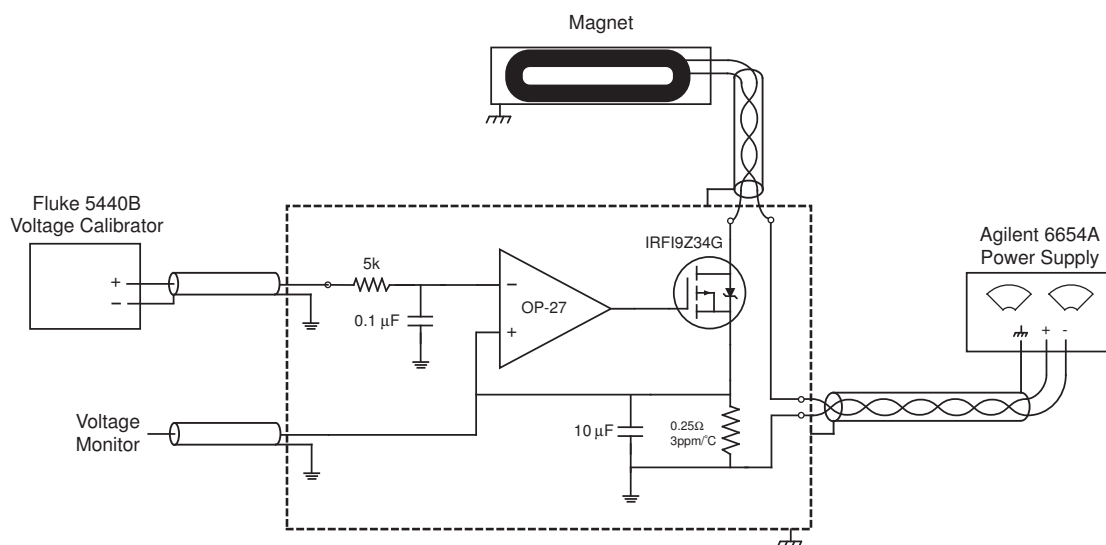


Figure 5.7: The magnet is driven by a high-stability current supply that provides up to 7A of current with a stability of $<3\text{ppm}$.

with 17 turns per layer.

To keep the magnet cool, chilled water is pumped through a pair of 1/4" diameter copper pipes that are soldered onto a 3/8" thick copper plate. The plate is bolted into the aluminum frame throughout its entire length. Water at $\sim 19^{\circ}\text{C}$ is supplied by a commercial chiller (FTS Systems RS33). To prevent vibrations from the chiller from reaching the magnet, the input and output water lines pass through 2' sections of copper pipe that pass through a 150 pound cement block. In addition, soft plastic tubing is used between the chiller and cement block, and between the cement block and magnet.

5.3.1 Magnet Power Supply

The magnet is driven using the current supply in Fig.5.7. A low-noise op-amp (OP-27) and power MOSFET (IRF19Z34G) stabilize the voltage across a high-power

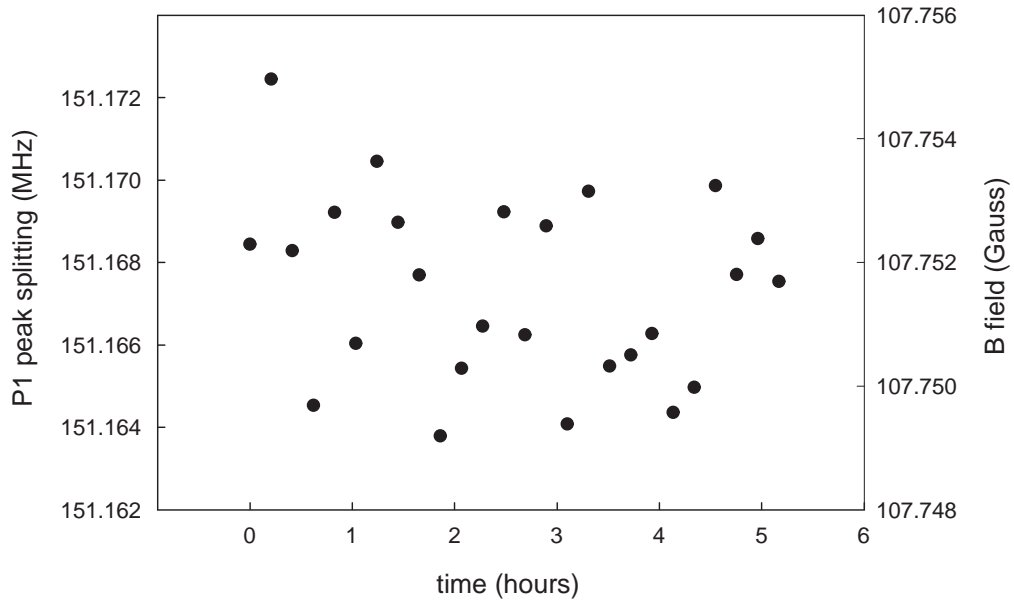


Figure 5.8: By measuring the frequency splitting of the $m = \pm 1$ sublevels of the $2^3S_1 \rightarrow 2^3P_1$ transition, the stability of the magnetic field is determined to be $< 3\text{ppm}$ over several hours.

current sense resistor (Vishay VCS331Z) by controlling the current through the resistor. Power is derived from a 60 volt, 9 amp DC power supply (Agilent 6654A). The voltage setpoint is supplied by a voltage calibrator (Fluke 5440) with a temperature coefficient of $0.1\text{ppm}/^\circ\text{C}$. The stability of the circuit is limited by the $3\text{ppm}/^\circ\text{C}$ temperature coefficient of the sense resistor. To reduce pickup of the 52.5 MHz RF discharge signal on the magnet current cables, twisted-pair cables are used. In addition, a $10\ \mu\text{F}$ capacitor across the current sense resistor significantly improves circuit performance.

5.3.2 Magnetic Field Stability

To determine the stability of the magnetic field, the frequency splitting between the $m=\pm 1$ sublevels of the $2^3S_1 \rightarrow 2^3P_1$ transition was measured over several hours. The measured value of 151.2 MHz corresponds to a magnetic field value of approximately 107.8 Gauss. Over five hours, the measured values show no drift to within the 440 Hz standard error of the measurements, corresponding to a stability of <3 ppm.

5.3.3 Magnetic Field Homogeneity

The measurement of the frequency splitting between the $m= \pm 1$ states of the $2S \rightarrow 2P_1$ transition measures the value of the magnetic field $\langle B \rangle$ averaged over the volume of atoms sampled by the laser beams. In a perfectly homogeneous magnetic field, the lowest-order Zeeman correction, which is proportional to $\langle B^2 \rangle$, is well-approximated by the square of the mean field $\langle B \rangle^2$. In an inhomogeneous magnetic field, where $\langle B^2 \rangle \neq \langle B \rangle^2$, this approach could lead to errors. The variance of the magnetic field, $\sigma^2 = \langle B^2 \rangle - \langle B \rangle^2$, estimates the error of the leading order Zeeman corrections.

To calculate magnetic field inhomogeneity, the magnet is modeled using a finite-element analysis software package (VectorFields Opera 3D). The geometry of the magnet and μ -metal shield is used with the permeability curve of μ -metal to compute a table of magnetic field values at approximately 66,000 points near the center of the magnet. A histogram of only those points that coincide with the laser beams is shown in Fig. 5.9. Variances of $10^{-4}G^2$ at 108 Gauss and $5.6 \cdot 10^{-5}G^2$ at 55 Gauss affect the Zeeman correction by less than 0.05 Hz.

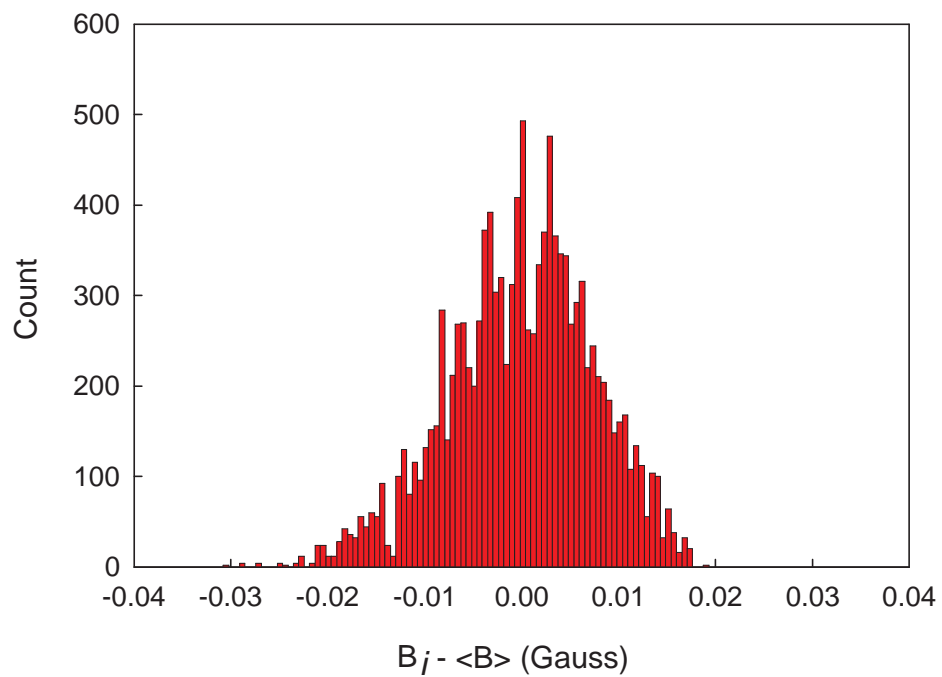
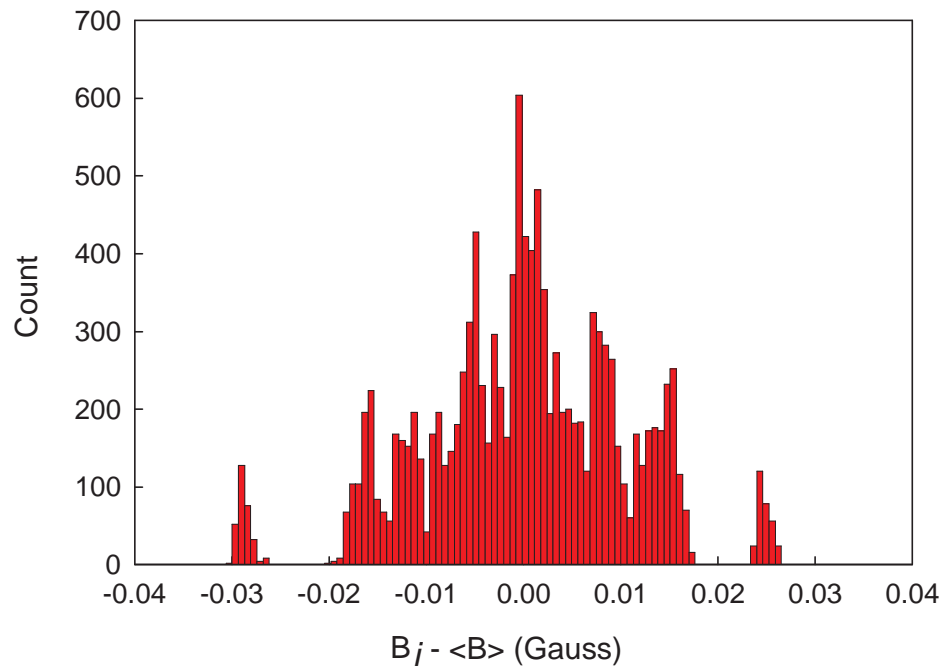


Figure 5.9: Histogram of numerically-simulated magnetic field values at (a) 108 Gauss and (b) 55 Gauss.

An additional error source that arises from field inhomogeneity is the distortion of linescans due to different Zeeman shifts across the atomic sample. To determine how well the the magnetic field $\langle B \rangle$ can be measured in the presence of this distortion, a composite $2S \rightarrow 2P_1$ lineshape was computed from the histogram data:

$$L(\omega) = \sum_{i=1}^N A_i \left(\frac{\Gamma^2}{\Gamma^2 + (\omega - \omega_Z^{(m=+1)}(B_i))^2} + \frac{\Gamma^2}{\Gamma^2 + (\omega - \omega_Z^{(m=-1)}(B_i))^2} \right)$$

where B_i are the magnetic field values of the bins in Fig.5.9a and A_i are weighting factors equal to the number of counts in the i th bin. The Zeeman shifts ω_Z are computed to all orders. Using a Levenberg-Marquardt algorithm, the composite lineshape is fit to a function of the form

$$F(\omega) = A \left(\frac{\Gamma^2}{\Gamma^2 + (\omega - \omega_1)^2} + \frac{\Gamma^2}{\Gamma^2 + (\omega - \omega_2)^2} \right) + y_0$$

where A , Γ , ω_1 , ω_2 , and y_0 are fit parameters. The frequency splitting obtained from the fit, $\omega_1 - \omega_2$, differs from the mean-field frequency splitting $\omega_Z^{(m=+1)}(\langle B \rangle) - \omega_Z^{(m=-1)}(\langle B \rangle)$ by 10 Hz. The corresponding error in the Zeeman correction is less than 0.7 Hz.

5.4 External-Cavity Diode Lasers

The helium experiment uses two identical external-cavity diode lasers, one for probing ^4He atoms and the other for providing frequency stability. Discussed in this section are the layout of the diode laser cavity, the current controller for driving the lasers, frequency control mechanisms, and laser linewidth measurements.

5.4.1 Cavity Layout

The layout of the diode laser cavity is shown in Fig.5.10. A Distributed Bragg Reflector laser diode (Spectra Diode Labs SDL-6702H), bolted into an aluminum endplate for good grounding and heat sinking, forms one end of the cavity. Light emitted by the diode, after collimated by a lens, passes through an anamorphic prism pair to correct for ellipticity. The other end of the cavity, located 45 cm from the laser diode, consists of a mirror epoxied onto a piezo transducer. A tip/tilt stage (Burleigh Instruments), bolted onto a second aluminum endplate, is adjusted to provide optical feedback to the laser diode. To minimize drift in the cavity length, the two aluminum plates are connected with four 1"-diameter INVAR rods. A $\lambda/2$ -plate and polarized beamsplitter cube control the output coupling, or percentage of light diverted from the cavity.

5.4.2 Current Controller

The laser diode is powered by a 150-200 mA DC current supplied by the controller in Fig.5.11. Similar to the design in Reference [114], the circuit acts as a current sink because the anode of the laser diode is grounded to its case. The controller replaces a commercial laser diode controller (ILX Lightwave LDC-3722B) that introduced several noise spikes into the laser's output (Fig.5.23). A plot of output power versus drive current is shown in Fig.5.12.

Using a FET as a voltage-controlled resistor, the circuit stabilizes the voltage across a pair of high-stability power resistors (Vishay VPR221) by controlling the current flowing through the resistors. A low noise op-amp (LT1128) compares the

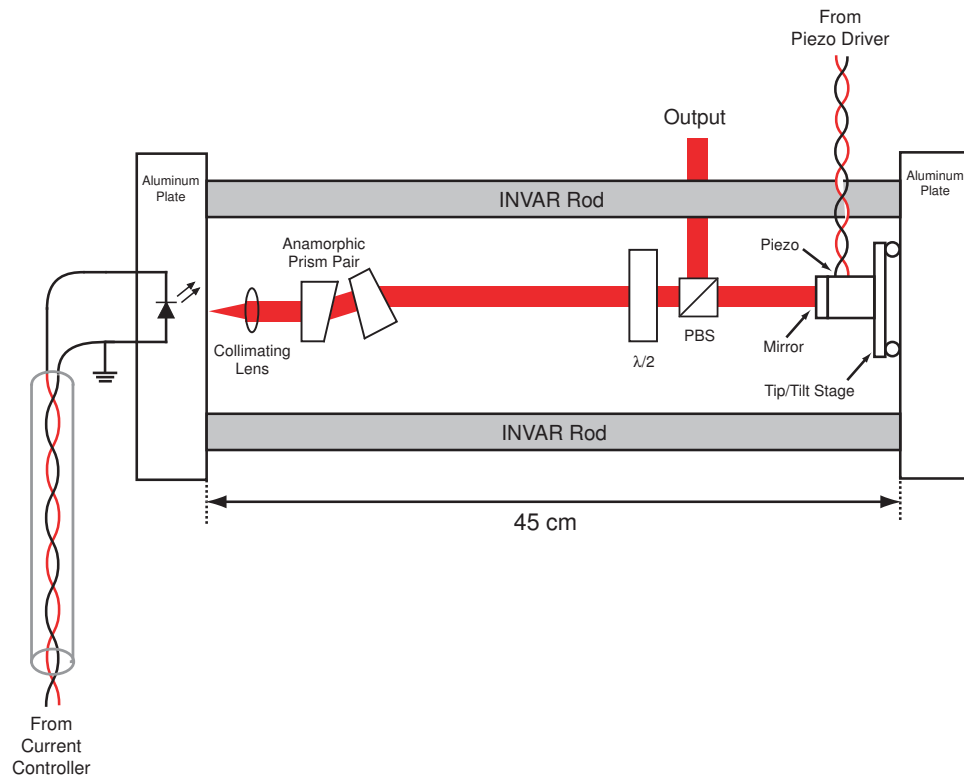


Figure 5.10: Layout of a 1083 nm external-cavity diode laser. Linearly-polarized light from an anode-grounded laser diode, after collimated by a lens, has its ellipticity removed by an anamorphic prism pair. Output coupling is controlled by a polarized beamsplitter and $\lambda/2$ -plate. Frequency tuning is achieved by modulating the cavity length with a piezoelectric transducer.

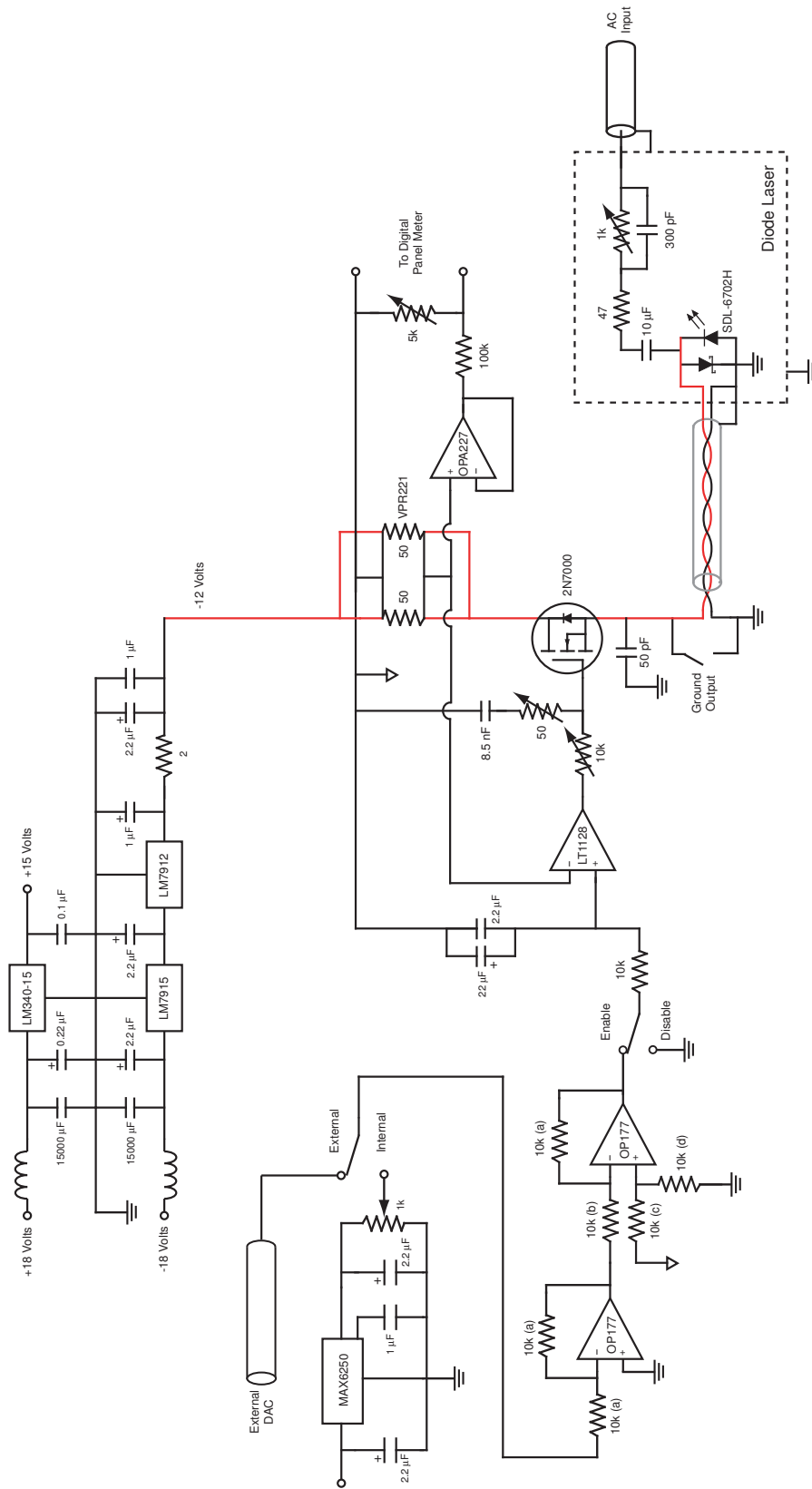


Figure 5.11: Schematic of the diode laser current controller. Using feedback, an op-amp (LT1128) controls a FET (2N7000) to stabilize the voltage across a pair of high-stability resistors (VPR221). The setpoint voltage is derived from either an internal voltage reference (MAX6250) or external DAC.

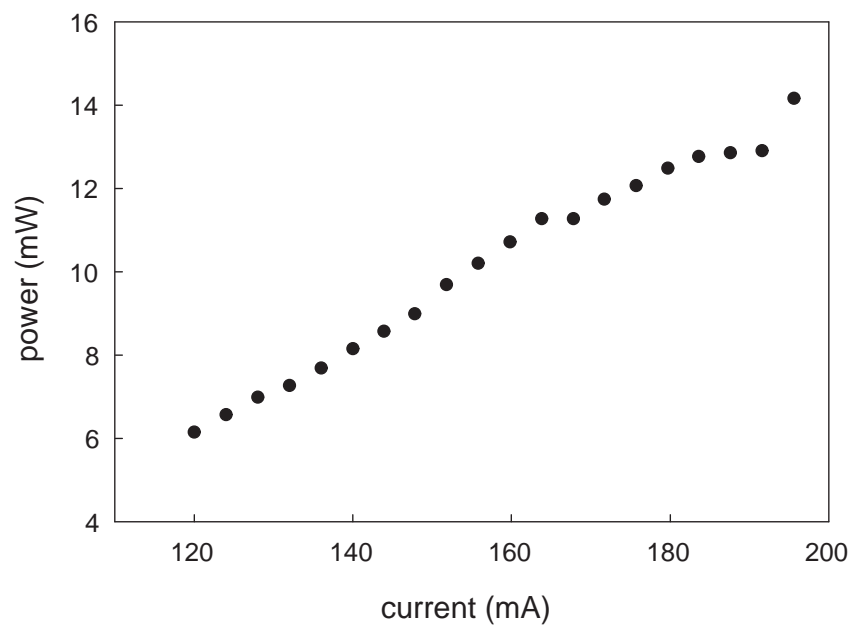


Figure 5.12: Diode laser output power scales linearly with drive current. The laser's output coupling is set to 50%. The jump at 200 mA is attributed to a mode-hop.

voltage across the VPR221's to a setpoint voltage derived from either an internal voltage reference (Maxim MAX6250) or an external DAC. A lead-lag filter on the output of the op-amp helps tailor the phase response of the feedback loop to maintain stability. The N-channel enhancement-mode FET (2N7000) was chosen because it offers low Miller capacitance while handling currents up to 200 mA DC. The stability of the circuit is determined by drift in the control voltage and the 3ppm/ $^{\circ}\text{C}$ temperature coefficient of the VPR221 resistors.

Several safety measures to protect the laser were incorporated into the circuit design. First, to prevent power spikes from damaging the diode, an RC low-pass filter on the positive input of the LT1128 ensures that the drive current changes slowly ($\tau=250$ ms). Second, a protection diode on the laser diode protects against applied voltages of the wrong polarity. Third, a pair of 15,000 μF capacitors on the input of the voltage regulators ensures that in the event of a power failure, the entire circuit will lose power slowly, helping to prevent short electrical transients from damaging the laser diode.

5.4.3 Frequency Control

Laser frequency is controlled in three ways. First, coarse tuning of the laser's output is achieved by changing the temperature of the laser diode via a thermoelectric cooler (TEC) that is built-in the diode housing. This mechanism can control the laser's frequency over tens of GHz with a tuning coefficient of -20 GHz/ $^{\circ}\text{C}$. The temperature is monitored with a thermistor, also built-in to the diode housing, and stabilized to $\pm 0.01^{\circ}\text{C}$ using a commercial temperature controller (ILX Lightwave

LDC-3722B). Typical temperatures are 23.1°C, 24.5°C, and 24.6°C for the $2P_0$, $2P_1$, and $2P_2$ states, respectively.

Changing the length of the external cavity with a piezoelectric transducer (Physik Instrumente PL055) is the second tuning mechanism. Driven by the high-voltage op-amp circuit in Fig.xxx, the piezo's maximum contraction of 3 μm at 100 volts can change the laser frequency by 1.8 GHz with a tuning coefficient of 18 MHz/volt. The bandwidth of this tuning mechanism is 50 kHz.

The third frequency tuning mechanism, changing the diode current, is used in two ways. First, the DC drive current is modified to achieve coarse frequency tuning. Since this also changes the laser output power, temperature tuning is preferred. Second, AC signals are coupled into the laser diode for high-bandwidth phase-locking of the laser. This second approach is discussed in more detail in the section on the offset-lock.

5.4.4 Measuring Diode Laser Linewidth

The linewidth of the diode laser was measured using the delayed self-heterodyne interferometer in Chapter 2. An 18 km length of fiber was used, corresponding to a delay time of $\tau_D=90 \mu\text{sec}$. The FWHM laser linewidth was determined from the width of the measured beat at 80 MHz using eqn.xxx. Fig.5.13 shows the measured linewidth as a function of output coupling. An output coupling of 50% was chosen since this gives the greatest output power while maintaining the smallest measured linewidth of 55 kHz.

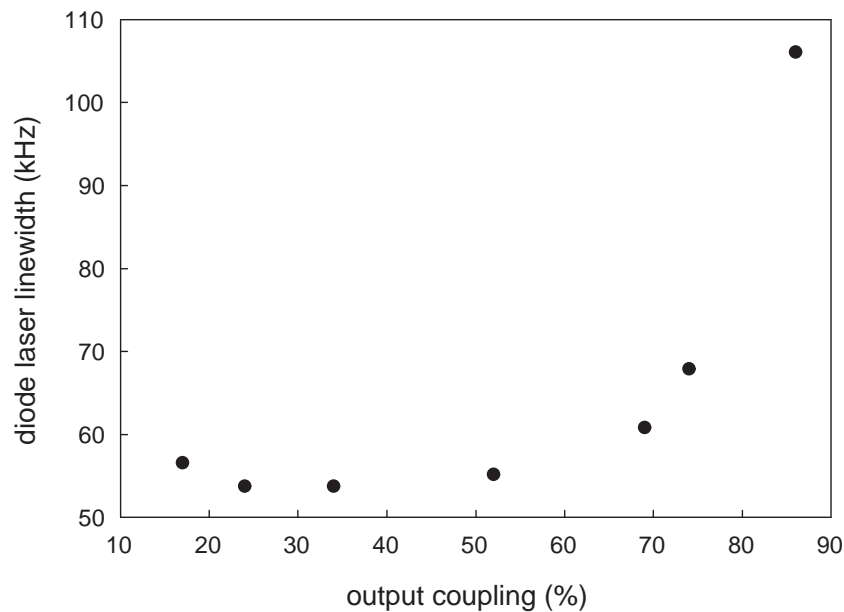


Figure 5.13: Diode laser linewidth versus output coupling.

5.5 Optics Components and Signal Detection

5.5.1 The Scan and Comb-Stabilized Diode Lasers

The layout of the two diode lasers is shown in Fig.5.14. The output of each laser, after passing through an optical isolator, is amplified to powers up to 500 mW in a polarization-maintaining Yb-doped fiber amplifier (Keopsys KPS-BT2-YFA-1083-SLM-PM-05-FA). Reflections off a pair of plate beamsplitters direct about $100 \mu\text{W}$ of each laser's output into the two inputs of a fiber-optic SPDT switch. The output of the switch goes to a wavemeter (Agilent 86120B) where the optical frequency of each laser can be measured with a 100 MHz resolution.

The beat between the lasers is measured by combining 1 mW of each laser's

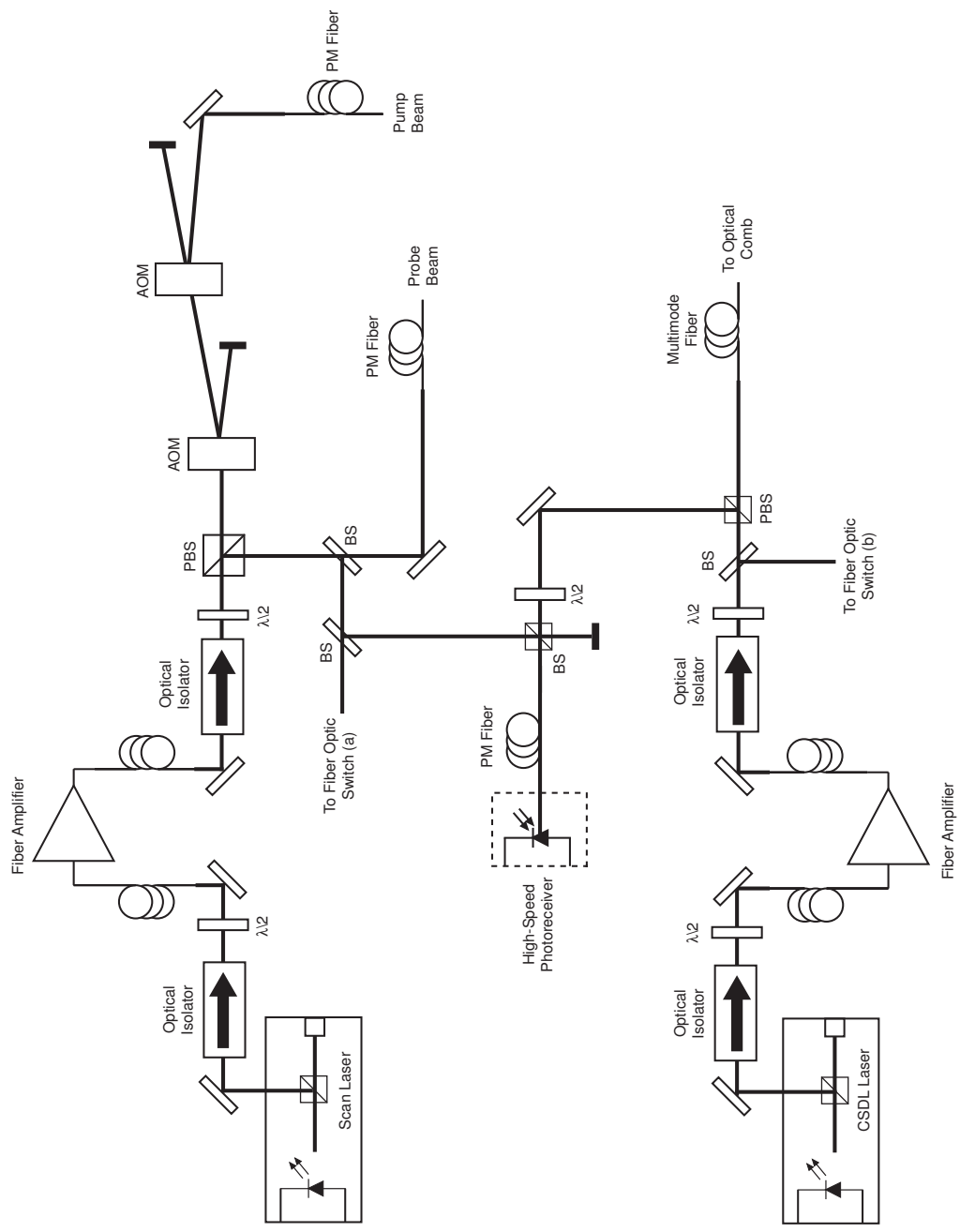


Figure 5.14: Layout of the scan laser and CSDL. After amplification in a pair of Yb-doped fiber amplifiers, approximately 1 mW of each laser's output is used to form a heterodyne beat for offset-locking. A polarized beamsplitter cube and $\lambda/2$ -plate split the scan laser output into pump and probe beams.

output with a non-polarized beamsplitter cube. The combined beam is launched into a polarization-maintaining (PM) fiber and the beat is measured with a high-speed 40 GHz amplified photoreceiver (New Focus 1011).

The remaining output of the CSDL, sent to the frequency comb in a multimode fiber, is used to form a beat with one of the comb's components at 1083 nm.

5.5.2 Pump and Probe Optics

The scan laser is split into pump and probe beams using a half-waveplate and polarized beamsplitter cube. The pump beam is frequency shifted by -2 MHz with a pair of Pb:MbO₄ acousto-optic modulators (Isomet 1205C-2). The first AOM is driven by an 80 MHz signal from a GPS-referenced frequency synthesizer that is amplified to 1.5 Watts in an RF amplifier (Mini-Circuits ZHL-1-2W). The second AOM, which shifts the optical beam by -82 MHz, is used to amplitude modulate the pump for signal detection using a digital lock-in amplifier (Stanford Research Systems SR-820). A 38 kHz signal, generated by the lock-in amplifier, modulates the 82 MHz output of a GPS-referenced frequency synthesizer (Fig.5.16). The carrier-suppressed double-sideband output of the mixer consists of two signals at 82.000 ± 0.038 MHz.

Several factors were considered when choosing the modulation frequency. Prior to this work, amplitude modulation of the pump beam was done with an optical chopper wheel operating at 1.5 kHz. By increasing the modulation frequency, the signal is now detected at a frequency where the laser's residual intensity noise is significantly lower. A negligible decrease in signal size due to the higher modulation frequency, as discussed in the next chapter, results in a much higher signal-to-noise ratio.

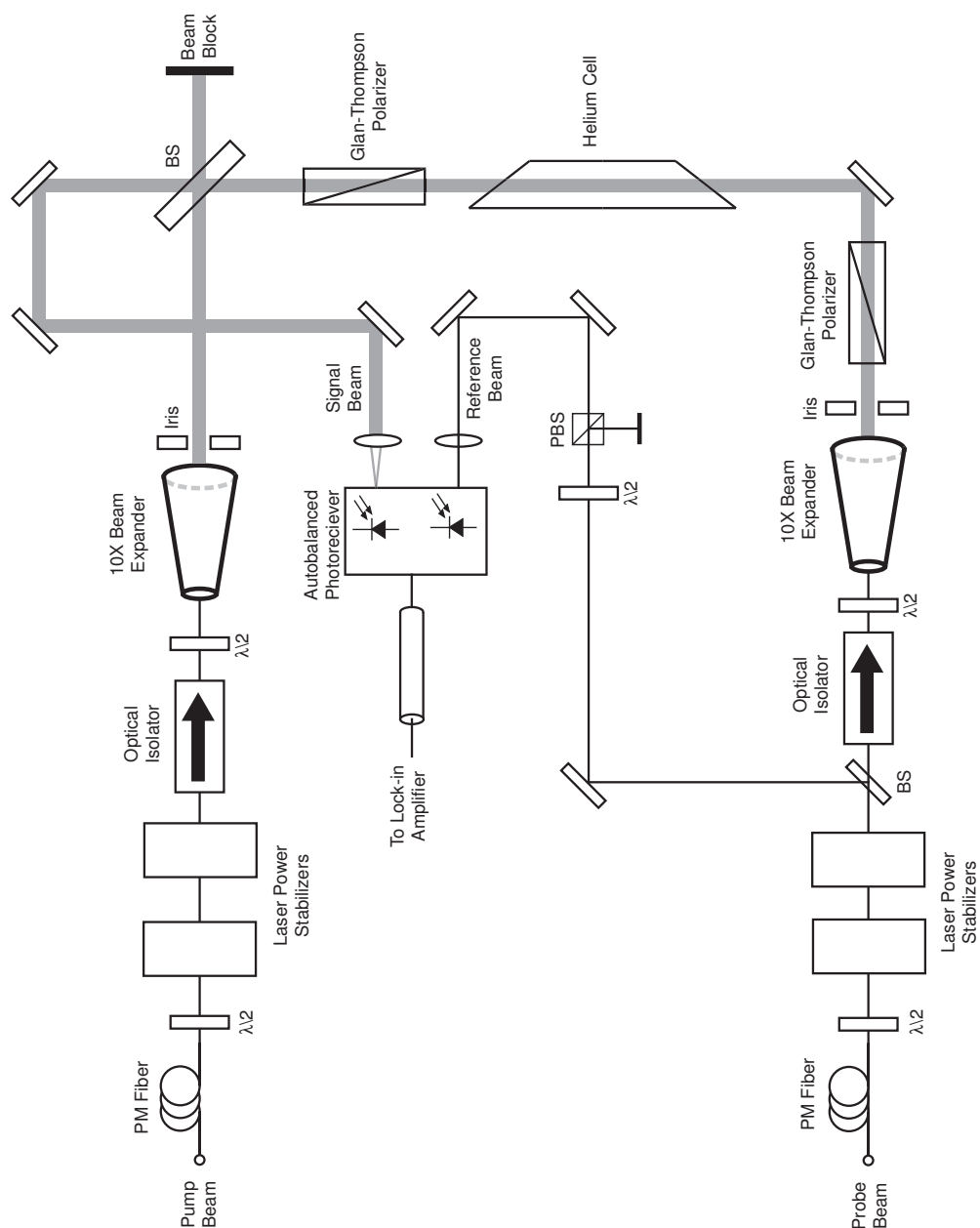


Figure 5.15: Optical components for pump and probe beams. Each beam is spatially filtered in a PM fiber, power-stabilized, and expanded in a telescope. The polarization of each beam is purified with a Glan-Thompson polarizer. An autobalanced photodetector reduces the effects of amplitude noise.

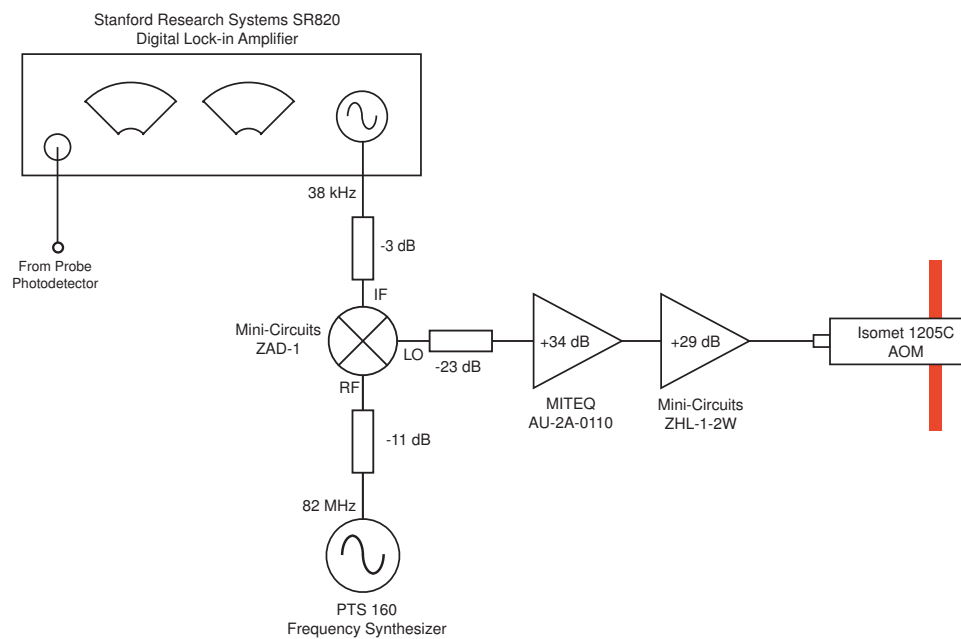


Figure 5.16: Electronic setup for amplitude modulation of the pump beam.

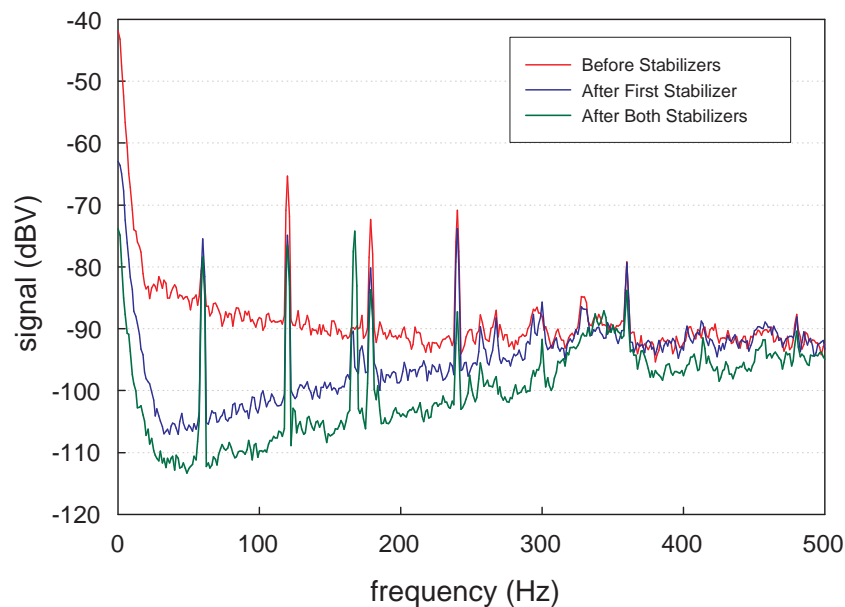


Figure 5.17: Reduction of laser intensity noise using two power levellers.

After spatial filtering in a PM fiber-optic patchcord (Fig.5.15), the power of each beam is stabilized using a pair of power levellers (Thor Labs CR200-B). With a bandwidth of 500 Hz, the power levellers significantly reduce low-frequency laser intensity noise (Fig.5.17). The output power is set by an external voltage from a DAC.

To limit the effects of wavefront curvature, a telescope (Special Optics 50-51-10X-1083) expands the diameter of each beam by a factor of 10 to 2 cm. To prevent drift and acoustical noise from degrading the pointing stability of the expanded beam, the telescopes are mounted on large plastic V-groove blocks, lined with rubber isolation pads and bolted onto the optical bench using three stainless steel pedestals. The telescopes are held in place using two rubber-tipped clamping arms.

An iris after each telescopes selects only the flattest part at the center of the beam's intensity profile. A probe diameter of 8 mm was chosen to be less than the pump's diameter of 10 mm to ensure that the entire probe beam is overlapped by the pump.

It was observed that the irises generate excess laser intensity noise from laser pointing instability. This effect was minimized by moving the probe iris several feet from its previous position in front of the photodetector to a point right after the probe telescope. This move significantly reduced laser intensity noise induced by optical mount instability, leading to an increase in signal-to-noise by a factor of 2.

The polarization of each beam is controlled with a Glan-Thompson calcite polarizer (Karl Lambrecht MGT25S14-V1083) that is mounted in a motorized rotation stage (Newport PR50-CC). The polarizers have an extinction ratio of $10^6:1$ and are

anti-reflection coated for 1083 nm. To prevent etalon effects and to prevent weak reflections of the pump beam from reaching the photodetector, the polarizers are slightly tilted by a few degrees in the horizontal plane. The large acceptance angle of $\pm 7^\circ$ ensures that the performance of the polarizers is unaffected when tilted.

To align the two polarizers, a crossed-polarizer transmission measurement aligns the angle of the pump polarizer in the same direction as the vertical axis of a polarizer mounted in a fixed, non-rotatable mount. This procedure aligns the pump polarization angle in the vertical direction to within 1 degree. A second crossed-polarizer transmission measurement aligns the angle of the probe polarizer to within $\pm 0.04^\circ$ of the angle of the pump polarizer.

The probe beam is separated from the pump beam with a non-polarized plate beamsplitter having 50% reflectivity. The back face of the beamsplitter is anti-reflection coated to reduce ghosting and is angled at 0.5° with respect to the front face to reduce etalon effects. The reflected pump beam is blocked while the transmitted probe beam is blocked by an optical isolator.

Previously, when a non-polarized beamsplitter cube was used for separating pump and probe beams, a reflection of the pump beam off one of the faces of the cube traveled collinearly with the probe beam into the photodetector. Although this reflection was very weak, an offset in the output of the lock-in amplifier was present because the reflection was amplitude modulated. A plate beamsplitter, on the other hand, uses a geometry that significantly minimizes this reflection. This effect can be seen in Fig.5.18, where scans of the $2^3S - 2^3P_0$ transition show a four-fold reduction in the background offset when the beamsplitter cube is replaced by a beamsplitter plate.

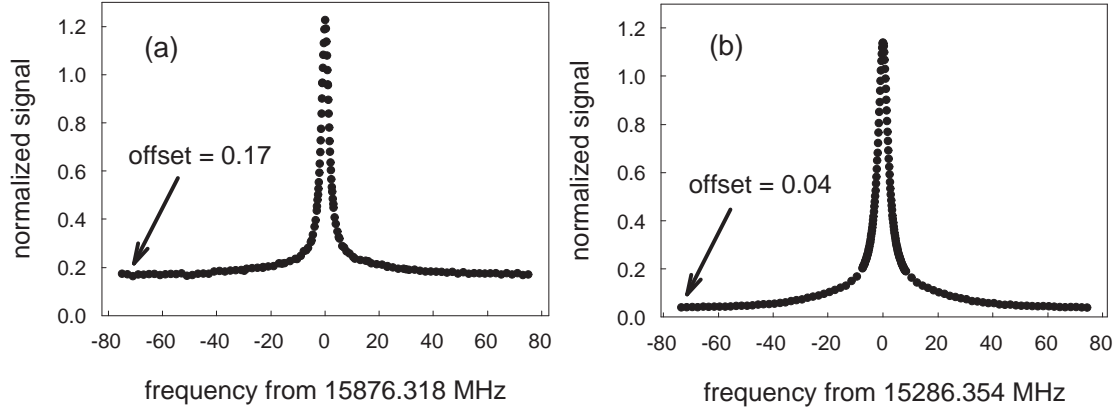


Figure 5.18: (a) Presence of a background offset due to a weak reflection of the pump beam off a beamsplitter cube; (b) a four-fold reduction of this offset is achieved with a beamsplitter plate.

5.5.3 Signal Photodetection

To reduce the effects of residual intensity noise, an autobalanced photodetector (New Focus Nirvana) is used to detect the probe beam. A plate beamsplitter after the probe power levers directs a small amount of power into the reference photodiode. The power of this reference beam, controlled by a half-waveplate and polarized beamsplitter cube, is set to be twice the power of the signal beam. At 76 kHz, the autobalancing reduces laser intensity noise by 3 dB (Fig.5.19). The remaining noise floor, equal to the shot noise of the combined signal and reference beams, is approximately 3 dB higher than the shot noise of the signal beam by itself.

The Nirvana detector's transimpedance gain of 20 V/mA is set by a 20 k Ω feedback resistor in the front-end transimpedance amplifier. For this value of the transimpedance gain, the Johnson noise of the feedback resistor is the dominant source of electronic noise. To increase the photodetector's sensitivity, the transimpedance

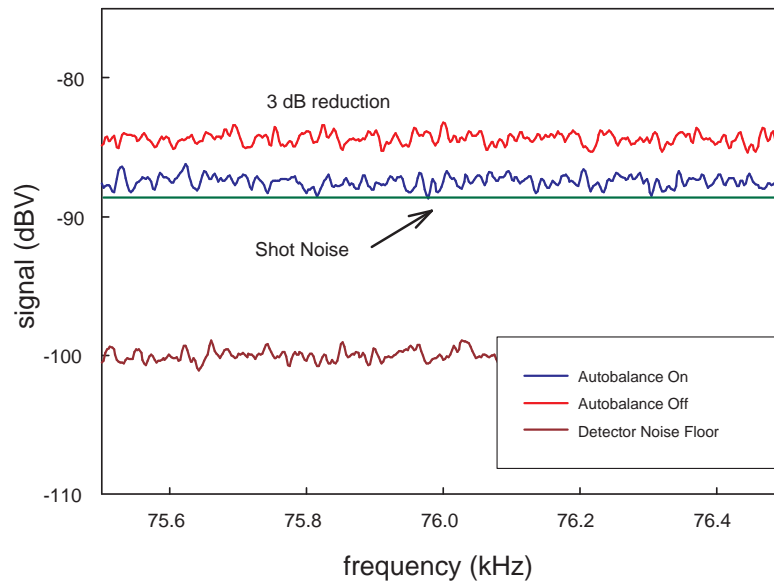


Figure 5.19: Reduction of laser intensity noise at 76 kHz with the autobalanced photodetector. The resolution bandwidth is 9.55 Hz.

gain was increased to 100 V/mA by replacing the 20 k Ω feedback resistor by a 100 k Ω resistor. With this change, the shot noise of optical powers as low as 3 μ W can be detected above the electronic noise floor. The extra factor of five in gain has no impact on the 125 kHz bandwidth of the circuit.

5.5.4 Lock-in Detection

The amplitude and phase of the helium absorption signal is detected using a digital lock-in amplifier (Stanford Research Systems SR-830). The output of the Nirvana photodetector is AC coupled into the lock-in amplifier, digitized using a 16-bit ADC, and digitally demodulated with the second harmonic of the lock-in's function generator output. The DC output is digitally-filtered with a four-pole low-pass filter

($\tau=10$ ms) and sampled at 64 Hz for storage in an internal memory buffer.

Prior to this work, the lock-in output was sent to the lab computer over GPIB as ASCII floating point numbers. In this format, each number is represented as 14 bytes of data. To increase data-transfer speed, the lock-in was reprogrammed to output numbers in a non-normalized logarithmic floating point format. Here, each number is represented as four bytes, two representing a mantissa m and two representing an exponent E , that represent the data value D by

$$D = m \cdot 2^{E-124}$$

By transferring the lock-in data in this compressed format, data-transfer speeds were increased by a factor of ten.

5.6 Scan Laser Offset-Lock

With thousands of $2P_J$ linescans measured, each with 100 to 500 different offset-lock frequencies, the offset-lock PLL is the workhorse of the experiment. For reliable data acquisition, robust automated control of the offset lock and scan laser frequency is crucial. Described in this subsection are details of the scan laser offset-lock, including microwave beat detection, phase-locking with a digital phase/frequency detector (PFD), and the procedures used for initiating lock.

5.6.1 Beat Detection and Signal Processing

The scan laser's frequency is controlled by offset-locking from the CSDL. To minimize the frequency of the beat between the two lasers, the CSDL is chosen to be near

276.748 GHz, which is half-way between the frequencies of the $2P_0$ and $2P_2$ states. The offset frequencies are approximately +16 GHz, -14 GHz, and -16 GHz for the $2P_0$, $2P_1$, and $2P_2$ states, respectively.

Previously, when the experiment relied on the ^3He reference, the offset frequency for the $2P_0$ state was 39 GHz. Two microwave synthesizers were used to mix this beat down to RF. The significant reduction in signal-to-noise from using two mixing stages affected the reliability of the offset lock. By switching the frequency of the CSDL, signal-to-noise is improved through the use of only one mixing stage for all three transitions.

The microwave circuit for detecting and processing the beat between the two diode lasers is shown in Fig.5.20. The output of a 40 GHz amplified photodetector (New Focus 1011) is amplified and mixed down to ~ 500 MHz in a mixer (Remec MM134P-1). The LO signal comes from a microwave synthesizer referenced to GPS (HP8672A). The RF beat is amplified and filtered before going to a digital phase/frequency detector (PFD) for phase-locking.

5.6.2 Digital Phase/Frequency Detector and PLL Filter

The digital PFD used for phase-locking the beat is identical to those used for phase-locking the beats of the optical frequency comb (see Chapter 2). The laser beat frequency is sent to the RF input of the PFD, while a GPS-referenced frequency synthesizer generates the REF signal. The RF signal is divided by $N=25$.

The PLL loop filter is shown in Fig.5.21. The output of the charge-pump filter is buffered by a pair of AD8021 op-amps. The output of one of these buffers is used to

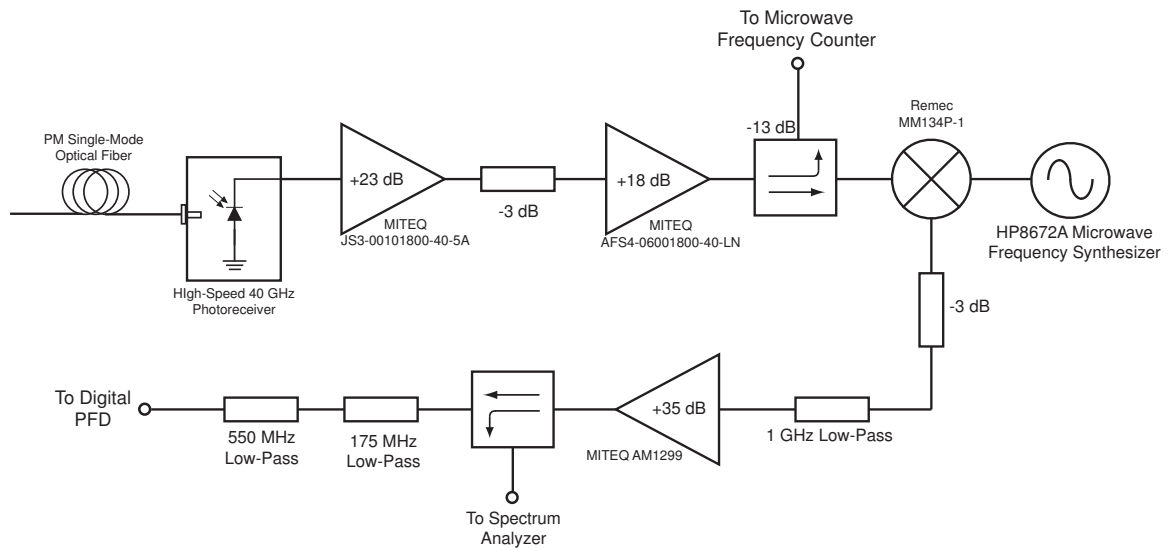


Figure 5.20: Microwave electronics for detection and processing of the beat frequency between the scan laser and CSDL.

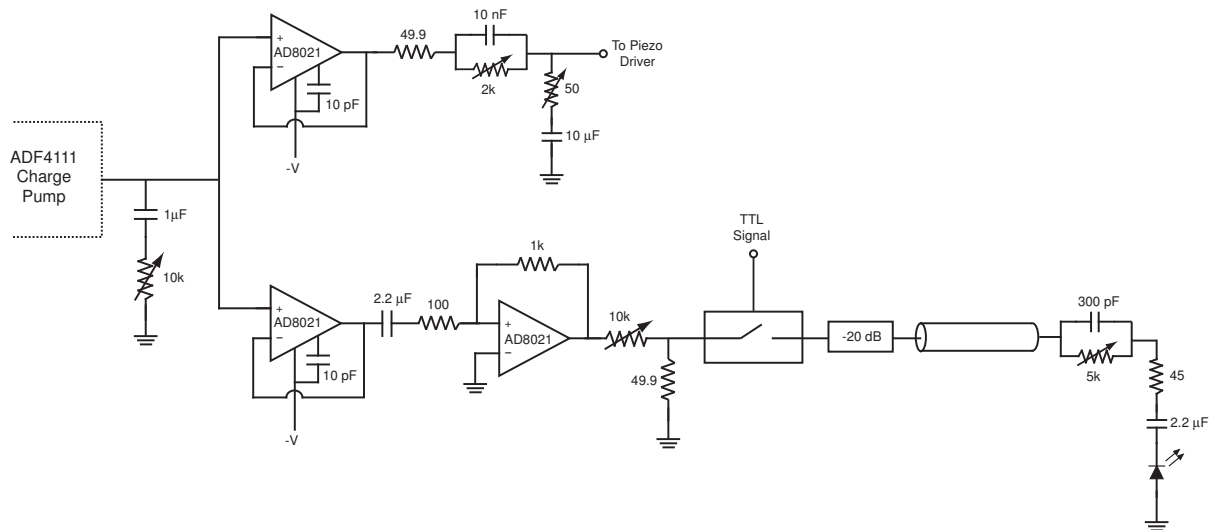


Figure 5.21: Loop filter for the diode laser offset PLL.

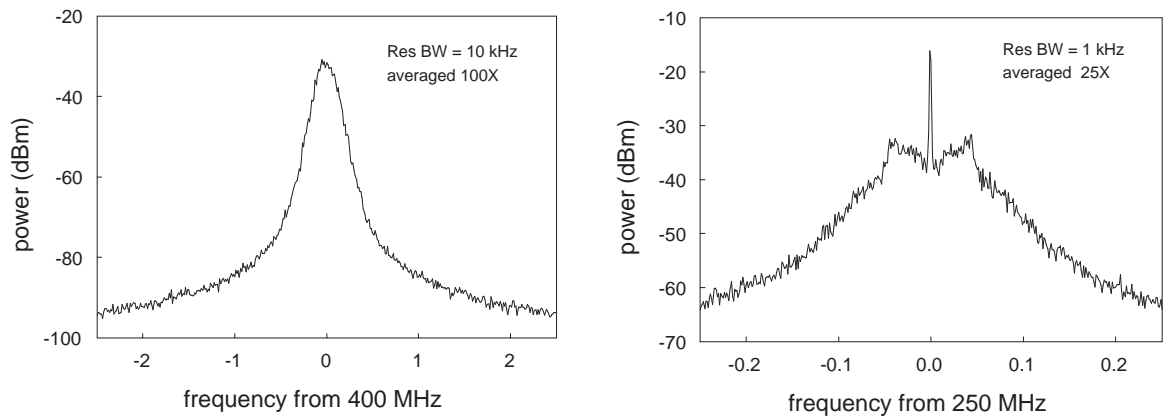


Figure 5.22: Spectrum analyzer traces of the phase-locked beat between the scan laser and CSDL show a 10-fold increase in locking bandwidth when the laser's piezo transducer is switched from (a) a low-bandwidth piezo tube to (b) a high-bandwidth monolithic piezo stack.

control the scan laser piezo. A phase-advance filter increases the bandwidth of this control. The output of the second op-amp buffer is used for current feedback to the laser diode. This signal is injected into the laser diode cathode with a phase-advance filter located at the diode itself. This filter increases loop bandwidth by cancelling a frequency pole introduced by the capacitance of the laser diode. A 45Ω resistor, in series with the $\sim 5\Omega$ impedance of the diode, ensures that high frequency signals are terminated into 50Ω .

Fig.5.22 shows spectrum analyzer traces of the phase-locked beat between the scan laser and CSDL using only feedback to the piezo transducer. The switch from a low-bandwidth piezo tube (Fig.5.22a) to a high-bandwidth monolithic piezo stack (Fig.5.22b) increased locking bandwidth by a factor of ten to 50 kHz.

In Fig.5.23b, current feedback to the laser diode increases the bandwidth to 500 kHz. The switch from commercial laser current supplies to the circuit in Fig.5.11

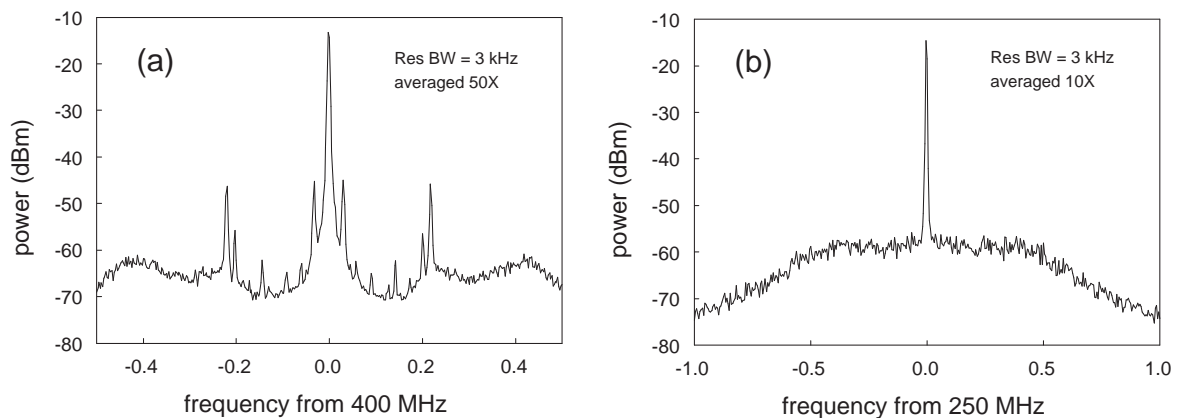


Figure 5.23: Spectrum analyzer traces of the phase-locked beat between the scan laser and CSDL show an increase in locking bandwidth to 500 kHz when current feedback is applied. (a) Several noise spikes are visible when the diode lasers are powered by commercial current supplies; (b) A cleaner spectrum is obtained when the lasers are powered by the circuit in Fig.5.11.

significantly reduces noise spikes in the laser's spectrum.

5.6.3 Offset-Locking Procedure

Coarse Frequency Tuning

In order to switch automatically between helium transitions, a procedure was developed for coarse and fine-tuning of the scan laser frequency. This procedure, which switches between transitions in approximately 5 seconds, increases the speed of the experiment by minimizing the time between scans.

At the beginning of each data run, the offset-lock frequencies are calculated from the optical frequency of the CSDL and the frequencies of the three $2P_J$ transitions. The algorithm for determining the CSDL frequency, as described in Chapter 4, yields values that are accurate to a few kHz. The $2P_J$ transition frequencies, obtained

from reference xxx, have accuracies of less than 100 kHz. However, these values are rounded to the nearest MHz in order to prevent biasing of the data.

The scan laser's frequency is coarsely-tuned via temperature-tuning of the laser diode. The temperature is tweaked in steps of 0.1°C until the frequency is within 1 GHz of the transition to be probed. Finer frequency control, obtained by tweaking the DC drive current, shifts the laser frequency to within 200 MHz of the helium frequency.

Initial Lock Acquisition

With the scan laser's frequency within 200 MHz of the helium frequency, the offset-lock is activated by a computer signal sent to the PFD controller board. Initial locking, which occurs in a few ms, uses only the piezo because current feedback adversely affects lock acquisition. An analog switch, controlled by a TTL signal from the PFD controller board, is open during lock acquisition (Fig.5.21).

Lock Detection

Before current feedback can be applied and before data-taking can start, coarse lock acquisition with the piezo must be confirmed. Previously, this was accomplished by measuring the frequency of the microwave beat between the two lasers. However, this approach was time consuming because the one-second gate time of the counter more than doubled the duration of the scan.

Implemented here is a faster lock-detection algorithm that relies on a digital lock detector built-in to the ADF4111 PLL chip. The circuit, which functions as a quadrature detector, outputs a high TTL signal when the phase delay between REF and

RF signals is less than 15 nsec for 5 consecutive cycles of f_{comp} . The TTL signal is read by the computer through the PFD microprocessor controller board. If lock is confirmed, the analog switch controlling current feedback is closed and data-taking commences. If lock cannot be established, the scan is aborted.

The status of the lock is always quickly available because the digital lock detector operates in parallel with the PFD lock. As a result, the lock status can be determined in a few ms, limited by the data bus speed between the computer and PFD chip. This faster approach to determining lock status has increased the speed of the experiment by a factor of 2 to 3.

Changing the Offset-Lock Frequency

The scan laser frequency is controlled by changing the output of the frequency synthesizer that supplies the REF signal for the PFD. Although current feedback is turned off during the change, feedback to the piezo remains on. Because the 1 GHz capture range of the piezo is wider than the frequency span of the linescans, the scan laser locks to a new frequency in only a few ms. When lock has been confirmed, current feedback is applied and data acquisition begins. The procedure repeats for every point in the scan.

5.7 Measuring Background Channels

In order to investigate the possible influence of various experimental parameters on the data, a number of background channels were monitored. Table 5.7 lists these background channels along with typical values and the instruments on which they

were measured. The Keithley 2701 is a 40-channel data acquisition system and the Neocera LTC-11 is a two-channel temperature controller/monitor. Three PLL voltages and the helium pressure in the cell were measured using Fluke 8842A digital multimeters.

5.8 Computer Interface

Whenever possible, electronic instruments are controlled through the lab computer. A 100 Mbps ethernet connection between the computer and an ethernet switch (Allied Telesyn AT-8024GB) is used to communicate with instruments over several buses. With the exception of the Keithley 2701 data acquisition system, which interfaces directly with the ethernet switch, all communication with commercial instruments is done with GPIB. Three different GPIB buses interface with the ethernet switch using ethernet-to-GPIB controllers (National Instruments GPIB-ENET/100). All DACs and PFD controller boards operate over two fiber serial rings that interface with the ethernet switch using an ethernet-to-serial converter (Control DeviceMaster DB9M 4-port) and two serial-to-fiber converters (B&B Electronics FOSTC).

Channel	Typical Value	Instrument
Magnet Temp.	24 ⁰ C	Keithley 2701
NPRO crystal temp	35.6 ⁰ C	Keithley 2701
Iodine NPRO piezo voltage	±2 volts	Keithley 2701
Magnet Setpoint Voltage	0.875 mV = 3.5 Amps	Keithley 2701
Discharge Forward Power	37.5 Watts	Keithley 2701
Discharge Reflected Power	30-35 Watts	Keithley 2701
Probe Photodiode Monitor	50-200 μ W	Keithley 2701
Iodine Cold Finger Temp.	-15 ± 0.02 ⁰ C	Neocera LTC-11
Ti:Saph Laser Baseplate Temp.	27 ± 0.003 ⁰ C	Neocera LTC-11
Iodine-Comb PLL Voltage	0-5 volts	Fluke 8842A
CSDL PLL Voltage	0-5 volts	Fluke 8842A
Comb Offset PLL Voltage	0-5 volts	Fluke 8842A
Helium Pressure	10-40 mTorr	Fluke 8842A

Table 5.1: Measured background signals with typical values and the instruments on which they are measured.

Chapter 6

Expected and Observed Lineshapes

Several physical mechanisms contribute to the specific helium lineshapes obtained from the experiment. Modulation transfer spectroscopy with an amplitude-modulated pump beam is used to generate Doppler-free Lorentzian lineshapes. The in-phase and quadrature components of these lineshapes are symmetric about the linecenter. Velocity-changing collisions (VCC) and the light-pressure effect modify these signals by altering the velocity distribution of the atoms. Although the effects of VCC on signal lineshape are symmetric, the light-pressure effect adds an asymmetry that introduces systematic frequency shifts. A method for correcting for these shifts uses a magnetic field to resolve the magnetic sublevels of the 2^3S and 2^3P states, giving rise to signals with several Lorentzian peaks and crossover resonances.

Center frequencies are extracted from the multi-peak signals by nonlinear regression. Proper choice of scan patterns, frequency patterns, and the order in which the transitions are measured is crucial for accurately measuring background signals and removing the effects of drift.

6.1 Amplitude Modulation Transfer Spectroscopy

Similar to the iodine reference (see Chapter 3), modulation transfer spectroscopy is used to generate Doppler-free absorption signals in helium [64, 65, 66]. This form of saturated absorption spectroscopy consists of a single-frequency probe laser beam and a multi-frequency pump laser beam that are overlapped as they counterpropagate through the helium gas. On resonance, four-wave mixing generates sidebands on the probe beam whose amplitude and phase are detected with a lock-in amplifier.

Compared to the iodine reference, there are two differences in how MTS is implemented for helium spectroscopy. First, multiple pump frequency components are generated via amplitude modulation, resulting in in-phase and quadrature signals that are both symmetric about the linecenter [64]. Second, modulation frequencies much smaller than the linewidth are used in order to maximize signal size.

Mathematically, the pump beam, amplitude modulated by the signal $A(t) = \mathcal{E}_M \cos(\delta t)$, is given by

$$E_S(z, t) = \mathcal{E}_S A(t) e^{i[(\omega+\Delta)t - kz + \phi]} + \text{c.c.} \quad (6.1)$$

$$= \mathcal{E}_S \mathcal{E}_M \left(\frac{e^{-i\delta t} + e^{i\delta t}}{2} \right) e^{i[(\omega+\Delta)t - kz + \phi]} + \text{c.c.} \quad (6.2)$$

$$= \mathcal{E}_S \mathcal{E}_M e^{i[(\omega \pm \delta + \Delta)t - kz + \phi]} + \text{c.c.} \quad (6.3)$$

where \mathcal{E}_S is the amplitude of the saturating pump beam, ω is the carrier frequency, Δ is an offset between the frequencies of the pump and probe beams, k is the wavenumber, and ϕ is a phase offset.

The presence of two frequencies in the pump yields two resonances at frequencies

$$\omega = \omega_0 - \frac{\Delta}{2} \pm \frac{3\delta}{2} \quad (6.4)$$

where ω_0 is the atomic transition frequency. These two resonances are separated in frequency by 3δ .

The signal S is equal to the heterodyne beat between the probe and the sidebands

$$S = \frac{C\mathcal{E}_P\mathcal{E}_M\mathcal{E}_S}{\sqrt{\gamma^2 + \delta^2}} [(L_{3/4} + L_{-3/4}) \cos(2\delta t + \phi) + (D_{3/4} - D_{-3/4}) \sin(2\delta t + \phi)]. \quad (6.5)$$

Here, \mathcal{E}_P is the amplitude of the probe beam and γ is the transition linewidth [64, 67].

The absorptive profile L_n and dispersive profile D_n are given by Eqns. 3.10 and 3.11.

The in-phase component of S is plotted in Fig. 6.1 for three different values of the modulation frequency δ . For $\delta \ll \gamma$, the doublet structure is not resolved, giving rise to lineshapes that are well-approximated by a single Lorentzian centered at the transition frequency ω_0 . At higher modulation frequencies $\delta \geq \gamma$, the doublet is resolved, but the signal size decreases with increasing modulation frequency due to the inability of the atoms to respond to these faster fields.

The quadrature component of S is plotted in Fig. 6.2. The signal, consisting of the difference between two dispersive profiles, is attractive for spectroscopy because its symmetric structure leaves measurements of the center frequency insensitive to the choice of lock-in phase. For small modulation frequencies $\delta \ll \gamma$, the quadrature signal is small because the two components mostly cancel. For $\delta \geq \gamma$, the two terms are resolved, with the signal size decreasing with increasing modulation frequency.

In order to maximize signal size, modulation frequencies much less than the transition linewidth γ were used in this work. In this regime, the doublet Lorentzian structure is approximated by a single Lorentzian whose measured width increases with modulation frequency as δ^2/γ and whose measured amplitude decreases with modulation frequency as $-\delta^2/\gamma$ [65]. These quadratic dependencies are demonstrated

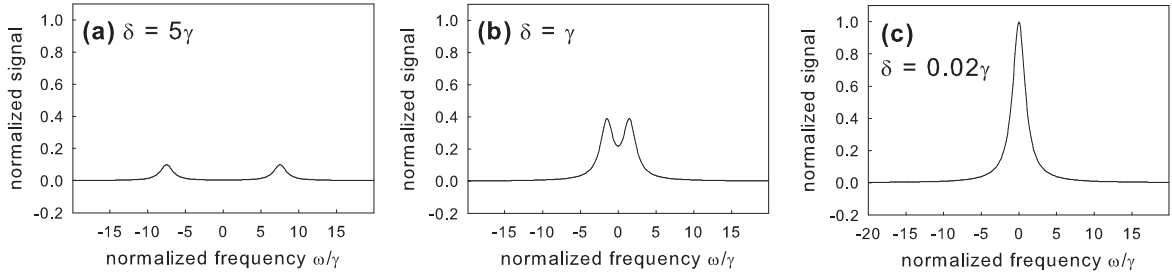


Figure 6.1: The in-phase component of the theoretical MTS lineshape for an amplitude-modulated pump. (a) For small modulation frequencies $\delta \ll \gamma$, the signal approximates a single Lorentzian centered at ω_0 . (b) For $\delta \sim \gamma$, two Lorentzian components are resolved. (c) For $\delta \gg \gamma$, the signal size decreases due to the inability of the atoms to respond to faster fields.

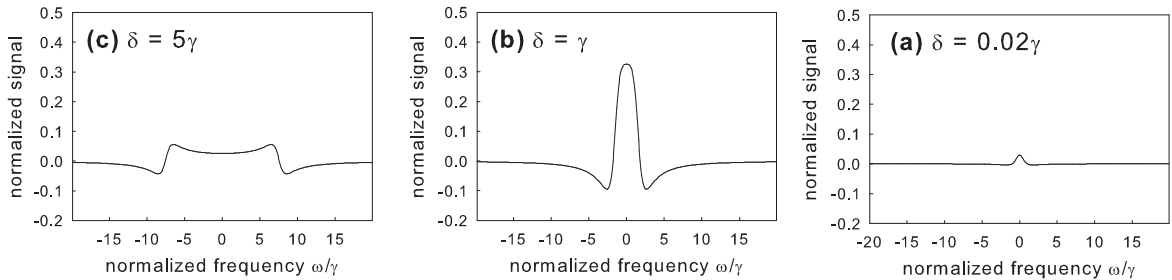


Figure 6.2: The quadrature component of the theoretical MTS lineshape for an amplitude-modulated pump. (a) For small modulation frequencies $\delta \ll \gamma$, the two dispersive components mostly cancel. (b) For $\delta \sim \gamma$, the two components are resolved and reach their maximum height. (c) For $\delta \gg \gamma$, the amplitude decreases due to the inability of the atoms to respond to faster fields.

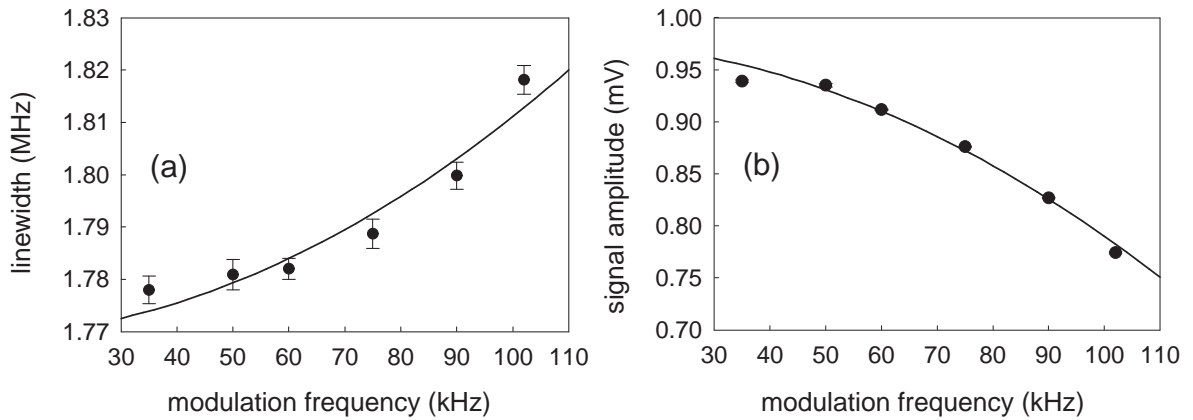


Figure 6.3: Measured values of the (a) linewidth and (b) signal amplitude depend quadratically on modulation frequency for small modulation frequencies $\delta \ll \gamma$. The data is taken from measurements of the $2^3S-2^3P_1$ transition at a cell pressure of 40 mtorr and laser power of $100 \mu\text{W}$ per beam.

experimentally in Fig. 6.3.

6.2 Light-Pressure

In saturated absorption spectroscopy, the pump beam excites ground-state atoms that are resonant with the laser fields, leading to Doppler-free Lorentzian lineshapes through the resulting increase in probe transmission. A more complete picture takes into account the alteration of the atomic velocity distribution due to recoil upon absorption of pump photons. The effect introduces a small dispersive contribution to the velocity distribution that in turn leads to systematic frequency shifts (Fig. 6.4).

Presented in this section is a brief treatment of the light-pressure effect, including a mathematical model for understanding how the re-distribution of atomic velocities leads to frequency shifts. A method for measuring these shifts relies on the different

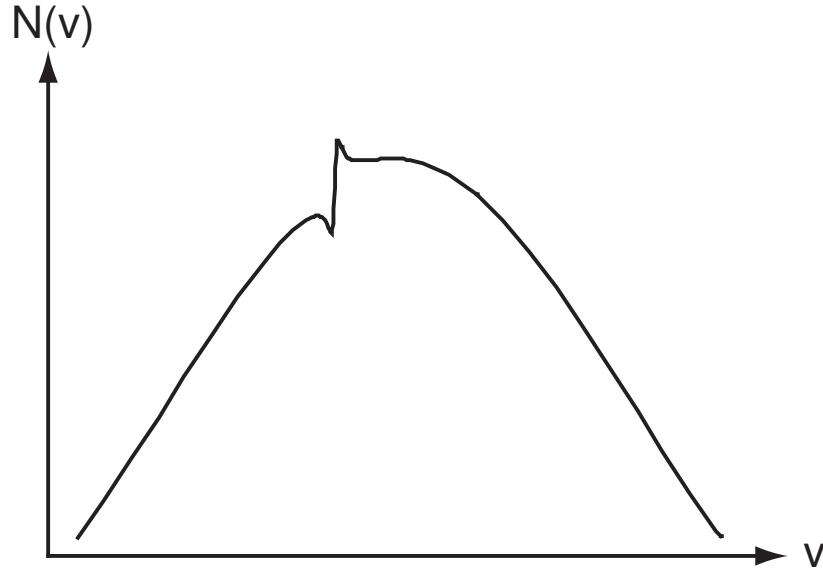


Figure 6.4: Recoil of atoms upon absorption of pump photons leads to a small dispersive modification of the atomic velocity profile that in turn introduces systematic frequency shifts.

coupling constants between the magnetic sublevels of the 2^3S and 2^3P states.

6.2.1 Atomic Recoil

Consider a two-level atom with ground-state energy E_a and excited state energy E_b . If the atom absorbs a photon with energy $\hbar\omega$ and momentum $\hbar\vec{k}$, then the atom's momentum changes from its initial value of \vec{p}_i to a final value \vec{p}_f of:

$$\vec{p}_f = \vec{p}_i + \hbar\vec{k} \quad (6.6)$$

$$= M\vec{v}_i + \hbar\vec{k} \quad (6.7)$$

where M is the atomic mass and \vec{v}_i is the initial velocity of the atom. The photon energy needed to excite the atom can be found through conservation of relativistic

energy and momentum [115]

$$\hbar\omega = \sqrt{p_f^2 c^2 + (Mc^2 + E_b)^2} - \sqrt{p_i^2 c^2 + (Mc^2 + E_a)^2}. \quad (6.8)$$

Expanding in orders of $(1/c)^2$ yields

$$\omega = \omega_0 + \vec{k} \cdot \vec{v}_i - \omega_0 \frac{v_i^2}{2c^2} + \frac{\hbar\omega_0^2}{2Mc^2} \quad (6.9)$$

where $\omega_0 = (E_b - E_a)/\hbar$. The terms $\vec{k} \cdot \vec{v}_i$ and $-\omega_0 v_i^2/(2c^2)$ are the first-order and second-order Doppler-shifts, respectively. The last term, $\omega_{rec} = \hbar\omega_0^2/(2Mc^2)$, is the recoil shift that represents the extra energy that must be imparted to the atom in order for momentum to be conserved. For the $2^3S - 2^3P_J$ transitions, the recoil shift frequency is $(2\pi)42$ kHz.

6.2.2 Light-Pressure Shifts in a Closed Two-Level System

Due to the fixed direction of the photon momentum \vec{k} , the pump beam imparts a net momentum to the atoms described by a classical scattering force $F_s(v)$

$$F_s(v) = \hbar k \gamma P_e(v) \quad (6.10)$$

where $\gamma = (2\pi)1.6$ MHz is the decay rate of the 2^3P states. $P_e(v)$ is the probability of an atom with velocity v to be excited by the pump, given by

$$P_e(v) = \frac{s}{2} \frac{\gamma^2}{\gamma^2 + k^2(v - v_p)^2} \quad (6.11)$$

Here, the saturation parameter $s = I/I_{SAT}$ is the ratio of laser intensity I to the saturation intensity $I_{SAT} = \pi h c \Gamma / (3\lambda^3)$, where h is Planck's constant, c is the speed of light, and λ is the transition wavelength [116]. The velocity class v_p is resonant with the pump beam [113].

The effects of the scattering force F_s on the Doppler profile $N(v, t)$ can be calculated using a continuity equation [117]

$$\frac{\partial}{\partial t} N(v, t) + \frac{\partial}{\partial v} \left(\frac{\partial v}{\partial t} N(v, t) \right) = 0. \quad (6.12)$$

Here we have assumed that the atomic sample is uniform in space. Rearranging terms gives

$$\frac{\partial}{\partial t} N(v, t) = -\frac{1}{m} \frac{\partial}{\partial v} [F_s(v) N(v, t)]. \quad (6.13)$$

Assuming that any modification to $N(v, t)$ is small, the first-order perturbative solution is

$$N(v, t) = N_0(v) - N_0(v_p) \frac{t}{m} \frac{\partial}{\partial v} F_s(v) \quad (6.14)$$

where we have assumed through the approximation $N_0(v) \approx N_0(v_p)$ that the scattering force only affects velocity-classes near v_p .

The coherent interaction time τ between the pump and atoms sets the timescale for this model. In the limit $t \gg \tau$, the Doppler profile approaches a steady-state value $N(v) = N(v, t - \infty)$. Making the substitution $t - \tau$ in Eqn. 6.14 and using Eqn. 6.10 gives the steady-state Doppler profile

$$N(v) = N_0(v) + N_0(v_p) \epsilon_r \tau \frac{4sk(v - v_p)\gamma^3}{[\gamma^2 + k^2(v - v_p)^2]^2} \quad (6.15)$$

where $\epsilon_r = \hbar\omega_r$ is the recoil energy. The resulting Doppler lineshape consists of the usual Doppler profile $N_0(v)$ plus an additional asymmetric term with amplitude $\epsilon_r \tau$.

The modified Doppler profile is used to calculate the susceptibility χ of the atomic ensemble [113, 118]. The normalized absorptive lineshape, equal to the imaginary part

of χ , is given by

$$S(\delta) = \frac{1}{2\delta^2 + 1} + \epsilon_r \tau \frac{\delta}{(\delta^2 + 1)^2} \quad (6.16)$$

where $\delta = (\omega - \omega_0)/\gamma$. In addition, it is assumed that the linewidth γ is much larger than the Doppler width. The first term of on the right-hand side of Eqn. 6.16 is the usual Lorentzian profile while the second term, with amplitude $\epsilon_r \tau$, is due to light-pressure. In the limit $\epsilon_r \tau \ll 1$, the signal lineshape simplifies to

$$S(\delta) = \frac{1}{2} \frac{1}{(\delta - \epsilon_r \tau)^2 + 1} \quad (6.17)$$

Here, the Lorentzian appears shifted in frequency by $\epsilon_r \tau \gamma$.

Collisions disrupt the coherence between the lasers and atoms. As a result, the mean time between collisions sets the interaction time τ . Mathematically,

$$\tau = \frac{1}{n v_p \sigma} \propto \frac{1}{p} \quad (6.18)$$

where the number density n is proportional to pressure p , v_p is the most probable speed, and σ is the collisional cross-section. A measured pressure broadening of 25 MHz/Torr gives [113]

$$\tau = 6.4(1)/p \text{ } \mu\text{s} \quad (6.19)$$

where the pressure p is in mtorr. The resulting frequency shift due to light-pressure therefore depends inversely-proportional on pressure. This shift occurs in addition to the usual linear pressure shift due to phase-changing collisions [115].

While the presence of a frequency shift that depends nonlinearly on pressure can severely affect the accuracy of linear frequency extrapolations to zero pressure, the

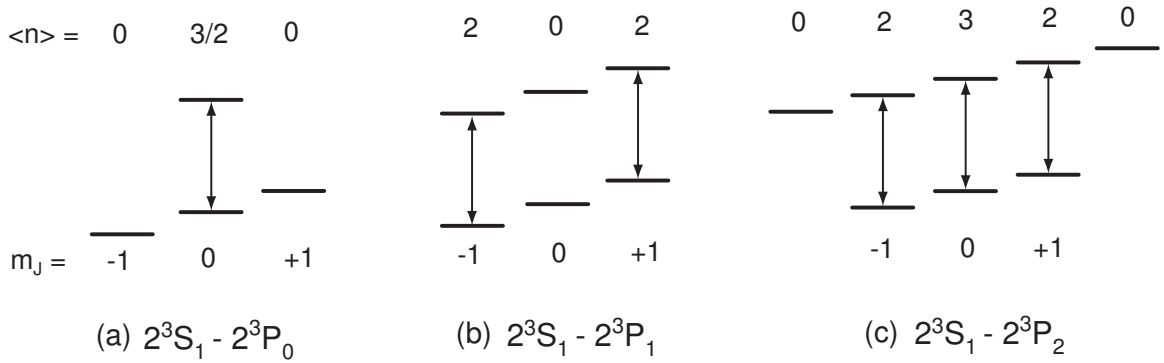


Figure 6.5: Allowed transitions when magnetic sublevels are resolved and both pump and probe beams have polarizations parallel to the magnetic field. Shown for each allowed transition is the mean number of photons $\langle n \rangle$ scattered before decaying to a ground state not resonant with the laser fields.

asymmetry introduced by the Lorentzian derivative has an amplitude that is more than 10 times smaller than the experimental resolution (see Section 8.2.1). Therefore, the only detectable effect of laser light-pressure is a shift of the Lorentzian center frequencies by $\epsilon_r \tau \gamma$. As shown in the next section, shifts of different sizes for the different transitions can be used to correct the data before extrapolating to zero pressure.

6.2.3 Correcting for Light-Pressure Shifts

A method of correcting for light-pressure shifts relies on lifting the degeneracy of the magnetic sublevels of the 2^3S and 2^3P states [113]. Pump and probe beams with polarizations parallel to the magnetic field can only drive transitions with $\Delta m_J = 0$, as shown in Fig. 6.5. The magnitude of the light-pressure effect is proportional to the mean number of photons $\langle n \rangle$ scattered by an atom before decaying to a ground-state 2^3S sublevel not resonant with the laser fields. Here, $\langle n \rangle$ is equal to the inverse of the

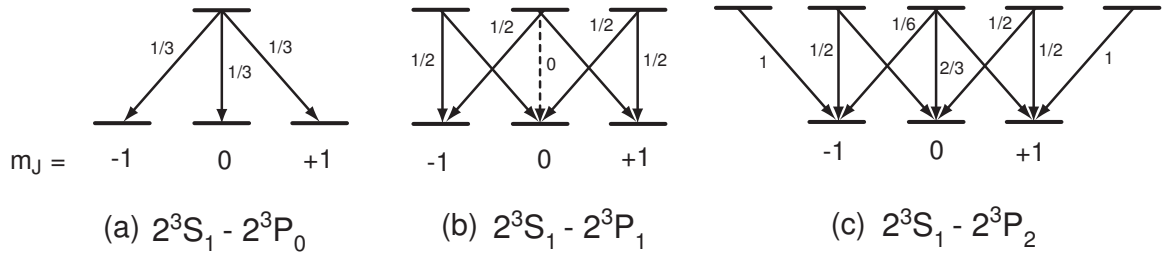


Figure 6.6: Clebsch-Gordan coefficients for the $2^3S - 2^3P_J$ transitions.

probability to decay out of the two-state system. This probability is proportional to the square of the Clebsch-Gordan coefficients (Fig. 6.6).

For the $2^3S - 2^3P_2$ transition, measurements of the $m = 0$ and $m = \pm 1$ peaks can be used to calibrate the shifts for all three transitions. The pressure-dependent difference $\Delta(p)$ between the $m = 0$ frequency and the average of the $m = \pm 1$ frequencies, after correcting for higher-order Zeeman shifts, gives the magnitude of the shift for $\langle n \rangle = 1$. The intervals f_{01} and f_{02} have light-pressure shifts proportional to $\langle n \rangle = 1/2$ that can be removed by subtracting $\Delta/2$. Light-pressure shifts cancel for the interval f_{12} because both transitions have the same dependence on $\langle n \rangle$. For the optical frequency measurements, each transition is corrected by multiplying the value Δ by the corresponding value of $\langle n \rangle$ in Fig. 6.5.

6.3 The Zeeman Effect in Helium

An external magnetic field of up to 120 Gauss is used to resolve the magnetic sublevels of the 2^3S and 2^3P states by several linewidths. By removing this degeneracy, the method of correcting for light-pressure shifts described in the previous section can be applied. Presented in this section is a description of the Zeeman effect in helium,

magnetic field measurements using the peak splitting of the $2^3S - 2^3P_1$ transition, and a qualitative description of signal lineshapes when magnetic sublevels are resolved.

6.3.1 Calculation of Zeeman Shifts

In the presence of an external magnetic field, the Hamiltonian is given by [36]

$$H = H_0 + H_{FS} + H_Z \quad (6.20)$$

where H_0 is the unperturbed atomic Hamiltonian, H_{FS} is the contribution from fine structure, and H_Z is the linear Zeeman energy. The terms H_0 and H_{FS} are diagonal in the $\vec{J} = \vec{L} + \vec{S}$ basis. The term H_Z is given by

$$H_Z = g'_L \mu_L \vec{L} \cdot \vec{B} + g'_S \mu_S \vec{S} \cdot \vec{B} + \vec{\mu}_{rel} \cdot \vec{B} \quad (6.21)$$

where $\vec{\mu}_{rel}$ is a relativistic correction that introduces a third g-factor g_X of order $\mathcal{O}(\alpha^2)$ [119]. The orbital g-factor g'_L differs from its expected value of $g_L = 1 - \mu/M$ due to relativistic corrections of order $\mathcal{O}(\alpha^2)$. Similarly, the value of the spin g-factor g'_S is close to that of the electron, but slightly modified due to relativistic effects within the atom. High-precision QED calculations yield the following values for the g-factors [119]

$$g'_L = 0.999\,8736 \quad (6.22)$$

$$g'_S = 2.002\,2388 \quad (6.23)$$

$$g_X = -0.000\,005\,39. \quad (6.24)$$

The quadratic Zeeman effect, which introduces two additional g-factors, produces negligible shifts due to the relatively small magnetic fields used in this experiment.

Working in the coupled $|J, m_J\rangle$ basis, matrices for the Zeeman term H_Z can be calculated using the Wigner-Eckhardt Theorem. Assuming the magnetic field \vec{B} is oriented in the \hat{z} direction, H_Z can only couple states with the same value of m_J . For the 2^3P states, this results in three matrices for the three different values of $|m_J|$:

$$\begin{aligned} \langle J', m_{J'} | H_0 + H_{FS} + H_Z | J, m_J \rangle = & \\ & \epsilon_J \delta_{J', J} + (\mu_B B) \delta_{m_{J'}, m_J} (-1)^{J-m_J} \sqrt{2J+1} \sqrt{2J'+1} \\ & \times \begin{pmatrix} J' & 1 & J \\ -m_{J'} & 0 & m_J \end{pmatrix} \langle J' || H_Z || J \rangle \end{aligned} \quad (6.25)$$

where ϵ_J is the energy of the 2^3P_J state, B is the magnetic field, and δ is the Kronecker delta. The value of the Bohr magneton μ_B is [14]

$$\mu_B = 1.399\,624\,58(12) \text{ MHz/G.} \quad (6.26)$$

The g-factors are contained in the reduced matrix element $\langle J' || H_Z || J \rangle$, which is calculated explicitly in reference [119].

For $m_J = \pm 2$, the matrix consists of a single number since only the 2^3P_2 state has sublevels with these values of m_J

$$\left[\epsilon_2 + \frac{1}{2} \mu_B B m_J (g'_L + g'_S + \frac{1}{15} g_X) \right] \quad (6.27)$$

For $m_J = \pm 1$, a 2x2 matrix reflects mixing between the 2^3P_1 and 2^3P_2 states:

$$\begin{bmatrix} \epsilon_1 + \frac{1}{2} \mu_B B m_J (g'_L + g'_S - \frac{1}{3} g_X) & \frac{1}{2} \mu_B B m_J (g'_L - g'_S + \frac{2}{15} g_X) \\ \frac{1}{2} \mu_B B m_J (g'_L - g'_S + \frac{2}{15} g_X) & \epsilon_2 + \frac{1}{2} \mu_B B m_J (g'_L + g'_S + \frac{1}{15} g_X) \end{bmatrix} \quad (6.28)$$

For $m_J = 0$, the 3x3 matrix

$$\begin{bmatrix} \epsilon_0 & \sqrt{\frac{2}{3}}\mu_B B(g'_L - g'_S - \frac{1}{6}g_X) & 0 \\ \sqrt{\frac{2}{3}}\mu_B B(g'_L - g'_S - \frac{1}{6}g_X) & \epsilon_1 & \sqrt{\frac{1}{3}}\mu_B B(g'_L - g'_S + \frac{2}{15}g_X) \\ 0 & \sqrt{\frac{1}{3}}\mu_B B(g'_L - g'_S + \frac{2}{15}g_X) & \epsilon_2 \end{bmatrix} \quad (6.29)$$

reflects mixing between all three 2^3P_J states.

In the limit of small magnetic fields, the eigenvalues of the three matrices can be expanded in powers of B . The first and second-order Zeeman shifts are given by

$$\begin{aligned} \delta\omega_Z^{(2^3P)}(J=0, m_J=0) &= (0.044\ 304\ \text{kHz/G}^2)B^2 \\ \delta\omega_Z^{(2^3P)}(J=1, m_J=\pm 1) &= \pm(2.100\ 917\ \text{MHz/G})B + (0.214\ 762\ \text{kHz/G}^2)B^2 \\ \delta\omega_Z^{(2^3P)}(J=2, m_J=\pm 1) &= \pm(2.100\ 917\ \text{MHz/G})B - (0.214\ 762\ \text{kHz/G}^2)B^2 \\ \delta\omega_Z^{(2^3P)}(J=2, m_J=0) &= -(0.286\ 350\ \text{kHz/G}^2)B^2 \end{aligned} \quad (6.30)$$

In order to prevent errors by ignoring higher order terms, all Zeeman shifts in the experiment are computed exactly by numerically diagonalizing the matrices in Eqns. 6.27-6.29. The largest uncertainty in this calculation is due to the Bohr magneton, which contributes a negligible 1 Hz error to the final Zeeman-corrected frequencies.

Due to the lack of fine-structure splitting or neighboring states, the calculation of Zeeman shifts for the 2^3S state is simplified since no significant mixing occurs. The resulting Zeeman shifts contain only a linear term:

$$\begin{aligned} \delta\omega_Z^{(2^3S)}(m_J) &= g_S^{2^3S} m_J \mu_B B \\ &= (2.802\ 381\ \text{MHz/G})B \end{aligned} \quad (6.31)$$

where $g_S^{2^3S} = 2.002\ 237$ is the calculated value of the 2^3S spin g-factor [119].

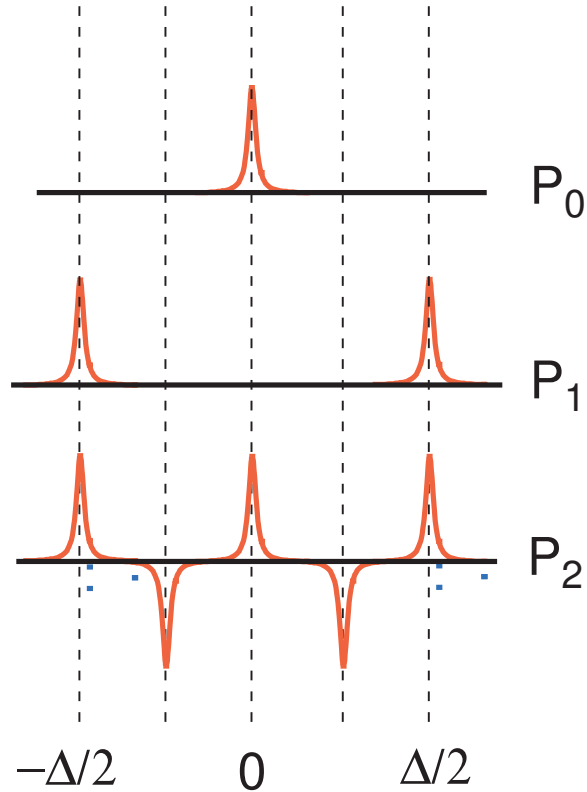


Figure 6.7: Position of signal peaks and dips for the $2^3S - 2^3P_J$ transitions in an external magnetic field when both pump and probe polarizations are parallel to the field [113]. The linear Zeeman splitting is $\Delta = \mu B$. The two dips in the P_2 lineshape are due to crossover resonances.

6.3.2 Helium Lineshapes in an External Magnetic Field

In the presence of an external field, transitions between magnetic sublevels are resolved, giving rise to a series of peaks and dips. To correct for light-pressure shifts, the pump and probe polarizations are aligned parallel to the magnetic field, allowing only $\Delta m_J = 0$ transitions.

The expected signals are shown schematically in Fig. 6.7. The dips in the P_2 signal are due to crossover resonances, which occur when pump and probe beams, each interacting with different velocity-classes of atoms, are simultaneously resonant with

two different transitions [115]. Because the Doppler-shift brings these two transitions into resonance, crossover signals only appear when the frequency separation of the transitions is less than the Doppler width. Occurring at the mean frequency of the two transitions, the resonance is usually manifested as a dip when the two transitions share a common lower level, and a peak when they share a common upper level. For the laser configuration in Fig. 6.7, where only $\Delta m_J = 0$ transitions are allowed, no pair of resonances have a single level in common. Instead, the two lower levels are linked via spontaneous emission between $\Delta m_J = \pm 1$ transitions.

When the polarization of either the pump or probe beam is perpendicular to the magnetic field, $\Delta m_J = \pm 1$ transitions are allowed. The resulting signal lineshapes are much more complex than those in Fig. 6.7. Details of the signal lineshapes for this laser configuration can be found in reference [113].

6.3.3 The P_1 Magnetometer

The value of the magnetic field in the cell is measured from the frequency splitting d_1 between the $m = \pm 1$ peaks of the $2^3S - 2^3P_1$ transition. The value of the splitting depends on the Zeeman shifts of both the 2^3S and 2^3P_1 states:

$$d_1 = \left[\delta\omega_Z^{(2^3S)}(m_J=1) - \delta\omega_Z^{(2^3S)}(m_J = -1) \right] - \left[\delta\omega_Z^{(2^3P)}(J = 1, m_J = 1) - \delta\omega_Z^{(2^3P)}(J = 1, m_J = -1) \right] \quad (6.32)$$

$$= (1.402\,928 \text{ MHz/G})B \quad (6.33)$$

The inverse of this quantity yields the magnetic field

$$B = 0.712\,795 (d_1/\text{MHz}) \text{ G}. \quad (6.34)$$

To remove the linear Zeeman splitting from the data for the 2^3P_1 and 2^3P_2 lineshapes, the average of the $m = \pm 1$ peaks is used. The value of the magnetic field, as determined by Eqn. 6.34, is used to correct for higher-order Zeeman shifts of all three transitions.

6.4 Velocity-Changing Collisions

In addition to the light-pressure effect, the Doppler profile of the atomic ensemble is modified by velocity-changing collisions (VCC). Although VCC do not introduce any frequency shifts, they have a significant effect on the detected lineshapes and must be taken into account when deriving models for fitting the data.

In saturated absorption spectroscopy, the pump laser excites atoms of a particular velocity out of the lower energy level, giving rise to a dip (Bennett hole) in the ground-state velocity distribution (see Fig. 6.8) [115]. VCC rethermalize the ground-state velocity distribution, thereby filling the hole. Atoms knocked into the hole become resonant with the laser fields and can contribute to the detected signal, resulting in an enhancement of the measured lineshapes [120, 121, 122].

Experimentally, the 2 MHz frequency offset between pump and probe beams shifts the Bennett hole only 1 MHz off the top of the 1 GHz-wide Doppler profile. In this situation, when the Bennett hole is at or near the top of the Doppler profile, equal numbers of atoms are knocked into the hole from both sides. As a result, the VCC signal is expected to be symmetric about the Doppler-free Lorentzian linecenter.

Mathematically, the effects of VCC can be calculated using a rate equation [122].

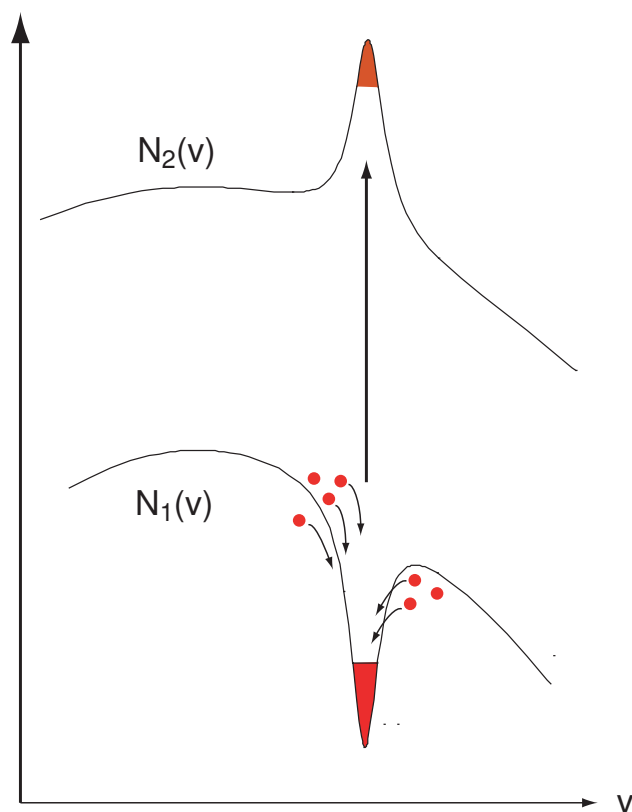


Figure 6.8: Depletion of a ground-state velocity class resonant with a laser leads to the formation of a Bennett hole [115]. Rethermalizing velocity-changing collisions (VCC) knock atoms into the hole, leading to an enhancement of the detected signal.

For a two-level system:

$$\begin{aligned}\frac{\partial n_a}{\partial t} &= -\gamma_a n_a(v) - [R_a(v) + R_b(v)][n_a(v) - n_b(v)] + c_a \\ \frac{\partial n_b}{\partial t} &= -\gamma_b n_b(v) + [R_a(v) + R_b(v)][n_a(v) - n_b(v)] + c_b\end{aligned}\quad (6.35)$$

where n_α is the population of the state $\alpha = \{a, b\}$, γ_α is the decay rate, and R_α is the transition rate. VCC are introduced through relaxation terms c_α

$$c_\alpha = \left. \frac{\partial n_\alpha}{\partial t} \right|_{relax} = \int n_\alpha(v') \Gamma(v, v') dv' - n_\alpha \int \Gamma(v, v') dv' \quad (6.36)$$

where the collision kernel $\Gamma(v, v')$ is the probability density per unit time for the velocity of an atom to change from v to v' . The first term on the right side of Eqn. 6.36 represents atoms that are knocked into the hole, while the second term represents the subsequent decay of these atoms.

For hard-sphere collisions, the kernel $\Gamma(v, v')$ is represented by a Gaussian function whose width is equal to the Doppler width. The experimental signal introduced by these collisions is negligible due to the small frequency range, relative to the Doppler width, over which the transitions are scanned.

For the more numerous “soft” collisions, where atoms probe the weakly attractive internuclear potential, there is no analytic form for $\Gamma(v, v')$. These collisions can only cause small changes in the velocity, thereby generating a signal that grows with decreasing detuning from the linecenter.

Given that the VCC lineshape cannot be described analytically, a Gaussian was used because it was observed to significantly improve the fit residuals (see Figs. 6.9 to 6.11). Although many groups in the past have also used a Gaussian [123, 124], Gibble and Gallagher have demonstrated that its flat top poorly estimates the highly-

peaked shape of experimental VCC signals [120]. Nevertheless, the Gaussian approximation should not introduce any systematic frequency shifts given the symmetry of the VCC signal about the Lorentzian linecenter.

6.5 Scan Patterns and Data Fitting

6.5.1 Scan Patterns

To minimize the effects of linear drift of the frequency reference from affecting the interval measurements, the three transitions were measured in an *ABCCBA* pattern. Previously, the stability of the ^3He reference was not high enough to implement these scan patterns. Instead, shorter scan patterns of the form *ABBA* were used. The experiment was repeated three times, once for each interval. In total, 6 measurements, 2 of each interval, were obtained from 12 linescans. With the *ABCCBA* scan patterns, the same 6 interval measurements are obtained from 6 linescans, thereby reducing the amount of data by a factor of 2. In addition, values for the P_1 splitting and the light-pressure shift δ_{LP} are obtained nearly concurrently with values for all three intervals and optical transition frequencies. As shown in Section 7.1, the measured values of δ_{LP} are more accurate, which significantly reduces their error contribution to the zero-pressure intercepts.

6.5.2 Frequency Patterns

Table 6.5.2 shows the parameters for the three patterns used to generate the frequencies at which the linescans are measured. Equally-spaced frequencies are chosen

Transition	Num. Pts.	Total Span	Peak Spacing	Dip Spacing
		(MHz)	(kHz)	(kHz)
$2^3S - 2^3P_0$	173	150	150	-
$2^3S - 2^3P_1$	294	300	200	-
$2^3S - 2^3P_2$	428	300	200	400

Table 6.1: Frequency pattern parameters for the three transitions. A total span of 150-300 MHz accurately measures the VCC Gaussian backgrounds while a frequency spacing of 150-200 kHz on the peaks is used to accurately measure the Lorentzian components.

over a 16 MHz span, or several helium linewidths, to properly measure the wings, sides, and peak of each Lorentzian. For accurate line-splitting, the 150-200 kHz spacing is much less than the 1.6 MHz helium linewidth. Farther from the peak centers, the effects of VCC are accurately measured by choosing a 2 MHz spacing and a total frequency span more than three times the 20 MHz width of the VCC Gaussian. For P_2 , a spacing of 400 kHz is used for the dips. With a lock-in time constant of 64 ms, a single frequency measurement, including the time needed to control the offset-lock, takes approximately 0.6 seconds. The total time to perform a complete *ABCCBA* sequence is a little over 1000 seconds. This duration is ideal since it coincides with the iodine frequency reference's timescale of lowest instability. This optimal use of the iodine reference's stability minimizes any coupling of frequency drift into the interval measurements.

6.5.3 Nonlinear Regression and Sample Linescans

Each P_0 linescan is fitted to the function

$$M^{(P_0)}(f) = A + \frac{B}{1 - \left(\frac{f-C}{D}\right)^2} + E \exp\left[-\frac{(f-C)^2}{2F^2}\right] \quad (6.37)$$

where $A-F$ are fit parameters that are adjusted to minimize χ^2 with the use of a Levenberg-Marquardt nonlinear regression algorithm [125]. Here, A is a constant offset, B is the Lorentzian amplitude, C is the center frequency of the Lorentzian and Gaussian, D is the Lorentzian linewidth, E is the Gaussian amplitude, and F is the Gaussian width. Using initial values for the fit parameters chosen from the data, the fitting algorithm typically converges in less than 30 iterations.

For P_1 linescans, a separate Lorentzian and Gaussian term is used for each peak, resulting in 9 fit parameters $A - I$

$$M^{(P_1)}(f) = A + \frac{B}{1 - \left(\frac{f-C}{D}\right)^2} + E \exp\left[-\frac{(f-C)^2}{2F^2}\right] + \frac{G}{1 - \left(\frac{f-H}{D}\right)^2} + I \exp\left[-\frac{(f-H)^2}{2F^2}\right] \quad (6.38)$$

Here, the widths of the Lorentzian peaks are constrained to be equal to the same value D . Similarly, the widths of the Gaussian peaks are constrained to be equal to the same value F .

For P_2 linescans, the linewidth of the center Lorentzian was observed to be wider than the linewidths of the $m = \pm 1$ peaks. This is due to the larger Clebsch-Gordan coefficient for the $m = 0$ transition, which leads to increased power broadening. With different linewidths for the center and outer peaks, the linewidths of the two crossover dips have a third value. Analogous to the fitting function functions for P_0 and P_1 ,

the resulting fitting function for P_2 has 20 fit parameters: 5 Lorentzian amplitudes, 5 Gaussian amplitudes, 5 center frequencies, 3 Lorentzian linewidths, 1 Gaussian width, and 1 constant offset.

Figs. 6.9-6.11 show sample linescans for the three transitions. Residuals with and without VCC Gaussian terms in the fitting functions are also shown. For all three scans, the cell pressure was 40 mtorr and the optical power of each laser beam was 100 μ W.

Prior to this work, error bars for each point in a scan were chosen to be the standard error of the measurements from the lock-in amplifier. However, for faster data-taking rates, correlations between these points were observed due to the response of the lock-in's low-pass filter. The undersized error bars due to these correlations resulted in fits with values of χ^2_ν , or χ^2 per degree of freedom, much greater than 1.

In order to derive more accurately sized error bars, the effects of different noise sources were studied by sampling the lock-in amplifier's output with the laser frequency fixed at points on the wings, sides, and top of an absorption profile. In the wings, laser amplitude noise dominates. The sides of the absorption profile are most sensitive to laser frequency noise, where the slope acts as a discriminator converting laser frequency jitter to amplitude noise. The top of the absorption profile, where signal size is largest, is most sensitive to fluctuations in pressure, optical power, and discharge power.

In all three cases, the scatter in the lock-in amplifier's output was similar, implying that laser amplitude noise dominates for all points in the scan. As a result, unweighted data fits were performed because the uncertainty for all points in the scan is equal.

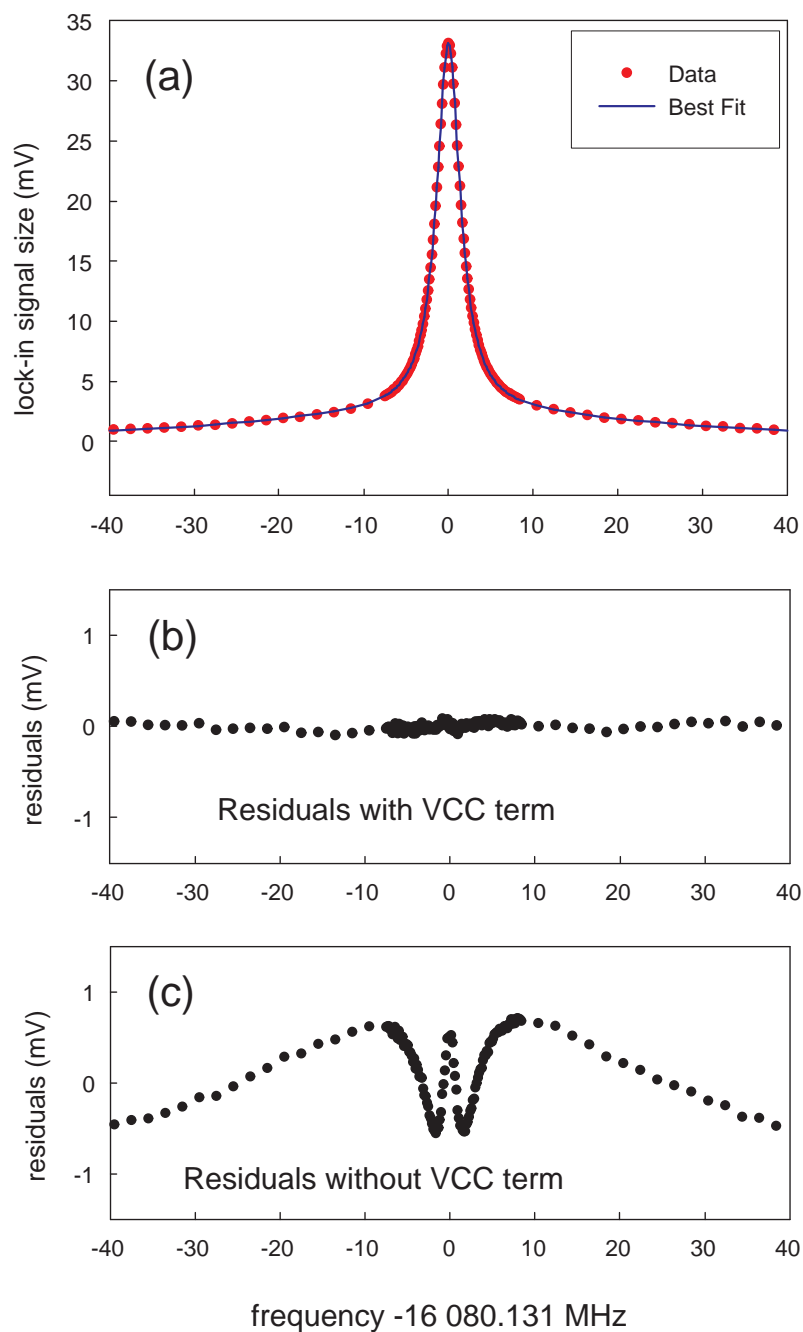


Figure 6.9: (a) Sample linescan of the $2^3S - 2^3P_0$ transition and best fit. (b) Residuals when a VCC Gaussian term is included in the fitting function. (c) A large Gaussian background appears in the residuals when the VCC Gaussian term is not included.

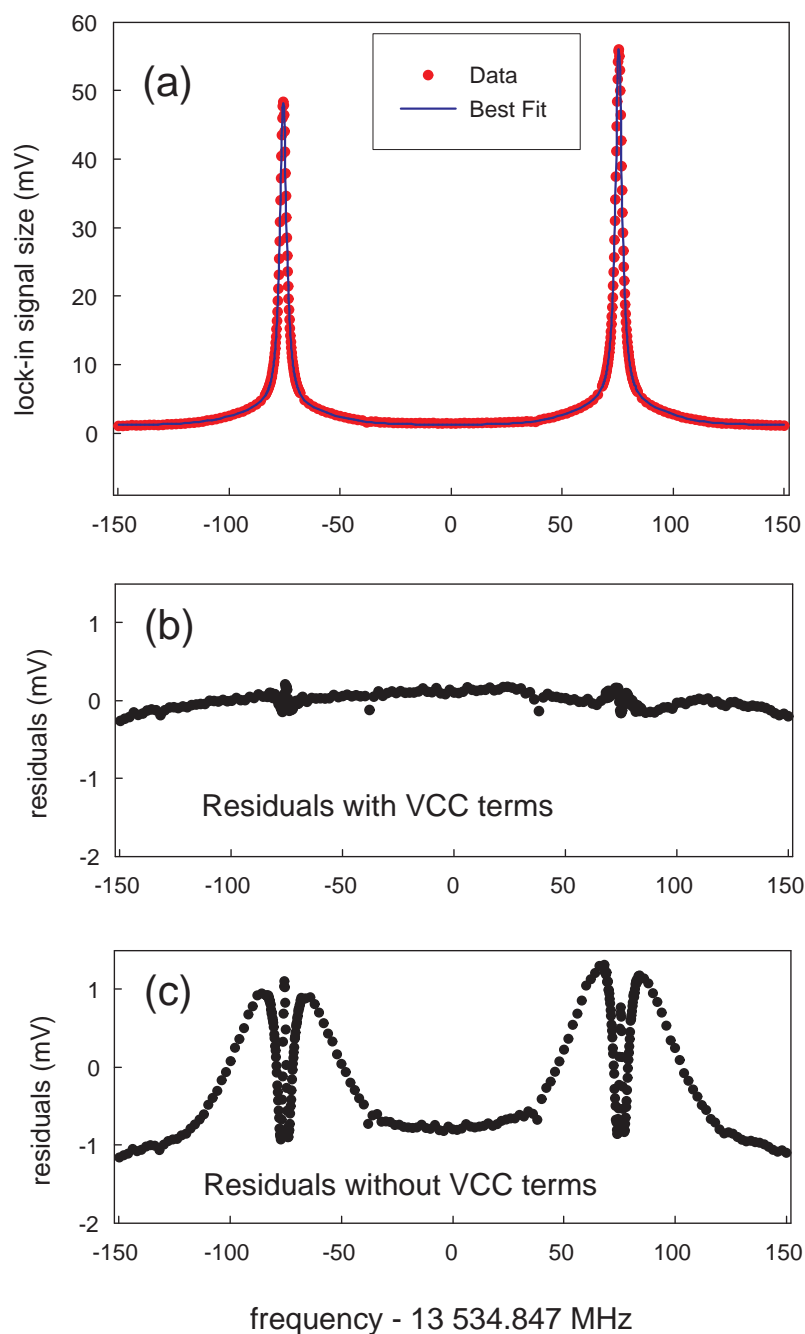


Figure 6.10: (a) Sample linescan of the $2^3S - 2^3P_1$ transition and best fit. (b) Residuals when VCC Gaussian terms are included in the fitting function. (c) Large Gaussian backgrounds appears in the residuals when VCC Gaussian terms are not included.

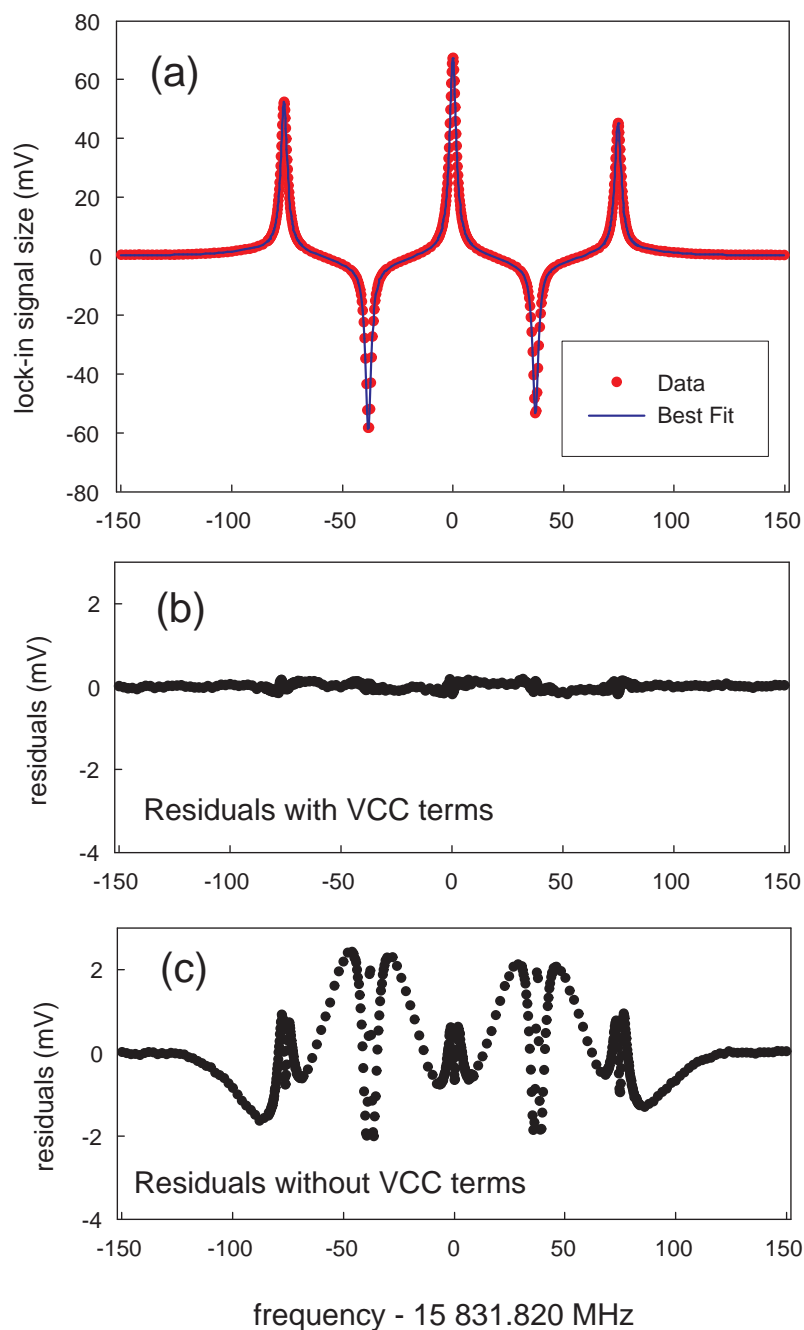


Figure 6.11: (a) Sample linescan of the $2^3S - 2^3P_2$ transition and best fit. (b) Residuals when VCC Gaussian terms are included in the fitting function. (c) Large Gaussian backgrounds appear in the residuals when VCC Gaussian terms are not included.

Switching to unweighted fits has also led to an unexpected 50% reduction in the scatter of the fitted linecenters.

Previously, the center frequencies of the VCC Gaussian terms in the fitting functions were allowed to change with respect to the Lorentzian center frequencies through the use of additional fit parameters. Although this resulted in slightly lower values of χ^2 , the regression always returned values for the Gaussian center frequencies that were consistently shifted from their corresponding Lorentzian frequencies by about 2 MHz. With this choice of fitting functions, fits converged only for P_0 and P_1 . In order for fits of P_2 linescans to converge, a fitting function without VCC Gaussian terms was used.

There is now evidence that these shifts of the VCC Gaussians were caused by a residual asymmetry in the linescans. The effects of this asymmetry are discussed in more detail in Chapter 8. As a result, the fitting functions were changed so that the center frequencies of the VCC Gaussian terms are fixed with respect to the centers of the Lorentzian peaks. This constraint not only agrees with the VCC model, but it allows fits of P_2 linescans to converge. As a result, all three transitions are now fit with VCC Gaussian terms included in the fitting functions.

6.5.4 Statistical Analysis

From each $ABCCBA$ scan sequence, two values are obtained for each of the three fine structure intervals and three optical transition frequencies. Over the course of several hours, this pattern is continuously repeated as many as 40 times for a fixed value of pressure, laser power, and discharge power. For each interval and optical

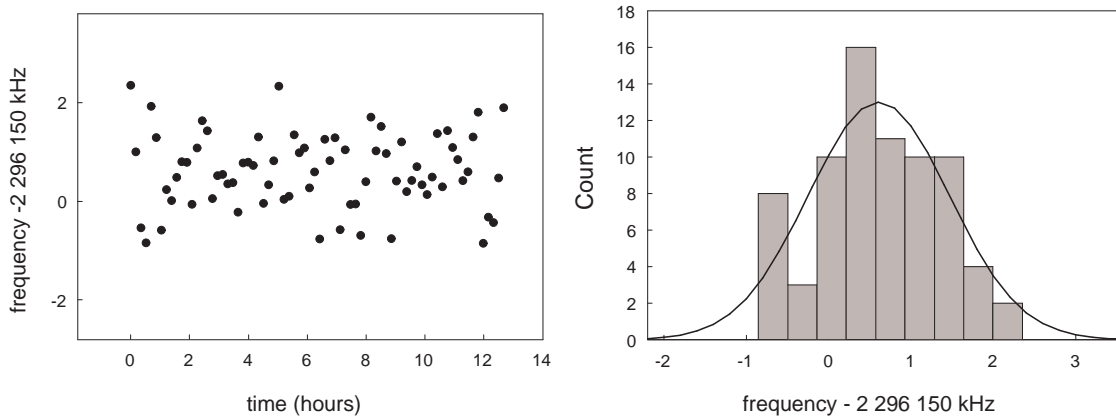


Figure 6.12: Measurements of the f_{12} fine structure interval. The cell pressure was 30 mtorr and the optical power of each laser beam was $100 \mu\text{W}$.

frequency, the unweighted mean of the measurements is used as the final value for the data run. The standard error of the mean is used as the uncertainty.

Measurements of the f_{12} interval and $2^3S - 2^3P_1$ optical transition frequency are shown in Figs. 6.12 and 6.13. Obtained from a single run, histograms of both data sets fit reasonably well to a Gaussian. For the f_{12} interval, the standard error of the mean is 88 Hz, demonstrating that sub-100 Hz measurements can be obtained in less than one day. For the optical frequency, the slight downward trend is due to drift in the Rb standard used to measure the optical frequency of the CSDL. Even with this drift, sub-kHz measurements are obtainable with a few hours of averaging.

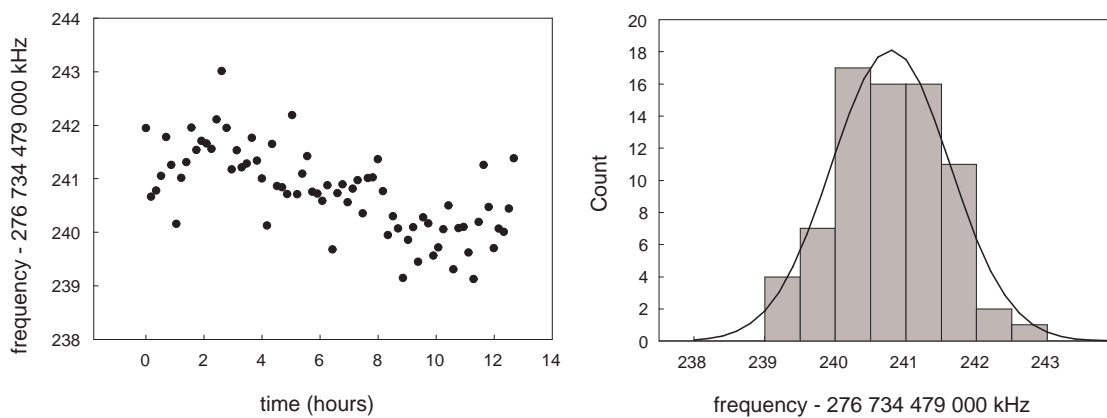


Figure 6.13: Measurements of the $2^3S - 2^3P_1$ transition. The cell pressure was 30 mtorr and the optical power of each laser beam was $100 \mu\text{W}$.

Chapter 7

Well-Understood Systematic Effects

Presented in this chapter are measurements of four systematic effects whose behavior is well-understood: light-pressure shifts, linear pressure shifts, discharge power shifts, and laser polarization shifts. Due to the increased resolution introduced by the iodine-stabilized frequency comb and other recent improvements to our system, the first three of these systematics were studied at a higher level of precision than what was previously attainable [13, 113]. For the first measurement of laser polarization shifts, no observed shifts at the level of 100 Hz agrees with expectations.

None of these systematics are the dominant error contributors to measurements of either the fine structure intervals or optical transition frequencies. For the fine structure intervals, all of these systematics have error contributions of 200 Hz or less. For measurements of the optical transition frequencies, correlated shifts due to the calibration of the Rb standard to GPS (see Section 4.3.4) and drift in the laser beam

alignment (see Section 8.1.4) limit the precision at which these systematics can be studied. Nevertheless, none of these systematics contribute uncertainties greater than 600 Hz.

7.1 Light-Pressure Shifts

Measurements of the f_{01} and f_{02} intervals, as well as all three optical transition frequencies, are shifted by the effects of laser light pressure (see Section 6.2). Corrections for this shift are obtained from measurements of the pressure-dependent difference $\Delta(p)$ between the $m = 0$ peak frequency and the average of the $m = \pm 1$ peak frequencies of P_2 linescans [13]. Values of the light-pressure shift $\delta_{LP}(p)$ are obtained from $\Delta(p)$ according to

$$\delta_{LP}(p) = \Delta(p) + Q_{2,0} - Q_{2,1}. \quad (7.1)$$

Averaging the $m = \pm 1$ peak frequencies cancels the linear Zeeman splitting, leaving the higher order Zeeman corrections $Q_{J,|m|}$ (see Section 6.3).

Fig. 7.1 shows histograms of δ_{LP} measured at (a) 30 mtorr, and (b) 15 mtorr. Each data set is fit to a Gaussian function; values for χ^2_ν of 1.4 and 0.4 indicate reasonable fits. At 30 mtorr, the standard deviation of 680 Hz is in agreement with the fitted Gaussian width of 628(72) Hz. At 15 mtorr, the standard deviation of 1.8 kHz agrees with the fitted Gaussian width of 2.0(2) kHz. The standard errors are 80 Hz and 228 Hz, respectively.

Fig. 7.2 shows plots of $\delta_{LP}(p)$ at two different values of the external magnetic field. For both data sets, δ_{LP} increases with decreasing pressure because of the increasing

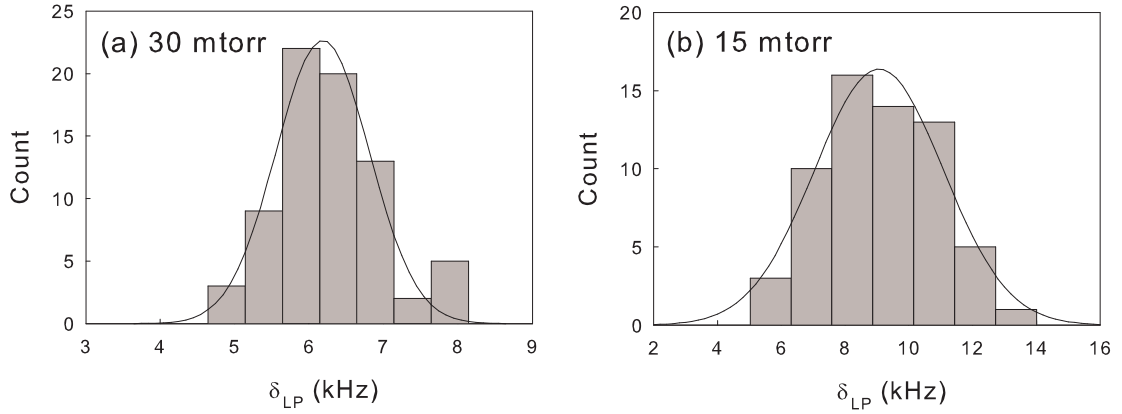


Figure 7.1: Histogram of measured values of δ_{LP} at (a) 30 mtorr, and (b) 15 mtorr. Each histogram fits well to a Gaussian function (solid line). Here, the optical power of each laser beam was $100 \mu\text{W}$, the discharge drive power was 4.5 Watts, and the external magnetic field was 108 Gauss.

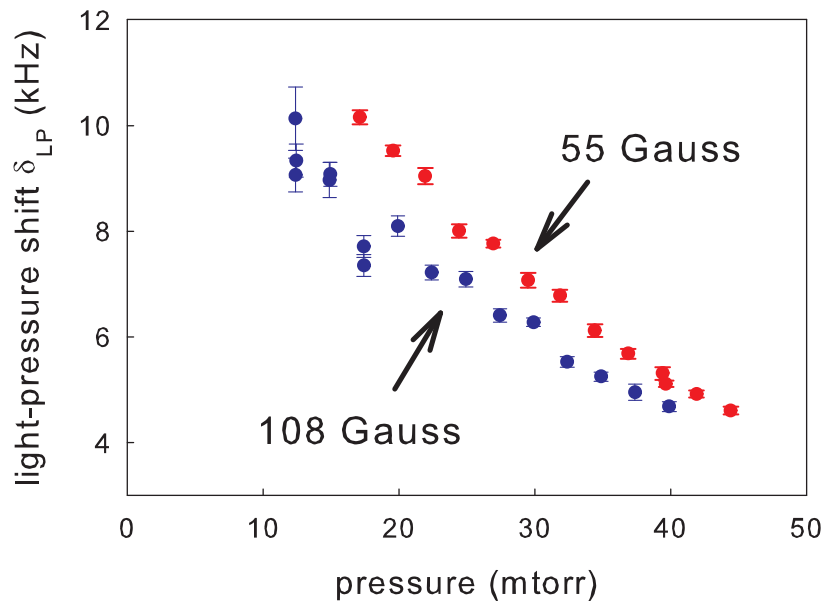


Figure 7.2: Measured values of the light-pressure shift $\delta_{LP}(p)$, obtained by measuring the difference $\Delta(p)$ between the $m = 0$ peak frequency and the average of the $m = \pm 1$ peak frequencies of P_2 linescans. The data has been corrected for nonlinear Zeeman shifts.

mean time between collisions. The data varies smoothly with the exception of two outliers at 17 mtorr in the data set at 108 Gauss. The slightly larger values obtained at 55 Gauss may be related to the $m = \pm 1$ peak imbalance discussed in Section 8.3.

The improved frequency stability obtained with the iodine reference allows us to measure all three optical transitions in an *ABCCBA* scan pattern (see Section 6.5.1), which in turn has significantly reduced the uncertainty of δ_{LP} . Previously, when frequency stability was derived from the ^3He reference, pairs of transitions were measured using an *ABBA* scan pattern [13]. Values of δ_{LP} were obtained from data runs of the f_{12} and f_{02} intervals. Discrepancies between values of δ_{LP} measured from data runs at the same pressure, but taken at different times over the course of several months, resulted in histograms of δ_{LP} that were not normally distributed [113]. The effect was most pronounced for lower cell pressures. As a result, for several values of δ_{LP} , the error was chosen to be the standard deviation of the measurements rather than the much smaller standard error. For the zero-pressure intercepts of the f_{01} and f_{02} intervals, the resulting error contribution due to δ_{LP} was between 540 and 650 Hz.

With the iodine reference and the *ABCCBA* scan sequence, values for δ_{LP} are obtained nearly concurrently with values for all three intervals and optical transition frequencies. This minimizes the impact of drift, resulting in more accurate values of δ_{LP} . As shown in Fig. 7.1, values of δ_{LP} are statistics limited, even at low pressures. As a result, the standard error is now used for the uncertainty of δ_{LP} . The corresponding error contribution to the zero-pressure intercepts of the f_{01} and f_{02} intervals (see Section 7.2) has been reduced by a factor of 8 to approximately 80 Hz.

7.2 Linear Pressure Shifts

In a dilute gas, phase-perturbing collisions between atoms in the cell introduce frequency shifts that scale linearly with gas pressure [115]. These shifts are due primarily to collisions with ground-state helium atoms since only 1 in 10^6 atoms is excited to the metastable state. To remove the effects of these collisions, data was measured as a function of cell pressure and extrapolated to zero pressure. This section describes the pressure extrapolations. Uncertainties in the zero-pressure intercepts as low as 120 Hz demonstrate the very high resolutions achieved.

7.2.1 Correcting for Light-Pressure and Zeeman Shifts

Interval frequencies f_{ij} for the $2^3P_i - 2^3P_j$ interval are determined from the average of the fitted center frequencies \bar{f}_i of the P_i linescans by [13]

$$f_{12}(p) = a_{12}p + \bar{f}_1 - \bar{f}_2 + Q_{1,1} - Q_{2,1} \quad (7.2)$$

$$f_{01}(p) = a_{01}p + \bar{f}_0 - \bar{f}_1 + Q_{0,0} - Q_{1,1} + \frac{1}{2}\delta_{LP} \quad (7.3)$$

$$f_{02}(p) = a_{02}p + \bar{f}_0 - \bar{f}_2 + Q_{0,0} - Q_{2,1} + \frac{1}{2}\delta_{LP} \quad (7.4)$$

where a_{ij} are linear pressure shifts extracted from linear extrapolations, p is the cell pressure, and \bar{f}_1 and \bar{f}_2 are the averages of the $m = \pm 1$ peak frequencies of their respective linescans. Averaging the $m = \pm 1$ peak frequencies cancels the linear Zeeman splitting, leaving the higher-order Zeeman corrections $Q_{j,|m|}$ (see Section 6.3). For f_{01} and f_{02} , a light-pressure correction $\delta_{LP}/2$ is included (see Section 7.1) [13].

For the optical frequencies f_i of the $2^3S - 2^3P_i$ transitions, the relationships are

$$f_0(p) = a_0p + \bar{f}_0 + Q_{0,0} + \frac{3}{2}\delta_{LP} + f_{CSDL} \quad (7.5)$$

$$f_1(p) = a_1p + \bar{f}_1 + Q_{1,1} + 2\delta_{LP} + f_{CSDL} \quad (7.6)$$

$$f_2(p) = a_2p + \bar{f}_2 + Q_{2,1} + 2\delta_{LP} + f_{CSDL} \quad (7.7)$$

where the different coefficients for the light-pressure correction δ_{LP} reflect different mean numbers of scattered photons (see Section 6.2). The optical frequency f_{CSDL} of the comb-stabilized diode laser is obtained from the measured comb repetition rate and the known PLL frequencies (see Chapter 4).

At given values of pressure, scans of the three $2^3S - 2^3P_j$ transitions were taken in an *ABCCBA* sequence, allowing for all three intervals f_{ij} and optical transition frequencies f_i to be obtained from the same data set. This scan sequence also allowed for values of the P_1 peak splitting, used to compute $Q_{j,|m|}$, and δ_{LP} to be measured nearly concurrently with the intervals and optical frequencies.

7.2.2 Assigning Error Bars

For each data point, the standard deviation is computed from a finite number of frequency measurements. Assuming the data is statistics-limited, the computed standard deviation determines the true standard deviation with an accuracy that improves with the sample size. To circumvent the small statistics at each pressure and provide improved estimates of the uncertainties, the measured standard deviations were plotted as a function of pressure and fit to a smooth line. From the best-fit values of the standard deviations, standard errors were computed by dividing by \sqrt{N} , where N is the sample size for each data set. These best-fit standard errors were used as the

error bars for the averages of the fitted frequencies. This procedure was not applied to error bars for the Zeeman corrections and light-pressure shifts because their error contributions to the corrected frequencies f_{ij} and f_i are negligible.

Fig. 7.4 shows the measured standard deviations and best-fit lines at 55 Gauss. The standard deviations $\sigma(p)$ are fit to the function $\sigma(p) = a + b/p + c/p^2$, where p is pressure, and a , b , and c are fit parameters.

To determine the effects on the zero-pressure intercepts of using best-fit standard errors instead of measured standard errors, the linear pressure extrapolations were performed using each each type of standard error as the uncertainties for the pressure data. For the fine structure intervals, the zero-pressure intercepts differed by as much as 65 Hz. This shift, which is significant compared to the uncertainty in the intercepts of 120 to 190 Hz, is due primarily to one data point at 40 mtorr whose measured standard deviation is half its best-fit value. This point is the average of only 14 frequencies, a very small sample size that makes the measured standard deviation a poor estimator of the true standard deviation. With the error bars computed from the measured standard error, this point was a outlier from the best-fit line between 2.5 and 4.5 standard deviations. Switching to best-fit standard errors reduced the discrepancy to 1.5 standard deviations and reduced χ^2 between 40% and 50%.

For the optical transition frequencies, the 300 Hz systematic uncertainty in the GPS calibration (see Section 4.3.4) is much larger than the statistical uncertainties. As a result, the switch from measured standard errors to best-fit standard errors negligibly changed the error bars. The zero-pressure intercepts shifted by less than 14 Hz.

Fig. 7.3 shows the measured standard deviations and best-fit lines at 108 Gauss. Comparing linear extrapolations that use the measured standard errors and the best-fit standard errors, zero-pressure intercepts shift by less than 10 Hz for all three intervals and optical transition frequencies.

7.2.3 Measurements of Linear Pressure Shifts

For a set of pressures $\{p_k\}$, the data sets $\{p_k, f_{ij}(p_k)\}$ and $\{p_k, f_i(p_k)\}$ are linearly extrapolated to zero pressure. Fig. 7.5 shows data measured with an external magnetic field of 55 Gauss. For the optical transitions (d-f), two data points were rejected. The first, at 40 mtorr, was taken almost two months before the other points. Due to drift in the optical mounts, we cannot confirm that the alignment of the laser beams remained unchanged over this period of time. As shown in the next chapter, a change in beam alignment can shift the measured optical frequencies by several kHz. However, these shifts only affect measurements of the fine structure intervals at the 200 Hz level, so the point was included for extrapolations of the fine structure intervals. The second data point, measured at a pressure of 30 mtorr, was an outlier by almost 9 standard deviations. The cause of this shift is unknown. However, the fact that all three optical frequencies were shifted identically and that the interval frequencies were not outliers suggest that either beam misalignment or the Rb standard may be the cause. The point was included for extrapolations of the fine structure intervals.

Fig. 7.6 shows frequency measurements at 108 Gauss. Two data points at 17 mtorr were removed because values of δ_{LP} obtained from them were outliers (see Fig. 7.2). In addition, the optical transition frequencies for three other data points

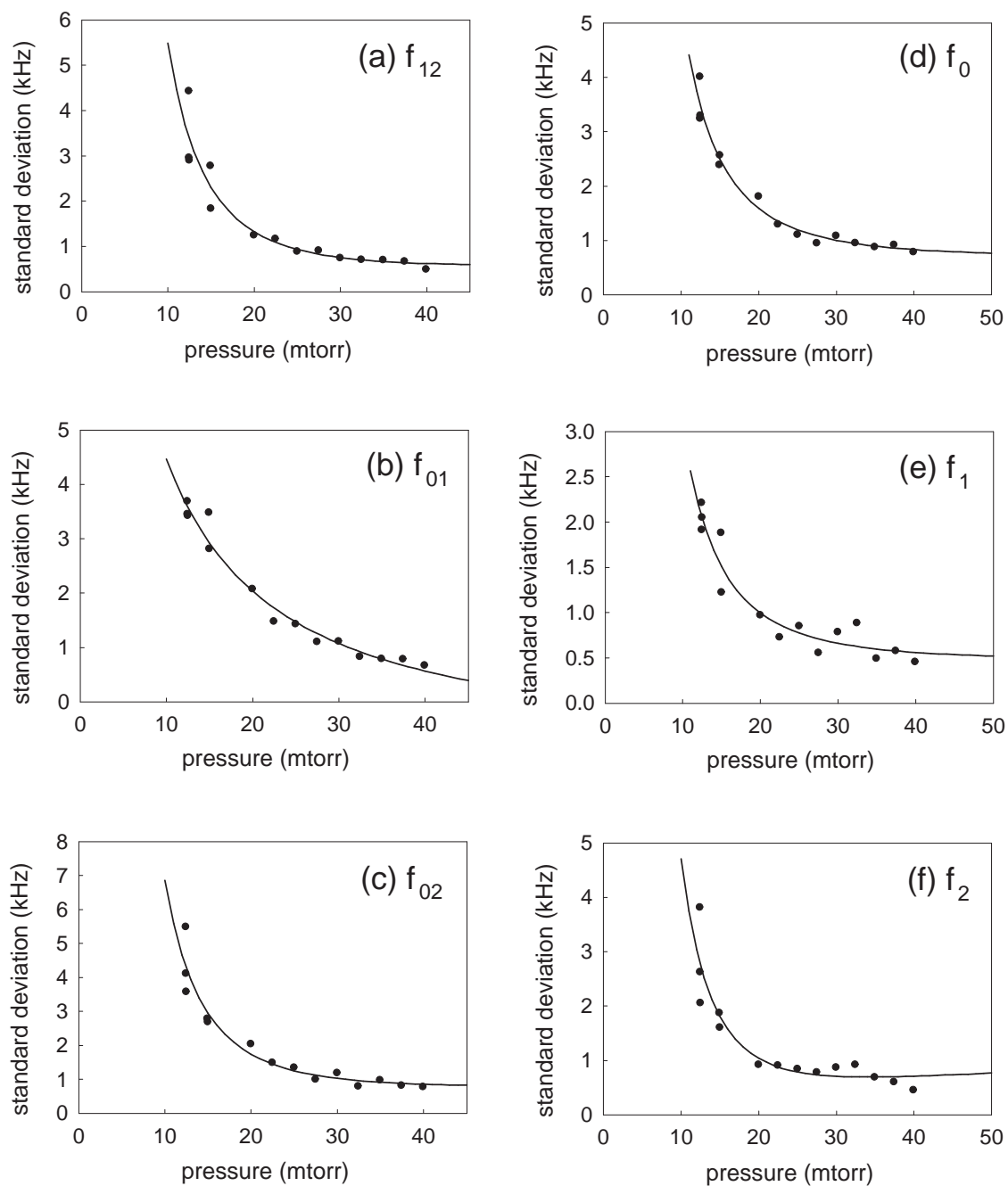


Figure 7.3: Standard deviation versus pressure at 108 Gauss. The solid lines are best-fits.

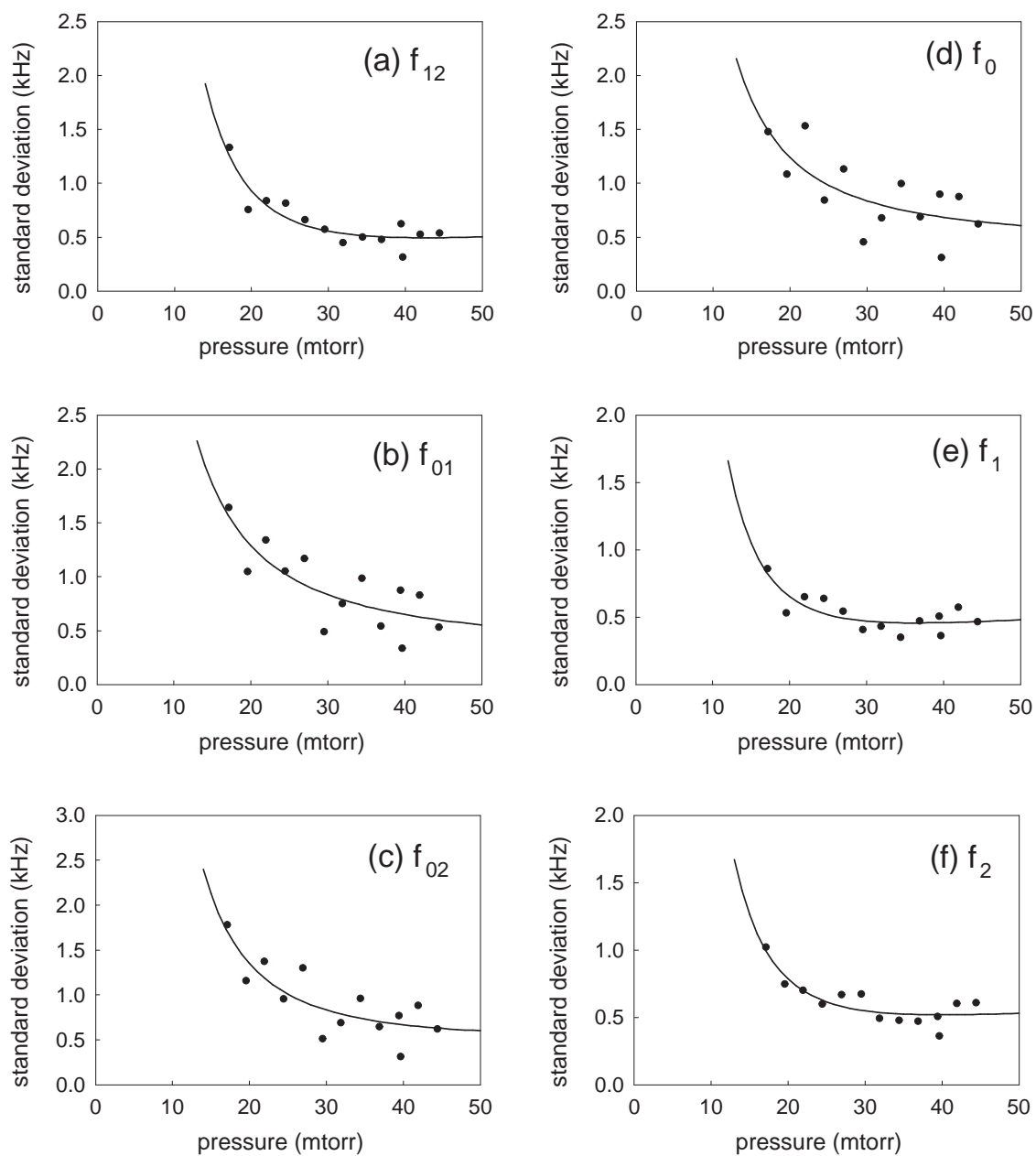


Figure 7.4: Standard deviation versus pressure at 55 Gauss. The solid lines are best-fits.

	intercept (kHz)	slope (kHz/mtorr)	χ_ν^2
$2^3P_1 - 2^3P_2$			
55 Gauss	2 291 174.61(12)	0.0293(34)	0.63
108 Gauss	2 291 174.62(18)	0.0317(57)	0.28
$2^3P_0 - 2^3P_1$			
55 Gauss	29 616 952.02(18)	0.0417(49)	1.26
108 Gauss	29 616 951.71(24)	0.0484(72)	1.01
$2^3P_0 - 2^3P_2$			
55 Gauss	31 908 126.61(19)	0.0713(51)	1.74
108 Gauss	31 908 126.41(25)	0.0784(80)	1.46

Table 7.1: Results of linear extrapolations of fine structure intervals to zero pressure.

were rejected. Measured at cell pressures of 12 and 15 mtorr, these points were shifted by several kHz due to a realignment of the laser beams that occurred just before they were measured (see Section 4.3.4). These points were included for extrapolations of the fine structure intervals.

The results of linear extrapolations for the fine structure intervals appear in Table 7.1. Here, values of χ_ν^2 close to 1 indicate good fits. For both the intercepts and slopes, values obtained with two different values of the magnetic field are in statistical agreement with each other.

The results of linear extrapolations for the optical transitions appear in Table 7.2. Here, values of χ_ν^2 greater than 1 indicate error bars that are slightly too small.

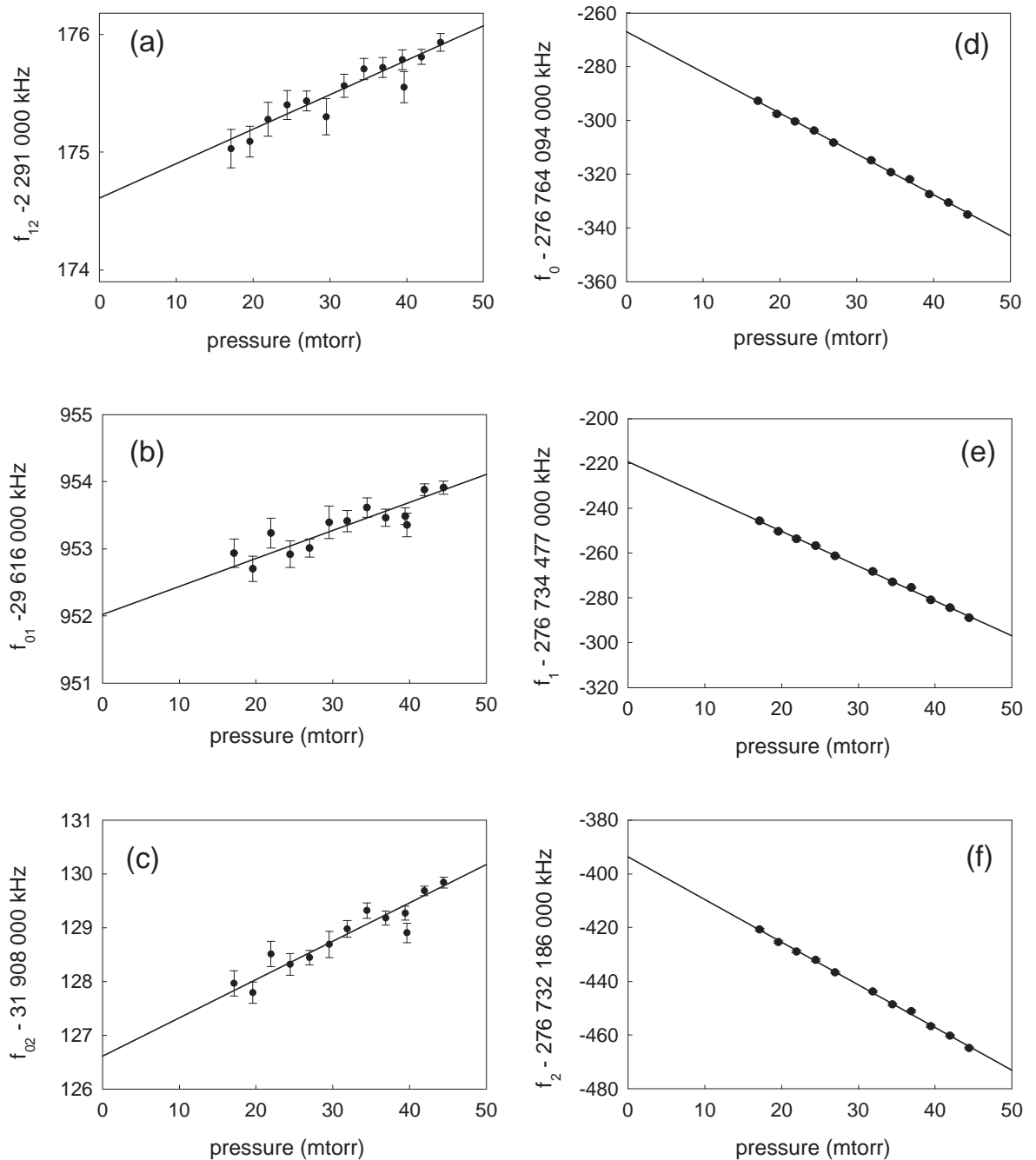


Figure 7.5: Linear extrapolations to zero pressure at 55 Gauss. The power of the pump and probe beams was $100\ \mu\text{W}$ each, and the power of the RF discharge was 1 Watt.

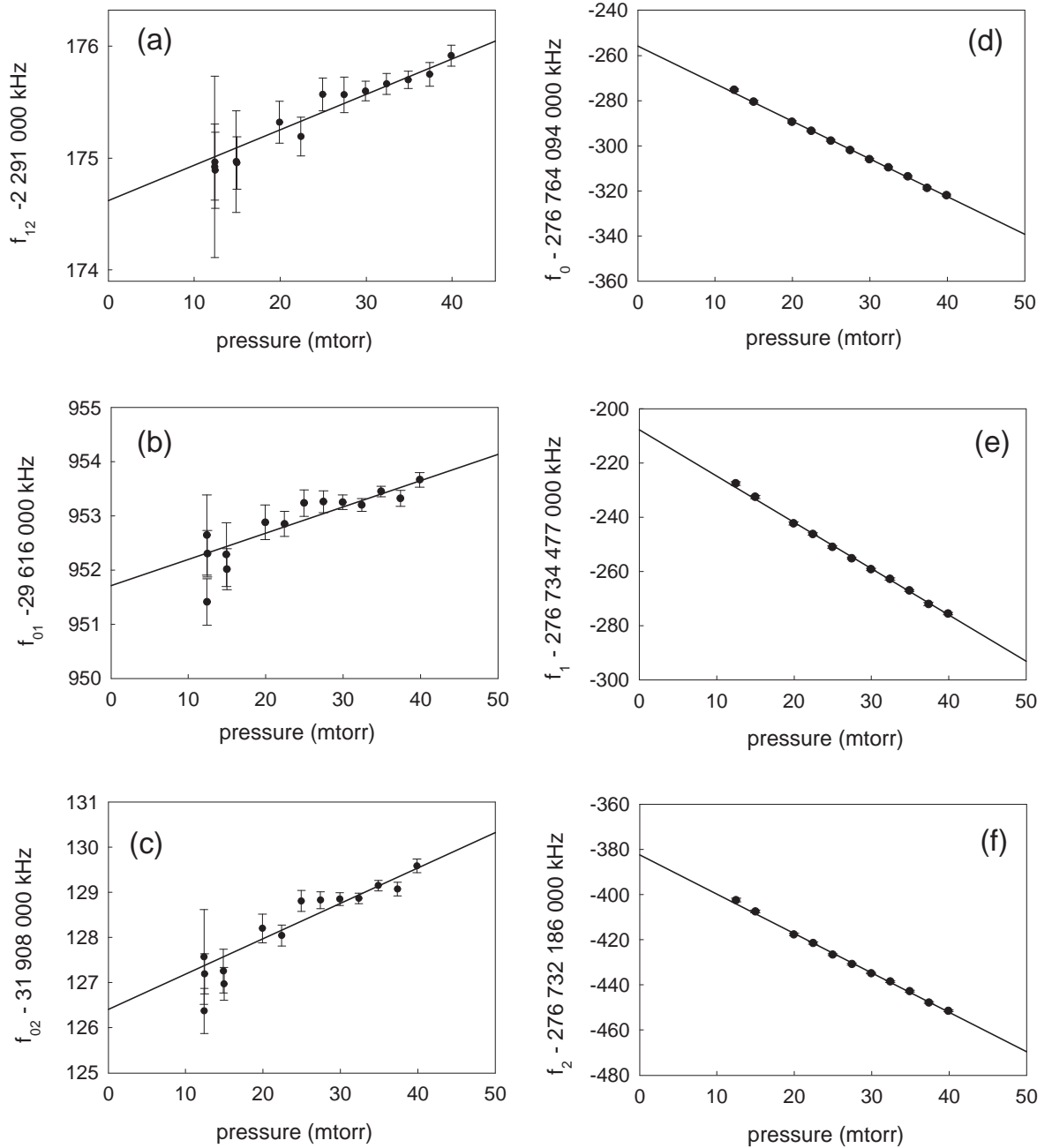


Figure 7.6: Linear extrapolations to zero pressure at 108 Gauss. The power of the pump and probe beams was $100\ \mu\text{W}$ each, and the power of the RF discharge was 4.5 Watts.

	intercept (kHz)	slope (kHz/mtorr)	χ^2_ν
$2^3S - 2^3P_0$			
55 Gauss	276 764 093 732.98(49)	-1.518(14)	2.22
108 Gauss	276 764 093 744.12(50)	-1.666(17)	1.34
$2^3S - 2^3P_1$			
55 Gauss	276 734 476 780.81(44)	-1.556(13)	2.40
108 Gauss	276 734 476 792.32(53)	-1.713(18)	1.63
$2^3S - 2^3P_2$			
55 Gauss	276 732 185 606.26(46)	-1.587(14)	2.21
108 Gauss	276 732 185 617.65(54)	-1.743(18)	1.94

Table 7.2: Results of linear extrapolations of optical transition frequencies to zero pressure.

As shown in Section 8.4, the uncertainties used should be increased to account for uncontrolled beam alignment shifts induced by drift of the laser optics. Furthermore, for all three optical transitions, the intercepts obtained with two different values of the magnetic field disagree with each other by 11 kHz. This difference is attributed to different laser beam alignment techniques used for the two data sets. Large frequency shifts due to beam alignment and measurements of alignment accuracy are discussed in more detail in the next chapter.

7.3 RF Discharge Power Shifts

Three data sets were taken to search for systematic frequency shifts that depend on RF discharge drive power. For the first two data sets, both taken with a magnetic field of 55 Gauss, the cell pressures were 20 mtorr and 40 mtorr. The third data set was taken with an external magnetic field of 108 Gauss and cell pressure of 30 mtorr. Pump and probe laser powers were $100 \mu\text{W}$ for all three data sets. Data was taken at several values of the discharge drive power and linear extrapolated to zero power.

It is assumed that in the regime of weak discharge powers, shifts would scale linearly with discharge power. It is important, therefore, that the discharge power be low enough to avoid the E-H transition [126]. Indicating a switch from capacitive to inductive coupling of the RF power to the atoms, this transition appears as a nonlinear jump in the intensity of the discharge glow as the drive power is increased. The transition is hysteretic and the improved coupling of power to the atoms can increase the cell temperature by as much as 100°C . The resulting signal size increases by as much as two orders of magnitude.

Fig. 7.7 shows plots of the Lorentzian amplitude of the $2^3S-2^3P_0$ transition versus drive power at (a) $B=55$ Gauss and $p=20$ mtorr, (b) $B=55$ Gauss and $p=40$ mtorr, and (c) $B=108$ Gauss and $p=30$ mtorr. Here, signal size does not vary linearly with drive power. In Fig. 7.7b, the signal amplitude increases suddenly above 1.5 Watts, an effect that is attributed to the onset of the E-H transition. For this data set, only points below 1.5 Watts were used in the linear extrapolation.

Fig. 7.8 shows the data and best-fit lines for the data set at $B=55$ Gauss and $p=20$ mtorr. For the optical frequencies, one outlying point at 1.4 Watts, lying 4

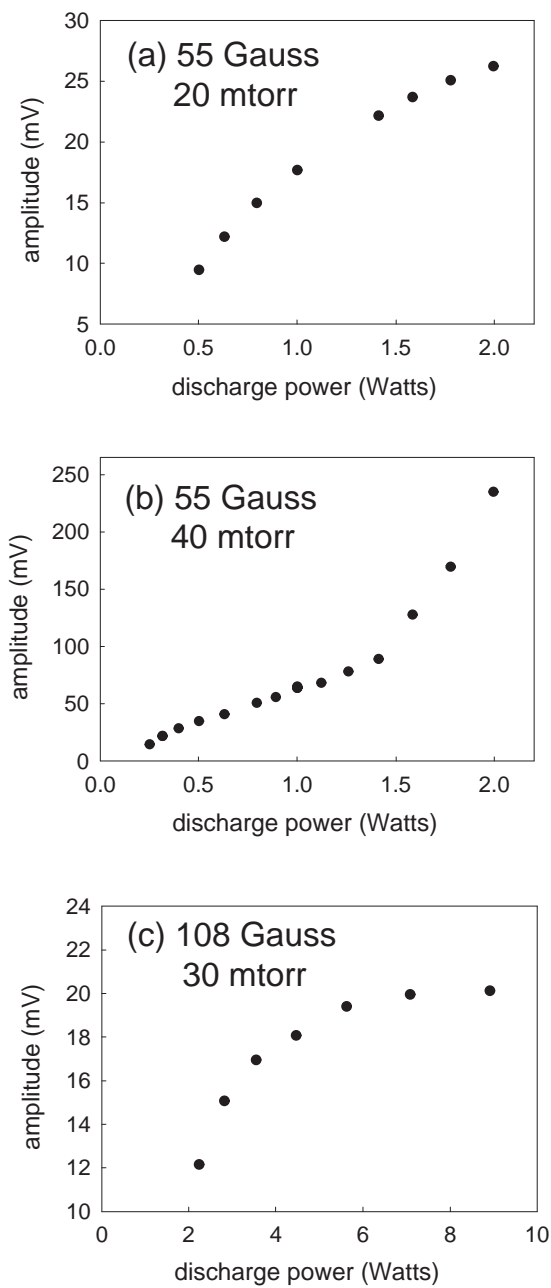


Figure 7.7: Lorentzian amplitudes of the $2^3S - 2^3P_0$ transition as a function of discharge power.

standard deviations below the best-fit line, was removed. It is not known for sure what caused this point to be an outlier. However, the fact that all three optical frequencies were shifted identically while the corresponding fine structure intervals were unshifted suggest that either beam misalignment (see Section 8.1.4) or the Rb standard may be the cause.

Results for the data set at $B=55$ Gauss and $p=40$ mtorr are shown in Fig. 7.9. For the optical frequencies, five data points were rejected. These data points were taken two months after the other data. It could not be confirmed that the laser beam alignment remained unchanged during this time. As shown in the next chapter, a change in beam alignment can shift the measured optical frequencies by several kHz. However, these shifts only affect measurements of the fine structure intervals at the 200 Hz level, so these points were included for extrapolations of the fine structure intervals. Results for the data set at $B=108$ Gauss are shown in Fig. 7.10. Here, no data points were rejected.

Results of the linear extrapolations to zero discharge power are shown in Table 7.3. For the data set at 55 Gauss and 20 mtorr, slopes for both the fine structure intervals and optical transition frequencies are statistically consistent with 0 to within 1 standard deviation. For a drive power of 1 Watt, the corresponding limits on a non-zero discharge-dependent frequency shift are 90 Hz, 130 Hz, and 130 Hz for the f_{12} , f_{01} , and f_{02} intervals, respectively. For the optical transitions, the limits are 240 Hz, 220 Hz, and 220 Hz for the $2^3S - 2^3P_0$, $2^3S - 2^3P_1$, and $2^3S - 2^3P_2$ transitions, respectively.

For the second data set at 55 Gauss and 40 mtorr, slopes for the f_{01} and f_{02}

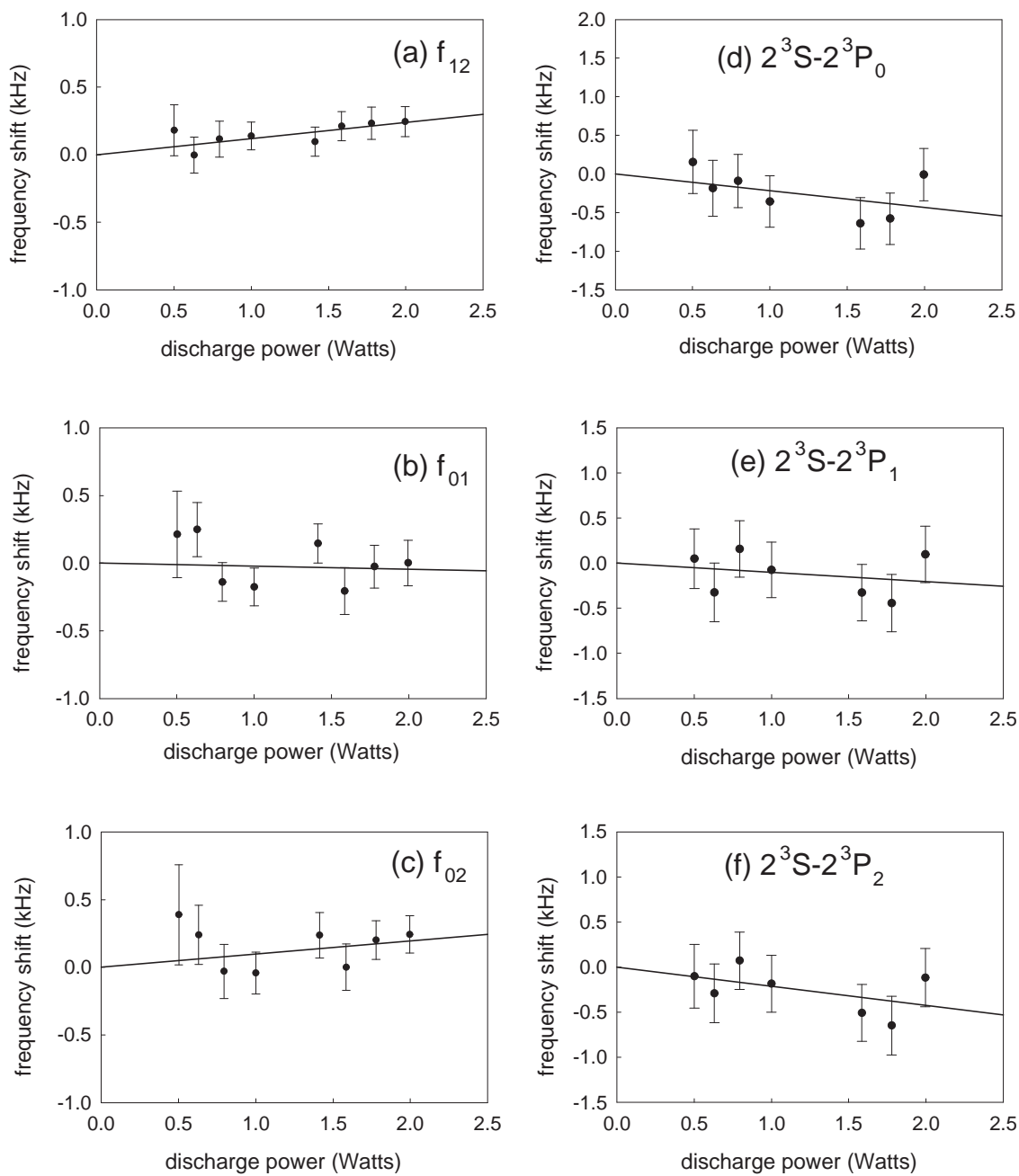


Figure 7.8: Linear extrapolations to zero discharge power for a magnetic field of 55 Gauss and cell pressure of 20 mtorr.

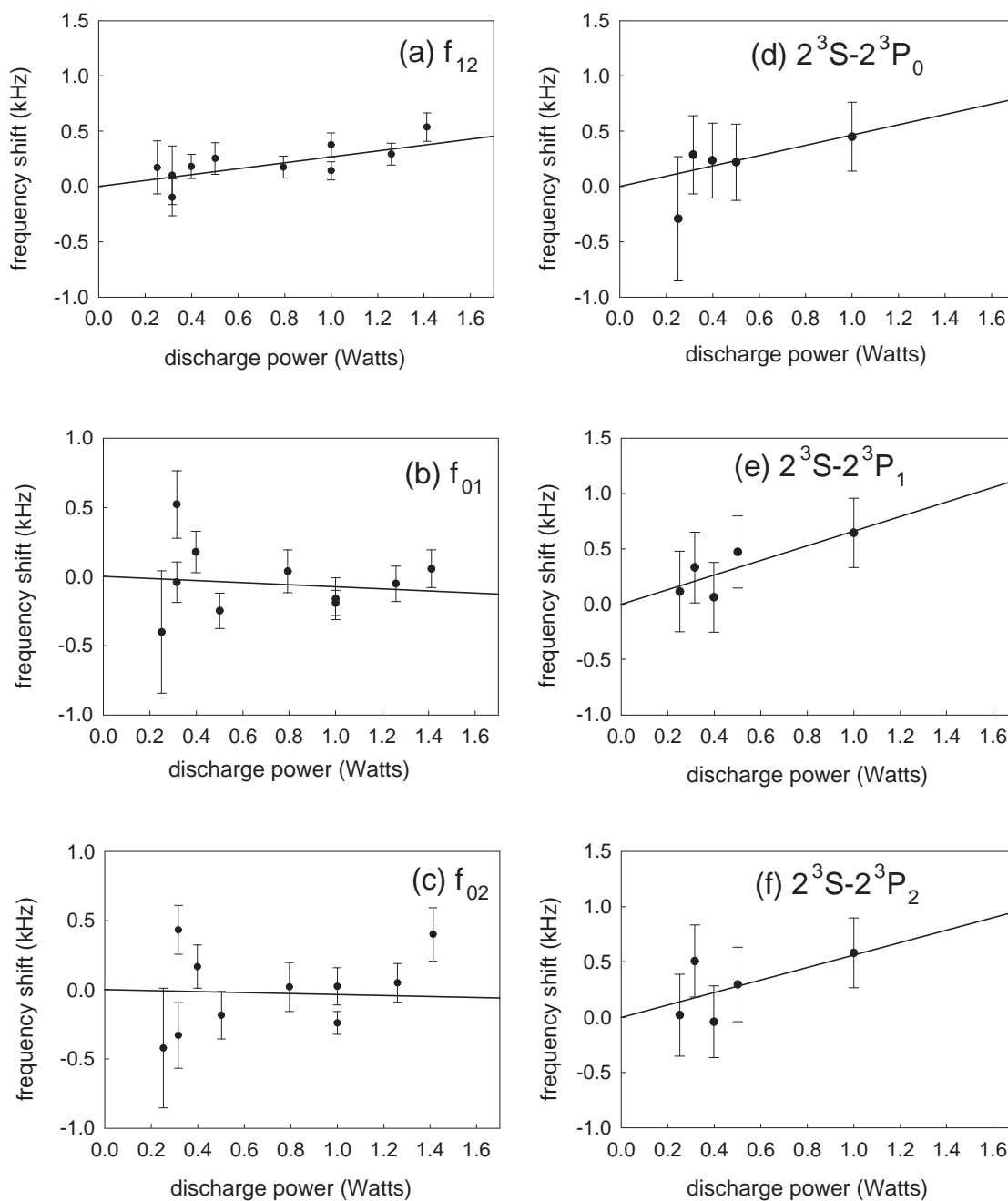


Figure 7.9: Linear extrapolations to zero discharge power for a magnetic field of 55 Gauss and cell pressure of 40 mtorr.

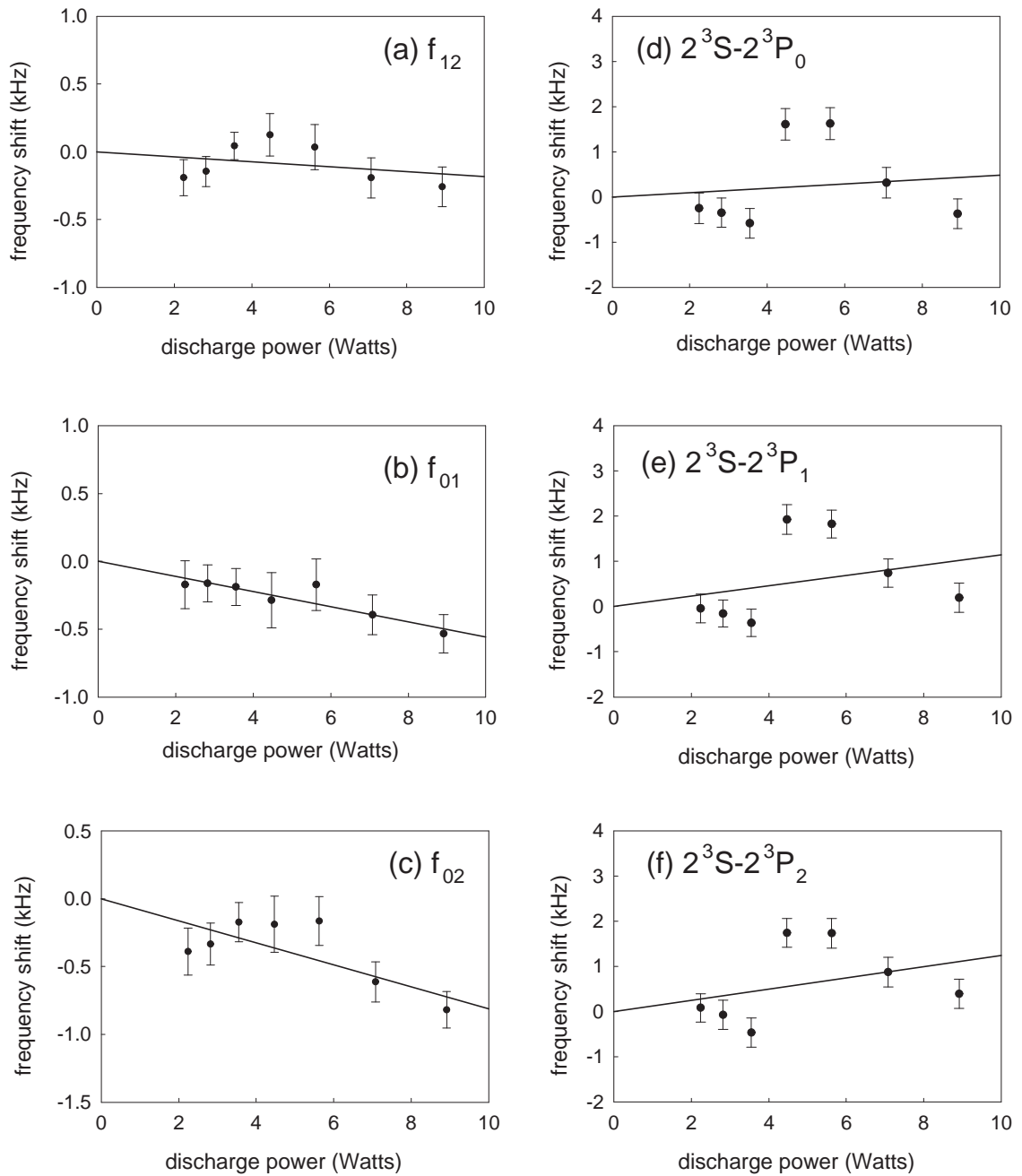


Figure 7.10: Linear extrapolations to zero discharge power for a magnetic field of 108 Gauss and cell pressure of 30 mtorr.

intervals are statistically consistent with 0 to within 1 standard deviation. For the f_{12} interval, a slope of 0.27(11) kHz/Watt is statistically inconsistent with 0 by 2.5 standard deviations. For a normal distribution, the probability of observing a discrepancy this large is only 1%. Although this small probability could be interpreted as evidence for a non-zero discharge shift, the inconsistency is due primarily to the highest discharge power point. As seen in Fig. 7.9a, the data point at 1.4 Watts is the highest frequency measured for the entire data set. With this data point removed, slopes of 0.18(12) kHz/Watt, -0.19(14) kHz/Watt, and -0.20(16) kHz/Watt disagree with zero by 1.5, 1.4, and 1.3 standard deviations. The largest discrepancy of 1.5 standard deviations corresponds to an observation probability of 13%. This probability is too large to confidently conclude that a non-zero shift has been observed. As a result, limits of 120 Hz, 140 Hz, and 160 Hz are obtained from this data set for the existence of a non-zero discharge shift.

The large impact of one data point at 1.4 Watts may be due to the onset of the E-H transition, which was observed in Fig. 7.7b to occur at 1.6 Watts. It is possible that for discharge powers close to the E-H transition, any discharge shift becomes nonlinear. This possibility stresses the importance of operating the discharge at low drive powers.

For optical frequencies measured at 55 Gauss and 40 mtorr, the three slopes are consistent with 0 to within 1.3 standard deviations. For a discharge drive power of 1 Watt, the resulting limits on a non-zero discharge shift are 570 Hz, 540 Hz, and 540 Hz for the $2^3S - 2^3P_0$, $2^3S - 2^3P_1$, and $2^3S - 2^3P_2$ transitions, respectively.

For the fine structure intervals at 108 Gauss, slopes for the f_{12} , f_{01} , and f_{02} in-

tervals disagree with 0 by 0.8, 2.2, and 3.2 standard deviations, respectively. Here, standard deviations much greater than 1 for two of the three intervals are due primarily to the data point at the highest discharge power. With this point removed from the extrapolations, slopes of 0.008(34) kHz/Watt, -0.044(38) kHz/Watt, and -0.46(39) kHz/Watt are consistent with 0 by 0.2, 1.2, and 1.2 standard deviations. For a drive power of 4.5 Watts, the corresponding limits on a non-zero discharge shift are 150 Hz, 170 Hz, and 180 Hz.

For the optical frequencies measured at 108 Gauss, the slopes are inconsistent with 0 by 0.9, 2.2, and 2.3 standard deviations. However, values of χ^2_ν between 8 and 10 indicate poor fits. As seen in Fig. 7.10d-f, the data fit poorly to straight lines because of large correlations between optical frequencies of different transitions. Largely absent from the interval data sets, these correlations are likely due to a change in the laser beam alignment (see Section 8.1.4) or the Rb standard. Although 300 Hz was added to the uncertainties of the optical frequencies to account for the accuracy of the Rb standard (see Section 4.3.4), this value is insufficient to account for frequency shifts due to drift in the laser optics. To obtain a limit on a non-zero discharge shift, the largest slope of 0.124 kHz/Watts is used. For a drive power of 4.5 Watts, a limit of 560 Hz is placed on all three transitions.

The largest limit obtained for each interval and optical transition is assigned as the uncertainty due to discharge power shifts. For the all three fine structure intervals, the uncertainty is 180 Hz. For all three optical transitions, the uncertainty is 570 Hz.

	55G, 20 mtorr		55G, 40 mtorr		108G, 30 mtorr	
	slope (kHz/W)	χ^2_ν	slope (kHz/W)	χ^2_ν	slope (kHz/W)	χ^2_ν
f_{12}	0.12(9)	0.22	0.27(11)	0.98	-0.018(23)	1.22
f_{01}	-0.02(13)	1.12	-0.07(11)	1.78	-0.056(25)	0.15
f_{02}	0.10(13)	0.66	-0.04(14)	2.95	-0.081(25)	1.29
$2^3S - 2^3P_0$	-0.22(24)	0.68	0.46(57)	0.24	0.048(56)	9.1
$2^3S - 2^3P_1$	-0.10(22)	0.64	0.66(54)	0.25	0.114(53)	10.0
$2^3S - 2^3P_2$	-0.21(22)	0.24	0.56(54)	0.60	0.124(55)	7.8

Table 7.3: Results of linear extrapolations of interval and optical transition frequencies to zero discharge power.

7.4 Polarization Shifts

As the polarization of the pump and probe laser beams is rotated away from the vertical direction of the external magnetic field, transitions between states with magnetic quantum numbers satisfying $\Delta m = \pm 1$ become allowed. The Zeeman shifts of these transitions and their corresponding crossover resonances are different than those for the $\Delta m = 0$ transitions [113]. Therefore, small rotations in the laser polarization angle introduce small peaks in the lineshapes that occur at different frequencies than the $\Delta m = 0$ peaks. Distortion to the lineshapes caused by these small $\Delta m = \pm 1$ peaks should negligibly affect fits to the much larger $\Delta m = 0$ peaks.

To test for a systematic dependency on laser polarization angle θ , data was taken at several values of θ . Fig. 7.11 shows plots of the fine structure intervals and light-pressure shift δ_{LP} as a function of θ . The angle $\theta = 0^\circ$ corresponds to polarization in the vertical direction, as determined using the polarizer alignment technique discussed in Chapter 5. The relative angle between the pump and probe polarizers was kept fixed. To account for the observed non-zero slope of δ_{LP} (Fig. 7.11d), all frequencies were corrected for light-pressure shifts and Zeeman shifts.

It was assumed that frequency shifts would scale as $\cos \theta$, a reasonable assumption given that the peak amplitudes depend sinusoidally on θ and that lineshapes for angles θ and $-\theta$ are expected to be the same. To lowest order in θ , this relationship is quadratic. Therefore, each data set was first fit to a quadratic function of the form $f(\theta) = a(\theta - b)^2 + c$, where a , b , and c are fit parameters. The center angles b returned by the fits are $0.7(8)^\circ$, $-6.9(150)^\circ$, and $-0.4(7)^\circ$ for the f_{12} , f_{01} , and f_{02} intervals, respectively. For f_{12} and f_{02} , the center angles are consistent with a laser

polarization aligned in the direction of the magnetic field to better than 1° . Although the center angle for f_{01} is consistent with 0° , the large error is likely due to the flatness of the data.

Having confirmed the polarizers were aligned in the direction of the magnetic field to within 1° , each data set was then fit to a quadratic function whose center angle b was fixed to equal 0° . The best fits appear as solid lines in Fig. 7.11. The best-fit parameters were used to estimate the frequency shifts introduced by a 1° change in the polarization angle. Shifts of 17(73) Hz, 1(102) Hz, and 16(94) Hz for the f_{12} , f_{01} , and f_{02} intervals, respectively, are consistent with 0 Hz to within 100 Hz.

Fig. 7.12 shows plots of the three $2^3S - 2^3P_J$ optical transition frequencies as a function of polarization angle. The data point at 0° was rejected because it was taken several weeks prior to the other points. It could not be confirmed that the laser beam alignment remained unchanged during this time. As shown in the next chapter, a change in beam alignment can shift the measured optical frequencies by several kHz. However, these shifts only affect measurements of the fine structure intervals at the 200 Hz level, so this point was included for extrapolations of the fine structure intervals.

Each data set in Fig. 7.12 was fit to a quadratic function with a center angle fixed at 0° . The best-fit parameters were used to estimate frequency shifts introduced by a 1° change in the polarization angle. Shifts of 3(249) Hz, 3(244) Hz, and 14(250) Hz for the $2^3S - 2^3P_0$, $2^3S - 2^3P_1$, and $2^3S - 2^3P_2$ transitions, respectively, are consistent with 0 Hz to within 250 Hz. This uncertainty is limited primarily by the 300 Hz GPS calibration error, which was the dominant error contribution to the optical

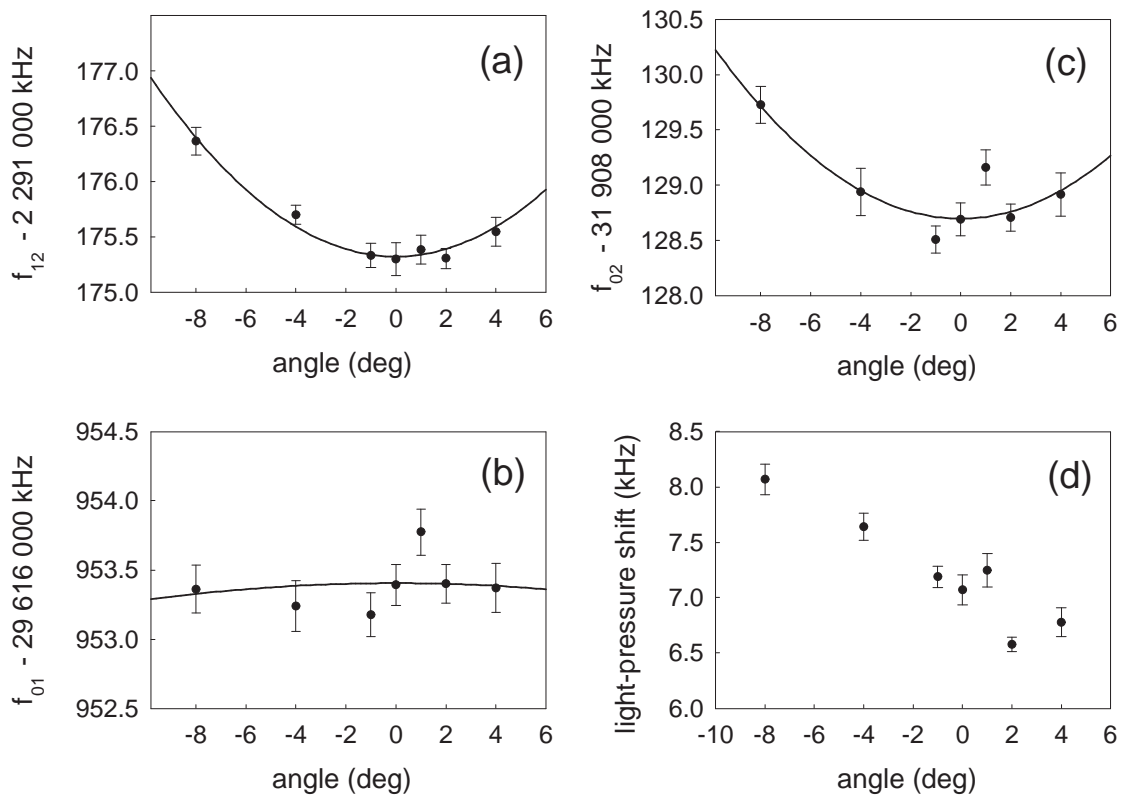


Figure 7.11: Frequency shifts as a function of pump and probe polarization angle for the fine structure intervals and light-pressure shift δ_{LP} . The cell pressure was 30 mtorr, the optical power of each laser beam was $100\ \mu\text{W}$, the discharge drive power was 1 Watt, and the external magnetic field was 55 Gauss.

frequencies.

7.5 Conclusions

Statistics-limited uncertainties of less than 200 Hz for the zero-pressure intercepts of the fine structure intervals demonstrate the very high stability and signal-to-noise ratios obtained experimentally. Compared to the uncertainties of these intercepts, corrections for light-pressure shifts and nonlinear Zeeman shifts contribute negligible

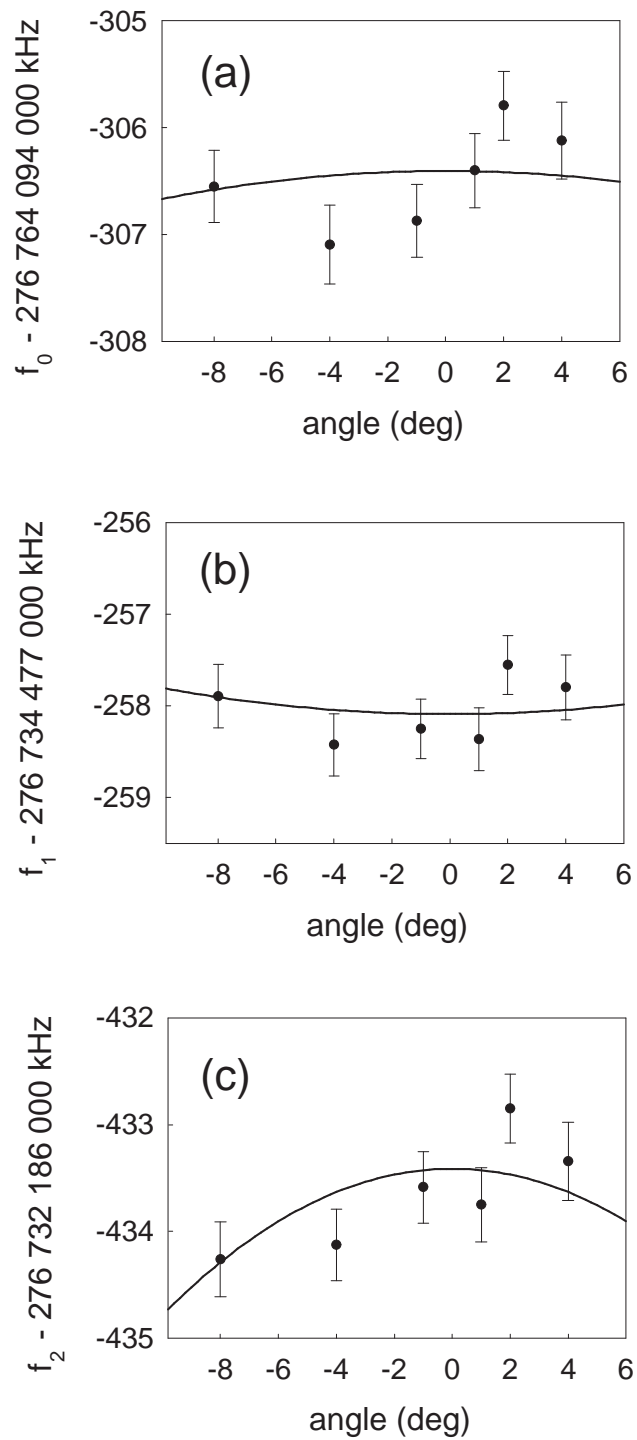


Figure 7.12: Frequency shifts as a function of pump and probe polarization angle for the $2^3S - 2^3P_J$ optical transitions.

error. In addition, no observation of non-zero discharge power shifts or laser polarization shifts at the level of 100 Hz to 200 Hz is encouraging for improved future measurements of the fine structure intervals.

Correlated shifts introduced by the Rb standard and drift in the beam alignment limited the precision at which these systematics could be studied for the optical transition frequencies. As a result, uncertainties no smaller than 250 Hz could be assigned to any systematic. Although these errors are larger than those for the fine structure intervals, none of the systematics studied in this chapter should prevent a measurement of the optical transition frequencies with sub-kHz accuracy.

Chapter 8

Systematics That Require Further Study

Increased frequency stability, improved signal-to-noise ratio, narrower laser linewidth, and the ability to accurately measure optical frequencies were important tools for searching for new systematic shifts that would arise for helium spectroscopy at a higher level of precision. Three new effects discovered during the experiment are discussed in this chapter. In addition, these new systematics have changed our understanding of a fourth systematic, optical power shifts, that had been previously studied.

The first new systematic effect is a residual Doppler shift that arises from misalignment of the pump and probe laser beams. Usually, a beam misalignment results in only a residual Doppler broadening. However, in a discharge, where the atomic velocities are not thermally distributed, beam misalignment results in Doppler shifts as well. From measurements of the accuracy of the beam alignment, error contributions

of several kHz are assigned to the optical transition frequencies. However, these shifts affect the optical transitions identically, leaving measurements of the fine structure interval significantly less affected.

The second new systematic effect is an observed lineshape asymmetry that may shift the center frequencies of the fitted Lorentzians by up to 20 kHz. Self-focusing of the laser beams by the helium gas can qualitatively predict the observed results, but underestimates the size of the shifts by several orders of magnitude. By taking the difference between center frequencies obtained from fits with and without dispersive lineshapes included in the fitting functions, the pressure and optical power dependency of the asymmetry can be studied.

The third new systematic effect is an imbalance in the amplitudes of $m = \pm 1$ peaks in P_1 and P_2 linescans. The effect is unexplained, although its dependencies on pressure, optical power, discharge power, and laser polarization angle were studied. There is indirect evidence that this peak imbalance shifts the $m = \pm 1$ peak frequencies by different amounts.

The last systematic, optical power shifts, was studied at a level of precision higher than what was previously attainable. Discrepancies between calculated AC Stark shifts and measurements seem to be related to the observed intensity dependence of the residual linescan asymmetry. As a result, calculated AC Stark shifts are used to correct for the finite laser power used in measurements of linear pressure shifts.

8.1 Laser Beam Misalignment Shifts

Very large frequency shifts were unexpectedly observed when the alignment of the pump and probe beams was slightly perturbed. Although beam misalignment in cell-based saturated absorption spectroscopy usually results in only residual Doppler broadening, the non-thermal distribution of atomic velocities created by the discharge and imprecise alignment of the laser beams gives rise to residual Doppler shifts as well. Shifts as large as 120 kHz/mrad, in conjunction with uncertainties as large as 0.09 mrad for the beam alignment, contribute errors between 6 and 14 kHz to the uncertainties of the optical transition frequencies. This effect is the largest source of systematic error for the optical frequencies measurements. However, the shifts affect all three transitions in a similar way, leaving measurements of the fine structure intervals much less affected.

8.1.1 Beam Misalignment for Thermally-Distributed Gases

In cell-based saturated absorption spectroscopy with atomic velocities that are thermally distributed, misalignment of pump and probe beams (Fig. 8.1) gives rise to residual Doppler broadening with no shift in the center frequency. Assuming the pump and probe beams are offset by an angle θ , consider an atom with velocity \vec{v} whose motion is at an angle ϕ with respect to the direction perpendicular to the probe beam. For pump and probe beams derived from the same laser, $k = |\vec{k}_{pump}| = |\vec{k}_{probe}|$. The atomic transition is detected when the Doppler shifts of the pump and probe

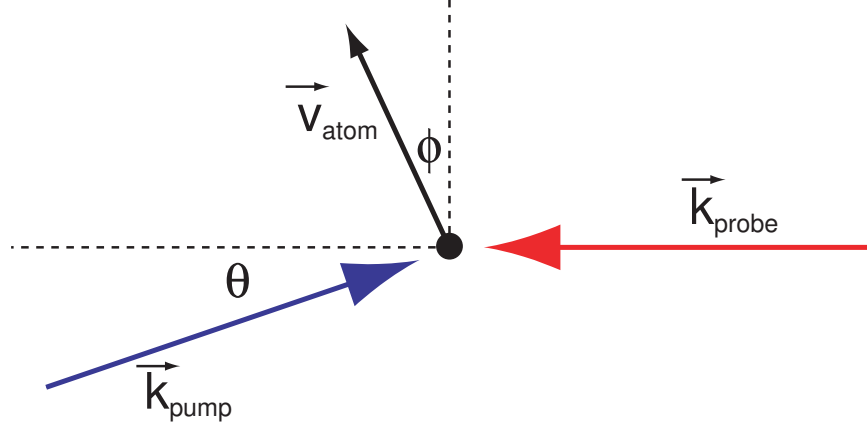


Figure 8.1: Imperfect alignment of pump k-vector \vec{k}_{pump} , probe k-vector \vec{k}_{probe} , and atomic velocity vector \vec{v}_{atom} .

beams are equal:

$$\vec{k}_{\text{pump}} \cdot \vec{v}_{\text{atom}} = \vec{k}_{\text{probe}} \cdot \vec{v}_{\text{atom}} \quad (8.1)$$

$$-kv \cos \theta \sin \phi + kv \sin \theta \cos \phi = kv \sin \phi \quad (8.2)$$

where $v = |\vec{v}_{\text{atom}}|$. Rearranging terms and assuming $\theta \ll 1$,

$$\tan \phi = \frac{\sin \theta}{1 + \cos \theta} \approx \frac{\theta}{2} \quad (8.3)$$

$$\phi \approx \frac{\theta}{2}, \frac{\theta}{2} + \pi. \quad (8.4)$$

For the case of perfectly aligned laser beams ($\theta = 0$), this reduces to the usual case of Doppler-free signals generated by atoms moving perpendicular to the laser beams ($\phi = 0, \pi$). However, for $\theta \neq 0$, detected atoms move in a direction $\phi \approx \theta/2$ and a small Doppler shift of $kv\theta/2$ arises. For atoms moving in the direction $\phi \approx \theta/2 + \pi$, the Doppler shift is $-kv\theta/2$.

If the atomic velocities in the cell are thermally distributed, then equal numbers of atoms have velocity \vec{v} (i.e. $\phi \approx \theta/2$) as and $-\vec{v}$ (i.e. $\phi \approx \theta/2 + \pi$). As a result, for

every velocity class that contributes a signal that is Doppler-shifted by $kv\theta/2$, there is a velocity class that contributes an equally-sized signal that is Doppler-shifted by $-kv\theta/2$. The two Doppler shifts have no net effect on the measured center frequency of the transition, and instead give rise to residual Doppler broadening.

8.1.2 Dynamics of an RF Discharge

The crucial assumption made in the previous section is that the laser beams probe equal numbers of atoms with velocities \vec{v} and $-\vec{v}$. In an RF discharge, this assumption is only true for perfect beam alignment ($\theta = 0$). For misaligned beams, the assumption fails, leading to residual Doppler shifts. To show this result, the dynamics of the plasma produced by the RF discharge [127, 128] are reviewed.

Neutral helium atoms in the cell are ionized upon absorption of RF energy from the discharge coil (Fig. 8.2a), resulting in populations of free electrons and positively-charged helium ions. Compared to the ions, the electrons have much larger velocities due to their lighter mass. As a result, they quickly travel throughout the cell, leaving behind at the ionization region a population of slower-moving helium ions.

Two mechanisms cause the ions to diffuse, or undergo a random walk. The first is collisions. The plasma is assumed to be weakly ionized, implying that collisions with neutral atoms dominate. The second diffusion mechanism is electrostatic repulsion. Here, the ions generate an electric field that both retards the diffusion of electrons and increases the diffusion of ions [127]. This process, called ambipolar diffusion, leads to an overall diffusion rate that is twice the rate due to collisions alone.

The spatial density profile of the ions is modeled using equations of motion and

continuity from fluid dynamics [127]. Ions and electrons recombine using the cell wall as a third body for momentum conservation. The resulting boundary condition is that the ion density is 0 at the cell walls. For a cylindrical cell, the resulting density profile is expressed in terms of Bessel functions $J_n(r)$. Here, r is a dimensionless radial coordinate and each order n corresponds to a different spatial mode of the cell.

Only RF power that can couple to the spatial mode of the cell will be absorbed by the atoms. For the simplest case where only the lowest order mode $n = 0$ is excited, the resulting density profile is peaked at the center of the cell ($r = 0$), implying that more ionization occurs in this region. This is consistent with the observation that the magnitude of the discharge glow is brightest in the center of the cell and weaker toward the edges.

When ions reach the cell wall, they recombine with electrons through three-body recombination, using the cell wall as the third body for momentum conservation (Fig. 8.2b) [127]. The result is a relatively large population of neutral helium atoms at the cell wall. In comparison, the population of neutral helium atoms in the center of the cell is relatively small due to the increased ionization. The result is a density gradient for neutral atoms that, for a cylindrical cell, directed radially inward. Neutral atoms diffuse toward the center, where they continuously replenish atoms that are ionized.

8.1.3 Residual Doppler Shifts in an RF Discharge

Due to their radial drift, the velocities of the helium atoms are not thermally distributed. As a result, the assumption of equal numbers of oppositely moving

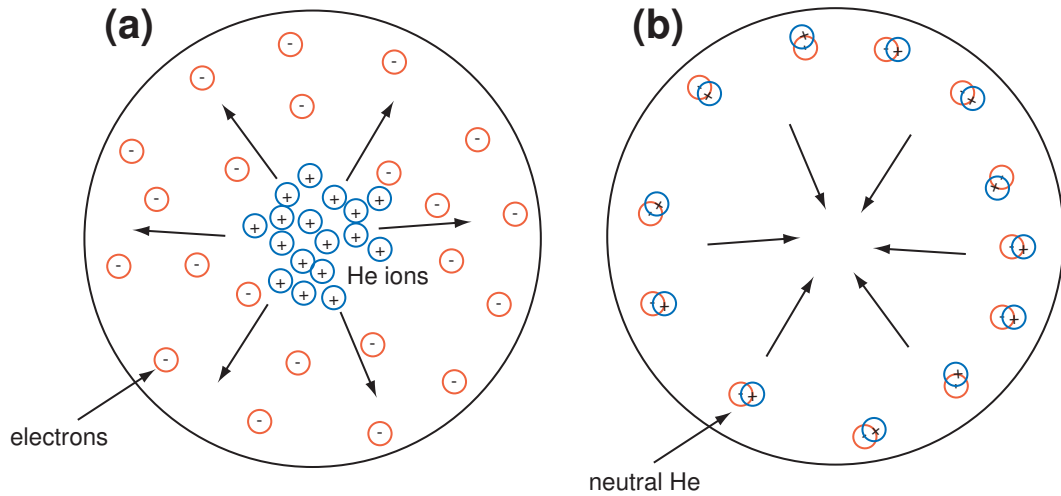


Figure 8.2: Ionization and recombination in a weakly-ionized gas. (a) Ionization: free electrons quickly travel throughout the cell, resulting in a population of helium ions at the center of the cell; (b) helium ions diffuse to the cell wall, where they recombine with electrons to form neutral helium atoms. These neutral atoms drift radially inward to replenish those atoms that are ionized at the center of the cell.

atoms does not necessarily hold. In fact, misalignment of the laser beams leads to residual Doppler shifts in addition to Doppler broadening. Some examples of different beam geometries demonstrate this effect.

Consider the simplest case of perfectly aligned laser beams ($\theta = 0$) whose common beam axis coincides exactly with the cylindrical axis of the discharge (Fig. 8.3). In this situation, equal numbers of oppositely moving atoms are illuminated by the lasers even though the atomic velocities are not thermally distributed. Once a misalignment is introduced, the laser beams probe unequal numbers of oppositely moving atoms, resulting in a residual Doppler shift. However, while a beam misaligned by angle θ probes more atoms of velocity \vec{v} (Fig. 8.3a), a misalignment by angle $-\theta$ probes more atoms of velocity $-\vec{v}$ (Fig. 8.3b). As a result, the sign of the Doppler shift is the same

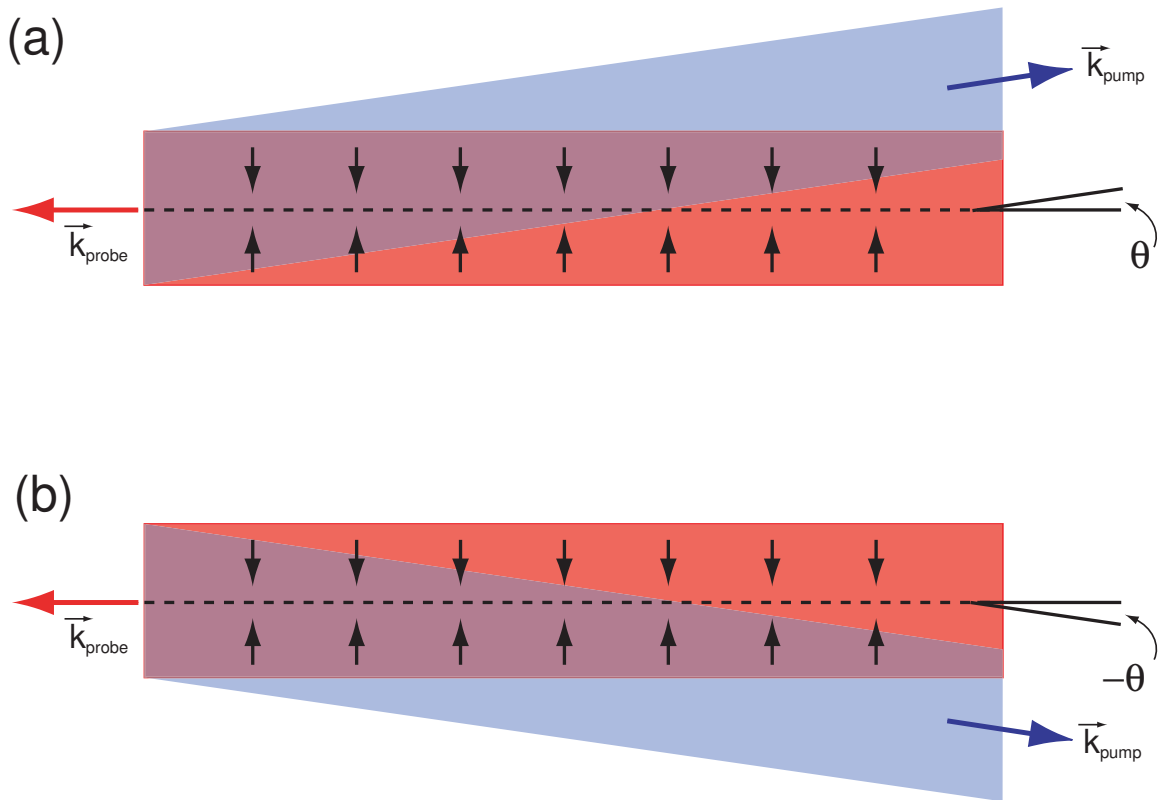


Figure 8.3: Side view of saturated absorption spectroscopy in an RF discharge cell. Due to the radial drift of the helium atoms, misaligned pump (blue) and probe (red) beams detect unequal numbers of oppositely-moving atoms (purple). (a) For a misalignment angle θ , more downward moving atoms are detected. (b) For a misalignment angle $-\theta$, more upward moving atoms are detected. The axis of the discharge is represented by the dashed line. Vertical arrows indicate the direction in which helium atoms diffuse.

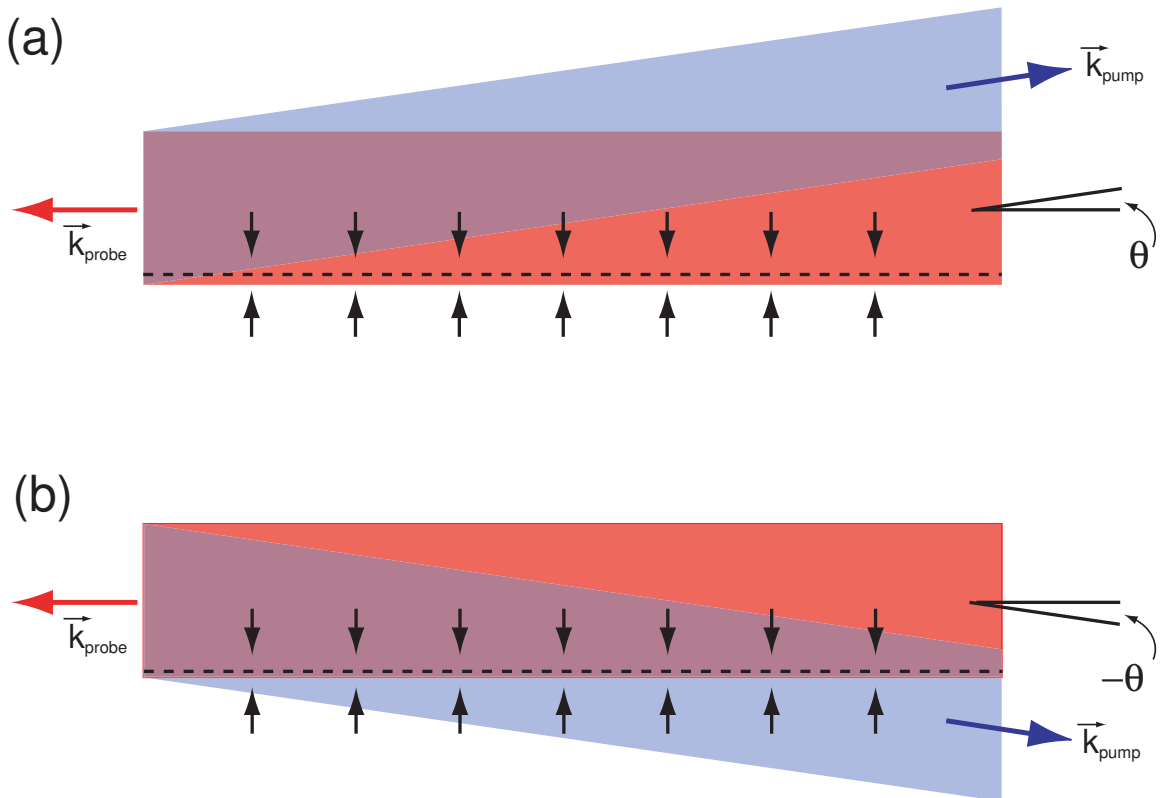


Figure 8.4: Side view of saturated absorption spectroscopy in an RF discharge cell. Pump (blue) and probe (red) beams detect atoms to the side of the discharge axis (dashed line). For both misalignment angles (a) θ and (b) $-\theta$, more downward moving atoms are detected (purple). Vertical arrows indicate the direction in which helium atoms diffuse.

for angles θ and $-\theta$. A plot of frequency versus angle θ would show an extremum at the point of optimal alignment. An observation of this extremum is one possible way to experimentally determine optimal beam alignment.

A more complicated scenario occurs when the common axis of perfectly aligned beams is parallel to, but laterally displaced from, the axis of the discharge (Fig. 8.4). Here, the laser beams probe more atoms of velocity \vec{v} for both misalignment angles θ (Fig. 8.4a) and $-\theta$ (Fig. 8.4b). As a result, the residual Doppler shifts for angles θ and $-\theta$ have the opposite sign. A plot of frequency versus angle θ would vary

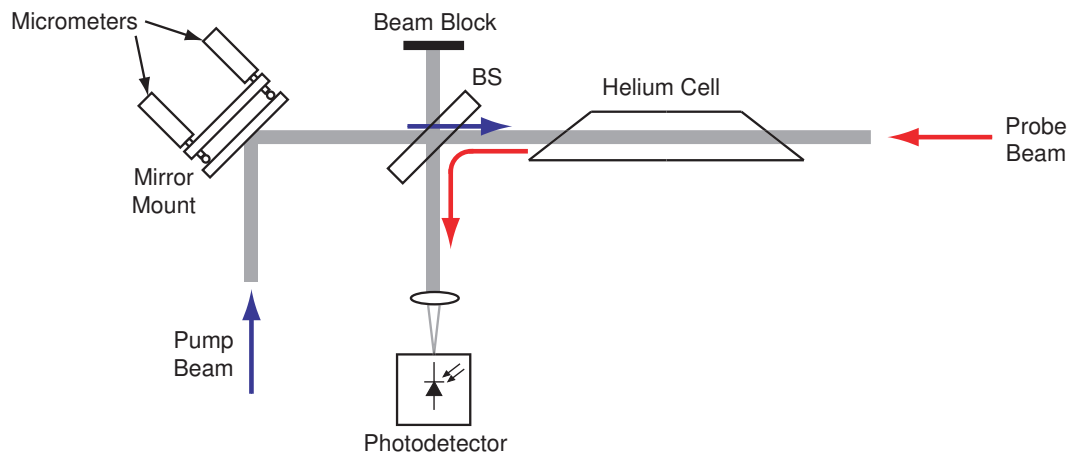


Figure 8.5: Experimental setup used to detect beam misalignment shifts. The horizontal and vertical angles at which the pump beam enters the cell are adjusted using a pair of micrometers mounted into a mirror mount.

linearly through the point of optimal alignment. The lack of an extremum prevents this scenario from being used to determine optimal alignment.

8.1.4 Measurements of Beam Misalignment Shifts

Beam misalignment shifts were discovered after the first of two data sets taken during this experiment was finished. For the alignment procedure of the first data set, pump and probe angles were adjusted in order to maximize transmission of each beam through two irises, one on each side of the cell. Transmission was crudely detected using an infrared viewing card.

To improve beam alignment for the second data set, a better new technique was implemented. Here, each beam was cross-coupled into the output of the other beam's single-mode fiber. When properly aligned, laser power coupled into the fiber's output will appear out of the fiber's input. Alignment is optimized when the cross-coupled

power coming out of each fiber's input is maximized. The technique was tried because it is known to be very sensitive to beam alignment [129].

After a review of the experimental setup used to measure misalignment shifts, this section presents measurements from which the accuracy of the two alignment methods can be determined. Also presented are measurements of misalignment shifts as functions of pressure, discharge power, and magnetic field.

Experimental Setup

Fig. 8.5 shows the experimental setup for studying beam misalignment shifts. The angle at which the pump beam is directed into the discharge cell is varied by adjusting the tip and tilt of a mirror mount. The mirror mount actuators were replaced with micrometers so that the beam angle could be controlled precisely and accurately. The micrometer could be reproducibly set to to $0.5 \mu\text{m}$, corresponding to an angular resolution of 0.02 mrad. The angle of the probe beam was not altered so that its coupling into the photodetector remained fixed.

Beam Alignment Accuracy

Fig. 8.6 shows how the optical frequency of the $2^3S - 2^3P_0$ transition shifts when the angle of the pump beam is varied in the (a) vertical, and (b) horizontal directions. The angle 0 corresponds to the best alignment of the laser beams that could be achieved with the alignment procedure used for the first data set. For Fig. 8.6a, the horizontal angle was set to 0, while for Fig. 8.6b the vertical angle was set to 0.

Fitting each data set to a straight line yields slopes of $-86(1)$ kHz/mrad and $23(3)$ kHz/mrad for the vertical and horizontal directions, respectively. These slopes

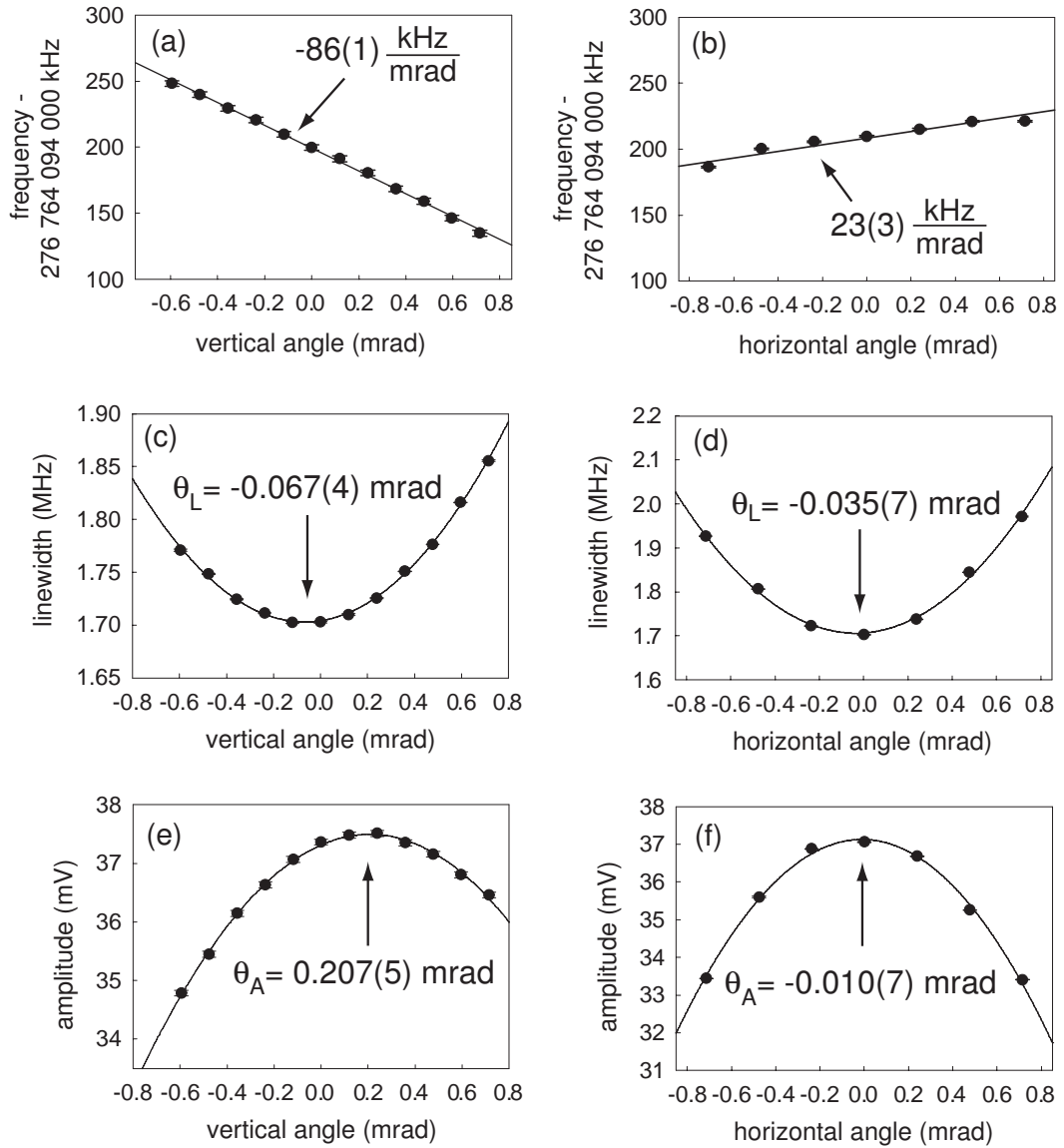


Figure 8.6: Frequency shifts as a function of beam alignment angle θ in the (a) vertical and (b) horizontal directions. Residual Doppler broadening gives rise to (c,d) a broadening of the Lorentzian linewidth, and (e,f) a decrease in the Lorentzian amplitude. The angle 0 corresponds to the best alignment that could be achieved by maximizing transmission through irises located on each end of the cell. The cell pressure was 40 mtorr, the optical power of both laser beams was $100 \mu\text{W}$, the discharge drive power was 4.5 Watts, and the external magnetic field was 108 Gauss.

correspond to a vertical drift speed of 17 cm/sec and a horizontal drift speed of 5 cm/sec. These values are much smaller than the mean thermal speed of 900 m/sec for helium at room temperature.

The lack of extrema in Figs. 8.6a and b is an indication that even for perfect beam alignment, the axes of the laser beams do not coincide with the axis of the plasma. A more likely scenario is that the plasma of the axis is poorly defined. This could be due to irregularities in the windings of the discharge coil, poor placement of the coil around the cell, oxide on the surface of the coil windings, etc. Nevertheless, the lack of extrema prevent this data from being used to experimentally determine optimal beam alignment.

As an alternative approach, optimal beam alignment can be determined by the presence of extrema in plots of linewidth as a function of angle θ . Here, the residual Doppler broadening introduced by beam misalignment causes the linewidth of the fitted Lorentzians to increase. Fig. 8.6 shows this effect experimentally in the (a) vertical and (b) horizontal directions. Each data set is fit to a quadratic function, from which the angles θ_L at which the extrema occur are extracted. Center angles of $-0.067(4)$ mrad and $-0.035(7)$ mrad for the vertical and horizontal directions, respectively, are slightly larger than the angular setpoint resolution of 0.02 mrad.

The magnitude of θ_L is used as the angular uncertainty for the beam alignment procedure. To determine the frequency uncertainty, the angular uncertainties are multiplied by the slopes in Fig. 8.6a and b. To accommodate the repeatability of the micrometers, the magnitude of both angular uncertainties is increased by 0.02 mrad. The resulting uncertainties of 0.087 mrad and 0.055 mrad in the vertical and

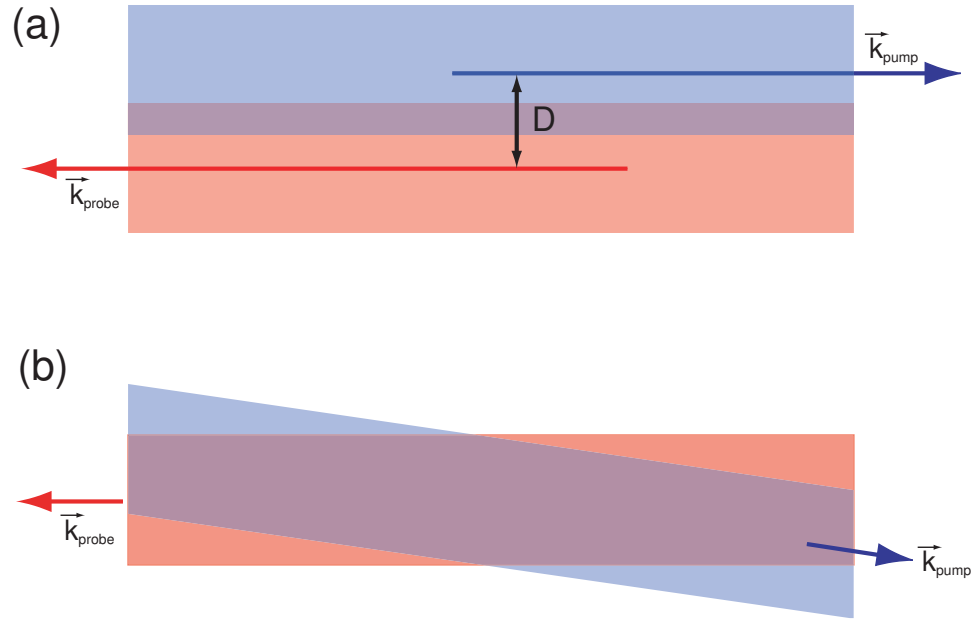


Figure 8.7: (a) The overlap (purple) between pump (blue) and probe (red) beams is small when the beams are parallel, but laterally displaced from each other by a distance D . (b) The overlap is improved when one of the beams is misaligned.

horizontal directions, respectively, correspond to frequency uncertainties of 7.5 kHz and 1.3 kHz. With these two values added in quadrature, the uncertainty for optical frequencies measured at 40 mtorr with this alignment procedure is 7.6 kHz.

Another effect of residual Doppler broadening introduced by beam misalignment is a decrease in the amplitude of the fitted Lorentzians. As shown in Figs. 8.6e and f, plots of amplitude versus angle θ have extrema at angles θ_A . However, as an indicator of optimal beam alignment, θ_A is not necessarily accurate. One example where this is the case is shown in Fig. 8.7a, where parallel pump and probe beams are laterally displaced a distance D from each other. Here, few atoms interact with both laser beams, resulting in small signals. Better beam overlap achieved by misaligning the pump (Fig. 8.7b) leads to larger signals. The result is larger Lorentzian amplitudes

for misaligned beams.

Values of θ_A and θ_L can be used together to estimate the displacement D in Fig. 8.7. To obtain values of θ_A , each data set is fit to a quadratic function. In the vertical direction (Fig. 8.6e), the angle $\theta_A = 0.207(5)$ mrad differs from θ_L by $0.274(6)$ mrad. Assuming the mirror used to misalign the pump beam is 1 meter from the center of the cell, the displacement is $D = 274(6)$ μm . In the horizontal direction (Fig. 8.6f), the angle $\theta_A = -0.010(7)$ differs from θ_L by $0.025(10)$ mrad. The corresponding displacement is $D = 25(10)$ μm .

Fig. 8.8 shows plots of frequency, linewidth, and amplitude that are used to determine the accuracy of the second beam alignment technique. Here, the angle 0 corresponds to the optimal alignment that could be achieved by cross-coupling each laser beam into the other beam's single-mode fiber. For the linewidth plots (c and d), center angles of $\theta_L = 0.012(5)$ mrad and $\theta_L = -0.057(8)$ mrad were measured for the vertical and horizontal directions, respectively. For the amplitude plots (e and f), center angles of $\theta_A = 0.17(2)$ mrad and $\theta_A = 0.03(17)$ mrad in the vertical and horizontal angles disagree with corresponding values of θ_L . This disagreement, also seen in Fig. 8.6, possibly indicates a lateral displacement between the beam axes (see Fig. 8.7).

In order to account for the angular setpoint resolution, the magnitudes of θ_L are increased by 0.02 mrad to obtain angular uncertainties of 0.032 mrad and 0.077 mrad in the vertical and horizontal directions, respectively. The corresponding frequency uncertainties of 2.5 kHz and 2.2 kHz are added in quadrature to obtain a total uncertainty of 3.4 kHz for optical frequencies measured at 40 mtorr with this alignment

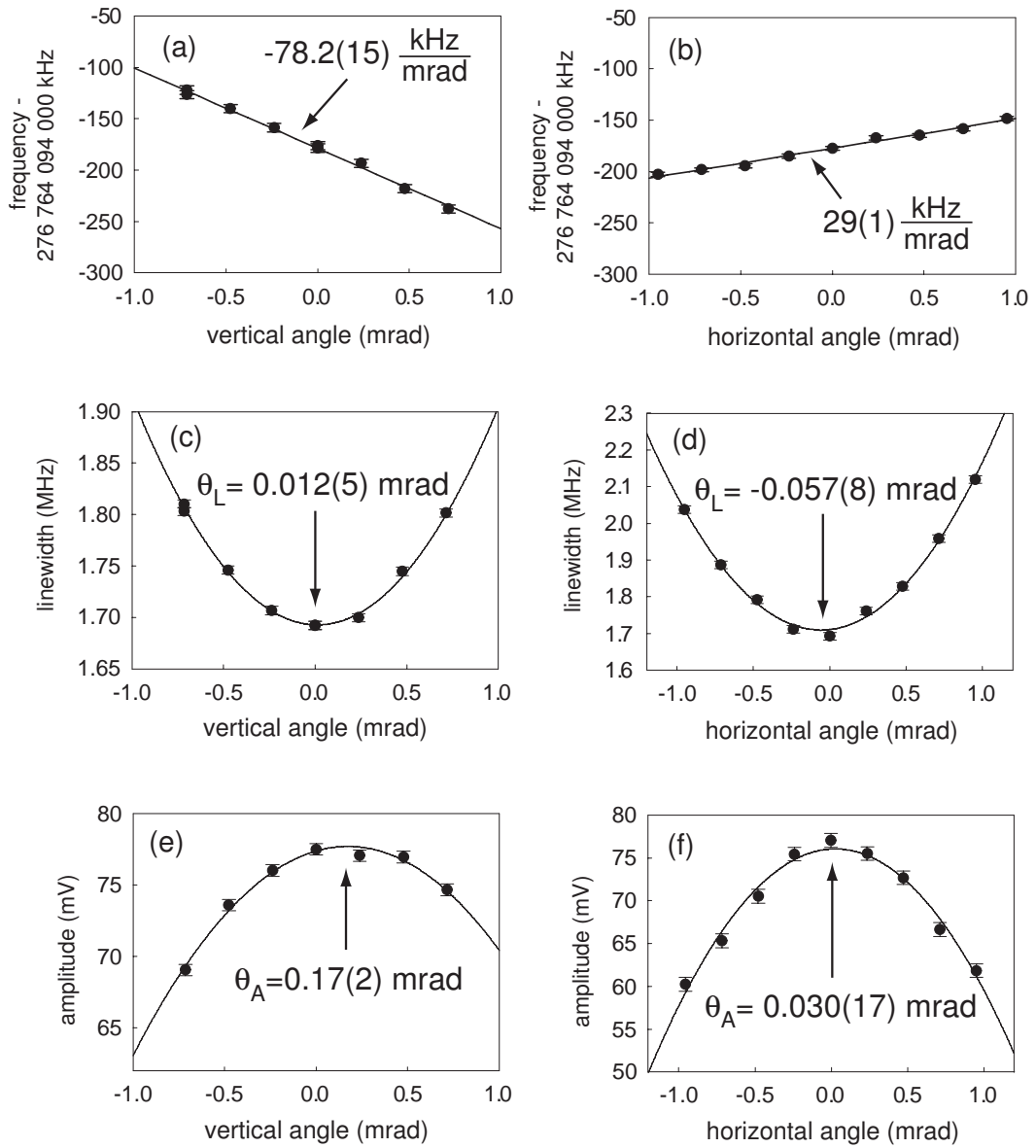


Figure 8.8: Frequency shifts as a function of beam alignment angle θ in the (a) vertical and (b) horizontal directions. Residual Doppler broadening gives rise to (c,d) a broadening of the Lorentzian linewidth, and (e,f) a decrease in the Lorentzian amplitude. The angle 0 corresponds to the best alignment that could be achieved using the technique of cross-coupling into single-mode fibers. The cell pressure was 40 mtorr, the optical power of both laser beams was $100 \mu\text{W}$, the discharge drive power was 1 Watt, and the external magnetic field was 55 Gauss.

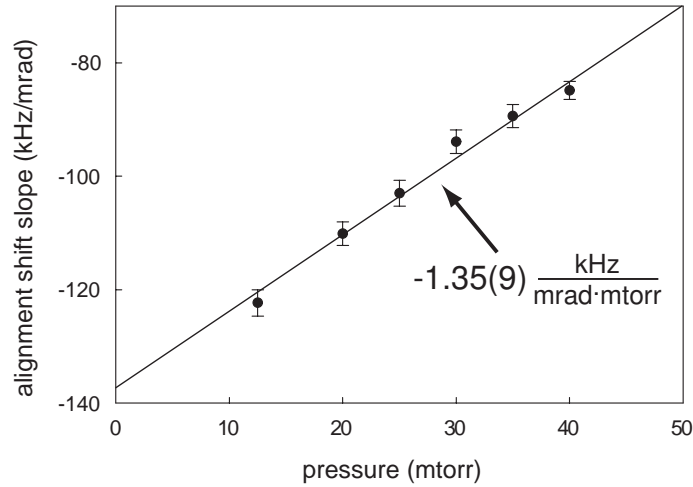


Figure 8.9: Beam misalignment shifts in the vertical direction have an angular sensitivity that decreases with pressure. The optical power of each laser beam was $100 \mu\text{W}$, the discharge power was 4.5 Watts, and the external magnetic field was 108 Gauss.

procedure. This value improves upon the uncertainty of the first alignment technique by more than a factor of two.

Physical Dependencies

Fig. 8.9 shows that the angular sensitivity of the vertical misalignment shift decreases linearly with pressure. This result is plausible because the increased number of collisions at higher pressures leads to slower drift velocities, resulting in smaller Doppler shifts. Fitting the data to a straight line gives a sensitivity of $-1.35(9)$ kHz/mrad·mtorr.

A sensitivity of $-3.9(6)$ kHz/mrad·Watt was measured for the dependency of the vertical misalignment shift on the discharge drive power (Fig. 8.10). This result is plausible because at higher discharge drive powers, an increase in ionization leads to

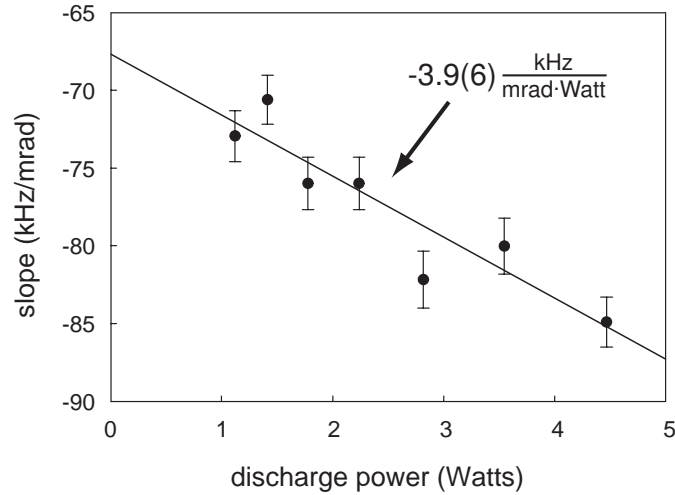


Figure 8.10: Beam misalignment shifts in the vertical direction have an angular sensitivity that depends weakly on discharge drive power. The cell pressure is 40 mtorr, the optical power of each laser beam is $100 \mu\text{W}$, and the external magnetic field is 108 Gauss.

more ions and fewer neutral atoms at the center of the cell. The result is an increase in the density gradient that causes ions to diffuse away from the center of the cell more rapidly. A similar increase in the density gradient for the neutral atoms causes them to diffuse back to the center of the cell more rapidly. This increase in the atomic drift velocity gives rise to larger residual Doppler shifts.

For the dependency on the external magnetic field, small sensitivities of $0.027(20)$ kHz/mrad·Gauss and $-0.003(36)$ kHz/mrad·Gauss were measured for the vertical and horizontal directions, respectively (Fig. 8.11).

Beam Alignment Drift

Beam misalignment shifts are large enough that even optical mount drift can cause appreciable effects. A stainless steel actuator in a standard mirror mount for 1" optics

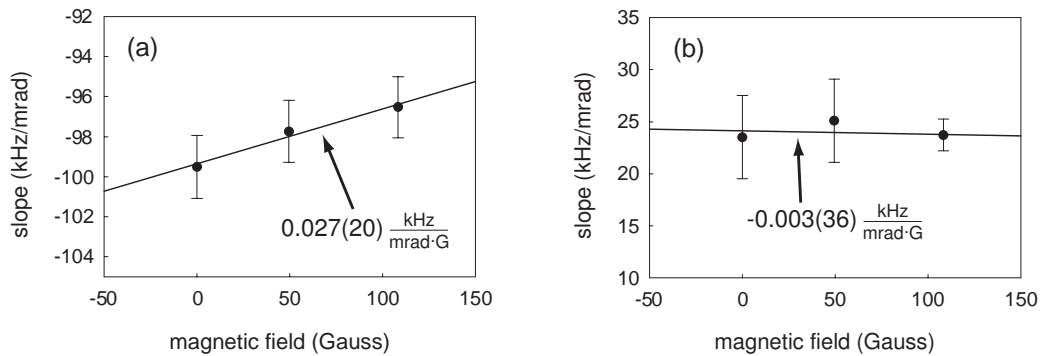


Figure 8.11: The angular sensitivity of the beam misalignment shifts in the (a) vertical, and (b) horizontal directions show little dependence on the magnitude of the external magnetic field. The cell pressure is 40 mtorr, the optical power of each laser beam is 100 μW , and the discharge power is 3.2 Watts.

has a typical temperature coefficient of 5 $\mu\text{rad}/^\circ\text{C}$. The lab temperature is stabilized to $\pm 1^\circ\text{C}$, resulting in frequency shifts up to 500 Hz. Large enough to be observed, these shifts appear as correlations between measurements of the optical transition frequencies.

8.1.5 Misalignment Shifts for the Optical Transition Frequencies

As shown in Chapter 7, measurements of optical transition frequencies are linearly extrapolated to zero pressure in order to remove linear pressure shifts. However, beam misalignment uncertainties of 7.6 kHz and 3.4 kHz were determined from measurements at a cell pressure of 40 mtorr. As shown in Fig. 8.9, the angular sensitivity to beam misalignment in the vertical direction increases in magnitude as pressure decreases. In the limit of zero pressure, the intercept of -137 kHz/mrad is approximately 75% larger than the values of -86 kHz/mrad and -78 kHz/mrad measured at 40 mtorr

(see Figs. 8.6a and 8.8a). To account for the pressure dependency of the angular sensitivity, the beam misalignment uncertainties are increased by 75%, assuming that the angular sensitivity in the horizontal direction increases a similar amount in the limit of zero pressure. The resulting uncertainties due to beam misalignment at zero pressure are 13.3 kHz and 6.0 kHz for the iris and fiber-coupled alignment techniques, respectively.

8.1.6 Misalignment Shifts for the Fine Structure Intervals

Although beam misalignment shifts are large for measurements of the optical transition frequencies, the three frequencies are shifted similarly, leaving values of the fine structure intervals less affected. This is demonstrated in Fig. 8.12, where the fine structure intervals are plotted as a function of beam alignment angle θ . Sensitivities between 0.1 kHz/mrad and 1.7 kHz/mrad are more than 50 times smaller than the shifts for the optical frequencies (see Fig. 8.6a and b, and Fig. 8.8a and b). For some of the intervals, the sensitivities are not consistent with 0, possibly indicating that the shifts do not cancel perfectly. Assuming a conservative value of 0.1 mrad for the beam misalignment, uncertainties of 70 Hz, 220 Hz, and 180 Hz are assigned to the f_{12} , f_{01} , and f_{02} intervals, respectively.

8.2 Asymmetries in the Linescans

Linescans with high signal-to-noise ratios reveal small asymmetric components to their lineshapes. An example is shown in Fig. 8.13, where the visibility of the asymmetry was enhanced by averaging 100 measurements of the lock-in amplifier's

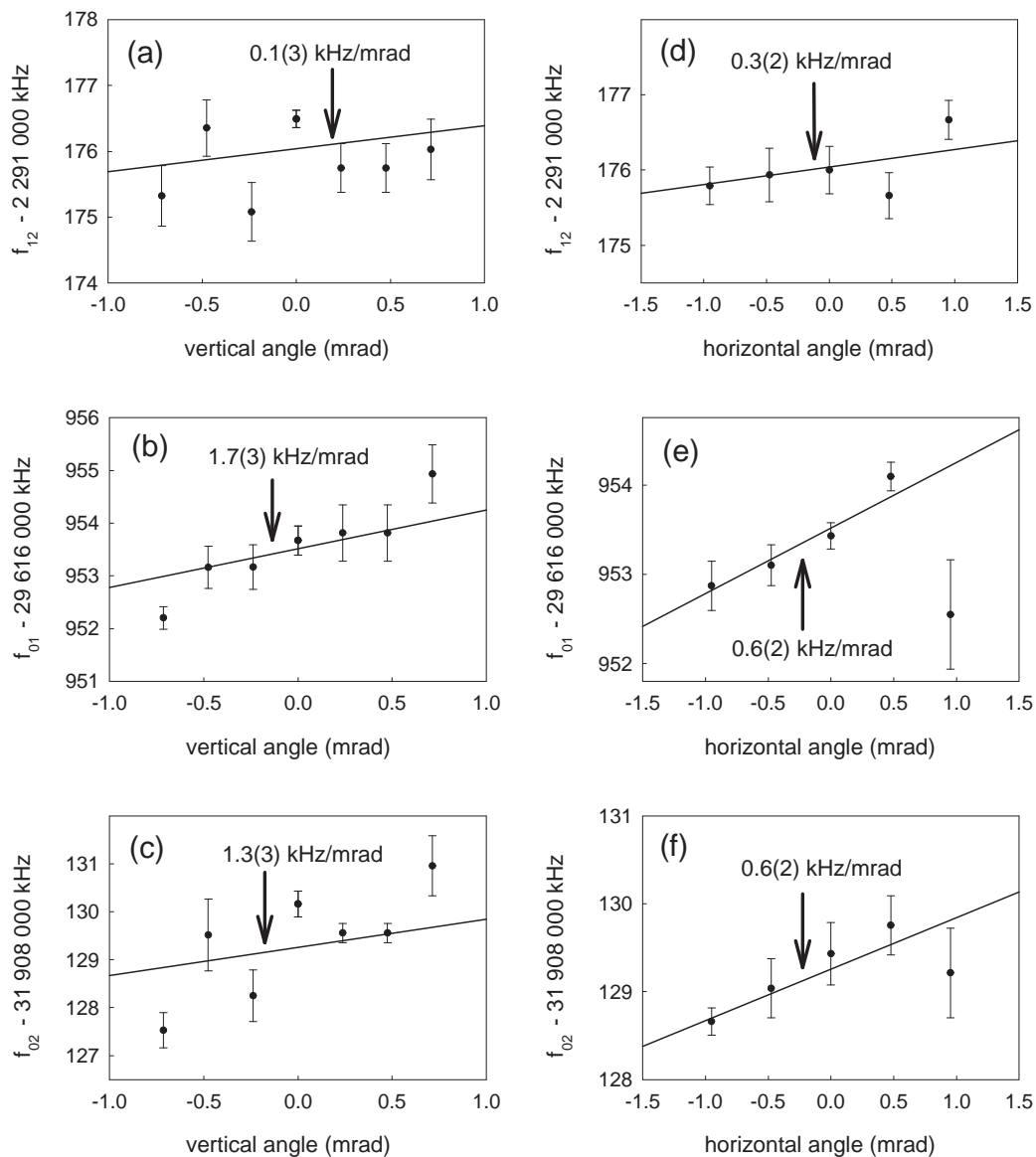


Figure 8.12: Measurements of the fine structure intervals as a function of beam alignment angle θ in the vertical and horizontal directions. The cell pressure was 40 mtorr, the optical power in each laser beam was $100\ \mu\text{W}$, the discharge drive power was 1 Watt, and the external magnetic field was 55 Gauss.

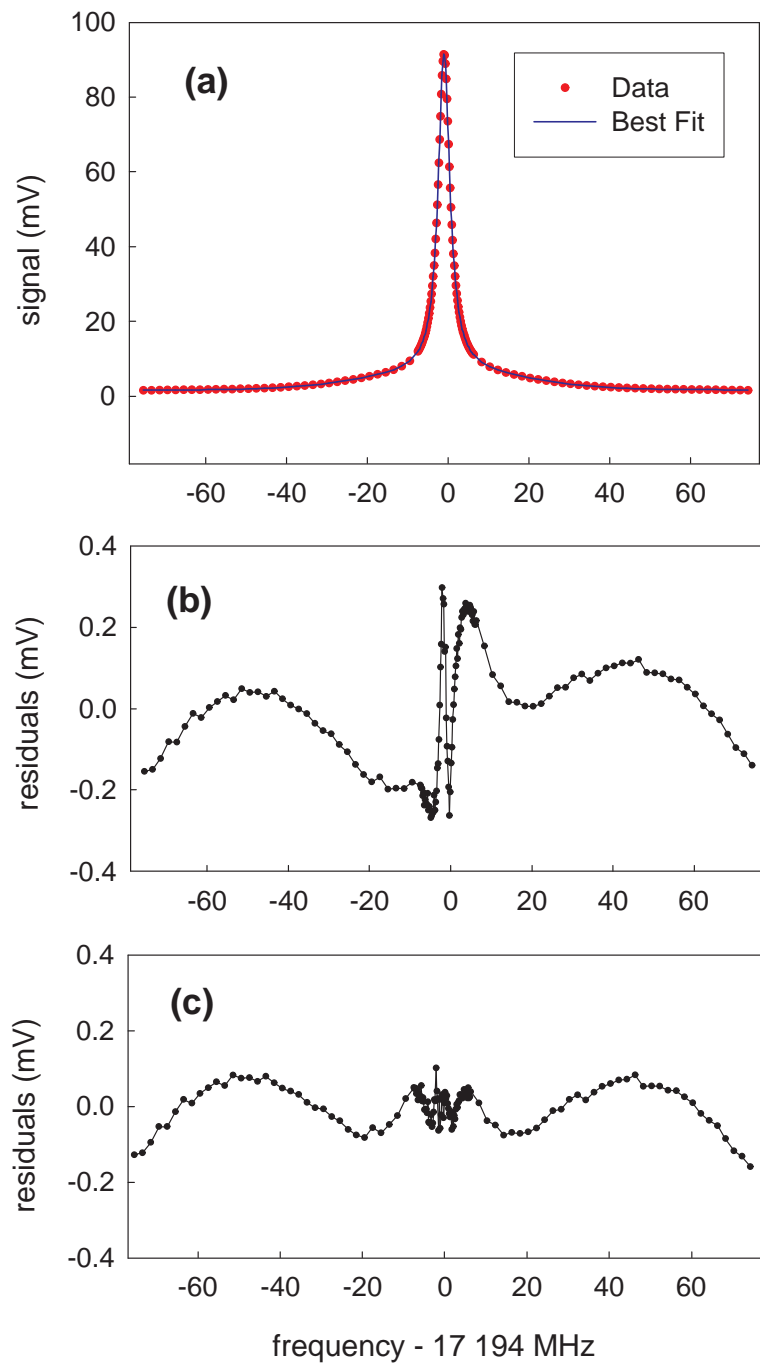


Figure 8.13: (a) A sample linescan of the $2^3S - 2^3P_0$ transition. (b) Residuals from a fit to a Lorentzian function and Gaussian background reveal an asymmetric component to the signal. (c) When a dispersive term $D(\Omega)$ is added to the fitting function, the asymmetry is largely removed. The cell pressure was 40 mtorr, the optical power of each laser beam was $100 \mu\text{W}$, the external magnetic field was 108 Gauss, and the discharge power was 4.5 Watts.

output per frequency point, an amount 10 times higher than usual for a typical linescan. Residuals when the data is fit to the sum of a Lorentzian peak, Gaussian background, and constant offset show the presence of an asymmetry (Fig. 8.13b). Empirically, this asymmetry is well-described by a dispersive component $D(\Omega)$

$$D(\Omega) = \frac{\Gamma\Omega}{\Omega^2 + \Gamma^2}. \quad (8.5)$$

Here Γ is the transition linewidth and $\Omega = \omega - \omega_0$ is the laser detuning from the atomic resonance frequency ω_0 . By including $D(\Omega)$ in the fitting function, the asymmetry is largely removed (Fig. 8.13c). The center frequencies obtained in Fig. 8.13b and Fig. 8.13c differ by 20 kHz, demonstrating that a small asymmetry can substantially shift measured values of the optical transition frequencies. In addition, shifts introduced by adding $D(\Omega)$ to the fitting functions were found to be different for the three transitions. As a result, measurements of the fine structure intervals are affected by this systematic as well.

Two explanations for this asymmetry were investigated. The first, the light-pressure effect, failed to explain the shape and magnitude of the observed asymmetry. The second explanation, self-focusing of the laser beams by the helium gas, can qualitatively predict several observed properties of the asymmetry, but underestimates its magnitude by several orders of magnitude. We therefore have no satisfying for the observed asymmetry at this time.

To study the properties of the asymmetry, each linescan was fit with and without $D(\Omega)$ included in the fitting function. The difference between the center frequencies obtained from the fits, called dispersive shifts, are plotted as functions of pressure and optical power. These dependencies help determine the effect of the asymmetry

on measurements of linear pressure shifts and optical power shifts.

8.2.1 Asymmetry Due to Laser Light Pressure

The first attempted explanation for the asymmetry is the light-pressure effect, which adds to the Lorentzian peak a small derivative of a Lorentzian (See Chapter 6). It was thought that for scans with a high signal-to-noise ratio, this distortion could be visible in the fit residuals. However, the asymmetry in Fig. 8.13b fits poorly to a derivative of a Lorentzian.

To confirm that the asymmetry is not due to light pressure, a mathematical model was implemented. A simulated signal $S(\Omega)$ is generated from the sum of a Lorentzian peak and a small Lorentzian derivative

$$S(\Omega) = \frac{A}{1 + \left(\frac{\Omega}{\Gamma}\right)^2} + 2\lambda \frac{\Omega/\Gamma}{\left[1 + \left(\frac{\Omega}{\Gamma}\right)^2\right]^2} \quad (8.6)$$

The amplitude λ of the derivative term is assumed to be small compared to the Lorentzian amplitude A (i.e. $\lambda \ll A$). In this approximation, the signal is well-approximated by a Lorentzian whose center frequency is shifted by $\lambda\Gamma/A$. Setting this shift equal to 10 kHz, a typical value for the light-pressure effect, determines the amplitude λ . The Lorentzian amplitude A is set to 1.

$S(\Omega)$ is used to generate a set of frequency and amplitude points that are fit to a Lorentzian. Fig. 8.14 shows the residuals. Their size, relative to the Lorentzian amplitude, is about 10^{-5} , an amount 100 times smaller than the residuals in Fig. 8.13b and 10 times smaller than the experimental resolution. In addition, the residuals appear symmetric about the center frequency.

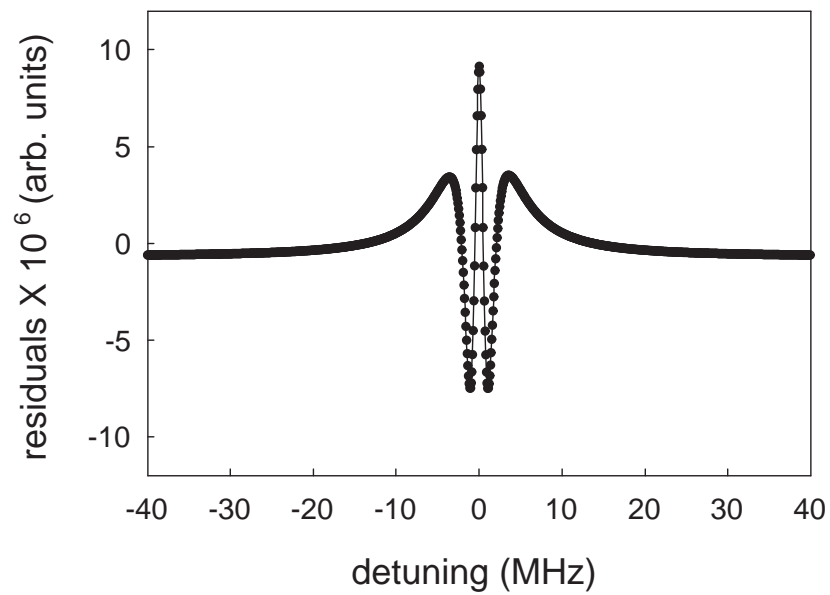


Figure 8.14: To test for lineshape distortions due to laser light pressure, a linescan was simulated by summing a Lorentzian and a much smaller Lorentzian derivative. After fitting to a Lorentzian, the residuals are 100 times smaller than those observed in Fig. 8.13b.

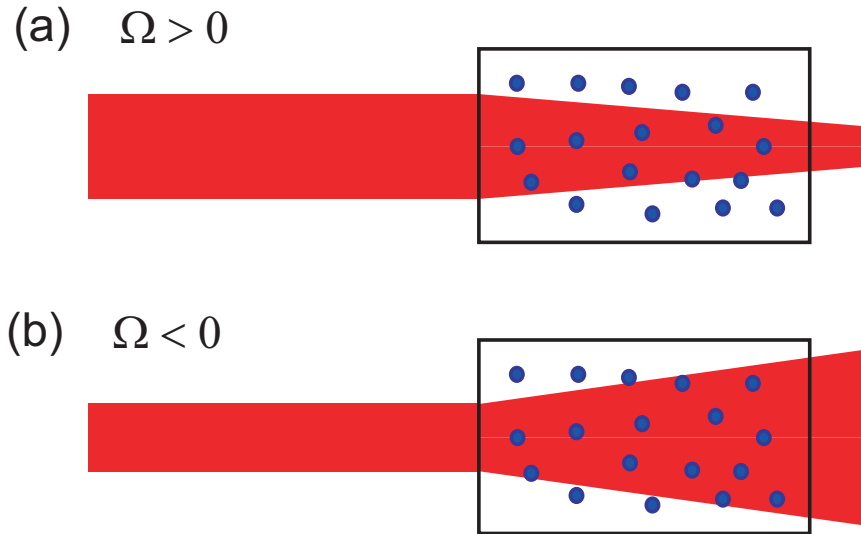


Figure 8.15: An intensity-dependent index of refraction gives rise to self-focusing. (a) For positive, or blue, detuning, the laser beams are focused; (b) for negative, or red, detuning, the laser beams are defocused.

8.2.2 Self-focusing

Self-focusing of the laser beams by the helium gas is an attractive explanation for the asymmetry in that it produces a dispersive addition to a Lorentzian lineshape [130, 131, 132]. A summary of this possible systematic is presented here. Unfortunately, a mathematical model predicts a size for the dispersive term that is three orders of magnitude smaller than what was observed.

An atomic sample driven near resonance gives rise to an intensity-dependent index of refraction [71, 133]

$$n = n_0 + n_2(\Omega, I) + \alpha ID(\Omega). \quad (8.7)$$

Here, the index of refraction $n_0 \approx 1$ is independent of intensity I , and the small, lowest-order, intensity-dependent contribution $n_2 \ll n_0$ is proportional to a dispersive lineshape $D(\Omega)$. For a laser beam with a Gaussian profile, the refractive index has a

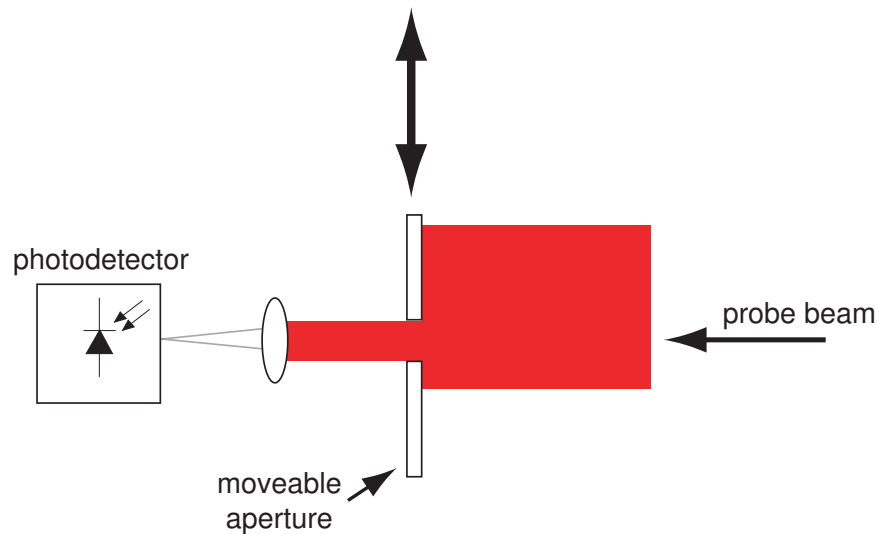


Figure 8.16: Experimental setup for observing self-focusing. A 2 mm aperture mounted on a translation stage clips the probe beam before being detected.

different value at the center of the beam, where the intensity is high, than in the wings, where the intensity is low. The resulting refractive index profile gives rise to focusing or defocusing of the laser beams, depending on the laser's detuning (Fig. 8.15).

Experimental Evidence for Self-focusing

An experimental test for observing self-focusing uses an aperture whose opening is smaller than the waist of the probe beam (Fig. 8.16) [132, 134]. When the aperture is centered on the laser axis, more of the focused laser beam is transmitted through the aperture compared to a collimated or less focused beam. Similarly, transmission through the aperture decreases when the probe is defocused. When the aperture is centered on the wings of the beam, the opposite effect occurs: focusing causes a decrease in probe beam transmission, while defocusing causes an increase in transmission.

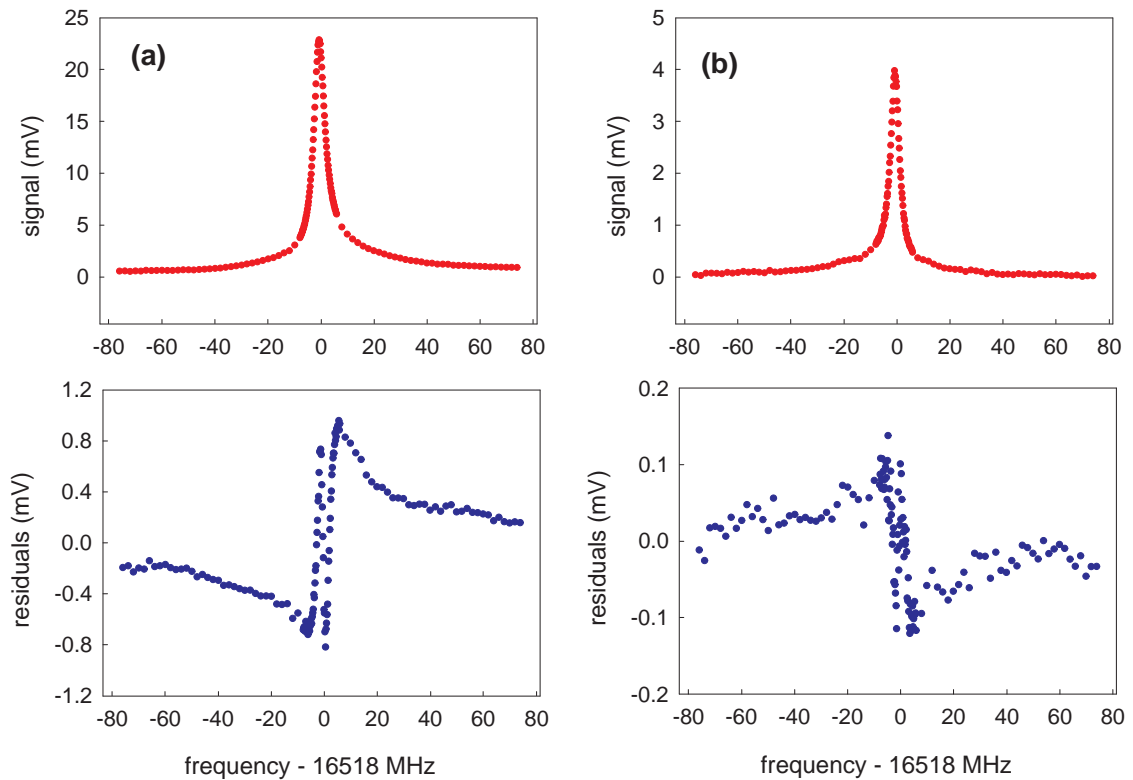


Figure 8.17: Sample linescans of the $2^3S - 2^3P_0$ transition when the 2 mm aperture is positioned (a) on the axis of the probe beam, and (b) 2 mm off the axis of the probe beam. The linescans are fit to the sum of a Lorentzian peak and Gaussian background. The residuals show a large dispersive component whose sign depends on the position of the aperture. The cell pressure was 40 mtorr, the optical power of each beam was $40 \mu\text{W}$, the discharge drive power was 1.9 Watts, and the external magnetic field was 108 Gauss.

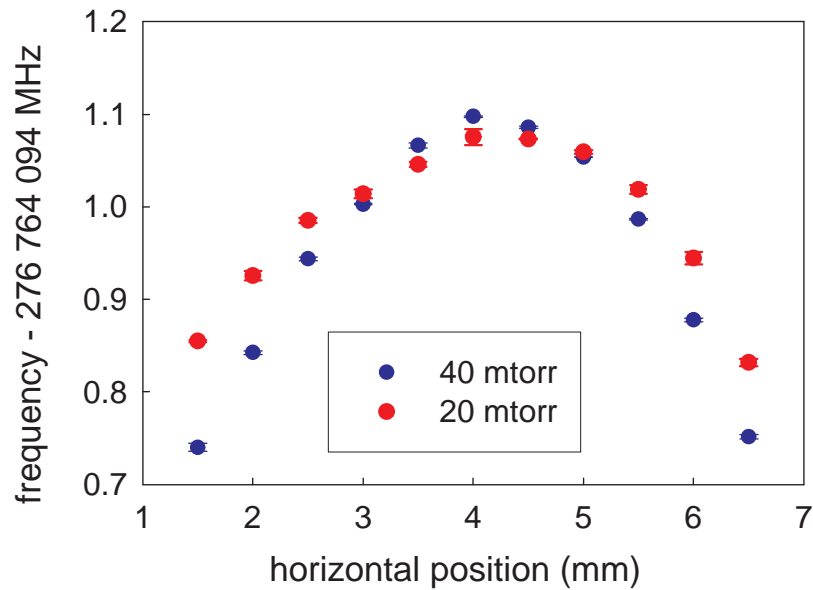


Figure 8.18: The large dispersive component of the signal shifts the fitted center frequency of the $2^3S - 2^3P_0$ transition by as much as 300 kHz, or 20% of the linewidth. The size of the shifts increases slightly with pressure. The optical power of each laser beam was $40 \mu\text{W}$, the discharge drive power was 1.9 Watts, and the external magnetic field was 108 Gauss.

The position of the aperture was adjusted using a translation stage; scans of the $2^3S - 2^3P_0$ transition were taken at each position. The linescans were fit to the sum of a Lorentzian peak, Gaussian background, and constant offset. Fig. 8.17 shows sample linescans when the 2 mm aperture was (a) centered on the beam axis, and (b) positioned 2 mm off the beam axis. A large dispersive component is observed in the fit residuals, and the sign of the dispersive component flips when the aperture's position is switched between on-axis and off-axis. The aperture was moved off-axis in both the vertical and horizontal directions. In each case, the dispersive component in the fit residuals had the same sign as those in Fig. 8.17b. All of these features are what would be expected for self-focusing.

Fig. 8.18 shows how the center frequencies of the fitted Lorentzians shift with aperture position. Due to the enhancement of the dispersive component by the aperture, these center frequencies shift as much as 300 kHz, or 20% of the linewidth. Showing a weaker dependency on position, a second data set at 20 mtorr indicates that these shifts scale with pressure, as would be expected for self-focusing.

Mathematical Modeling of Self-focusing

To confirm or refute the explanation of self-focusing, a mathematical model was developed to explain the results observed in Fig. 8.17 [131, 132].

For a two-level system in a standing-wave field of arbitrary intensity, the index of refraction as seen by one of the waves is given by [117]

$$n_s = 1 + \frac{\alpha_0}{2k} \Omega \left[1 - \frac{A}{B} \right] [(A + B)^2 - 4\Omega^2]^{-1/2} \quad (8.8)$$

where α_0 is the linear absorption coefficient on resonance, k is the laser wave number, and Ω is the laser detuning. Here,

$$A = (\Omega^2 + \Gamma^2)^{1/2}, \quad (8.9)$$

$$B = [\Omega^2 + \Gamma^2(1 + 2S)]^{1/2}, \quad (8.10)$$

and Γ is again the transition linewidth. The saturation parameter $S = I/I_{SAT}$ is the ratio of laser intensity I to the saturation intensity $I_{SAT} = \pi h c \Gamma / (3\lambda^3)$, where h is Planck's constant, c is the speed of light, and λ is the transition wavelength. The profile of the laser beams are represented by a Gaussian function, of which only the

first two terms of a Taylor expansion in r are kept:

$$I(r) = I_0 \exp\left(-\frac{2r^2}{w(z)^2}\right) \quad (8.11)$$

$$\approx I_0 \left(1 - \frac{2r^2}{w(z)^2}\right). \quad (8.12)$$

Here, the beam waist $w(z)$ is equal to the full-width of the beam profile at $1/e^2$ of the maximum intensity [133].

In the paraxial approximation, the angle ϕ between a light-ray and the beam axis is assumed to be small enough that $\sin \phi \approx \phi$ [133]. In this approximation, the trajectory of a light-ray is determined by the differential equation [131, 132]

$$\frac{d^2 r}{dz^2} = \frac{1}{n} \frac{dn}{dr} \approx \frac{dn_s}{dr} = \frac{\partial n_s}{\partial I} \frac{\partial I}{\partial r} = -\frac{4r}{w^2} I_0 \frac{\partial n_s}{\partial I} = -C_a r \quad (8.13)$$

where the convergence C_a is given by

$$C_a = \frac{4S}{w^2} \cdot \frac{\alpha_0}{2k} \cdot \Gamma^2 \Omega [(A+B)^2 - 4\Omega^2]^{-3/2} \quad (8.14)$$

$$\times \left[\frac{A \cdot [(A+B)^2 - 4\Omega^2]}{B^3} - 1 + \frac{A^2}{B^2} \right]. \quad (8.15)$$

The solution to Eqn. 8.13 gives rise to ray-transfer matrices that govern the propagation of the laser beam through the medium [133]

$$\mathbf{R}_a = \begin{pmatrix} \cos(\sqrt{C_a}L) & \frac{1}{\sqrt{C_a}} \sin(\sqrt{C_a}L) \\ -\sqrt{C_a} \sin(\sqrt{C_a}L) & \cos(\sqrt{C_a}L) \end{pmatrix} \quad \text{for } C_a > 0 \quad (8.16)$$

$$\mathbf{R}_a = \begin{pmatrix} \cosh(\sqrt{|C_a|}L) & \frac{1}{\sqrt{|C_a|}} \sinh(\sqrt{|C_a|}L) \\ \sqrt{|C_a|} \sinh(\sqrt{|C_a|}L) & \cosh(\sqrt{|C_a|}L) \end{pmatrix} \quad \text{for } C_a < 0 \quad (8.17)$$

where L is the length of the medium.

Eqns. 8.16 and 8.17 can be used to model the experimental setup in Fig. 8.16. The probe beam, upon entering the cell, is modeled as a Gaussian beam with infinite

radius of curvature. It is more convenient to express the radius of curvature $R(z)$ and beam waist $w(z)$ in terms of a parameter $q(z)$ [133],

$$\frac{1}{q(z)} = \frac{1}{R(z)} - \frac{i\lambda}{\pi w(z)^2}. \quad (8.18)$$

At the position z_0 where the probe beam enters the cell, this simplifies to

$$\frac{1}{q(z_0)} = \frac{1}{R(z_0)} - \frac{i\lambda}{\pi w(z_0)^2} = -\frac{i\lambda}{\pi w(z_0)^2}, \quad (8.19)$$

where λ is the wavelength.

The cell is modeled as a series of N thin cells, each of length L/N . Each thin cell is represented by matrices 8.16 and 8.17. The beam waist is calculated at the output of cell i ($i = 1, N$), and then used to compute the convergence C_a of cell $i + 1$.

After the cell, the beam propagates a distance d through free space until it reaches the aperture. The ray-transfer matrix is given by [133]

$$\mathbf{R}_b(d) = \begin{pmatrix} 1 & d \\ 0 & 1 \end{pmatrix}. \quad (8.20)$$

The complete ray-transfer matrix for the system is obtained by multiplying all the individual matrices

$$\mathbf{R}_{tr} = \begin{pmatrix} A & B \\ C & D \end{pmatrix} = \mathbf{R}_b(d) \prod_{i=1}^N \mathbf{R}_a(z_i). \quad (8.21)$$

The q -parameter at the aperture position z_a ,

$$q(z_a) = \frac{Aq(z_0) + B}{Cq(z_0) + D}, \quad (8.22)$$

is used with Eqn. 8.19 to calculate the waist $w(z_a)$.

With knowledge of the beam waist $w(z_a)$ at the position z_a , normalizing the area of the Gaussian beam profile determines the amplitude of the Gaussian. Transmission through the aperture is modeled by numerically integrating a Gaussian function between two limits r_0 and r_1

$$T(z_a) = \int_{r_0}^{r_1} \exp\left(-\frac{2r'^2}{w(z_a)^2}\right) dr'. \quad (8.23)$$

The integration limits r_1 and r_0 are chosen either for on-axis or off-axis transmission.

The Doppler-free lineshape is simulated by generating a Lorentzian whose signal at each frequency is proportional to the intensity $T(z_a)$ of the beam transmitted through the aperture. The result is fit to a Lorentzian from which the center frequency is extracted.

Fig. 8.19 shows Lorentzian signals and fit residuals from the model. An initial beam waist of 5 mm was used. In Fig. 8.19a, r_1 and r_2 were chosen to model a 1 mm aperture centered on the beam axis. In Fig. 8.19b, different values for r_1 and r_2 model a 1 mm aperture positioned 5 mm off-axis. An absorption coefficient of $\alpha_0 = 1 \text{ m}^{-1}$ was assumed.

Qualitatively, the residuals in Fig. 8.19 correctly predict the signs of the dispersive signals observed experimentally in Fig. 8.17. Quantitatively, however, the results predict values for the convergence C_a that are too small by more than three orders of magnitude. The resulting frequency shift due to the dispersive component is only 200 Hz, much smaller than the few hundred kHz shifts seen experimentally.

This quantitative disagreement by orders of magnitude has been seen in previous attempts to model self-focusing. In reference [132], the author attributes the discrepancy to the representation of the cell by a single ray-transfer matrix. This approach

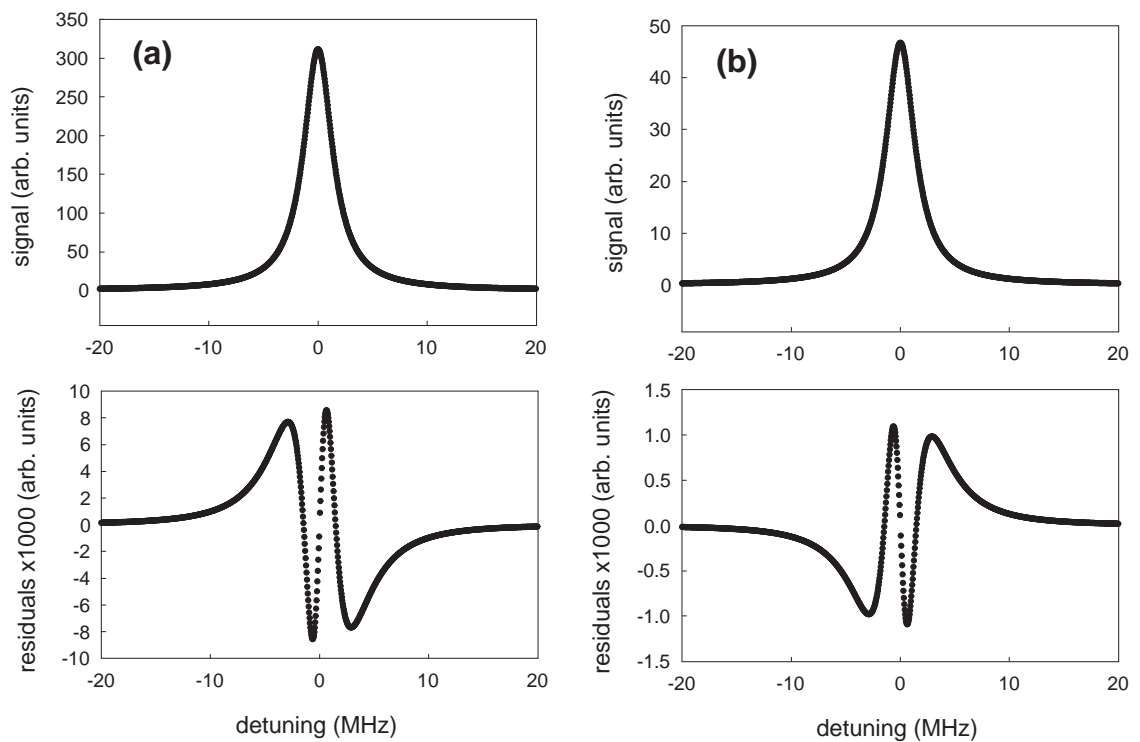


Figure 8.19: Lorentzian signals and fit residuals generated by the mathematical model for self-focusing. A 1 mm wide aperture is modeled (a) on the beam axis, and (b) 5 mm off the beam axis. The initial beam waist is 5 mm.

fails to account for changes in the convergence and waist that occur as the beam propagates inside the cell. The approach used here, representing the cell as a series of multiple thin cells, did not demonstrate any significant improvement.

Another prediction made by the self-focusing model is that the size of the dispersive frequency shifts scales linearly with laser power and pressure. This can be seen in Eqn. 8.15, where the convergence C_a that characterizes the strength of self-focusing scales linearly with saturation parameter S and absorption parameter α_0 . In turn, S is proportional to laser intensity and α_0 is proportional to cell pressure. An observation of these linear dependencies is shown in the next section.

There are two possible conclusions. The first is that the self-focusing model is incorrect due to an assumption that was made. A likely candidate is the Taylor expansion in Eqn. 8.12. With this Taylor expansion made, the beam profile is flat to lowest order, preventing any significant self-focusing from occurring. The other possibility is that self-focusing is not the cause of the observed dispersive signals. Even though it correctly predicts the qualitative structure of the residuals in Fig. 8.17, the large quantitative discrepancy may not be fixed by any of the assumptions made in the analysis. Therefore, at this point, we cannot attribute this effect to self-focusing with any certainty.

8.2.3 Analyzing the Linescan Asymmetry

Regardless of the physical origin of the asymmetry, a method is needed to study its effect on the data. In the method used here, linescans are fit to two different fitting functions, from which the differences in center frequencies, called dispersive shifts,

are obtained. The first fitting function is the sum of a Lorentzian peak, Gaussian background, and constant offset. As described in Chapter 6, this is the same fitting function used for the final data analysis as well as in Fig. 8.13b. The second fitting function differs from the first by the inclusion of a dispersive component. This is the same fitting function used in Fig. 8.13c. Here, the center frequency of the dispersive component is fixed to be equal to the centers of the Lorentzian and Gaussian terms. Similarly, its width is fixed to be equal to the Lorentzian width. Therefore, the second fitting function contains one extra fit parameter, the dispersive amplitude, per peak.

A crucial assumption made here is that the asymmetry in the linescan can be mathematically represented by a dispersive function. Without a physical explanation from which a successful model can be derived, the possibility that the asymmetry has some other form cannot be ruled out. The decision to use a dispersive term is based entirely on the empirical evidence presented in Fig. 8.13. Similarly, the decision to constrain the width and center of this term is also based on empirical evidence: slightly lower values of χ^2 were obtained from the fit with these constraints included.

Even without a physical mechanism, there are still two important reasons for studying dispersive shifts. The first reason is that their dependency on external parameters is useful for understanding the physical mechanism that generates the asymmetry. The second reason is that these shifts can be used to estimate the effects of the asymmetry on zero-pressure intercepts and optical power corrections. However, without a demonstrably correct physical model that justifies the use of the dispersive lineshape, using these estimates may seem crude. Nevertheless, the possibility remains that the asymmetry is truly a dispersive lineshape. Therefore, the error contribution

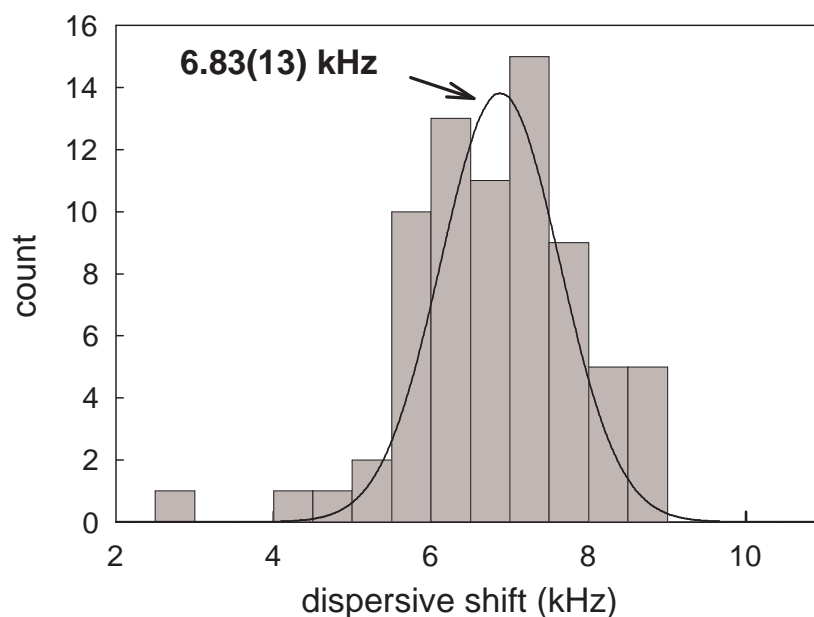


Figure 8.20: Histogram of dispersive shifts for the $2^3S - 2^3P_0$ transition. The values are obtained by subtracting the center frequencies of each linescan when fit with and without a dispersive term. The cell pressure was 30 mtorr, the discharge drive power was 4.5 Watts, and the external magnetic field was 108 Gauss.

due to linescan asymmetry must be large enough to accommodate this outcome.

Fig. 8.20 shows a sample histogram of asymmetry shifts for the $2^3S - 2^3P_0$ transition. A shift of 6.83(13) kHz was obtained, where the uncertainty is equal to the standard error. The presence of a non-zero shift indicates that the signal-to-noise ratio of the asymmetry is high enough for the fits with the dispersive term to converge. If this were not the case, the asymmetry shifts would be scattered around zero.

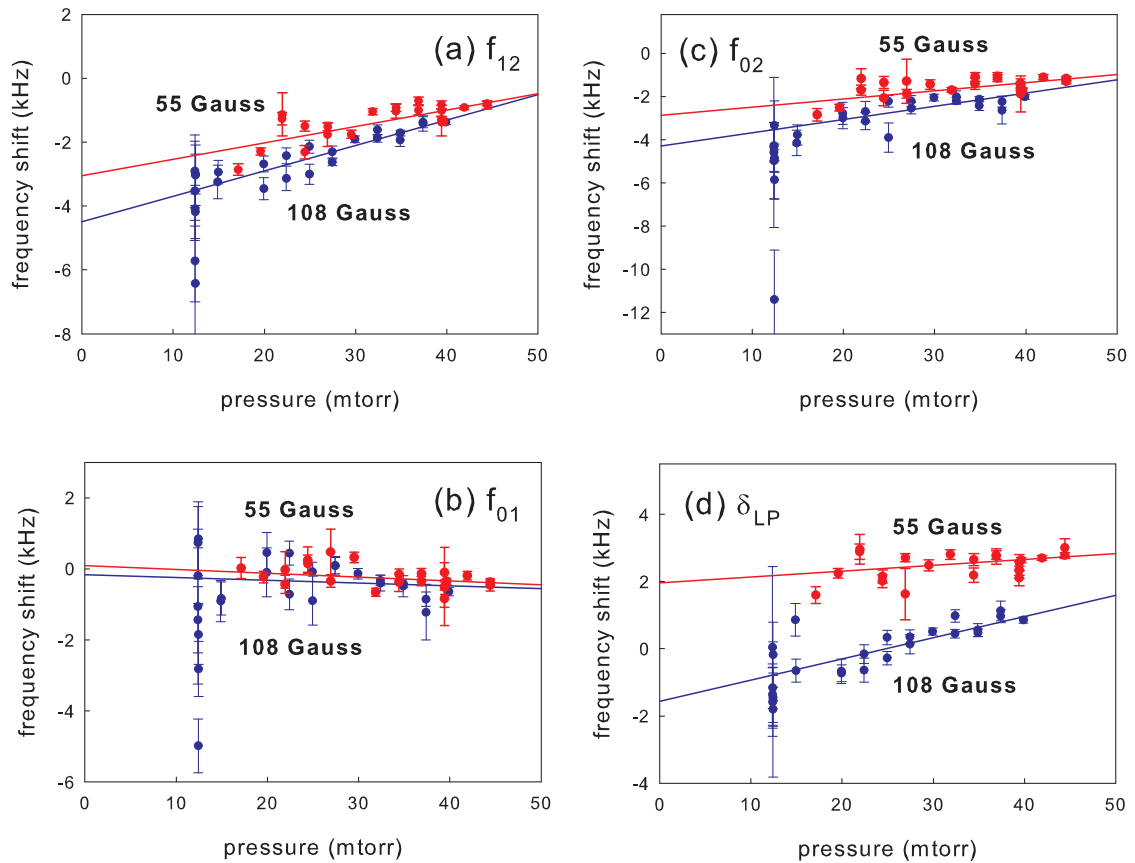


Figure 8.21: Dispersive shifts vary linearly as a function of pressure for the three fine structure intervals and light-pressure shift δ_{LP} . The optical power of each laser beam was $100 \mu\text{W}$ and the discharge drive power was 1 Watt and 4.5 Watts for the data at 55 Gauss and 108 Gauss, respectively.

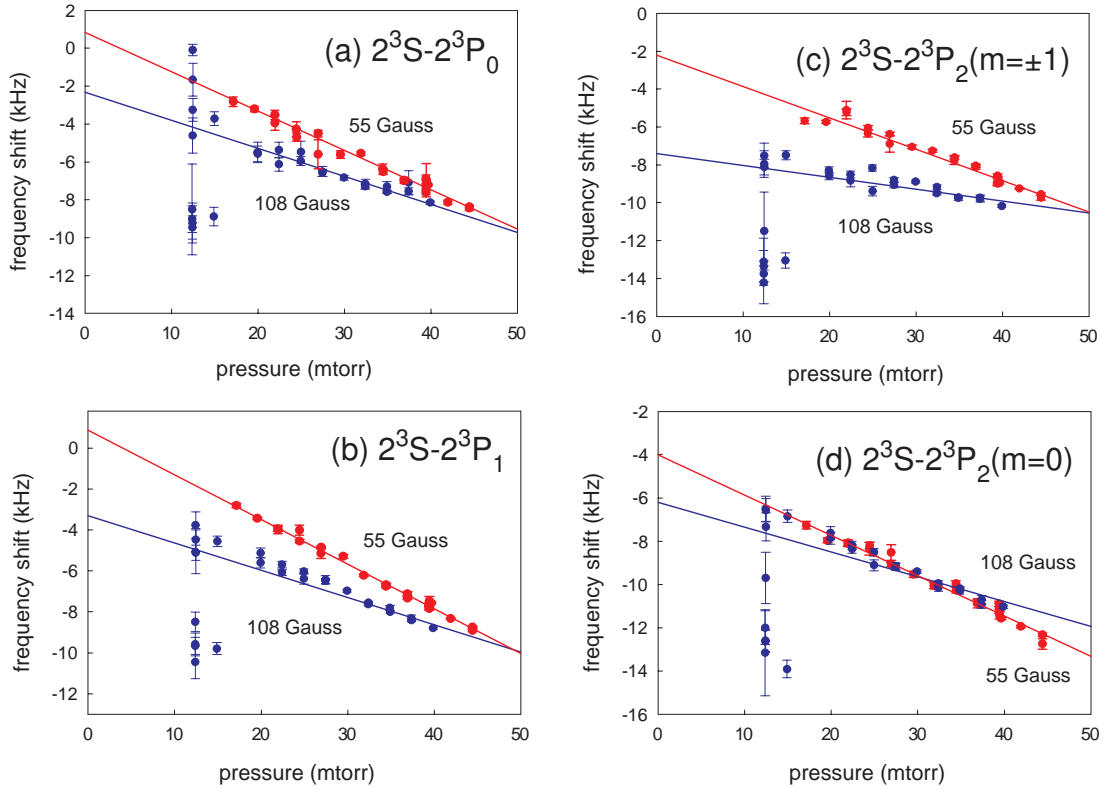


Figure 8.22: Dispersive shifts vary linearly as a function of pressure for the optical transition frequencies.

Pressure Dependency

Fig. 8.21 shows plots of dispersive shifts as a function of pressure for the fine structure intervals and light-pressure shift δ_{LP} . None of the data has been corrected for Zeeman shifts or light-pressure shifts. The dispersive shifts scale linearly with pressure and only for f_{01} do the shifts approach zero at zero pressure. This linear dependency is correctly predicted by self-focusing.

Fig. 8.22 shows plots of dispersive shifts for the optical transitions as a function of pressure. With the exception of some outliers at 12 and 15 mtorr, the shifts decrease

linearly with pressure. Also, the slopes and intercepts of the best-fit lines are different for the two values of the magnetic field. This magnetic field dependence, which cannot be explained by self-focusing, may be due to an imbalance in the amplitudes of $m = \pm 1$ peaks in linescans of P_1 and P_2 . This peak imbalance is described in more detail in the next section.

To estimate the effects of the linescan asymmetry on the zero-pressure intercepts obtained in Section 7.2, the pressure extrapolations were redone using center frequencies obtained the fits with dispersive terms included in the fitting functions. The differences between these zero-pressure intercepts and those in Tables 7.1 and 7.2 represent the shifts due to the asymmetry. For the interval data at 55 Gauss, the differences in the zero-pressure intercepts are -2.78 kHz, 0.87 kHz, and -1.90 kHz for the f_{12} , f_{01} , and f_{02} intervals, respectively. For the interval data at 108 Gauss, the corresponding differences are -4.16 kHz, -0.85 kHz, and -4.97 kHz. For the optical transitions at 55 Gauss, the differences in the zero-pressure intercepts are -3.83 kHz, -4.75 kHz, and -2.15 kHz for the $2^3S - 2^3P_0$, $2^3S - 2^3P_1$, and $2^3S - 2^3P_2$ transitions, respectively. At 108 Gauss, the corresponding differences are 5.17 kHz, 6.31 kHz, and 10.31 kHz.

Since the assumption that the asymmetry is represented by a dispersive lineshape cannot be confirmed, the possibility remains that the asymmetry has a different mathematical form that, when included in the fitting functions, gives rise to even larger shifts. Nevertheless, shifts of the zero-pressure intercepts as large as 5 kHz for the fine structure intervals and 10 kHz for the optical transition frequencies are much larger than statistical uncertainties of 100 Hz.

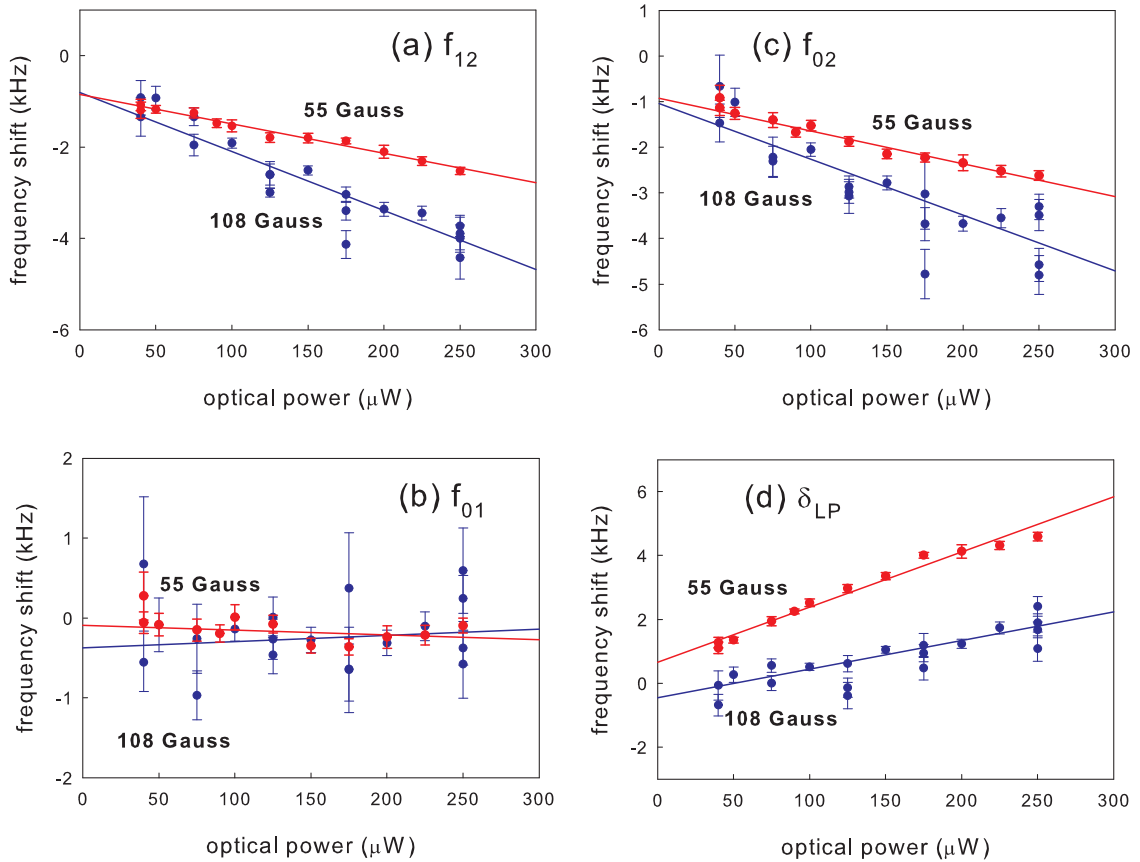


Figure 8.23: Dispersive shifts vary linearly as a function of optical power for the three fine structure intervals and light-pressure shift δ_{LP} . The cell pressure was 30 mtorr and the discharge drive power was 1 Watt and 4.5 Watts for the data at 55 Gauss and 108 Gauss, respectively.

Optical Power Dependency

Figs. 8.23 and 8.24 show plots of dispersive shifts as a function of optical power. None of the data has been corrected for Zeeman shifts or light-pressure shifts. All of the dispersive shifts scale linearly with optical power, an effect that is correctly predicted by self-focusing. Again, a magnetic field dependence, evident in the different intercepts and slopes for data obtained at different magnetic fields, is not predicted

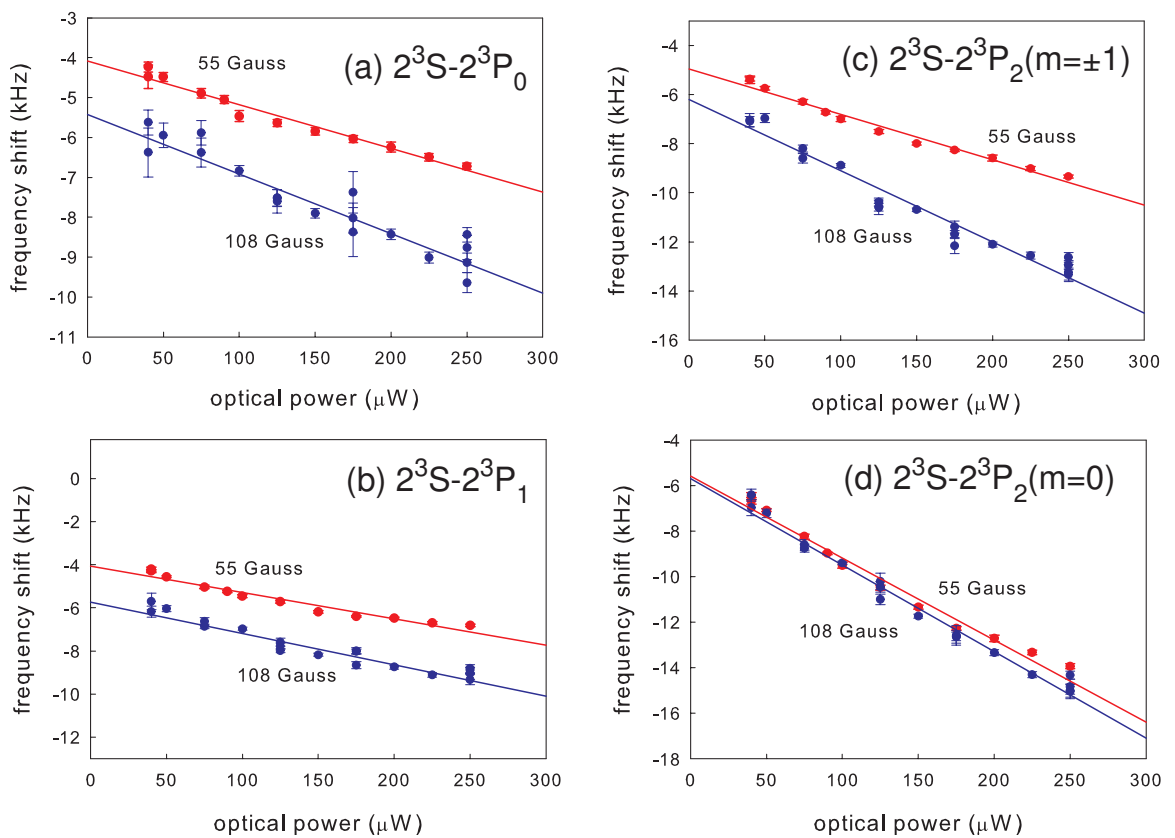


Figure 8.24: Dispersive shifts vary linearly as a function of optical power for the optical transition frequencies.

by self-focusing and may be the result of an imbalance between amplitudes of $m = \pm 1$ peaks in linescans of P_1 and P_2 .

8.2.4 Conclusions

Asymmetries in the linescan that appear to have the form of a dispersive lineshape result in systematic frequency shifts of the fitted Lorentzian linecenters by as much as 30 kHz. An attempt to model the effect as the result of self-focusing gave qualitative agreement with observations, but underpredicted the size of the frequency shifts by several orders of magnitude.

Dispersive shifts, obtained from fits with and without dispersive terms included in the fitting functions, show that the asymmetry scales linearly with pressure and optical power. However, these dispersive shifts do not go to 0 when extrapolated to zero pressure. Therefore, an additional uncertainty should be assigned to this effect. Although a value for this uncertainty could be obtained from dispersive shifts, the assumption that the asymmetry is represented by a dispersive lineshape may be incorrect. Until a demonstrably correct model is found, it is still possible that the asymmetry is represented by a different function that, when included in the fitting function, gives rise to even larger shifts in the fitted linecenters. As a result, dispersive shifts only give a lower bound on the shift caused by the asymmetry.

8.3 Peak Imbalances

A third systematic is an imbalance in the amplitudes of the $m = \pm 1$ peaks in P_1 and P_2 linescans (Figs. 8.25 and 8.26) that is not understood. There is evidence that

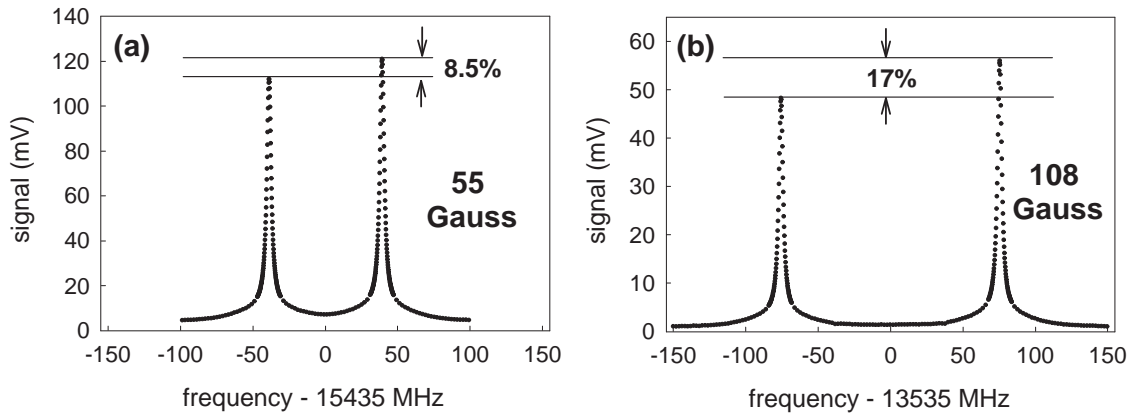


Figure 8.25: Sample scans of the $2^3S - 2^3P_1$ transition for external magnetic fields of (a) 55 Gauss, and (b) 108 Gauss, show an imbalance in the amplitudes of the two peaks. The right peak, corresponding to the $m = +1$ transition, is larger. For both scans, the cell pressure was 40 mtorr and the optical power of each laser beam was $100 \mu\text{W}$.

this peak imbalance affects the fitted center frequencies of the left and right peaks differently, potentially introducing a source of systematic error. Although its origins are unknown, several observed dependencies on experimental parameters help rule out possible explanations for the effect.

8.3.1 Measurements of Peak Imbalance

Plotted in Fig. 8.27, as a function of magnetic field, are the ratios of the left and right peak amplitudes of P_1 and P_2 linescans. For P_1 , a ratio greater than 1 corresponds to a larger right peak, while for P_2 a ratio less than 1 corresponds to a larger left peak. In both cases, the larger peak corresponds to the transition between $m = +1$ states. The peak imbalance depends linearly on the magnitude of the external magnetic field. Zero-field intercepts of 0.997(2) and 0.996(1) for P_1 and

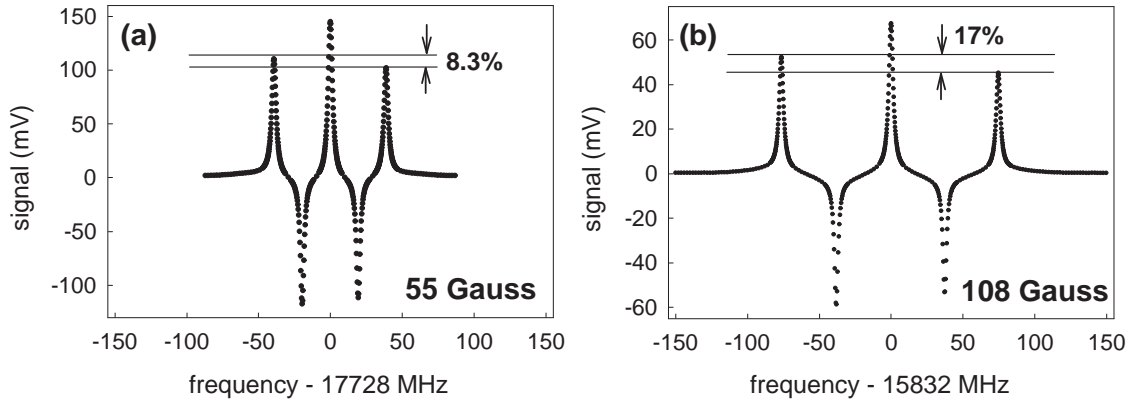


Figure 8.26: Sample scans of the $2^3S - 2^3P_2$ transition for external magnetic fields of (a) 55 Gauss, and (b) 108 Gauss, show an imbalance in the amplitudes of the outer peaks. The left peak, corresponding to the $m = +1$ transition, is larger. For both scans, the cell pressure was 40 mtorr and the optical power of each laser beam was $100 \mu\text{W}$.

P_2 ratios, respectively, are almost in agreement with unity. When the direction of the magnetic field was flipped, the $m = +1$ peak remained larger than the $m = -1$ peak, indicating that the effect is independent of the direction of the field.

The peak imbalance has a linear dependence on pressure (Fig. 8.28a). Slopes of $6.19(12) \cdot 10^{-4}/\text{mtorr}$ at 55 Gauss and $12.16(13) \cdot 10^{-4}/\text{mtorr}$ at 108 Gauss have a ratio of 1.965(44), in agreement with the magnetic field ratio of 1.94. The optical power of each laser beam was $100 \mu\text{W}$ and the discharge drive powers were 1 Watt and 4.5 Watts for the data at 55 Gauss and 108 Gauss, respectively.

The peak imbalance decreases nonlinearly with optical power (Fig. 8.28b). Here, the cell pressure was 30 mtorr and the discharge drive powers were 1 Watt and 4.5 Watts for the data at 55 Gauss and 108 Gauss, respectively.

Small dependencies on discharge powers of $40.3(146) \cdot 10^{-5}/\text{Watt}$ and

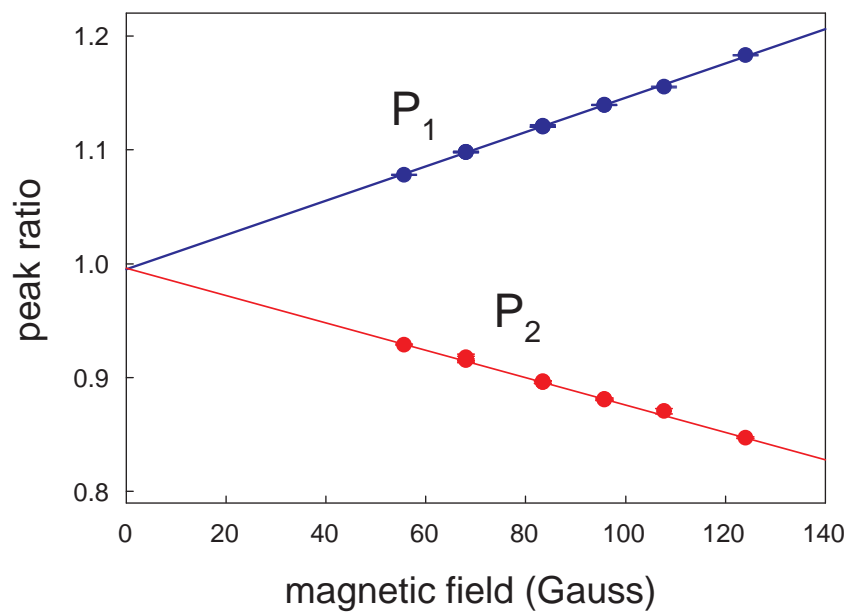


Figure 8.27: Ratios of the left and right peak amplitudes of P_1 and P_2 lines—can scale linearly with the magnitude of the external magnetic field. The cell pressure was 30 mtorr, the optical power of each laser beam was $100 \mu\text{W}$, and the discharge drive power was 1 Watt.

$3.2(20)\cdot 10^{-5}/\text{Watt}$ were measured at magnetic fields of 55 Gauss and 108 Gauss, respectively (Fig. 8.28c and d). Here, the optical power of each laser beam was $100\ \mu\text{W}$ and the cell pressure was 40 mtorr and 30 mtorr for the data at 55 Gauss and 108 Gauss, respectively.

With a measured dependency of $-6.4(65)\cdot 10^{-5}/\text{deg}$, no dependency on the laser polarization angle was observed (Fig. 8.28e). Here, the cell pressure was 30 mtorr, the optical power of each laser beam was $100\ \mu\text{W}$, and the discharge drive power was 1 Watt.

8.3.2 Searching for an Explanation for the Peak Imbalance

We consider three ways in which an imbalance in the $m = \pm 1$ peak amplitudes could arise. First, could the two transitions have different strengths? This seems to be unlikely given that their reduced matrix elements are identical and their Clebsch-Gordan coefficients have the same value. The second scenario is that there is an imbalance in the populations of the $m = \pm 1$ sublevels of the 2^3S state. One way this could happen is by optical pumping with circularly-polarized light. However, the laser beams are linearly polarized with a very high polarization extinction ratio of $10^6:1$, making this explanation unlikely.

Third, magnetic field inhomogeneity was one attractive candidate for an explanation of the peak imbalance. Here, $m = 1$ and $m = -1$ states, acting as high-field and low-field seekers in the presence of field inhomogeneity, spatially separate in a way that leaves more $m = +1$ states in the center of the cell. The lasers probe more $m = +1$ atoms, giving rise to an imbalance in the peak amplitudes. To check for the

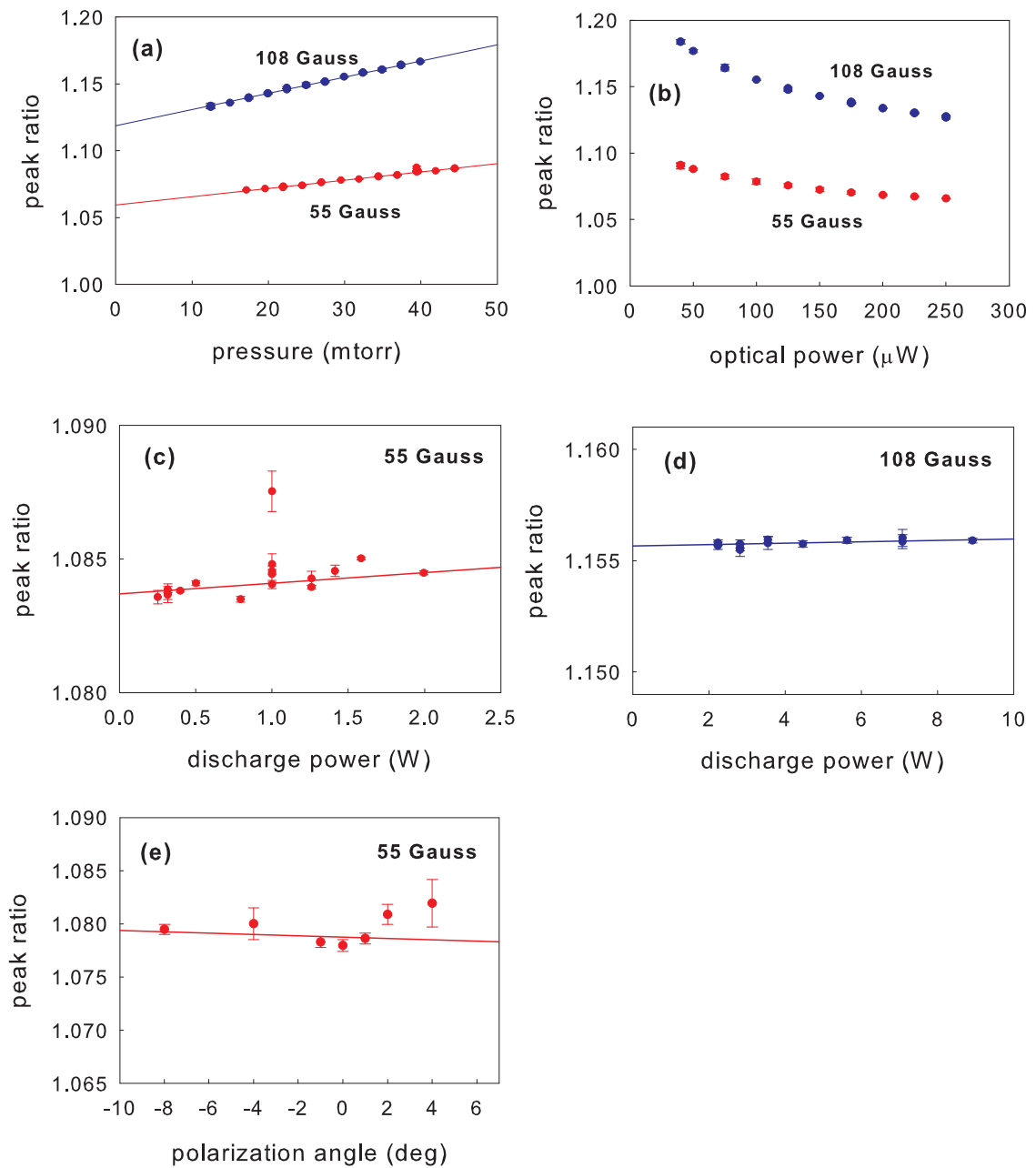


Figure 8.28: The ratio of the amplitudes of the two peaks of P_1 (a) scales linearly with pressure, and (b) decreases nonlinearly with optical power. Weak dependencies on discharge drive power were observed at (c) 55 Gauss and (d) 108 Gauss. (e) No dependency on laser polarization was observed.

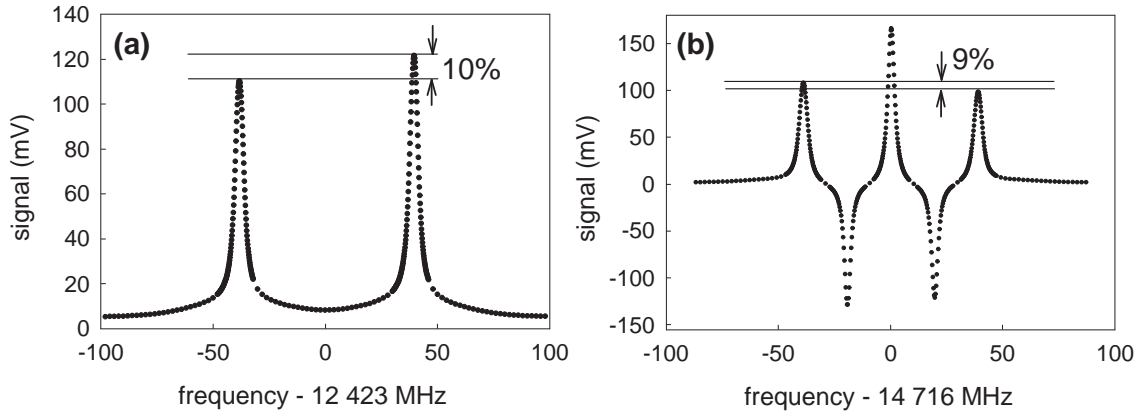


Figure 8.29: (a) P_1 and (b) P_2 linescans taken in an inhomogeneous magnetic field produced by running current through one of the Helmholtz coils. The cell pressure was 40 mtorr, the optical power of each laser beam was $100 \mu\text{W}$, the discharge drive power was 1 Watt, and the magnetic field in the cell was approximately 55 Gauss.

effects of magnetic field inhomogeneity, linescans of the $2^3S - 2^3P_1$ and $2^3S - 2^3P_2$ transitions were measured with current passing through only one of the Helmholtz coils. The current was doubled so that the magnitude of the field was not changed significantly. No significant change in the peak imbalance was observed (Fig. 8.29).

8.3.3 Frequency Shifts Due to Peak Imbalance

We have no clear way to determine if the peak imbalance results in systematic frequency shifts. Indirect evidence can be seen in Figs. 8.21-8.24, where plots of dispersive shifts (see Section 8.2.3) show different results for data taken at two different values of the external magnetic field. If the linescan asymmetry is due to a physical mechanism that treats the $m = \pm 1$ transitions equally (self-focusing is one example), then this magnetic field dependence may be the result of the peak imbalance. An-

other possibility is that this magnetic field dependence and the peak imbalance are both results of a single underlying mechanism. Either way, the possibility that the peak imbalance introduces systematic frequency shifts still remains.

To account for the peak imbalance, separate fit parameters are used for the amplitudes of the left and right peaks. However, the presence of a peak imbalance may also imply the presence of systematic frequency shifts. One way to check for this possibility is to compare dispersive shifts for the $m = +1$ and $m = -1$ peaks of P_1 and P_2 linescans. The approach of using dispersive shifts relies on the assumption that the amplitude of the linescan asymmetry scales with transition strength and the number of atoms interacting with the laser beams. With this assumption, which would be reasonable if the asymmetry could be explained by self-focusing, dispersive shifts for the left and right peaks of P_1 and P_2 should have the same dependency on laser power and pressure. In addition, they should differ in magnitude by at most 5-15%, the level of the amplitude discrepancy. Any deviation from this expected behavior could be linked to the peak imbalance, the only other effect that was observed to affect the two peaks differently.

Fig. 8.30 shows dispersive shifts for the $m = \pm 1$ peaks of the $2^3S - 2^3P_1$ transition as functions of (a,b) optical power, and (c,d) cell pressure. Two important effects can be seen. First, the $m = +1$ shifts are larger than the $m = -1$ shifts. This could be explained by either a significant discrepancy in the magnitude of the asymmetry or by the presence of additional linescan distortions that are different for the two peaks. The second feature is that there is a magnetic field dependence for dispersive shifts of the $m = -1$ peak (Fig. 8.30a and c), as demonstrated by the different slopes and

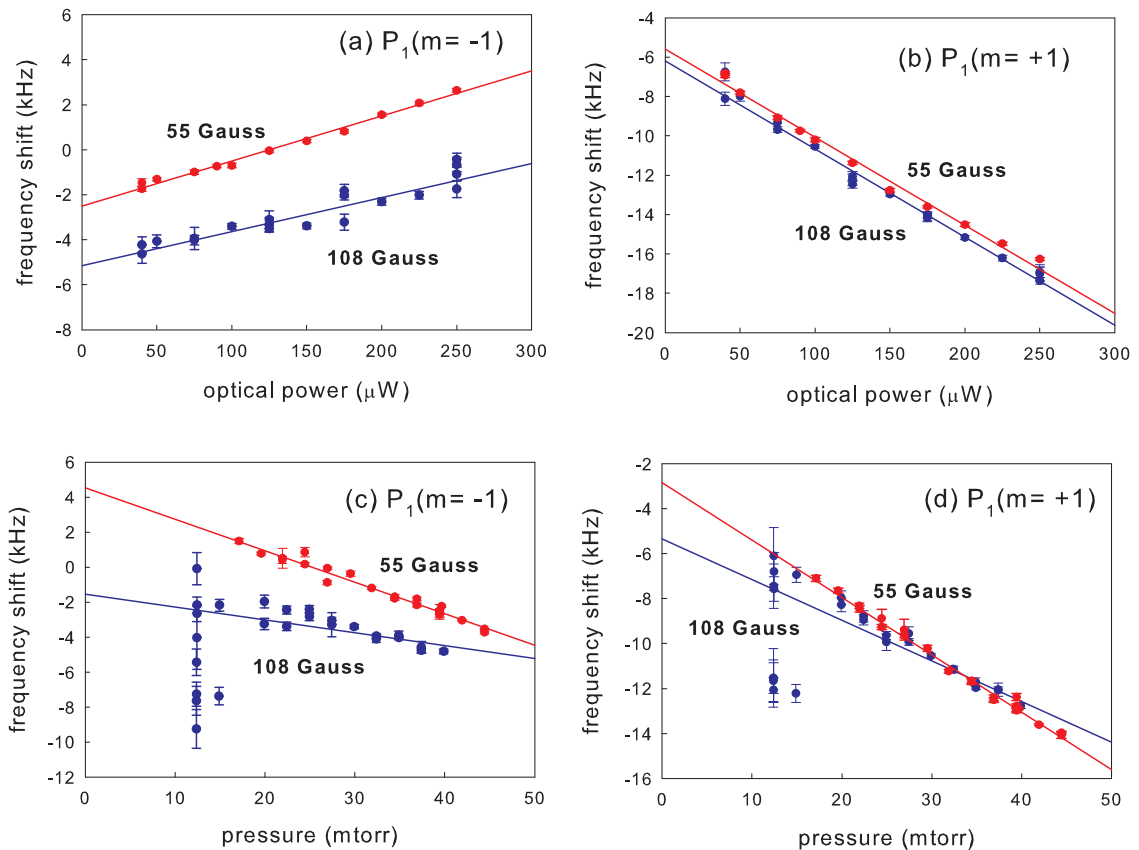


Figure 8.30: Dispersive shifts obtained by subtracting the center frequencies of P_1 linescans from fits with and without dispersive terms included in the fitting functions: (a) the $m = -1$ peak, and (b) the $m = +1$ peak as a function of optical power. Here, the cell pressure is 30 mtorr. (c) The $m = -1$ peak, and (d) the $m = +1$ peak as a function of cell pressure. Here, the optical power of each laser beam is $100 \mu\text{W}$. The discharge drive power is 1 Watt and 4.5 Watts for the data at 55 Gauss and 108 Gauss, respectively.

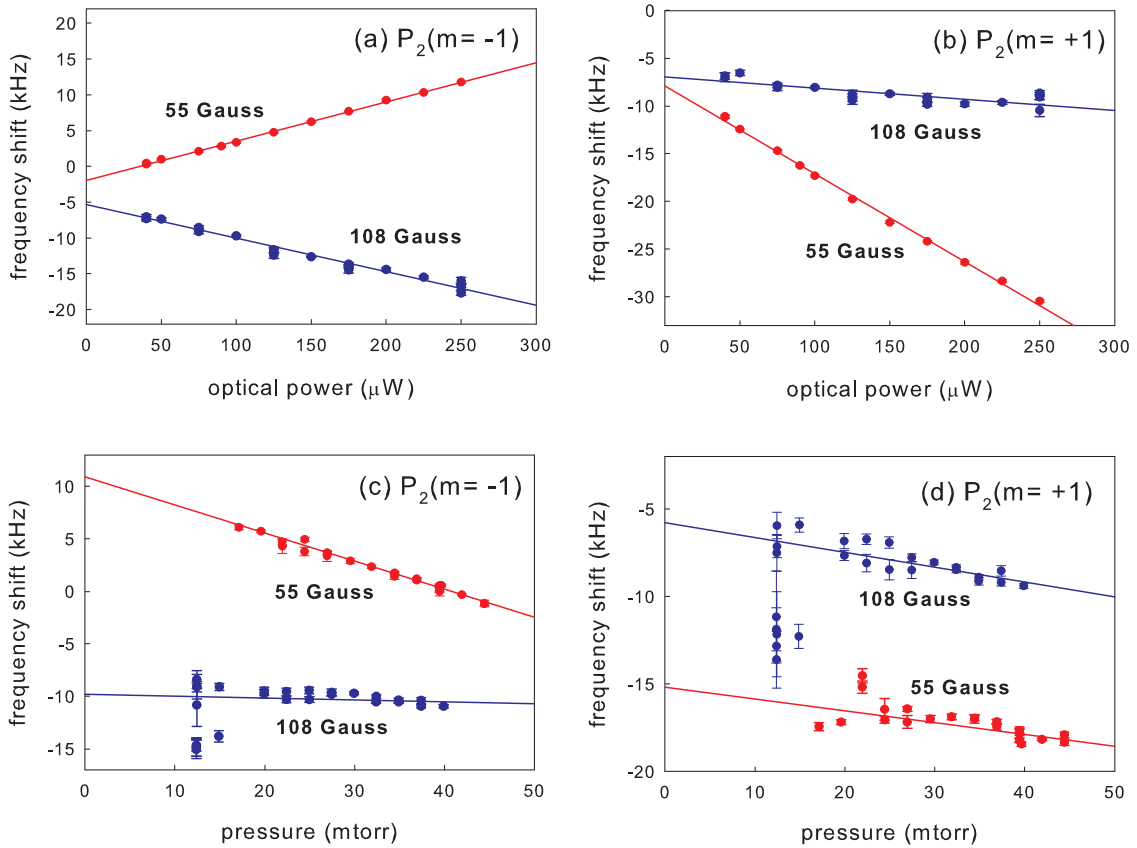


Figure 8.31: Dispersive shifts obtained from P_2 linescans: (a) the $m = -1$ peak, and (b) the $m = +1$ peak as a function of optical power. Here, the cell pressure is 30 mtorr. (c) The $m = -1$ peak, and (d) the $m = +1$ peak as a function of cell pressure.

intercepts obtained at two values of the magnetic field.

Fig. 8.31 shows dispersive shifts for the $m = \pm 1$ peaks of the $2^3S - 2^3P_2$ transition as functions of (a,b) optical power, and (c,d) cell pressure. Here, shifts up to 30 kHz are much larger than the corresponding P_1 shifts. Again, $m = +1$ shifts and $m = -1$ shifts differ in magnitude and depend on the value of the magnetic field. Two unique features are slopes of opposite sign in Fig. 8.31a and shifts of opposite sign in Fig. 8.31b.

There are three conclusions that could be made from Figs. 8.30 and 8.31. The first is that there is a correlation between the peak imbalance and the discrepancy between $m = \pm 1$ dispersive shifts. Here, either the peak imbalance shifts the fitted center frequencies of the $m = \pm 1$ peaks by different amounts, or both effects are the result of a single underlying cause. The argument in favor of this outcome is that the peak imbalance and the discrepancies between $m = \pm 1$ dispersive shifts are the only two observed effects that both result in different properties of the two peaks and have a magnetic field dependence. This conclusion would indicate that the peak imbalance is an important source of systematic frequency shifts.

A second possible outcome is that the linescan asymmetry affects $m = \pm 1$ peaks differently, and the peak imbalance has no effect on the fitted center frequencies. However, for this outcome to be true, a model for the asymmetry that predicts different shifts for the $m = \pm 1$ transitions is necessary.

A third outcome is that the discrepancy between $m = \pm 1$ dispersive shifts does not depend on the asymmetry or peak imbalance. In this case, a field-dependent effect other than the peak imbalance would be needed.

The only definite conclusion that can be made is that the peak imbalance may be a source of systematic frequency shifts. A stronger conclusion cannot be made because the use of dispersive shifts is complicated by the lack of a good model to explain the linescan asymmetry. Therefore, any conclusion that could be made here about the peak imbalance could also be attributed to the asymmetry. A better analysis technique is needed to distinguish between shifts due to the linescan asymmetry and shifts due to the peak imbalance.

8.4 Optical Power Shifts

AC Stark shifts give rise to systematic frequency shifts that scale linearly with the optical power of the laser beams. Presented in this section are AC Stark shift calculations and measurements of optical power shifts. Discrepancies between these calculations and measurements could be due to the intensity-dependence of the linescan asymmetry. Assuming this to be the case, calculated AC Stark shifts are used to correct for the finite laser power used in measurements of linear pressure shifts (see Section 7.2).

8.4.1 AC Stark Shifts Calculations

AC Stark shifts arise from coupling of multiple energy levels by the laser fields [116, 135]. For a two-level system, AC Stark shifts scale as Ω^2/δ , where Ω is the Rabi frequency and $\delta = \omega_o - \omega_L$ is the detuning of the laser frequency ω_L from the atomic transition frequency ω_o . Here, it is assumed that $\Omega \ll |\delta|$.

For a two-level system, Stark shifts that arise when the laser is red-detuned have the opposite sign of shifts that arise when the laser is blue-detuned. As a result, the shifts cancel for center frequencies obtained by fitting the complete lineshape. Non-zero AC Stark shifts arise only when coupling of the laser fields to additional energy levels is considered.

Due to the inverse scaling with detuning, only states with energies close to the ground and excited states of the two-level system will have a non-negligible contribution to the AC Stark shift. For each of the 2^3P_J states, there are two 2^3P_J states nearby. The 2^3S state has no neighboring energy levels.

It is assumed that the pump and probe polarizations are aligned perfectly with the external magnetic field. Therefore, non-zero coupling only occurs for $\Delta m = 0$ transitions. This assumption is reasonable even for imperfect alignment of the laser polarizations, for which coupling of $\Delta m = \pm 1$ transitions becomes non-zero. For measurements of the $2^3S - 2^3P_0$ transition, Stark shifts from $\Delta m = \pm 1$ transitions have opposite signs, and therefore cancel. For the $2^3S - 2^3P_1$ and $2^3S - 2^3P_2$ transitions, AC Stark shifts from $\Delta m = \pm 1$ transitions are nonzero for the $m = \pm 1$ peaks of the linescan. However, these shifts have opposite signs, and therefore cancel when the left and right peak frequencies are averaged.

The AC Stark shift of the $2^3S - 2^3P_i$ transition ($i=0,1,2$) is computed from a 4×4 matrix $\hat{\mathbf{H}}$ that describes the couplings of all three 2^3P_J energy levels to the ground 2^3S state in the presence of a laser field $E(t) = E_0 \cos(\omega_L t)$. Working in a reference frame that rotates at frequency ω_L , and making the rotating-wave approximation, $\hat{\mathbf{H}}$ can be written in block-form:

$$\hat{\mathbf{H}} = \begin{pmatrix} \hat{\mathbf{H}}_0 & \hat{\mathbf{V}}^\dagger \\ \hat{\mathbf{V}} & \hat{\mathbf{H}}' \end{pmatrix} = \left(\begin{array}{cc|cc} 0 & \frac{\Omega_i}{2} & \frac{\Omega_j}{2} & \frac{\Omega_k}{2} \\ \frac{\Omega_i}{2} & \delta & 0 & 0 \\ \hline \frac{\Omega_j}{2} & 0 & \delta - \epsilon_j & 0 \\ \frac{\Omega_k}{2} & 0 & 0 & \delta - \epsilon_k \end{array} \right) \quad (8.24)$$

where ϵ_j , the detuning of the 2^3P_j state from the 2^3P_i state, is given by the fine structure splitting f_{ij} . The same relation holds for ϵ_k . The coupling strength between the ground 2^3S state and excited 2^3P_i state is given by the Rabi frequency $\Omega_i = (\mu_i E_0)/\hbar$, where μ_i is the dipole matrix element of the $2^3S - 2^3P_i$ transition.

The matrix $\hat{\mathbf{H}}_0$ is the 2×2 Hamiltonian of the two-state system in the absence of

neighboring states [116, 135]. The diagonal matrix $\hat{\mathbf{H}}'$ contains all the detunings for non-resonant states that generate non-zero AC Stark shifts. The matrices $\hat{\mathbf{V}}^\dagger$ and $\hat{\mathbf{V}}$ contain the couplings of the two non-resonant states to the ground state.

Consisting of a 2×2 matrix, an effective Hamiltonian $\hat{\mathbf{H}}_{\text{eff}}$ is computed [136]

$$\hat{\mathbf{H}}_{\text{eff}} = \hat{\mathbf{H}}_0 + \hat{\mathbf{V}} \cdot (\delta \hat{\mathbf{I}} - \hat{\mathbf{H}}')^{-1} \cdot \hat{\mathbf{V}}^\dagger = \begin{pmatrix} a & b \\ c & d \end{pmatrix}, \quad (8.25)$$

where $\hat{\mathbf{I}}$ is the 2×2 identity matrix, and the four matrix elements are represented as a , b , c , and d .

$\hat{\mathbf{H}}_{\text{eff}}$ can be used to solve for the 2×2 density matrix $\hat{\rho}$. In the steady-state,

$$\frac{d\hat{\rho}}{dt} = -\frac{i}{\hbar} [\hat{\mathbf{H}}_{\text{eff}}, \hat{\rho}] = 0. \quad (8.26)$$

The absorptive lineshape $S(\delta)$ is proportional to the imaginary component of the off-diagonal density matrix element ρ_{12} . Eqn. 8.26 is used to express ρ_{12} in terms of a , b , c , and d . The result is

$$S(\delta) = \text{Im}[\rho_{12}(\delta)] = \frac{b(\delta)}{d(\delta) - a(\delta) - i\Gamma} \quad (8.27)$$

where the decay rate Γ is added phenomenologically.

Eqns. 8.24, 8.25, and 8.27 are implemented numerically in Mathematica. The electric field amplitude E_0 , used for computing the Rabi frequencies, is obtained from measurements of the laser power and the 1 cm diameter of the beams. The maximum value of the lineshape $S(\delta)$ is obtained numerically; the corresponding value of δ is the AC Stark shift.

8.4.2 Measurements of Optical Power Shifts

To measure optical power shifts, data was taken at several values of the laser power and linearly extrapolated to zero power. Fig. 8.32 shows the data, best-fit lines, and calculated AC Stark shifts for the optical transition frequencies. Fig. 8.33 shows the results for the fine structure intervals and light-pressure shift δ_{LP} . All frequencies were corrected for nonlinear Zeeman shifts, but not light-pressure shifts.

There are two important features in Figs. 8.32 and 8.33. First, for the optical transitions, the calculated AC Stark shifts are smaller than the measured optical power shifts. One explanation for this feature is that measurements of optical power shifts probe the intensity dependence of the linescan asymmetry as well as the AC Stark shift. The intensity dependence of the asymmetry was studied in Section 8.2.3, where each linescan was fit with and without dispersive lineshapes included in the fitting function. Differences in the center frequencies scaled linearly with optical power (see Fig. 8.24). In addition, these frequency differences shifted the same way for all three optical transitions.

The second feature is that for the $2^3S - 2^3P_1$ and $2^3S - 2^3P_2$ transitions (Fig. 8.32b and c), shifts measured at two values of the external magnetic field have different values. This is unexpected since the dependency of the AC Stark shifts on magnetic field is expected to be weak. Here the largest Zeeman shifts of 75 MHz represent at most a 3% change in the Stark shift detunings of 2.3 GHz to 32 GHz. The expected 3% change in the values of the Stark shifts contrasts sharply with measured shifts at 55 Gauss that are 50% and 140% larger than the measured shifts at 108 Gauss.

Since the $2^3S - 2^3P_1$ and $2^3S - 2^3P_2$ frequencies are obtained by averaging tran-

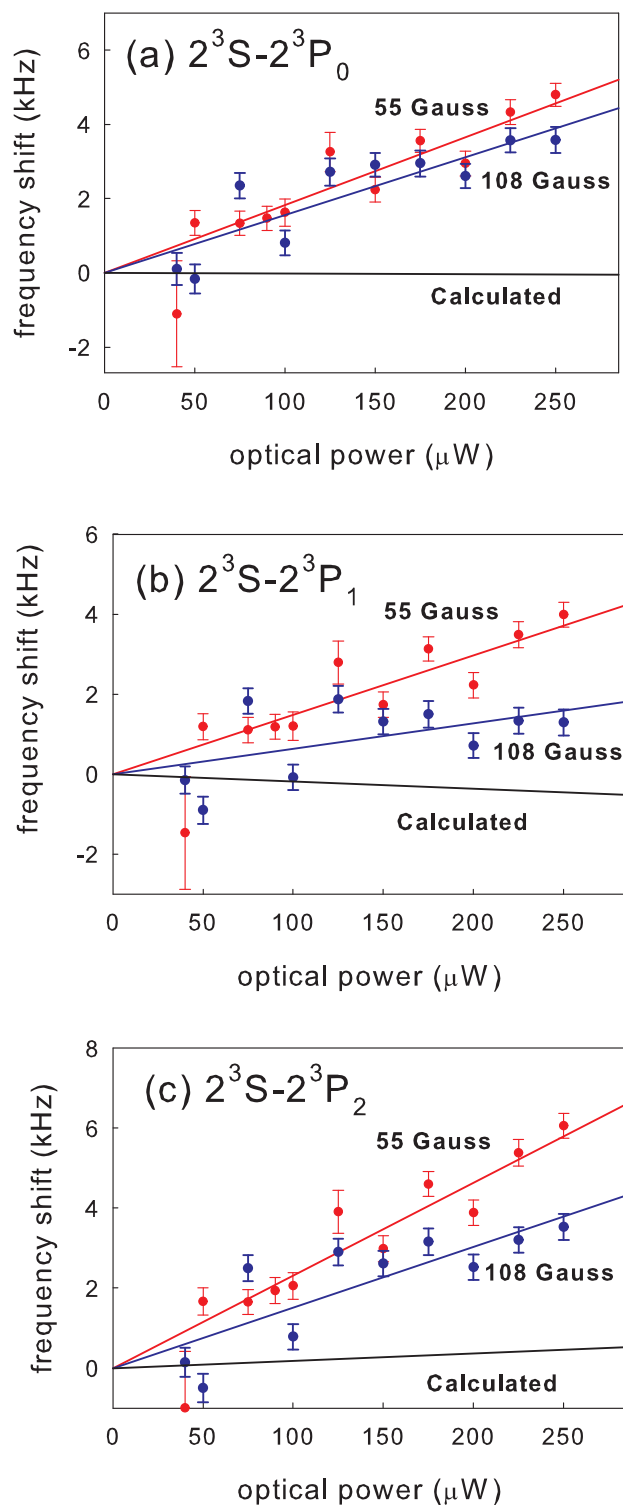


Figure 8.32: Calculated AC Stark shifts (black) and measured optical power shifts at 55 Gauss (red) and 108 Gauss (blue) for the optical transitions. The colored lines are the best-fit results when the data is extrapolated to zero optical power. The cell pressure was 30 mtorr.

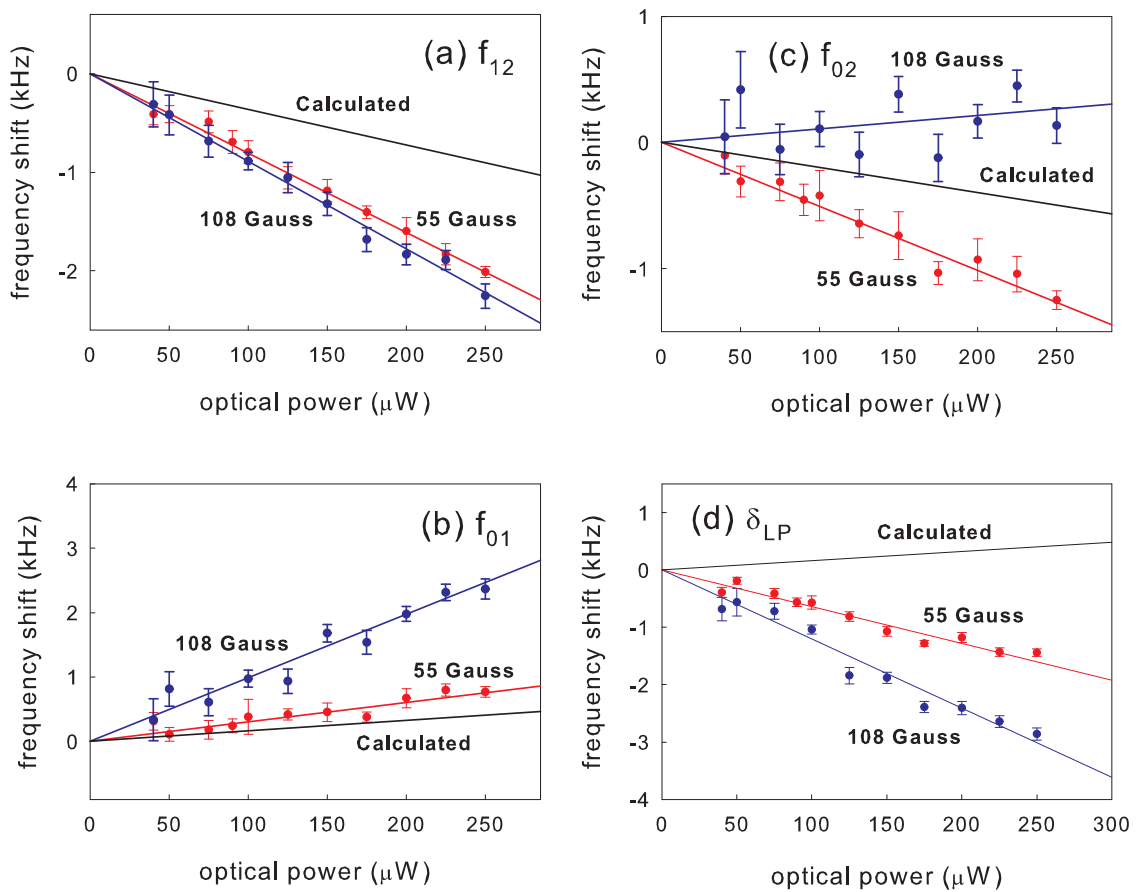


Figure 8.33: Calculated AC Stark shifts (black) and measured optical power shifts at 55 Gauss (red) and 108 Gauss (blue) for the fine structure intervals and light-pressure shift δ_{LP} . The colored lines are the best-fit results when the data is extrapolated to zero optical power. The cell pressure was 30 mtorr.

sition frequencies between $m = +1$ and $m = -1$ states, the observed magnetic field dependence may be related to the $m = \pm 1$ peak imbalance discussed in the previous section. In fact, the two transitions depend similarly on magnetic field, resulting in measured shifts of the f_{12} interval that are independent of the magnetic field (Fig. 8.33a). The magnetic field dependencies observed for the $2^3S - 2^3P_1$ and $2^3S - 2^3P_2$ transitions, but not the $2^3S - 2^3P_0$ transition, lead to measurements of optical power shifts for the f_{01} and f_{02} intervals that were also observed to depend on the magnetic field (Fig. 8.33b and c).

Due to different transition strengths for the $m = 0$ peak and the $m = \pm 1$ peaks of the $2^3S - 2^3P_2$ transition, the light-pressure shift δ_{LP} is expected to have a non-zero AC Stark shift. Although measured optical power shifts of δ_{LP} are non-zero, they disagree with the calculated AC Stark shifts. This disagreement could be due to the linescan asymmetry. As shown in Figs. 8.24c and d, dispersive shifts for the $2^3S - 2^3P_2(m = 0)$ transition are larger in magnitude than shifts for the average of the $2^3S - 2^3P_2(m \pm 1)$ transitions.

Table 8.1 lists the slopes and values of χ_ν^2 obtained from linear extrapolations of the fine structure intervals, light-pressure shift, and optical transition frequencies to zero optical power. For the intervals, values of χ_ν^2 close to 1 indicate good fits. The resulting errors of less than 1 kHz/mW are more than a factor of 2 smaller than previously measured [13]. For the optical transitions, values of χ_ν^2 greater than 1 indicate poor fits. As seen in Fig. 8.32, correlated scatter of the data points about the best-fit lines indicate a non-Gaussian noise source. Two likely causes of this correlation are the Rb standard (see Section 4.3.4) and drift in the beam alignment

	slope (Hz/ μ W)	χ^2_ν	slope (Hz/ μ W)	χ^2_ν
$f_{12} = 2^3P_1 - 2^3P_2$			$2^3S - 2^3P_0$	
55 Gauss	-8.04(37)	0.24	18.3(16)	1.83
108 Gauss	-8.89(63)	0.36	15.6(17)	4.43
$f_{01} = 2^3P_0 - 2^3P_1$			$2^3S - 2^3P_1$	
55 Gauss	3.03(47)	0.90	14.9(16)	2.20
108 Gauss	9.87(84)	1.08	06.3(15)	6.82
$f_{02} = 2^3P_0 - 2^3P_2$			$2^3S - 2^3P_2$	
55 Gauss	-5.07(49)	0.50	23.2(16)	6.67
108 Gauss	1.07(82)	1.58	15.2(15)	5.98
δ_{LP}				
55 Gauss	-6.38(32)	3.05		
108 Gauss	-12.04(59)	2.98		

Table 8.1: Results of linear extrapolations of the fine structure intervals, light-pressure shift, and optical transition frequencies to zero optical power.

(see Section 8.1.4). To account for the accuracy limitation of the Rb standard, 300 Hz was added to the uncertainty of each optical frequency point. No uncertainty was included for beam alignment drift.

8.4.3 AC Stark Shift Corrections

Previously, measured optical power shifts were used to correct for the finite laser power used in measurements of linear pressure shifts (see Section 7.2). However, discrepancies between the calculated AC Stark shifts and the measured optical power shifts may be explained by the intensity dependence of the linescan asymmetry. Assuming this to be true, frequency corrections derived from the measured shifts correct for shifts due to the AC Stark effect and the linescan asymmetry. If the asymmetry had been found to depend only on optical power, this correction would conveniently correct for two systematics simultaneously. However, the linescan asymmetry was also found to depend on pressure (see Section 8.2.3). Therefore, to correct for the finite laser power, it seems unlikely that using the measured optical power shifts is the best procedure. Instead, calculated AC Stark shifts are used.

The largest source of uncertainty in the AC Stark shift calculations is the non-uniform intensity profile of the laser beams. Although the uniformity was improved by increasing the beam diameter with telescopes and blocking the wings of the beam profile with irises (see Chapter 5), a 25% variation in the beam intensity across the profile is expected. Therefore, the uncertainty in the calculated AC Stark shifts is taken to be $\pm 25\%$ of the value of the shift.

The AC Stark shift corrections, calculated for an optical power of 100 μW per

laser beam, are 0.36(9) kHz, -0.25(5) kHz, and 0.12(5) kHz for the f_{12} , f_{01} , and f_{02} intervals, respectively. For the optical frequencies, the corrections are -0.23(6) kHz, -0.15(9) kHz, and -0.51(9) kHz for the $2^3S - 2^3P_0$, $2^3S - 2^3P_1$, and $2^3S - 2^3P_2$ transitions, respectively.

8.5 Conclusions

Improved experimental resolution has led to the discovery of three new systematics and an improved understanding of a fourth systematic. A misalignment of the pump and probe laser beams, in conjunction with the non-thermal distribution of atomic velocities in an RF discharge cell, leads to residual Doppler shifts that are larger than 6 kHz. Although this effect is now one of the two dominant error sources for the optical frequency measurements, measurements of the fine structure intervals are significantly less affected. An observed asymmetry in the linescans, which has not yet been successfully described by a physical mechanism, affects measurements of the fine structure intervals and optical transition frequencies by as much as 10 kHz. It is the dominant source of uncertainty for measurements of the fine structure intervals and one of two dominant error sources for the optical frequency measurements. An observed imbalance in the amplitudes of $m = \pm 1$ peaks in P_1 and P_2 linescans remains unexplained. Last, the observed intensity dependence of the linescan asymmetry may explain discrepancies between calculated AC Stark shifts and measured optical power shifts. These calculated AC Stark shifts are now used to correct for the finite laser power used in measurements of linear pressure shifts.

Chapter 9

Conclusions

The 2^3P fine structure intervals and $2^3S - 2^3P_J$ optical transition frequencies in helium were measured to a precision that was higher than what was previously attained. The improved stability from an iodine optical frequency reference removed what had been the largest source of experimental drift. Its high stability and narrow linewidth were transferred to 1083 nm using an optical frequency comb that also allowed optical frequencies to be measured accurately with respect to the SI second. The higher resolutions that were achieved from these improvements were crucial for discovering new systematic effects and for improving our understanding of already-known systematics.

This chapter summarizes the major advances that were achieved toward improving both the precision and accuracy of helium spectroscopy in an RF discharge cell. A comparison of systematic effects indicates what steps must be taken next in order to improve accuracy even further. Suggestions are given for future improvements to the experiment, including some possibilities for removing shifts due to laser beam mis-

alignment. This chapter ends with a brief discussion of a measurement that could be done using our system that could help reveal the source of the discrepancies between theoretical and calculated values of the 2^3P fine structure intervals.

9.1 Experimental Resolution Has Been Significantly Improved

Several modifications to the experiment significantly improved experimental resolution to the 100 Hz level. Previously, the largest source of drift in the experiment was the ^3He optical frequency reference. By switching to an iodine reference, frequency drift was reduced by a factor of 40. Occurring at approximately 500 seconds, the lowest Allan deviation of $5 \cdot 10^{-14}$ corresponds to a frequency uncertainty of only 15 Hz at the helium wavelength of 1083 nm.

The utility of the optical frequency comb for laser spectroscopy was demonstrated by its ability to simultaneously compare optical frequencies to the SI second and transfer high clock stabilities across the visible and infrared spectra. Contrary to how most groups utilize a frequency comb, phase-locking the 1083 nm scan laser to the comb allowed us to use an optical frequency reference with higher stability and narrower linewidth compared to any that could be constructed at 1083 nm. In addition, the phase-coherent transfer of the low phase noise of the iodine reference was also demonstrated. Here, the 50 kHz free-running linewidth of the scan diode laser at 1083 nm was reduced a factor of 10 to 5 kHz when phase-locked to the iodine-stabilized frequency comb.

Much effort went into stabilizing the optical frequency comb, as needed to keep the experiment running uninterruptedly for as long as possible. To minimize phase noise introduced by air currents, the Ti:Saph laser was housed in a stainless-steel enclosure with o-ring sealed electrical feedthroughs and laser ports. All optical components were epoxied into mirror mounts that were mounted onto a temperature-stabilized Invar baseplate. To minimize phase noise in the comb offset frequency, the amplitude noise in the output of the Verdi pump laser was lowered by modifying the laser's power supply. Coupling to the air-silica microstructure fiber was stabilized by splicing the ends of the fiber to larger diameter single-mode fiber. In addition, tracking oscillators were used to improve signal-to-noise ratios of all beat frequencies with the comb.

The improved stability obtained from the iodine reference allowed for longer scan patterns to be implemented. Previously, when stability was derived from the ^3He reference, pairs of transitions were measured using an *ABBA* scan pattern. By switching to an *ABCCBA* sequence, values for all three fine structure intervals and optical transition frequencies were obtained from half the number of linescans. In addition, for all data sets, measurements of the P_1 Zeeman splitting and light-pressure shift δ_{LP} were obtained almost concurrently with values of the intervals and optical transition frequencies. As a result, the uncertainty in measurements of δ_{LP} are now statistics-limited; their contribution to the uncertainties of the zero-pressure intercepts has been reduced by a factor of 8 to less than 100 Hz.

Many modifications reduced the impact of the scan diode laser's amplitude noise on measurements of the helium transitions. First, the modulation frequency was increased from 1.5 kHz to 38 kHz, where the amplitude noise is more than a factor

of 10 lower. Second, the use of an autobalanced photodetector canceled amplitude noise that was more than 3 dB above the shot noise limit. Last, an improved layout of the optical components reduced sensitivity to acoustical noise and drift.

Switching to equal-weighted fits of the linescans reduced the scatter of the fitted center frequencies by 50%. In addition, several changes made to the data-taking procedure increased by a factor of 10 the rate at which data was taken. These changes include a faster lock-detector for the offset-lock PLL and faster data transmission over the GPIB bus.

9.2 Preparing the Way for Improved Spectroscopy of the $2^3S - 2^3P_J$ Transitions

The greatly increased experimental precision achieved here is an important step toward a more accurate measurement of the 2^3P fine structure intervals and $2^3S - 2^3P_J$ optical transition frequencies. A comparison of known systematics reveals that most of the effects studied in this work have error contributions that are close to, if not below, the statistical uncertainties. This comparison also shows that shifts due to beam misalignment and the linescan asymmetry are the dominant systematic effects. Presented are some ways to improve our understanding of these effects as well as some ideas for eliminating them. Other upgrades to the apparatus are also discussed.

	$2^3P_1 - 2^3P_2$	$2^3P_0 - 2^3P_1$	$2^3P_0 - 2^3P_2$
Zero-Pressure Intercept	0.00(12)	0.00(18)	0.00(19)
Typical δ_{LP}	2.56(3)	2.56(3)	0.00(0)
Typical Zeeman Shift	-1 330.018(5)	527.782(2)	-802.235(3)
Magnetic Field Inhomogeneity	<0.000(1)	<0.000(1)	<0.000(1)
Laser Beam Alignment	0.00(7)	0.00(22)	0.00(18)
Asymmetry	≥ 2.78	≥ 0.87	≥ 1.90
AC Stark Shift	0.36(9)	-0.25(5)	0.12(5)
RF Discharge Power Shift	0.00(18)	0.00(18)	0.00(18)
Polarization Shift	0.00(10)	0.00(10)	0.00(10)

Table 9.1: Table of uncertainties and systematic frequency corrections for measurements of the three 2^3P fine structure intervals. All values are in kHz.

9.2.1 Comparison of Known Systematic Effects

Table 9.1 summarizes the uncertainties and frequency corrections for measurements of the 2^3P fine structure intervals. The biggest effect is due to the residual linescan asymmetry. Here, the inability to justify the use of the dispersive lineshape (see Section 8.2.3) for analyzing these shifts prevents us from determining an upper bound for the effect. Nevertheless, shifts between 0.9 kHz and 2.8 kHz when the dispersive lineshape is used are significantly larger than any other error source.

To minimize the effects of the $m = \pm 1$ peak imbalance, values quoted in Table 9.1 are taken from the data set at the smaller magnetic field of 55 Gauss. The uncertainties of the zero-pressure intercepts, which include uncertainties for light-pressure shifts and nonlinear Zeeman shifts, are statistics-limited. The typical values of the light-pressure shift δ_{LP} and Zeeman shift are taken from the data run at 40 mtorr.

Table 9.2 summarizes the uncertainties and frequency corrections for measurements of the $2^3S - 2^3P_J$ optical transition frequencies. The two largest effects are due to beam misalignment and the linescan asymmetry. The 6 kHz uncertainty due to beam misalignment corresponds to the more accurate alignment technique of cross-coupling into single-mode fibers. In addition, drift in the beam alignment limits the resolution of several other systematic studies, including linear pressure shifts, discharge shifts, and polarization shifts. For the linescan asymmetry, shifts as large as 5 kHz are obtained when the dispersive lineshape is assumed. Again, the inability to justify this lineshape prevents us from obtaining an upper bound for this shift.

Values presented in Table 9.2 are taken from the data set at the lower magnetic field of 55 Gauss for two reasons. First, the smaller magnetic field, compared to

	$2^3S - 2^3P_0$	$2^3S - 2^3P_1$	$2^3S - 2^3P_2$
Zero-Pressure Intercept	0.00(49)	0.00(44)	0.00(46)
GPS Calibration	0.00(30)	0.00(30)	0.00(30)
Typical δ_{LP}	-7.97(18)	-10.62(24)	-10.62(24)
Typical Zeeman Shift	-137.127(1)	-664.527(2)	664.527(2)
Magnetic Field Inhomogeneity	<0.000(1)	<0.000(1)	<0.000(1)
Asymmetry	≥ 3.83	≥ 4.75	≥ 2.15
Pump/Probe Frequency Offset	1000.00	1000.00	1000.00
AC Stark Shift	-0.23(6)	-0.15(9)	-0.51(9)
Recoil Shift	-42.47	-42.46	-42.46
2nd Order Doppler Shift	2.88(20)	2.88(20)	2.88(20)
Beam Alignment	0.00(600)	0.00(600)	0.00(600)
Beam Alignment Drift	0.00(50)	0.00(50)	0.00(50)
RF Discharge Power Shift	0.00(57)	0.00(57)	0.00(57)
Polarization Shift	0.00(25)	0.00(25)	0.00(25)

Table 9.2: Table of uncertainties and systematic frequency corrections for measurements of the three $2^3S - 2^3P_J$ optical transition frequencies. All values are in kHz.

108 Gauss, minimizes shifts due to the $m = \pm 1$ peak imbalance. Second, the more accurate beam alignment technique was used for this data set. Uncertainties for the zero-pressure intercepts include uncertainties due to light-pressure shifts, Zeeman shifts, and the GPS calibration. Values for the typical Zeeman shift and light-pressure shift are taken from the data point at 40 mtorr. A 1 MHz shift corrects for the 2 MHz offset between the frequencies of the pump and probe beams. Kinematic corrections for the recoil shift and second-order Doppler shift (see Section 6.2) are computed from the atomic mass of helium, the mean thermal speed of helium atoms at room temperature, and the optical transition frequencies. A 150 Hz uncertainty in the second-order Doppler shift accounts for a 10% variation in the gas temperature due to heating of the cell by the discharge.

9.2.2 Understanding and Eliminating the Dominant Systematic Effects

Several new systematic effects discovered during the course of this work are now the largest contributors to the experimental uncertainties. It is imperative that these systematics be understood, eliminated, or corrected in order to attain more accurate measurements of the fine structure intervals and optical transition frequencies. Once problems associated with these systematics are solved, accuracies as low as a few hundred Hz could be achieved for measurements of the fine structure intervals. For measurements of the optical transition frequencies, sub-kHz accuracies are possible.

The inability to assign a physical mechanism to the presence of the linescan asymmetry remains one of the most immediate problems at hand. Attempts to model the

asymmetry as a result of self-focusing of the laser beams by the helium gas led to predictions that were smaller than observed results by more than 3 orders of magnitude. However, one assumption made in the model may be responsible for this disagreement. Specifically, a Taylor expansion of the laser beam profile was made in order to make a differential equation describing the beam propagation through the gas solvable by analytic means. With this Taylor expansion made, the beam profile is flat to lowest order, preventing any significant self-focusing from occurring. By using the full mathematical form of the profile, the propagation of the beams through the gas must be solved numerically. Other groups have had success in modeling self-focusing using fully numerical methods [137]. These techniques should be tried here.

Once a physical mechanism has been found, whether it be self-focusing or some other effect, the true lineshape of the asymmetry can be determined. In addition, dependencies on pressure and optical power can be obtained and compared to observations. From this, upper bounds can be placed on the size of the resulting frequency shifts.

Two solutions to eliminate beam misalignment shifts have been proposed. The first approach is to place the helium cell inside of a Fabry-Perot cavity. Here, laser power can only propagate along the longitudinal modes of the cavity, resulting in a pair of well-collimated counterpropagating beams. The approach has been successfully used to accurately measure weak overtone transitions in molecules [138, 139, 140].

Although placing the cell inside a cavity would ensure a much more accurate beam alignment, a significant decrease in signal size is also expected. For a 1 meter cavity, the fundamental Gaussian mode has a waist of approximately 1 mm, 10 times

smaller than the 10 mm waist currently used in the experiment. This has two important consequences. First, the laser beams will interact with 100-times fewer atoms, significantly decreasing signal size. Second, the intracavity laser power will also need to be reduced by a factor of 100 to $1 \mu\text{W}$ in order to achieve a saturation parameter less than unity. Assuming a cavity with a Q of 10, only $0.1 \mu\text{W}$ is transmitted through the cavity. Detecting this little laser power at the shot-noise level is unfeasible with room-temperature PIN photodetectors. For comparison, the autobalanced photodetector used in the experiment can detect $3 \mu\text{W}$ at the shot-noise level, but only after the feedback of the front-end transimpedance amplifier was modified.

A second approach to removing beam alignment shifts is to generate pump and probe beams by retroreflecting a single beam through the cell with a cat's-eye system. These optical setups are known for producing strictly parallel incident and reflected beams.

One downside to retroreflection is that generating an experimental signal by amplitude modulating the pump beam may lead to different intensities for pump and probe beams. Here, the amplitude modulation must be applied after the laser beam has passed once through the cell, otherwise both pump and probe beams will be modulated. After passing through the cell, part of the unmodulated probe beam must be deflected for detection before being modulated and retroreflected. In this situation, the retroreflected pump beam will have a smaller intensity than the incoming probe beam.

An alternative to amplitude modulation is frequency modulation of both pump and probe beams, which is typically done for derivative spectroscopy. Although this

approach is easy to implement experimentally with a retroreflector, the downside is that the in-phase and quadrature components of the experimental signals have even and odd symmetry, respectively, about the linecenter. If the lock-in phase is not chosen carefully, the symmetric absorption profile may contain a small asymmetric dispersive component, leading to systematic frequency shifts.

9.2.3 Improving Experimental Resolution

Although a significant improvement in experimental resolution was achieved, many more improvements in the signal-to-noise ratio, clock stability, and data-taking rate could further improve resolution. Some potential future upgrades are presented here.

Although the stability achieved with the iodine reference was more than sufficient for the experiment, other groups using similar setups have obtained instabilities up to 5 times lower [54, 63, 76, 141]. One possible source of instability in the iodine reference is distorted windows on the iodine cell. These windows modify the pump and probe beam profiles upon entering the cell, limiting the signal size due to poor overlap of the beams. The performance of the iodine reference could be improved by simply replacing the cell with one that has flatter windows.

Improving the long-term stability of the optical frequency comb is always a major goal of the experiment. The stability of the comb is currently limited by dirt that accumulates on the face of the Ti:saph crystal, resulting in a slow degradation of the laser's output power that affects the spectral broadening of the femtosecond pulses and ultimately the signal-to-noise of all beat frequencies with the comb. The effect is likely due to the dipole force exerted on small particles of dust by the high intensities

of the Ti:Saph pump beam.

This effect could be slowed by reducing the Ti:Saph pump power. One way to achieve this is to switch to a longer crystal that more efficiently absorbs pump power. The downside to this approach is that the intracavity mirrors would also need to be replaced in order to compensate for the extra dispersion of the longer crystal.

Another approach to improving the performance of the optical frequency comb is to replace the Ti:Saph laser with a femtosecond fiber laser. Not only can these lasers run uninterruptedly for several consecutive days, but they are significantly easier to operate due to the lack of external-cavity mirrors that need aligning. In addition, fiber lasers tend to be less sensitive to acoustical noise and drift compared to their external-cavity counterparts.

Two changes to the helium apparatus could improve signal-to-noise ratio by 6 dB. First, active stabilization of the pump and probe laser intensities could reduce the laser amplitude noise by 3 dB compared to what is achievable using the autobalanced photodetector [70]. Second, the use of a 50/50 beamsplitter plate to separate the probe and pump beams (see Fig. 5.15) results in half the probe beam being discarded. The corresponding loss in SNR is 3 dB. Two ways to prevent or limit this loss are to use a beamsplitter plate with a different reflection/transmission ratio or to use an optical isolator to separate the laser beams [50].

9.3 Measurements of the $2^3S - 3^3P_J$ Fine Structure Intervals and Optical Transition Frequencies

One way to address the discrepancy between theory and experiment for the 2^3P fine structure splittings is to more accurately measure the 3^3P fine structure splittings. Experimentally, the f_{12} and f_{01} intervals have been measured with uncertainties of 18 kHz and 28 kHz, respectively [142]. A measurement of these fine structure splittings could be performed using our apparatus to an accuracy that is as good, if not better, than the 6 kHz accuracy of current theoretical calculations. A measurement of the 3^3P intervals at this level could reveal a discrepancy between theory and experiment that is similar in size to the 14 kHz and 6 kHz discrepancies for the corresponding 2^3P fine structure intervals.

Experimentally, the 3^3P_J states are accessed from the metastable 2^3S_1 state using radiation at 389 nm. Light at this wavelength can be obtained by frequency-doubling the 778 nm output of a diode laser or Ti:Saph laser. The presence of strong frequency comb components at this wavelength makes stabilizing the laser to the comb convenient. In addition, identical angular momenta quantum numbers gives rise to an energy level structure that is identical to that of the 2^3P multiplet. As a result, the techniques used here to measure Zeeman splittings, calculate nonlinear Zeeman shifts, and correct for light-pressure shifts could be implemented in the same way.

By incorporating the optical frequency comb into the experiment, the optical frequencies of the $2^3S - 3^3P_J$ transitions can be accurately measured. These transitions have been measured with respect to a calibrated 2-photon Rb standard to an

accuracy of 190 kHz [143]. Even with beam misalignment shifts and the linescan asymmetry, it seems possible to measure these transitions 10 times more accurately to an uncertainty of 20 kHz.

9.4 Conclusions

The 2^3P fine structure intervals and $2^3S - 2^3P_J$ optical transition frequencies in helium can now be measured with precisions at the 100 Hz level, representing a major step toward more accurate measurements of these frequencies. Studies of several systematic effects show that accuracies at the level of a few hundred Hz are certainly attainable in the near future. For the dominant systematics, a new optical layout to improve beam alignment seems reasonable to implement and very likely to succeed in removing misalignment shifts. In addition, there is still much to be learned about self-focusing and the linescan asymmetry. However, we are optimistic that future improvements in our understanding will lead to novel techniques to correct for or eliminate this effect.

A measurement of the fine structure intervals at the level of 200 Hz would not only be the most accurate measurement of an atomic fine structure interval, but its uncertainty would match that of theoretical predictions for these frequencies. Once the discrepancies between theory and experiment have been resolved, this measurement would determine the fine structure constant α to less than 4 ppb. Only the determination from the electron g-factor would be more accurate. Similarly, a measurement of the $2^3S - 2^3P_J$ optical transitions at this level of accuracy would be the most accurate measurement of an optical transition frequency in helium. By improv-

ing experimental precision and our understanding of systematic effects, this work has set the stage for these future measurements to become reality. We are confident that they are not far off.

Bibliography

- [1] Scott A. Diddams, David J. Jones, Jun Ye, Steven T. Cundiff, John L. Hall, Jinendra K. Ranka, Robert S. Windeler, Ronald Holzwarth, Thomas Udem, and T. W. Hänsch, *Phys. Rev. Lett.* **84**, 5102 (2000).
- [2] J. Reichert, M. Niering, R. Holzwarth, M. Weitz, Th. Udem, and T.W. Hänsch, *Phys. Rev. Lett.* **84**, 3232 (2000).
- [3] R. Holzwarth, Th. Udem, T. W. Hänsch, J. C. Knight, W. J. Wadsworth, and P. St. J. Russell, *Phys. Rev. Lett.* **85**, 2264 (2000).
- [4] David J. Jones, Scott A. Diddams, Jinendra K. Ranka, Andrew Stentz, Robert S. Windeler, John L. Hall, and Steven T. Cundiff, *Science* **288**, 635 (2000).
- [5] V. Gerginov, C.E. Tanner, S.A.Diddams, A.Bartels, and L.Hollberg, *Opt. Lett.* **30**, 1734 (2005).
- [6] R. Holzwarth, A.Yu. Nevsky, M. Zimmermann, Th. Udem, T.W. Hänsch, J. Von Zanthier, H. Walther, J.C. Knight, W.J. Wadsworth, P.St.J. Russell, M.N. Skvortsov, and S.N. Bagayev, *Appl. Phys. B* **73**, 269 (2001).
- [7] S.A. Diddams, Th. Udem, J.C. Bergquist, E.A. Curtis, R.E. Drullinger, L. Hollberg, W.M. Itano, W.D. Lee, C.W. Oates, K.R. Vogel, and D.J. Wineland, *Science* **293**, 825 (2001).
- [8] Th. Udem, S.A. Diddams, K.R. Vogel, C.W. Oates, E.A. Curtis, W.D. Lee, W.M. Itano, R.E. Drullinger, J.C. Bergquist, and L. Hollberg, *Phys. Rev. Lett.* **86**, 4996 (2001).
- [9] Andrew D. Ludlow, Martin M. Boyd, Tanya Zelevinsky, Seth M. Foreman, Sebastian Blatt, Mark Notcutt, Tetsuya Ido, and Jun Ye, *Phys. Rev. Lett.* **96**, 033003 (2006).
- [10] Jörn Stenger, Christian Tamm, Nils Haverkamp, Stefan Weyers, and Harald R. Telle, *Opt. Lett.* **26**, 1589 (2001).

-
- [11] Adela Marian, Matthew C. Stone, Daniel Felinto, and Jun Ye, *Phys. Rev. Lett.* **95**, 023001 (2005).
- [12] P. Cancio Pastor, G. Giusfredi, P. De Natale, G. Hagel, C. de Mauro, and M. Inguscio, *Phys. Rev. Lett.* **92**, 023001 (2004).
- [13] T. Zelevinsky, D. Farkas, and G. Gabrielse, *Phys. Rev. Lett.* **95**, 203001 (2005).
- [14] Peter J. Mohr and Barry N. Taylor, *Rev. Mod. Phys.* **77**, 1 (2005).
- [15] B. Odom, D. Hanneke, B. D’Urso, and G. Gabrielse, *Phys. Rev. Lett.* **97**, 030801 (2006).
- [16] G. Gabrielse, D. Hanneke, T. Kinoshita, M. Nio, and B. Odom, *Phys. Rev. Lett.* **97**, 030802 (2006).
- [17] R. S. VanDyck, P. B. Schwinberg, and H. G. Dehmelt, *Phys. Rev. Lett.* **59**, 26 (1987).
- [18] W. Liu *et al.*, *Phys. Rev. Lett.* **82**, 711 (1999).
- [19] Krzysztof Pachucki and Jonathan Sapirstein, *J. Phys. B* **33**, 5297 (2000).
- [20] G. W. F. Drake, *Can. J. Phys.* **80**, 1195 (2002).
- [21] K. Pachucki, *Phys. Rev. Lett.* **97**, 013002 (2006).
- [22] Michael P. Bradley, James V. Porto, Simon Rainville, James K. Thompson, and David E. Pritchard, *Phys. Rev. Lett.* **83**, 4510 (1999).
- [23] Andreas Wicht, Joel M. Hensley, Edina Sarajlic, and Steven Chu, *Phys. Scr.* **102**, 82 (2002).
- [24] Pierre Cladé, Estefania de Mirandes, Malo Cadoret, Saïda Guellati-Khélifa, Catherine Schwob, François Nez, Lucile Julien, and François Biraben, *Phys. Rev. Lett.* **96**, 033001 (2006).
- [25] E. Krüger, W. Nistler, and W. Weirauch, *Metrologia* **36**, 147 (1999).
- [26] K. von Klitzing, G. Dorda, and M. Pepper, *Phys. Rev. Lett.* **45**, 494 (1980).
- [27] Peter J. Mohr and Barry N. Taylor, *Rev. Mod. Phys.* **72**, 351 (2000).
- [28] B. D. Josephson, *Phys. Lett.* **1**, 251 (1962).
- [29] Gordan W. F. Drake, in *Long-Range Casimir Forces*, edited by Frank S. Levin and David A. Micha (Plenum Press, New York, 1993), Chap. High-Precision Calculations for the Rydberg States of Helium, pp. 107–214.

- [30] E. Borie and G.A. Rinker, *Phys. Rev. A* **18**, 324 (1978).
- [31] H. A. Bethe and E. E. Salpeter, *Quantum Mechanics of One- and Two-Electron Atoms, 2nd edition* (Plenum, New York, 1977).
- [32] G.W.F. Drake and W.C. Martin, *Can. J. Phys.* **76**, 679 (1998).
- [33] Krzysztof Pachucki, *Phys. Rev. Lett.* **84**, 4561 (2000).
- [34] Krzysztof Pachucki, *J. Phys. B* **35**, 3087 (2002).
- [35] F. M. J. Pichanick, R. D. Swift, C. E. Johnson, and V. W. Hughes, *Phys. Rev.* **169**, 55 (1968).
- [36] S. A. Lewis, F. M. J. Pichanick, and V. W. Hughes, *Phys. Rev. A* **2**, 86 (1970).
- [37] A. Kponou, V. W. Hughes, C. E. Johnson, S. A. Lewis, and F. M. J. Pichanick, *Phys. Rev. A* **24**, 264 (1981).
- [38] W. Frieze, E. A. Hinds, V. W. Hughes, and F. M. J. Pichanick, *Phys. Rev. A* **24**, 279 (1981).
- [39] D. Shiner, R. Dixon, and P. Zhao, *Phys. Rev. Lett.* **72**, 1802 (1994).
- [40] D. Shiner and R. Dixon, *IEEE Trans. Instrum. Meas.* **44**, 518 (1995).
- [41] J. Castilleja, D. Livingston, A. Sanders, and D. Shiner, *Phys. Rev. Lett.* **84**, 4321 (2000).
- [42] C. H. Storry, M. C. George, and E. A. Hessels, *Phys. Rev. Lett.* **84**, 3274 (2000).
- [43] M. C. George, L. D. Lombardi, and E. A. Hessels, *Phys. Rev. Lett.* **87**, 173002 (2001).
- [44] G. Giusfredi, P. De Natale, D. Mazzotti, P. Cancio Pastor, C. de Mauro, L. Fallani, G. Hagel, V. Krachmalnicoff, and M. Inguscio, *Can. J. Phys.* **83**, 301 (2005).
- [45] F. Minardi, M. Artoni, P. Cancio, M. Inguscio, G. Giusfredi, and I. Carusotto, *Phys. Rev. A* **60**, 4164 (1999).
- [46] P. Juncar, H.G. Berry, R. Damaschini, and H.T. Duong, *J. Phys. B* **16**, 381 (1983).
- [47] E. Giacobino and F. Biraben, *J. Phys. B* **15**, L385 (1982).
- [48] Ping Zhao, J.R. Lawall, A.W. Kam, M.D. Lindsay, F.M. Pipken, and W. Lichten, *Phys. Rev. Lett.* **63**, 1593 (1989).

- [49] D.A. Howe, D.W. Allan, and J.A. Barnes, Properties of Oscillator Signals and Measurement Methods, <http://tf.nist.gov/timefreq/phase/Properties/main.htm> (accessed June 2002).
- [50] G. Bianchini, P. Cancio, F. Minardi, F.S. Pavone, F. Perrone, M. Prevedelli, and M. Inguscio, *Appl. Phys. B* **66**, 407 (1998).
- [51] B.C. Young, F.C. Cruz, W.M. Itano, and J.C. Bergquist, *Phys. Rev. Lett.* **82**, 3799 (1999).
- [52] Jun Ye, Tai Hyun Yoon, John L. Hall, Alan A. Madej, John E. Bernard, Klaus J. Siemsen, Louis Marmet, Jean-Marie Chartier, and Annick Chartier, *Phys. Rev. Lett.* **85**, 3797 (2000).
- [53] J. Ye, L. S. Ma, and J. L. Hall, *Phys. Rev. Lett.* **87**, 270801 (2001).
- [54] Mark L. Eickhoff and J.L. Hall, *IEEE Trans. Instrum. Meas.* **44**, 155 (1995).
- [55] Feng-Lei Hong, Jun Ishikawa, Jun Yoda, Jun Ye, Long-Sheng Ma, and John L. Hall, *IEEE Trans. Instrum. Meas.* **48**, 532 (1999).
- [56] John L. Hall, Long-Sheng Ma, Matthew Taubman, Bruce Tiemann, Feng-Lei Hong, Oliver Pfister, and Jun Ye, *IEEE Trans. Instrum. Meas.* **48**, 583 (1999).
- [57] Thomas J. Kane and Robert L. Byer, *Opt. Lett.* **10**, 65 (1985).
- [58] Axel Schenzle, Ralph G. DeVoe, and Richard G. Brewer, *Phys. Rev. A* **25**, 2606 (1982).
- [59] G.C. Bjorklund and M.D. Levenson, *Phys. Rev. A* **24**, 166 (1981).
- [60] J.L. Hall, L. Hollberg, T. Baer, and H.G. Robinson, *Appl. Phys. Lett.* **39**, 680 (1981).
- [61] Jon H. Shirley, *Opt. Lett.* **7**, 537 (1982).
- [62] G. Camy, Ch.J. Borde, and M. Ducloy, *Opt. Commun.* **41**, 325 (1982).
- [63] Susanne Picard, Lennart Robertsson, Long-Sheng Ma, Kaj Nyholm, Mikko Merimaa, Tero E. Ahola, Petr Balling, Petr Kren, and Jean-Pierre Wallerand, *Appl. Opt.* **42**, 1019 (2003).
- [64] R.K. Raj, D. Bloch, J.J. Snyder, G. Camy, and M. Ducloy, *Phys. Rev. Lett.* **44**, 1251 (1980).
- [65] J.J. Snyder, R.K. Raj, D. Bloch, and M. Ducloy, *Opt. Lett.* **5**, 163 (1980).

-
- [66] M. Ducloy and D. Bloch, *J. Phys.* **43**, 57 (1981).
- [67] Esa Jaatinen, *Opt. Commun.* **120**, 91 (1995).
- [68] Thomas J. Kane, Alan C. Nilsson, and Robert L. Byer, *Opt. Lett.* **12**, 175 (1987).
- [69] *Lightwave Electronics Series 125/126 User's Manual*, Lightwave Electronics, Mountain View, CA.
- [70] Philip C. D. Hobbs, *Appl. Opt.* **36**, 903 (1997).
- [71] Robert W. Boyd, *Nonlinear Optics* (Academic Press, New York, 1992).
- [72] W.J. Kozlovksy, C.D. Nabors, and R.L. Byer, *Opt. Lett.* **12**, 1014 (1987).
- [73] M.M. Fejer, G.A. Magel, D.H. Jundt, and R.L. Byer, *IEEE J. Quantum Electron.* **28**, 2631 (1992).
- [74] Dieter H. Jundt, *Opt. Lett.* **22**, 1553 (1997).
- [75] Y. Furukawa, K. Kitamura, S. Takekawa, A. Miyamoto, and N. Suda, *Appl. Phys. Lett.* **77**, 2494 (2000).
- [76] Feng-Lei Hong, Jun Ishikawa, Zhi-Yi Bi, Jing Zhang, Katuo Seta, Atsushi Onae, Jun Yoda, and Hirokazu Matsumoto, *IEEE Trans. Instrum. Meas.* **50**, 486 (2001).
- [77] Christopher C. Davis, *Lasers and Electro-Optics: Fundamentals and Engineering* (Cambridge University Press, New York, 2000).
- [78] Edward A. Whittaker, Manfred Gehrtz, and Gary C. Bjorklund, *J. Opt. Soc. Am. B* **2**, 1320 (1985).
- [79] E. Jaatinen and J.-M. Chartier, *Metrologia* **35**, 75 (1998).
- [80] Louis J. Gillepsie and H.D. Fraser, *J. Am. Chem. Soc.* **58**, 2260 (1936).
- [81] Jun Ye, Long-Sheng Ma, Lennart Robertsson, Susanne Picard, and John L. Hall, *IEEE Trans. Instrum. Meas.* **48**, 544 (1999).
- [82] Thanks to Ron Walsworth and David Phillips of the Harvard-Smithsonian Center for Astrophysics for providing the maser.
- [83] C.R. Pollack, D.A. Jennings, F.R. Peterson, J.S. Wells, R.E. Drullinger, E.C. Beaty, and K.M. Evenson, *Opt. Lett.* **8**, 133 (1983).

-
- [84] D.A. Jennings, C.R. Pollack, F.R. Petersen, R.E. Drullinger, K.M. Evensen, J.S. Wells, J.L. Hall, and H.P. Layer, *Opt. Lett.* **8**, 136 (1983).
- [85] L. Hollberg, C.W. Oates, G. Wilpers, C.W. Hoyt, Z.W. Barber, S.A. Diddams, W.H. Oskay, and J.C. Bergquist, *J. Phys. B* **38**, S469 (2005).
- [86] J.N. Eckstein, A.I. Ferguson, and T.W. Hänsch, *Phys. Rev. Lett.* **40**, 847 (1978).
- [87] Jinendra K. Ranka, Robert S. Windeler, and Andrew J. Stentz, *Opt. Lett.* **25**, 25 (2000).
- [88] Jinendra K. Ranka, Robert S. Windeler, and Andrew J. Stentz, *Opt. Lett.* **25**, 796 (2000).
- [89] V. Gerginov, K. Calkins, C.E. Tanner, J.J. McFerran, S. Diddams, A. Bartels, and L. Hollberg, *Phys. Rev. A* **73**, 032504 (2006).
- [90] Th. Udem, J. Reichert, R. Holzwarth, and T.W. Hänsch, *Phys. Rev. Lett.* **82**, 3568 (1999).
- [91] M. Niering, R. Holzwarth, J. Reichert, P. Pokasov, Th. Udem, M. Weitz, T. W. Hänsch, P. Lemonde, G. Santarelli, M. Abgrall, P. Laurent, C. Salomon, and A. Clairon, *Phys. Rev. Lett.* **84**, 5496 (2000).
- [92] Long-Sheng Ma, Zhiyi Bi, Albrecht Bartels, Lennart Robertsson, Massimo Zucco, Robert S. Windeler, Guido Wilpers, Chris Oates, Leo Hollberg, and Scott A. Diddams, *Science* **303**, 1843 (2004).
- [93] Scott A. Diddams, L. Hollberg, Long-Sheng Ma, and Lennart Robertsson, *Opt. Lett.* **27**, 58 (2002).
- [94] Th. Udem, J. Reichert, R. Holzwarth, and T.W. Hänsch, *Opt. Lett.* **24**, 881 (1999).
- [95] Jun Ye, John L. Hall, and Scott A. Diddams, *Opt. Lett.* **25**, 1675 (2000).
- [96] A. Bartels, C.W. Oates, L. Hollberg, and S.A. Diddams, *Opt. Lett.* **29**, 1081 (2004).
- [97] Daniel Farkas and Gerald Gabrielse, *Proceedings of the 2005 IEEE International Frequency Control Symposium*, (2006).
- [98] Steven T. Cundiff, Jun Ye, and John L. Hall, *Rev. Sci. Instrum.* **72**, 3749 (2001).
- [99] L. Xu, Ch. Spielmann, A. Poppe, T. Brabec, F. Krausz, and T.W. Hänsch, *Opt. Lett.* **21**, 2008 (1996).

- [100] Nicolai Matuschek, Franz X. Kärtner, and Ursula Keller, *IEEE J. Quantum Electron.* **4**, 197 (1998).
- [101] A. Bartels, T. Dekorsy, and H. Kurz, *Opt. Lett.* **24**, 996 (1999).
- [102] R. Ell, U. Morgner, F.X. Kärtner, J.G. Fujimoto, E.P. Ippen, V. Scheuer, G. Angelow, T. Tschudi, M. J. Lederer, A. Boiko, and B. Luther-Davies, *Opt. Lett.* **26**, 373 (2001).
- [103] Kevin W. Holman, R. Jason Jones, Adela Marian, Steven T. Cundiff, and Jun Ye, *Opt. Lett.* **28**, 851 (2003).
- [104] J. D. Jackson, *Classical Electrodynamics, 2nd Edition* (John Wiley and Sons, Inc., New York, 1975).
- [105] *GigaJet 30 Ultracompact 3 GHz Femtosecond Ti:Sapphire laser: User's manual*, GigaOptics GmbH, Mülheim, Germany.
- [106] *Verdi V-8/V-10 Diode-Pumped Lasers: Operator's Manual*, Coherent Laser Group, Santa Clara, CA.
- [107] Picture taken from certificate of conformity for NL-2.0-760 microstructure fiber (Crystal Fibre A/S).
- [108] Connectorization done by Crystal Fibre A/S.
- [109] Roland E. Best, *Phase-Locked Loops* (McGraw-Hill, New York, 1999).
- [110] M. Prevedelli, T. Freearge, and T.W. Hänsch, *Appl. Phys. B* **60**, S241 (1995).
- [111] Technical report, ADF4110/ADF4111/ADF4112/ADF4113 RF PLL Frequency Synthesizers, Analog Devices, Inc. (unpublished).
- [112] Technical report, An Analysis and Performance Evaluation of a Passive Filter Design Technique for Charge Pump PLLs, National Semiconductor Corporation (unpublished).
- [113] Tanya Zelevinsky, Ph.D. thesis, Harvard University, 2004.
- [114] K.G. Libbrecht and J.L. Hall, *Rev. Sci. Instrum.* **64**, 2133 (1993).
- [115] Wolfgang Demtröder, *Laser Spectroscopy* (Springer-Verlag, Berlin, 1998).
- [116] Harold J. Metcalf and Peter van der Straten, *Laser Cooling and Trapping* (Springer, New York, 1999).
- [117] V. S. Letokhov and V. P. Chebotayev, *Nonlinear Laser Spectroscopy, Springer Ser. Opt. Sci. 4* (Springer, London, 1977).

-
- [118] R. Grimm and J. Mlynek, *Phys. Rev. Lett.* **63**, 232 (1989).
- [119] Zong-Chao Yan and G. W. F. Drake, *Phys. Rev. A* **50**, R1980 (1994).
- [120] K.E. Gibble and A. Gallagher, *Phys. Rev. A* **43**, 1366 (1991).
- [121] C. Brechignac, R. Vetter, and P.R. Berman, *Phys. Rev. A* **17**, 1609 (1978).
- [122] P.W. Smith and T. Hänsch, *Phys. Rev. Lett.* **26**, 740 (1972).
- [123] M. Pinard, C.G. Aminoff, and F.Laloë, *Phys. Rev. A* **19**, 2366 (1979).
- [124] Michel Gorlicki, Christian Lermينياux, and Michel Dumont, *Phys. Rev. Lett.* **49**, 1394 (1982).
- [125] William H. Press, Saul A. Teukolsky, William T. Vetterling, and Brian P. Flannery, *Numerical Recipes in C: The Art of Scientific Computing* (Cambridge University Press, New York, 1988-1992).
- [126] U. Kortshagen, N.D. Gibson, and J.E. Lawler, *J. Phys. D* **29**, 1224 (1996).
- [127] Francis Chen, *Introduction to Plasma Physics* (Plenum Press, New York, 1974).
- [128] James Lawler, private communication.
- [129] Tanya Zelevinsky, private communication.
- [130] Jun Ye, private communication.
- [131] Pierre Cérez and Raymond Felder, *Appl. Opt.* **22**, 1251 (1973).
- [132] Lennart Robertsson, *J. Mod. Opt.* **41**, 1327 (1994).
- [133] Amnon Yariv, *Quantum Electronics* (John Wiley and Sons, New York, 1989).
- [134] M. Glaser, *IEEE Trans. Instrum. Meas.* **36**, 604 (1987).
- [135] Dmitry Budker, Derek F. Kimball, and David P. DeMille, *Atomic Physics* (Oxford University Press, New York, 2004).
- [136] Jake Taylor, private communication.
- [137] C.F. McCormick, D.R. Solli, R.Y. Chiao, and J.M. Hickmann, *Phys. Rev. A* **69**, 023804 (2004).
- [138] Jun Ye, Long-Sheng Ma, and John L. Hall, *Opt. Lett.* **21**, 1000 (1996).
- [139] Jun Ye, Long-Sheng Ma, and John L. Hall, *J. Opt. Soc. Am. B* **15**, 6 (1998).

-
- [140] Long-Sheng Ma, Jun Ye, Pierre Dube, and John L. Hall, *J. Opt. Soc. Am. B* **16**, 2255 (1999).
- [141] Gianluca Galzerano, Elio Bava, Marco Bisi, Fabrizio Bertinetto, and Cesare Svelto, *IEEE Trans. Instrum. Meas.* **48**, 540 (1999).
- [142] P. Mueller, L.-B. Wang, G.W.F Drake, K. Bailey, Z.-T. Lu, and T.P. O'Connor, *Phys. Rev. Lett.* **94**, 133001 (2005).
- [143] F.S. Pavone, F. Marin, P. De Natale, and M. Inguscio, *Phys. Rev. Lett.* **73**, 42 (1994).